Studying Charge Production in a Liquid Argon Time Projection Chamber



Fabio Spagliardi

New College

University of Oxford

A thesis submitted for the degree of

Doctor of Philosophy

Michaelmas 2021

Studying Charge Production in a Liquid Argon Time Projection Chamber

Fabio Spagliardi

New College
University of Oxford

A thesis submitted for the degree of Doctor of Philosophy

Michaelmas 2021

Abstract

Liquid Argon Time Projection Chambers (LArTPCs) have become widely used neutrino detectors. They primarily take advantage of the ionisation charge produced by the interaction of charged particles to achieve high spatial resolution and excellent calorimetry reconstruction. LArTPC is the technology chosen by the Deep Underground Neutrino Experiment (DUNE) to investigate challenging open questions in physics, such as the extent of CP violation in the lepton sector and the neutrino mass ordering, through the study of neutrino oscillations. These studies rely on the precise reconstruction of the energy of final-state particles resulting from neutrino interactions. The work in this thesis addresses this topic by looking at the relation between the energy deposited by charged particles and the resulting ionisation charge in the context of the ProtoDUNE-SP experiment. In particular, a selection of fully-reconstructed cosmic muons that stop in the detector was developed. Stopping muons are a useful calibration source, since their energy is precisely known at any point along their trajectory, and can be used for many detector response studies. The result of this selection was used to measure the parameters of two charge recombination models, and the reconstructed dE/dx resulting from both models was compared. The postulated angular dependence of the response was also explored.

Statement of Originality

This thesis and the work presented in it are my own and were produced by me as a result of my own original research. Results and figures from published works by others have been clearly attributed, and this work has not been submitted for another qualification at this or any other university.

Chapter 1 contains a brief introduction to the content of the thesis and it is my own work. Chapter 2 presents an overview of the current status and knowledge in neutrino physics and Chapter 3 presents the ProtoDUNE-SP experiment, whose data are analysed in this thesis. A description of the fundamental processes that culminate with the charge and light creation in liquid argon experiments is contained in Chapter 4 while Chapter 5 provides an overview of the theory relevant to understand cosmic rays and the energy loss of particles through matter. These chapters are a summary of the theory and the background knowledge relevant for the thesis and are the work of others, except for Section 5.4 which is my own work.

The development of a selection of cosmic muons that stop in the ProtoDUNE-SP detector is contained in Chapter 6. The selection is my own work and is based on the reconstruction algorithms developed by others, described and referenced in Chapter 3, particularly from Section 3.8 onward.

The work on the measurement of the charge recombination model parameters in Chapter 7 and in Appendices A, B and C is my own. Similarly to Chapter 6, this work relies on reconstruction tools and calibration factors developed by others, which are described and referenced in the first chapters.

Finally, the conclusions contained in Chapter 8 are my own.

Acknowledgements

The work in this thesis would not have been possible without the help and support of many people. First, I would like to thank my supervisor, Alfons Weber. His guidance and help throughout my DPhil have been fundamental for my progress. I am also grateful to all the members and former members of the Oxford Neutrino Physics group who I had the pleasure to meet. In particular, I want to thank Phil Rodrigues, Aidan Reynolds and Marco Del Tutto for always finding the time to help me, especially when I had just started dealing with the reconstruction software, and Giles Barr for guiding me during my first experience as a lab demonstrator.

I am indebted to the members of the DUNE collaboration, whose guidance throughout these years has been invaluable. Thanks to Leigh Whitehead and Tingjun Yang, for always being there to answer my many questions. I wish to also thank all the members of the DUNE UK office at CERN for making my time there really enjoyable.

I would also like to show my appreciation to the many members of the Particle Physics sub-department. To all the DPhil students, especially those who started with me in 2017, thank you for making these last four years more fun. My life in Oxford and at CERN would have been much harder without the assistance of Sue Geddes and Kim Proudfoot, who are truly outstanding.

Finally, special thanks go to my friends and family for their support.

Contents

List of Figures **v**

List of Tables **xi**

List of Abbreviations **xii**

1 Introduction **1**

2 Neutrino Physics **5**

2.1 History of Neutrino Discoveries 6

2.2 Neutrinos in the Standard Model 14

2.3 Neutrino Interactions 15

2.4 Neutrino Oscillations 16

2.4.1 Oscillations in Vacuum 18

2.4.2 Oscillations in Matter 20

2.4.3 Summary of Current Knowledge of Neutrino Oscillation Parameters 21

2.4.4 Overview of Accelerator Neutrino Experiments 24

3 The ProtoDUNE-SP Experiment **26**

3.1 The Deep Underground Neutrino Experiment 27

3.2 Liquid Argon Time Projection Chambers 30

3.2.1 Charge Detection 31

3.2.2 Light Detection 32

3.3 ProtoDUNE-SP Overview and Goals 32

3.4 Detector . . . 33
3.4.1 The LArTPC . . . 34
3.4.2 The Photon Detection System . . . 36
3.5 Beam Line . . . 39
3.6 Cosmic-Ray Tagger . . . 41
3.7 Data Acquisition, Timing and Trigger . . . 42
3.8 Simulation . . . 44
3.9 Track Object Reconstruction . . . 45
3.9.1 Signal Processing . . . 46
3.9.2 Hit Finding . . . 46
3.9.3 Pattern Recognition . . . 48
3.10 Charge and Energy Calibration . . . 51
3.10.1 Space Charge Effect Calibration . . . 52
3.10.2 Drifting Electron Lifetime . . . 54
3.10.3 Detector Effect Mitigation . . . 55
3.10.4 Calorimetry . . . 57

4 Fundamental Micro-Physics Processes in Liquid Argon 58
4.1 Ionisation and Excitation . . . 59
4.2 Initial Microscopic Fast Processes . . . 60
4.3 Processes Occurring During Drift Time . . . 65
4.4 Electron-Ion Recombination in Liquid Argon . . . 66
4.4.1 Recombination Models . . . 67
4.4.2 Application of Recombination Models to LArTPC detectors . 69

5 Cosmic Muons in ProtoDUNE-SP 75
5.1 Cosmic Ray Overview . . . 75
5.2 Energy Loss of Muons in Liquid Argon . . . 78
5.3 Michel Electrons . . . 81
5.4 Monte Carlo dE/dx: Muon Particle Gun in ProtoDUNE-SP . . . 84

6 A Selection of Stopping Cosmic Muons in ProtoDUNE-SP 89

6.1 Introduction and Motivations . . . 90

6.2 Cathode-Crossing Muons . . . 94

6.3 Anode-Crossing Muons . . . 97

6.3.1 t_0 Calculation . . . 104

6.4 Removing Broken Tracks . . . 104

6.4.1 Multiple Segments . . . 105

6.4.2 Single Segment . . . 106

6.5 Cuts Validation . . . 108

6.6 Summary of the Selected Sample . . . 114

6.7 Michel Electron Contamination . . . 116

6.8 dE/dx Shape Discriminator . . . 118

6.9 Sample Preparation . . . 122

7 Electron-Ion Recombination Studies 124

7.1 Introduction . . . 125

7.2 Monte Carlo Study . . . 126

7.2.1 Simulating Angular Effects . . . 126

7.2.2 Methodology . . . 129

7.2.3 Fit Results . . . 132

7.3 Validation of Method on the ProtoDUNE-SP Monte Carlo . . . 135

7.4 Extracting Recombination Model Parameters . . . 136

7.4.1 Angular Dependence . . . 141

7.5 dE/dx Calculation . . . 145

7.6 Discussion on Systematic Uncertainties . . . 146

7.6.1 Selection Cuts, Reconstruction and Space Charge Effects . . . 147

7.6.2 Electron Lifetime Measurement . . . 151

7.6.3 Determination of the Calibration Constant C_{cal} . . . 153

7.6.4 Effect of δ-rays . . . 155

7.7 Conclusion . . . 156

8 Conclusion **159**

A Additional Plots for Anode and Cathode-Crossing Muon Comparison **161**

B Additional Plots to Evaluate the Impact of the Electron Lifetime **163**

C Additional Plots to Evaluate the Impact of different C_{cal} values **165**

References **167**

List of Figures

2.1 Solar neutrino fluxes 8
2.2 Measurement of the solar neutrino flux composition performed by the SNO experiment 10
2.3 Super-Kamiokande results 12
2.4 KamLAND results 13
2.5 Neutrino and anti-neutrino nucleon CC cross sections 17
2.6 Feynman diagrams of neutrino interactions in matter 20
2.7 Neutrino mass ordering 22
2.8 Global fit for δ_{CP} 23

3.1 The DUNE experiment 28
3.2 Schematic of the DUNE near detector components 29
3.3 Single phase LArTPC functioning scheme 31
3.4 ProtoDUNE-SP TPC scheme 35
3.5 ProtoDUNE-SP photo at the Neutrino Platform. 37
3.6 Principle of a light guide 38
3.7 ARAPUCA detection principle 39
3.8 Diagram of the ProtoDUNE-SP beam line 39
3.9 Prediction and measurement of the time of flight for different particle species 40
3.10 Top and side view of the Cosmic-Ray Tagger installation 41
3.11 ProtoDUNE-SP DAQ system, data flow, timing and trigger signals . 43
3.12 Effect of the 2D deconvolution on a raw waveform 47

3.13 Example of the hit fitting procedure 47
3.14 Illustration of two track segments stitched at the cathode 49
3.15 Example of reconstructed particle hierarchy using Pandora 51
3.16 Track-like CNN score for a reconstructed event in ProtoDUNE-SP . . 52
3.17 Space charge effect distortions at the TPC boundaries in ProtoDUNE-SP 54
3.18 Two slices of the SCE electric field distortions map 55

4.1 Cartoon summarising the two processes of $Ar^{+}$and Ar^{*} 61
4.2 Ar potential energy curves in the solid state 62
4.3 Fraction of electrons that survive recombination (R) dependence on dE/dx and electric field. 63
4.4 Complementary behaviour of charge and light yield in liquid argon, krypton and xenon 65
4.5 Fraction of electrons surviving recombination as a function of dE/dx as measured by the ICARUS 3-ton prototype 71
4.6 Qualitative comparison of the modified Birks formula and the box model 72

5.1 Vertical fluxes of cosmic ray particles in the atmosphere as a function of the altitude 77
5.2 Angular dependence of cosmic ray muons at the Earth surface 79
5.3 Mean dE/dx vs. kinetic energy and residual range for a muon in liquid argon 81
5.4 Plot of the most probable value of dE/dx as a function of the residual range for different values of argon thickness 82
5.5 Feynman diagram for a negative muon decay in an electron, and electron anti-neutrino and a muon neutrino 82
5.6 Stopping power for electrons in liquid argon highlighting the collision and radiative components 83
5.7 Event display of a stopping muon decaying into an electron in ProtoDUNE-SP data 84

5.8 Simulated energy loss dE/dx as a function of residual range for a sample of stopping muons . . . 86
5.9 dE/dx calculated with a simulation step of 0.75 cm as a function of residual range for a sample of stopping muons . . . 87
5.10 Mean of the simulated dE/dx as a function of the muon residual range 88

6.1 Geometry for the ProtoDUNE-SP active volume . . . 93
6.2 Definition of the angular reference system in ProtoDUNE-SP . . . 94
6.3 Distribution of θ_{yz} and θ_{xz} . . . 95
6.4 Diagram showing a through-going cathode-crossing track entering the TPC before the readout window is opened . . . 96
6.5 Preliminary spatial selection cuts for cathode-crossing stopping muons 98
6.6 Preliminary time selection cuts for cathode-crossing stopping muons . 99
6.7 Diagram showing the selection principle for cosmic-ray muons that enter crossing the detector anode . . . 100
6.8 Diagram representing the requested condition on the start point to be considered as an anode-crossing track . . . 100
6.9 Preliminary selection cuts for the start points of anode-crossing stopping muons . . . 101
6.10 Diagrams showing early and late tracks that can be mistaken for anode-crossing stopping muons . . . 102
6.11 Preliminary time selection cuts for anode-crossing stopping muons . . 102
6.12 Preliminary selection cuts for the end points of anode-crossing stopping muons . . . 103
6.13 Examples of broken tracks in ProtoDUNE-SP . . . 106
6.14 Diagram showing the definition of the angles for broken tracks removal 107
6.15 Event display showing a partially reconstructed track . . . 108
6.16 Event display showing a partially reconstructed track . . . 108
6.17 N-1 plots for the spatial selection of cathode-crossing stopping muons 110

6.18 N-1 selection plots for the time selection cuts for cathode-crossing stopping muons . . . 111
6.19 N-1 plots for the spatial selection of anode-crossing stopping muons . 112
6.20 N-1 selection plots for the time selection cuts for anode-crossing stopping muons . . . 113
6.21 dQ/dx as a function of the residual range for anode-crossing muons in Monte Carlo and data . . . 114
6.22 Hit positions in the xy plane for cathode and anode-crossing tracks in data . . . 115
6.23 Calculated t_0 for cathode and anode-crossing stopping muons . . . 116
6.24 Hits on the collection wires for a selected stopping muon before and after the Michel hits are removed. . . . 117
6.25 CNN score for stopping muon hits in data and Monte Carlo . . . 118
6.26 CNN score distributions for stopping muon hits in Monte Carlo and different electron energy contribution . . . 119
6.27 Fit to the theoretical dE/dx shape as a function of the residual range for an anode-crossing muon in data . . . 120
6.28 Distributions of the scale factor and the shift in the residual range for each track in the sample of anode-crossing stopping muons in MC and data . . . 121
6.29 dQ/dx as a function of the residual range for anode-crossing muons in data before and after the final quality cuts are applied . . . 122

7.1 Sanity check plots for the simulation of the angular dependence of recombination. . . . 128
7.2 Distribution of the angle ϕ for each reconstructed hit in the generated Monte Carlo sample . . . 130
7.3 Charge per unit length (dQ/dx) for each hit vs. the expected theoretical mean dE/dx for $\phi = 80^\circ$ . . . 130

7.4 Example of fit to the most probable value with a convoluted Landau and Gaussian function for $\phi = 70°$ 131
7.5 Comparison of the mean and most probable values of dQ/dx with the Monte Carlo truth dependence of dQ/dx vs. dE/dx for each angular bin 132
7.6 Fit to determine the recombination parameters α and β' used for muons in the particle gun simulation in each angular bin 134
7.7 Comparison between the electric field at the location of each hit for the sample of cathode and anode-crossing muons 136
7.8 Recombination fit to determine the modified box model parameters used in the Monte Carlo simulation of ProtoDUNE-SP for both sample of cathode and anode-crossing muons separately 137
7.9 Reconstructed dQ/dx as a function of the residual range and the mean dE/dx for anode and cathode-crossing muons and data run 5387 . . . 137
7.10 Electric field at the location of each hit considered in run 5387 according to the space charge calibration map 138
7.11 Fit to the modified box model and Birks model for the combined sample of cathode and anode-crossing stopping muons and for any angle ϕ . . 139
7.12 Comparison of the recombination parameters of the modified box model and Birks law between the values obtained from the stopping muon fit and the values from other liquid argon experiments 140
7.13 Comparison of the distributions of the angle between the local direction of the track at the position of each hit and the local electric field ϕ in data and Monte Carlo 141
7.14 Recombination fits for the merged sample of anode and cathode-crossing muons for different values of the angle ϕ 142
7.15 Comparison of the recombination parameters of the modified box and Birks model for each angle ϕ in data run 5387 144
7.16 Parameters β and K as a function of ϕ 144
7.17 Calibrated dE/dx using the modified box model as a function of the residual range for the selected muons in run 5387 146

7.18 Calibrated dE/dx using the Birks model as a function of the residual range for the selected muons in run 5387 147
7.19 Modified box model recombination parameters as a function of the angle ϕ for the separate sample of cathode and anode crossing muons 149
7.20 Birks recombination parameters as a function of the angle ϕ for the separate sample of cathode and anode crossing muons 150
7.21 Recombination parameters obtained with different values of the electron lifetime 152
7.22 Recombination parameters obtained with different values of C_{cal} . . . 154

A.1 Recombination fits for cathode and anode-crossing stopping muons without the $\sin\phi$ dependence in data 161
A.2 Recombination fits for cathode-crossing stopping muons for different angular bins 162
A.3 Recombination fits for anode-crossing stopping muons for different angular bins 162

B.1 Recombination fits for the selected stopping muons using all values of ϕ for different electron lifetime values 163
B.2 Recombination fits for the selected stopping muons for each angular bin in the case of an electron lifetime 10% larger 164
B.3 Recombination fits for the selected stopping muons for each angular bin in the case of an electron lifetime 10% smaller 164

C.1 Recombination fits for the selected stopping muons using all values of ϕ for different values of C_{cal} 165
C.2 Recombination fits for the selected stopping muons for each angular bin in the case of C_{cal} 3% larger 166
C.3 Recombination fits for the selected stopping muons for each angular bin in the case of C_{cal} 3% smaller 166

List of Tables

2.1 Global fit values of neutrino oscillation parameters for both normal (NO) and inverted (IO) neutrino mass ordering 24

4.1 Summary of liquid argon parameters 60
4.2 Summary of the fitted recombination parameters for the ICARUS, ArgoNeuT and MicroBooNE experiment 74

6.1 Preliminary cut values for cathode-crossing stopping muons 97
6.2 Preliminary cut values for anode-crossing stopping muons 103
6.3 Final cut values for cathode-crossing stopping muons 111
6.4 Final cut values for anode-crossing stopping muons 113

7.1 Recombination parameters of the modified box and Birks model as obtained from a global fit with different angles ϕ 143
7.2 Recombination parameters of the modified box and Birks model for the anode and cathode sample separately without angular dependence 148
7.3 Average percentage difference of the recombination parameters obtained with different electron lifetime values 153
7.4 Average percentage difference of the recombination parameters obtained with different C_{cal} values 155
7.5 Summary of the values obtained for the recombination parameters when ignoring the angular modulation in the fit functions 156
7.6 Summary of the measurements of the recombination parameters for the different angular bins 157

List of Abbreviations

APA Anode Plane Assembly

CC Charged Current

CE Cold Electronics

CERN European Organization for Nuclear Research

CNN Convolutional Neural Network

CP Charge Parity

CPA Cathode Plane Assembly

CR Cosmic Ray

CRT Cosmic-Ray Tagger

CTB Central Trigger Board

DAQ Data Acquisition

DIS Deep Inelastic Scattering

DP Dual Phase

DUNE Deep Underground Neutrino Experiment

ECAL Electromagnetic Calorimeter

FEMB Front-End Motherboard

Fermilab Fermi National Accelerator Laboratory

HV High Voltage

IO Inverted Ordering

KamLAND Kamioka Liquid Scintillator Anti-neutrino Detector

LArTPC Liquid Argon Time Projection Chamber

LNGS Laboratori Nazionali del Gran Sasso

MBM Modified Box Model

MC Monte Carlo

MIP Minimum Ionising Particle

MPV Most Probable Value

NC Neutral Current

NO Normal Ordering

PDS Photon Detection System

PFParticle Particle Flow Particle

PMNS Pontecorvo Maki Nakagawa Sakata

PMT Photo-multiplier

QE Quasi Elastic

RCE Reconfigurable Cluster Element

RES Resonant

ROI Region of Interest

SCE Space Charge Effect

SiPM Silicon Photomultipliers

SNO Sudbury Neutrino Observatory

SP Single Phase

SPS Super Proton Synchrotron

SSM Standard Solar Model

SSP SiPM Signal Processor

SURF Sanford Underground Research Facility

TOF Time of Flight

TPB Tetraphenyl-Butadiene

TPC Time Projection Chamber

WIB Warm Interface Board

WLS Wavelength Shifter

Chapter 1

Introduction

Following the discoveries that neutrinos exist in three weakly-interacting states, or flavours, and that they can transform from one flavour to another, a phenomenon called "neutrino oscillations", neutrino physics has undergone a rapid development. Many experiments have been designed, built and operated to study neutrinos and neutrino oscillations, since they can offer insights on many open questions in physics and cosmology. The existence of neutrino masses, as implied by flavour oscillations, opens a number of questions on the mechanism that gives origin to the neutrino masses and whether neutrinos are Dirac or Majorana particles. Limits on the absolute neutrino masses exist (for example from cosmological data [1]), but they can not be studied using neutrino oscillations, since oscillations depend on the neutrino mass differences. Another interesting topic is whether the probability of neutrino oscillation is different from that of anti-neutrinos. If this were experimentally confirmed, it could help to explain the observed matter and anti-matter asymmetry in the universe. A further question is if other neutrinos, to be added to the three-flavour paradigm, exist. Those neutrinos would have to be sterile or, in other words, only interact through gravity, but would participate in the oscillation mechanism.

The different experiments conceived address one or more of the open problems mentioned by using different neutrino sources like solar, atmospheric, reactor or accelerator neutrinos. Neutrino detectors are typically large in size to increase the interaction probability, and have to be able to precisely measure the energy and the type of particles produced by the neutrinos interacting with the detector material. This is

particularly important for oscillation experiments, for which the final state lepton is used to identify the flavour of the interacting neutrino. The Deep Underground Neutrino Experiment (DUNE) is a state-of-the-art future neutrino experiment that has a broad physics program including the study of neutrino oscillation parameters within the three-flavour model with great details, the potential discovery of matter and anti-matter asymmetries and the determination of the relative ordering of the neutrino masses. The DUNE design is centered around the liquid argon time projection chamber (LArTPC) technology, which has been shown to possess excellent tracking and calorimetry reconstruction capabilities. DUNE will face many technical challenges in its development, given the level of sophistication of its design. A substantial prototyping effort was therefore undertaken to study and benchmark the construction and installation of the various DUNE modules and to validate the detector performance. The prototype detectors also serve as a test-bed to develop reconstruction software and analysis techniques.

This thesis presents an analysis of the data taken by the ProtoDUNE Single Phase (SP) prototype LArTPC detector at CERN in late 2018 during a test-beam run. LArTPC detectors rely on the collection of the charge created following the ionisation of argon atoms by charged particles traveling in the medium. The amount of charge is related to the initial energy deposited. To precisely reconstruct the energy of the particles, the detector is calibrated using known sources of energy depositions. ProtoDUNE-SP is a surface detector and is therefore exposed to an abundant flux of cosmic rays, mainly composed of muons. The energy loss of muons in a material is well known and, for muons that stop inside the detector, it can be reconstructed by using the length of the track. In particular, minimum ionising muons represent a known constant energy deposition that can be used to calibrate the energy response. This thesis contains the description of a selection of cosmic muons that stop inside the protoDUNE-SP detector. The selection is characterised by a high-purity sample of fully reconstructed muons that span the majority of the detector volume, allowing to explore the detector response uniformly. The selection procedure

is optimised to identify muons with a well-reconstructed end point, which allows the correct characterisation of the energy loss profile along the muon trajectories.

The work in this thesis also details a study that uses the selected muons to compare the collected charge resulting from their interaction with the liquid argon to their theoretical energy loss, obtained with a Monte Carlo simulation. This analysis provides insights into the mechanism of charge creation and recombination, which result in an algorithm to calibrate the energy measurement of the detector.

In the following, a brief outline of the thesis content is given. Chapter 2 gives an overview of the physics of neutrinos starting from the history of the main discoveries, including neutrino oscillations. The role of neutrinos in the standard model and the neutrino interactions that are key for the detection are also presented. The mechanism of neutrino oscillations, how they are studied at accelerator experiments and the current knowledge of oscillation parameters are also discussed.

The ProtoDUNE-SP experiment is presented in Chapter 3. A description of the DUNE program and the working principles of LArTPC detectors are included. The main components of ProtoDUNE-SP are outlined and characterised, together with a presentation of the data acquisition systems. Additionally, a presentation of the steps for simulating and reconstructing events is given.

Chapter 4 contains an overview of the fundamental processes that lead to the creation of free electrons and photons following the interaction of charged particles in liquid argon. A particular emphasis is given to the phenomenon of electron recombination with the parent ions immediately after the ionisation has occurred.

Chapter 5 is dedicated to briefly introducing cosmic rays and the electromagnetic energy loss of muons and electrons in liquid argon. A simulation of the muon energy loss in liquid argon is also illustrated.

Chapter 6 will detail a selection of stopping cosmic muons. The selection is developed using a Monte Carlo simulation and is later validated using data. A list of cuts dedicated to cleaning the sample and selecting exclusively well-reconstructed muons is presented.

The sample of cosmic muons is employed in Chapter 7 to study the charge creation as a function of the deposited energy, by using the Bragg peak of the muons as a tool to explore different dE/dx values. The analysis is first developed and validated using two different Monte Carlo simulations, before applying it to ProtoDUNE-SP data to extract a data-driven parametrisation that characterises the collected charge for a variable energy loss. Considerations on the systematic uncertainties related to the analysis are also presented.

Finally, Chapter 8 contains a summary of the results.

Chapter 2

Neutrino Physics

Contents

2.1 History of Neutrino Discoveries 6
2.2 Neutrinos in the Standard Model 14
2.3 Neutrino Interactions 15
2.4 Neutrino Oscillations 16
2.4.1 Oscillations in Vacuum 18
2.4.2 Oscillations in Matter 20
2.4.3 Summary of Current Knowledge of Neutrino Oscillation Parameters 21
2.4.4 Overview of Accelerator Neutrino Experiments 24

Neutrinos are the second most abundant particles in the universe, after photons. Since they interact only through the weak force,[1] neutrinos are challenging to detect and study. This chapter contains an overview of neutrino physics. Section 2.1 will give a brief summary of the main historical experiments and discoveries, from the hypothesis of the existence of a neutral weakly-interacting particle to the discoveries of three different neutrino flavours. The main puzzles that characterised the physics of neutrinos in the 20^{th} century and eventually led to the discovery of neutrino oscillations will also be illustrated therein. Section 2.2 will present how neutrinos are included in the Standard Model and will briefly touch upon the Dirac and/or Majorana mass problem. Section 2.3 contains a description of the neutrino interactions with nucleons, which also represent the detection mechanism for most experiments.

[1] Neglecting gravity due to the neutrino small masses.

Finally, Section 2.4 will introduce the formalism of neutrino oscillations in vacuum and matter. The current knowledge of neutrino oscillation parameters and a description of the basic principles of an accelerator neutrino experiment are also illustrated in Section 2.4.

2.1 History of Neutrino Discoveries

The history of neutrinos begins in 1914 when the β-decay was being studied by Chadwick [2]. Unlike the α and γ decays, where a mono-energetic spectrum was observed, the β-decay showed a continuous energy spectrum, which could have hinted at a violation of the energy conservation law. In 1930, Pauli proposed the existence of a third particle in the final state of β-decays [3] (later called "neutrino"), that could explain the continuous energy spectrum. A few years later, Fermi made the first attempt to include the neutrino in a theoretical framework, by describing the β-decay as a four-fermion point interaction [4]. The theory was successful in explaining the observed properties of the β-decay, but Bethe and Peierls calculated the magnitude of the neutrino interaction using Fermi's theory concluding that it was too weak for a neutrino to ever be observed [5].

Bethe and Peierls' prediction seemed to hold until 1956 when the neutrino was eventually discovered by Reines and Cowan in their famous experiment at the Savannah River Plant in South Carolina [6]. The problem of the low neutrino cross section was solved by using a large flux. Reines and Cowan measured the positron and the neutron resulting from the interaction of a neutrino (in reality an anti-neutrino) with a proton:

$$\bar{\nu}_e + p \rightarrow n + e^+. \tag{2.1}$$

They used a nuclear reactor as a neutrino source and two tanks of water as a detector. The water tanks were surrounded by liquid scintillator, used to detect the photons created by the positron annihilation. To make sure that it truly was an inverse β-decay reaction, Cadmium was added to the water to allow for the neutron detection. The rate of neutrino events was compared to the rate of detection when the reactor

was shut down, resulting in a significant excess of events that allowed Reines and Cowan to claim the discovery.

The lower than expected experimental limits on the process $\mu \to e + \gamma$ suggested the conservation of the family lepton number, leading to the expectation that the process $\nu_\mu + n \to p + e^-$ was forbidden. Therefore, if neutrinos produced by $\pi \to \mu + \nu_\mu$ cannot induce electrons when interacting, then ν_e and ν_μ are different particles. In 1962 the muon neutrino was discovered at the Brookhaven National Laboratory [7], proving that more than one type of neutrino exists. In their experiment, Lederman and his colleagues set up a beam of neutrinos created by a beam of decaying pions and observed the charged leptons created by the neutrino interactions. If more types of neutrinos existed, only muons were expected to be observed. They eventually found a clear predominance of single muon events in the data, leading to the conclusion that another type of neutrino, which only produces muons, exists.

When the tau lepton was discovered in 1977, it was natural to expect that a third type, a tau neutrino, could exist. In 2001 the DONUT experiment observed the tau neutrino [8]. Accelerated protons were used to produce charmed mesons that subsequently decay into tau neutrino. The detection technique consisted in using an emulsion detector to observe the short track of the tau lepton created by the tau neutrino interaction. The signature was a short track followed by a "kink" at the end indicating a subsequent decay.

The measurement of the decay width of the Z boson at LEP in 1992 puts the limit on the number of light neutrinos [9], defined as a neutrino with mass lower than half of the Z mass, to three. While heavier neutrinos can exist, no compelling experimental evidence has been found so far.

It is interesting to discuss a series of experiments that from 1968 to 2002 led to the discovery of the mechanism for which neutrinos change flavour while travelling in vacuum or through matter, also known as neutrino oscillations. The Standard Solar Model (SSM) predicts a certain electron neutrino flux [10], as a result of the fusion reactions occurring in the sun. The flux for each reaction can be seen in Figure 2.1 as a function of the neutrino energy.

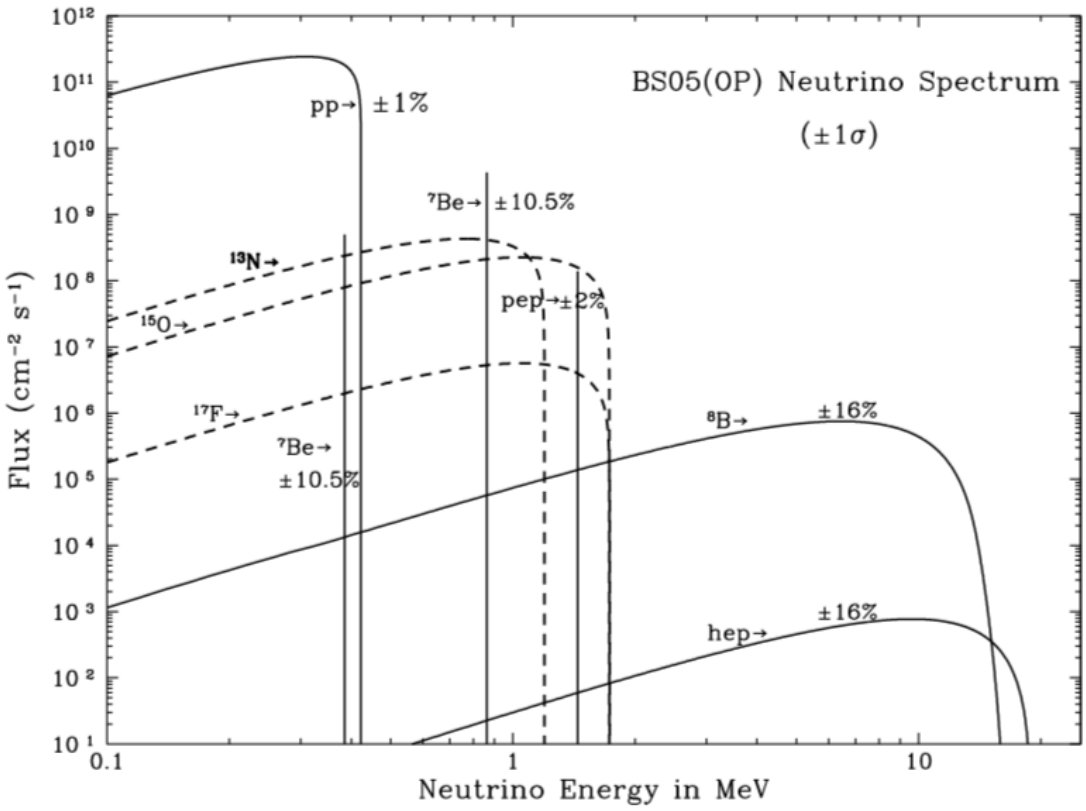


Figure 2.1: Solar neutrino fluxes for different reactions in the SSM as a function of the neutrino energy. Figure taken from [10].

From 1968 Davis et al. [11] carried out the first experiment to detect solar neutrinos with the intention of verifying the SSM. They employed a tank of chlorine in the underground Homestake mine in South Dakota to detect neutrinos through the interaction

$$\nu_e + {}^{37}\mathrm{Cl} \rightarrow {}^{37}\mathrm{Ar} + e^-. \tag{2.2}$$

The technique to measure the flux of ν_e relied on counting the number of ^{37}Ar produced in the chlorine tank. Surprisingly, the number estimated by Davis was only about one third of the number predicted by the SSM. This is normally referred to as the solar neutrino problem. While initially this result was not taken very seriously by the community, it slowly became of interest when the deficit was later confirmed by other experiments like GALLEX [12]. Uncertainties in the solar models and in the detection methods left the conclusion uncertain until 2002 when the Sudbury Neutrino Observatory (SNO) was able to demonstrate that neutrinos are changing type (also known as flavour) [13]. Heavy water (D_2O) was used to enable the detection of both the electron neutrino flux and the total neutrino flux, by offering an exclusive channel for ν_e to be detected (via a charged-current interaction with a neutron) in addition to the elastic scattering with electrons and the neutral-current interactions available to any neutrino flavour. By comparing the data from each interaction channel, it was possible to measure the composition of the neutrino flux which resulted in the plot shown in Figure 2.2. The plot shows the measurement of the flux for the various interaction types together with the best fit point. The band defined by the two dashed lines represents the SSM, showing agreement between the measurement and the model. These results eventually solved the neutrino solar problem: since the total neutrino flux is consistent with the prediction, the observed deficit in electron neutrino is due to the presence of muon and tau neutrinos in the solar flux. However, the exact cause of this effect was still under investigation at the time and a few hypotheses were proposed, among which decoherence and neutrino oscillations [14].

A similar puzzle was found when looking at atmospheric neutrinos. Atmospheric neutrinos are produced when high-energy protons from outer space interact with the

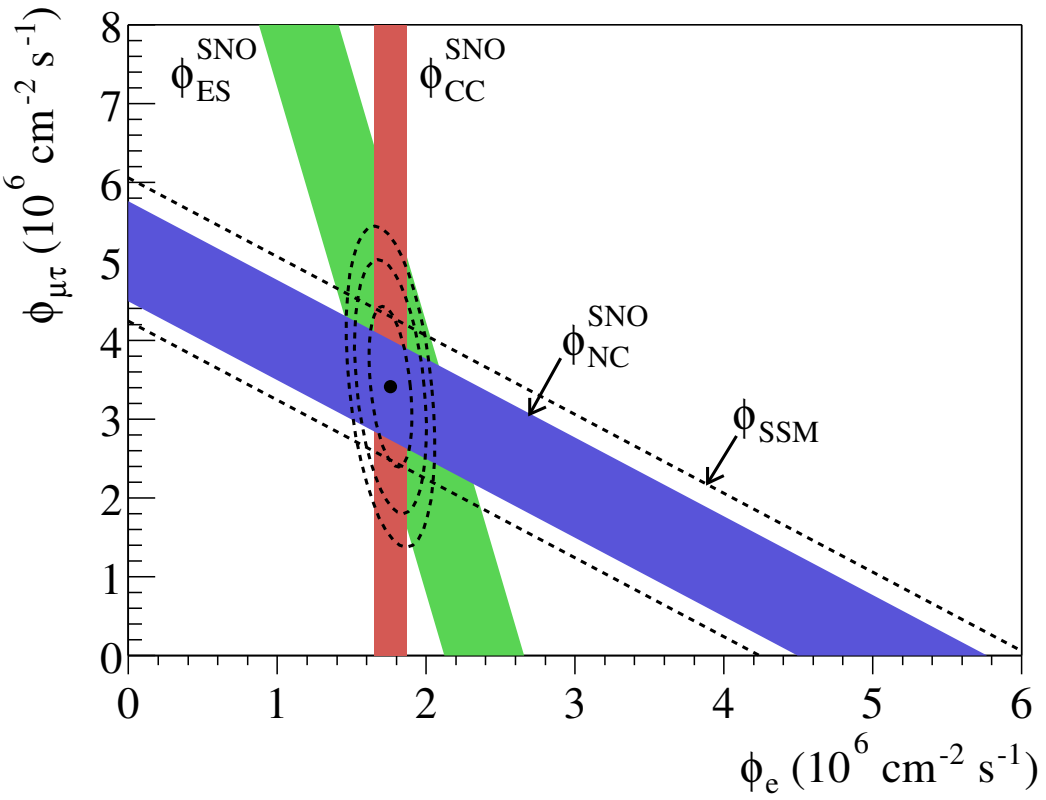


Figure 2.2: Measurement of the solar neutrino flux composition performed by the SNO experiment. Each coloured band represents the measured flux for each interaction mode. The band drawn by the two dashed lines represents the $\pm 1\sigma$ spread on the prediction by the SSM. The elliptical contours define the various confidence level intervals for the best fit point in the center. Figure taken from [13].

atmosphere creating pions and muons, which in turn decay into neutrinos. Since pions mainly decay into muons, a 2:1 ratio is expected for muon and electron neutrinos. In the early 1990s, the Kamiokande experiment measured a roughly equal number of ν_e and ν_μ [15]: this was a strong suggestion that the muon neutrinos were changing flavour. The results were confirmed in 1998 by the upgraded Super-Kamiokande experiment [16]. Super-Kamiokande consisted of a large water Cerenkov detector able to distinguish between the electrons and muons created by a neutrino interaction, thanks to the pattern of Cerenkov light detected by photomultiplier tubes. Crucially, it was also sensitive to the direction of the incoming neutrino and it was eventually observed that the ratio of neutrino flavour depended on the direction of the incoming neutrinos. Those with a small zenith angle arrived in the expected ratio, but the ratio decreased at larger zenith angles, indicating a dependence of the ratio on the distance travelled: atmospheric neutrinos are produced close to the Earth surface so those incoming at a small angle must necessarily come from overhead and travelled a short distance ($\sim$10 km), while those coming at a large angle must have travelled through the Earth ($\sim$13.000 km). Figure 2.3 shows the ratio between the Super-Kamiokande data and the Monte Carlo prediction in the absence of neutrino oscillation for both ν_e and ν_μ interactions. The ratio is plotted as a function of the ratio L/E_ν (L is the distance travelled, E_ν is the neutrino energy) and clearly shows a deficit of ν_μ at high L/E_ν.

To ideally test the hypothesis of neutrino oscillation, a fixed source and a movable detector would be necessary. This way, studying the variation of flux as a function of the distance from the source would be possible. However, due to their low interaction probabilities, neutrinos can only be detected in large detectors and the typical oscillation lengths are of the order of hundreds of kilometers. Alternatively, it is possible to study the oscillations at a fixed distance as a function of the neutrino energy, thanks to the L/E_ν dependence of the oscillation probability (more details will be given in Section 2.4). The Kamioka Liquid Scintillator Anti-neutrino Detector (KamLAND) measured $\bar{\nu}_e$ oscillations using neutrinos from several reactors 150-200 km away in the $\sim$MeV energy scale [17, 18]. Not only they observed a deficit in $\bar{\nu}_e$ events, but the

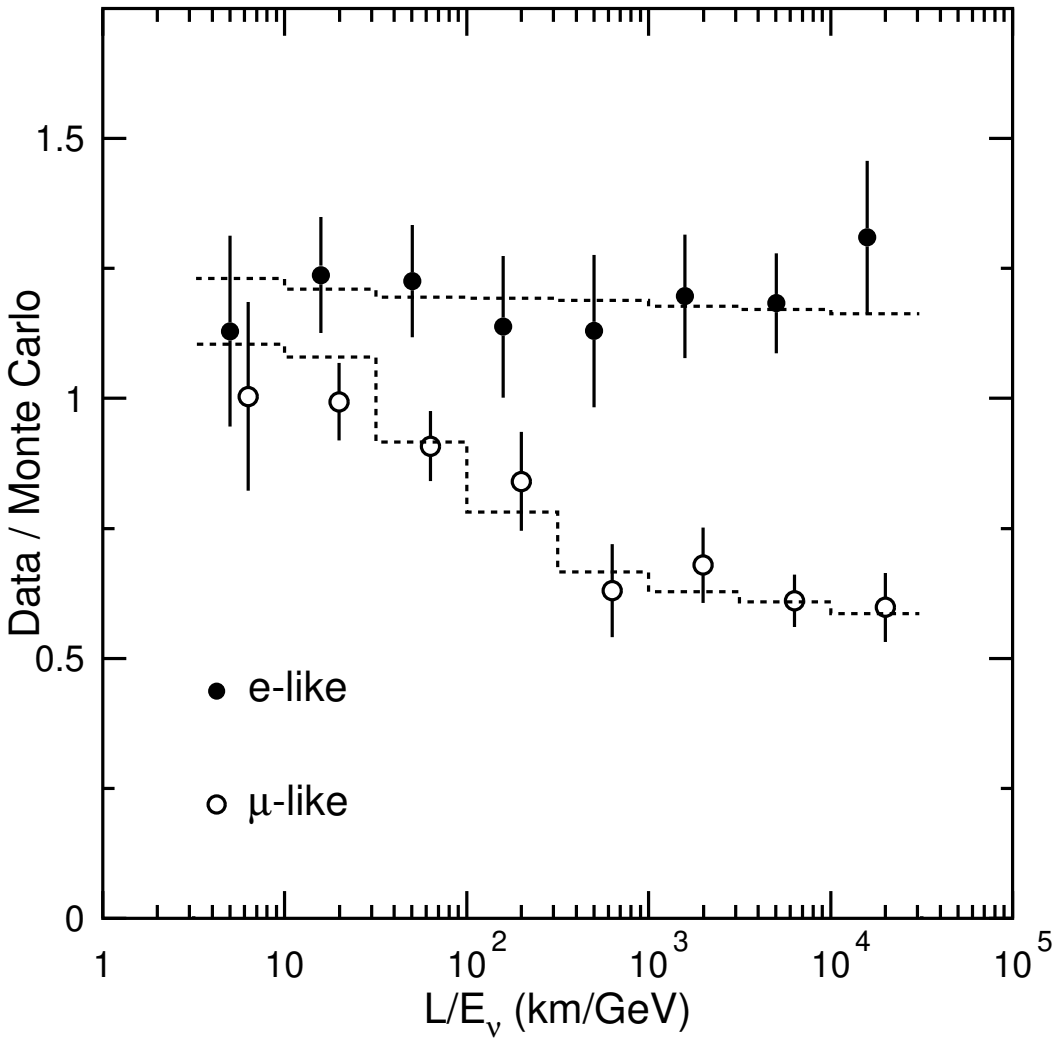


Figure 2.3: Ratio of the Super-Kamiokande data to the MC prediction under the hypothesis of no neutrino oscillations. The dashed line represents the shape for the oscillation $\nu_\mu \to \nu_\tau$ with the best fit parameters $\Delta m^2 = 2.2 \cdot 10^{-3}\text{eV}^2$ and $\sin^2 2\theta = 1$. Taken from [16].

study of the flux as a function of the energy offered experimental support to the oscillation neutrino hypothesis. Figure 2.4 shows the ratio of the measured ν_e flux to the expected flux in absence of oscillations, as a function of $L_0/E_{\bar{\nu}_e}$ with $L_0 = 180\,\text{km}$ as if all neutrinos came from the same reactor. The blue, red and green curves represent the neutrino oscillation, the neutrino decay and the decoherence model respectively. It appears evident from the plot that the neutrino oscillation hypothesis is the best fit to the data.

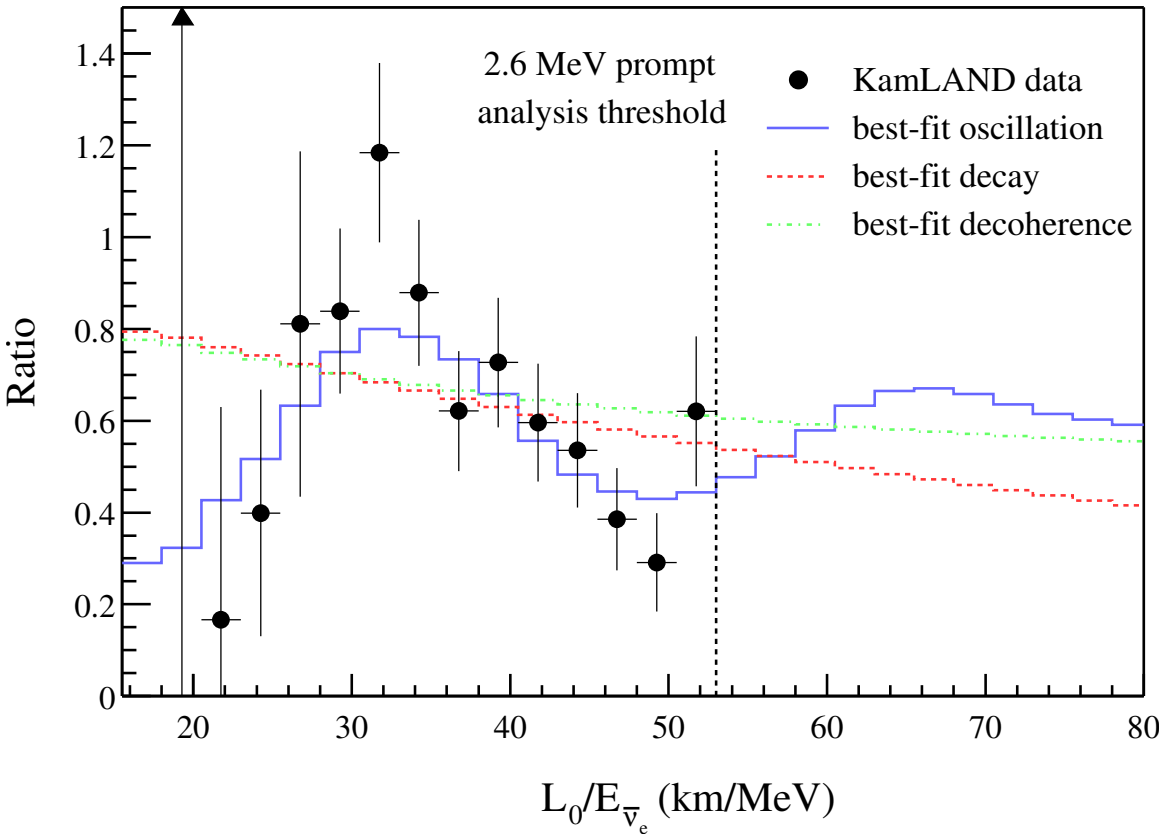


Figure 2.4: Ratio of $\bar{\nu}_e$ flux and the expected flux for no spectral distortion as a function of $L_0/E_{\bar{\nu}_e}$. The three coloured curves represent the models for various distortion hypotheses as indicated by the legend. The oscillation model gives the best agreement with the data. Taken from [18].

The MINOS experiment at Fermilab adopted the similar technique of studying the neutrino oscillation probability as a function of energy. Unlike KamLAND, a proton accelerator was used to produce a beam of ν_μ. In 2006, the MINOS experiment reported the observation of ν_μ disappearance [19] and, interestingly, they did not

measured any significant ν_e appearance, leading to the hypothesis that the muon neutrinos were oscillating into tau neutrinos. Oscillations to tau neutrinos were first observed in 2006 by the OPERA experiment at the Laboratori Nazionali del Gran Sasso (LNGS) [20]. A beam of ν_μ was prepared at CERN and travelled to Gran Sasso through a 750 km baseline to be detected by an emulsion target. Ten ν_τ candidates were observed, eventually confirming the $\nu_\mu \to \nu_\tau$ oscillation [21].

Since then, many experiments were built to measure and constrain the neutrino oscillation parameters. Their main results and the current knowledge will be summarised in Section 2.4.

2.2 Neutrinos in the Standard Model

In the Standard Model of particle physics, the left and right-handed fermions are assigned to different representations of $SU(2) \times U(1)$ and the interactions of neutrinos are described in the electroweak theory. In particular, the left-handed fermions are assigned to the doublets

$$\psi_i = \begin{pmatrix} \nu_i \\ l_i \end{pmatrix}_L , \tag{2.3}$$

where the index i indicates one of three lepton flavours e, μ or τ. The fields ν_{iL} enter into the Standard Model Lagrangian for both the charge current (CC) and neutral current (NC) interaction, respectively:

$$\mathcal{L}^{CC}(x) = -\frac{g}{2\sqrt{2}} j_\alpha^{CC}(x) W^\alpha(x) + \text{h.c.} \tag{2.4}$$

and

$$\mathcal{L}^{NC}(x) = -\frac{g}{2\cos\theta_W} j_\alpha^{NC}(x) Z^\alpha(x) + \text{h.c.} \tag{2.5}$$

In these expressions,

$$j_\alpha^{CC}(x) = 2 \sum_{\beta=e,\mu,\tau} \bar{\nu}_{\beta L}(x) \gamma_\alpha l_{\beta L}(x) \tag{2.6}$$

represents the leptonic charged current and

$$j_\alpha^{NC}(x) = 2 \sum_{\beta=e,\mu,\tau} \bar{\nu}_{\beta L}(x) \gamma_\alpha \nu_{\beta L}(x) \tag{2.7}$$

is the neutrino neutral current. $W^\alpha(x)$ and $Z^\alpha(x)$ are the fields of the $W^\pm$ and Z^0 vector bosons, g is the electroweak interaction constant and θ_W is the Weinberg angle.

An interesting open question is that of the neutrino mass. Typically, mass is included in the Standard Model with the Dirac mass term in the Lagrangian:

$$m_D \bar{\nu}\nu. \tag{2.8}$$

The spinor ν can be decomposed into its chiral components $\nu = \nu_L + \nu_R$ resulting in

$$m_D \bar{\nu}\nu = m_D(\overline{\nu_L + \nu_R})(\nu_L + \nu_R) = m_D(\bar{\nu}_L\nu_R + \bar{\nu}_R\nu_L). \tag{2.9}$$

A Dirac mass for the neutrino would therefore imply the existence of a right-handed neutrino that is not observed in the electroweak interactions. A right-handed neutrino might exist and be sterile or, in other words, only has the role of giving the neutrino a mass but does not participate in the electroweak interaction. Alternatively, the neutrino can just be a purely left-handed field and have a Majorana mass. In this case, additional mass terms need to be introduced in the Lagrangian: for a general spinor ψ, the Majorana mass term is of the form

$$\frac{1}{2} m_L \bar{\nu_L^c} \nu_L \tag{2.10}$$

where ν_L^c is the right-handed component $C\bar{\nu_L}^T$, with C indicating the charge conjugation operation.

2.3 Neutrino Interactions

In most experiments, neutrinos are detected when they interact with protons and neutrons making up the detector active material. Cross sections of neutrino interactions with electrons are much smaller [22]. Broadly speaking, there are two types of neutrino interactions with matter: charged-current (CC) interactions and neutral-current (NC) interactions. In the neutral-current interaction, which is mediated by the Z^0 boson, a neutrino of the same flavour is found in both the initial and final state. Conversely, in a charged-current interaction, mediated by the W boson, the

neutrino is replaced in the final state by a charged lepton of the same flavour. For neutrinos in the energy range of ∼GeV, the CC interactions can be further classified based on whether the target nucleon breaks up:

- **quasi-elastic scattering** (QE): the target nucleon remains intact;
- **nuclear resonance** (RES): the target goes into an excited state (for example Δ^{++}) and subsequently decays to hadrons;
- **deep inelastic scattering** (DIS): the nucleon breaks up in a number of hadrons.

The contribution of each process varies with the neutrino energy and flavour. This dependence is different for neutrinos and anti-neutrinos and can be observed in Figure 2.5 for ν_μ in both cases. Predictions and data are shown for each CC process as well as the total cross section. For a typical energy range of a neutrino oscillation experiment, multiple processes are simultaneously relevant. This implies that having a precise understanding of the neutrino interaction cross section is essential to perform oscillation experiments.

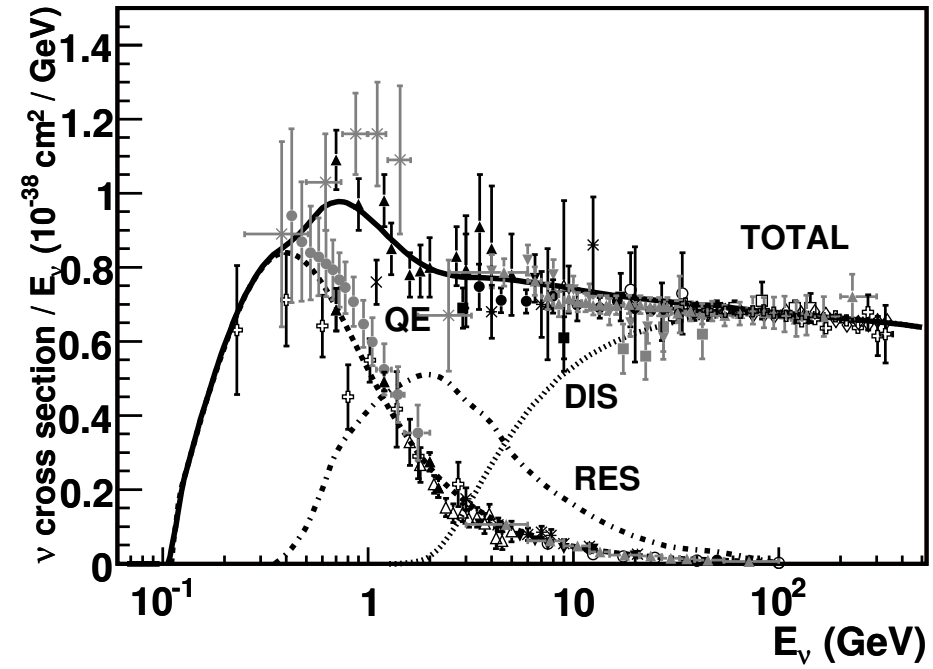
2.4 Neutrino Oscillations

Neutrino oscillation generally refers to the phenomenon for which neutrinos spontaneously change flavour when travelling in vacuum or through matter. Neutrinos are produced in a defined flavour state in a charged-current or neutral-current weak interaction process such as

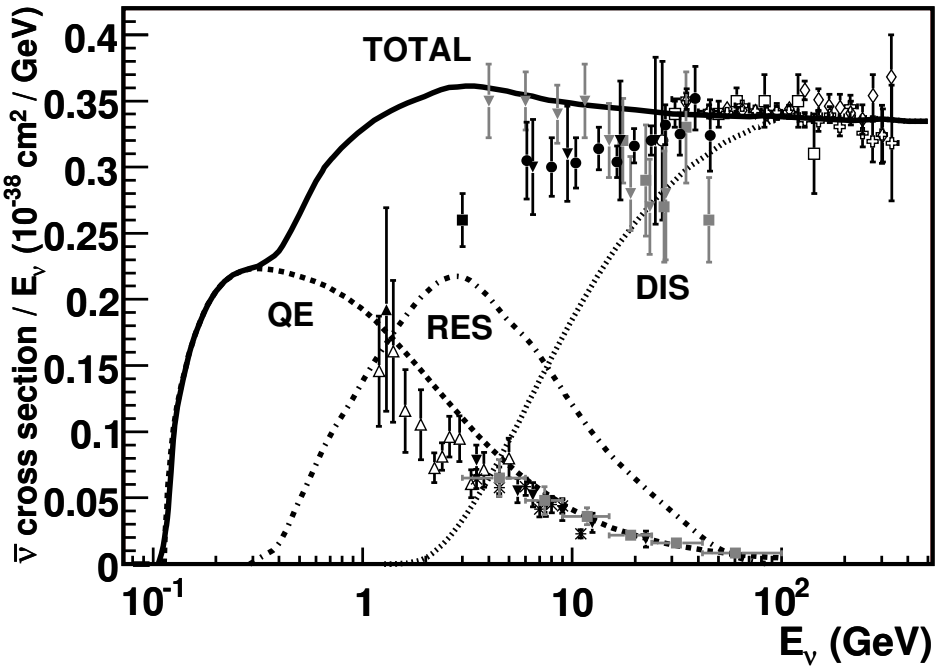
$$W^- \to l_\alpha^- \bar{\nu}_\alpha,\ W^+ \to l_\alpha^+ \nu_\alpha,\ Z \to \nu_\alpha \bar{\nu}_\alpha, \tag{2.11}$$

with $\alpha = e, \mu, \tau$. These states are different from the mass eigenstates. The resulting mixing between mass and flavour states is at the origin of the oscillation mechanism. A generic flavour state $|\nu_\alpha\rangle$ ($\alpha = e, \mu, \tau$) can be expressed as a linear combination of mass states $|\nu_k\rangle$ ($k = 1, 2, 3$) [24]:

$$|\nu_\alpha\rangle = \sum_{k=1,2,3} U_{\alpha k}^* \, |\nu_k\rangle \,, \tag{2.12}$$



(a) ν_μ nucleon CC cross sections.



(b) $\bar{\nu}_\mu$ nucleon CC cross sections.

Figure 2.5: Predictions and data of total neutrino nucleon CC cross section for ν_μ. Contribution from quasi-elastic (QE), resonant (RES) and deep inelastic scattering (DIS) processes are also shown. Plots from [23].

where U is a unitary matrix, called PMNS (Pontecorvo, Maki, Nakagawa, Sakata) matrix. The PMNS matrix is the matrix whose entries determine the coefficients of the mixing between mass and flavour states:

$$U = \begin{pmatrix} U_{e1} & U_{e2} & U_{e3} \\ U_{\mu 1} & U_{\mu 2} & U_{\mu 3} \\ U_{\tau 1} & U_{\tau 2} & U_{\tau 3} \end{pmatrix}. \tag{2.13}$$

2.4.1 Oscillations in Vacuum

The mass states $|\nu_k\rangle$ are eigenstates of the free-particle Hamiltonian $\mathcal{H}$,

$$\mathcal{H} |\nu_k\rangle = E_k |\nu_k\rangle , \tag{2.14}$$

where the energy eigenvalue is

$$E_k = \sqrt{\vec{p}^2 + m_k^2}, \tag{2.15}$$

with $\vec{p}$ and m_k the momentum and mass of the neutrino state. According to the Schrödinger equation [24]

$$i\frac{d}{dt} |\nu_k(t)\rangle = \mathcal{H} |\nu_k(t)\rangle , \tag{2.16}$$

the mass state evolves in time by gaining a complex phase

$$|\nu_k(t)\rangle = e^{-iE_k t} |\nu_k\rangle . \tag{2.17}$$

By substituting Equation 2.17 into Equation 2.12, a flavour state $|\nu_\alpha(t)\rangle$ at a generic time t can be written as

$$|\nu_\alpha(t)\rangle = \sum_k U^*_{\alpha k} e^{-iE_k t} |\nu_k\rangle , \tag{2.18}$$

with $|\nu_\alpha(t=0)\rangle = |\nu_\alpha\rangle$. Thanks to the unitary relation

$$\sum_\alpha U^*_{\alpha k} U_{\alpha j} = \delta_{jk}, \tag{2.19}$$

the massive states can be written in terms of the flavour states:

$$|\nu_k\rangle = \sum_{k=1,2,3} U_{\alpha k} |\nu_\alpha\rangle . \tag{2.20}$$

It is now possible to substitute Equation 2.20 into Equation 2.17 to obtain

$$|\nu_\alpha(t)\rangle = \sum_{\beta=e,\mu,\tau} \left(\sum_k U^*_{\alpha k} e^{-iE_k t} U_{\beta k} \right) |\nu_\beta\rangle \,. \tag{2.21}$$

Equation 2.21 expresses that the initial pure flavour state $|\nu_\alpha\rangle$ becomes a superposition of flavour states at time t. The probability to observe a flavour state $|\nu_\beta\rangle$ at time t is therefore

$$P_{\nu_\alpha \to \nu_\beta}(t) = |\langle \nu_\beta | \nu_\alpha(t) \rangle|^2 = \sum_{k,j=1,2,3} U^*_{\alpha k} U_{\beta k} U_{\alpha j} U^*_{\beta j} e^{-i(E_k - E_j)t}. \tag{2.22}$$

In the case of ultra-relativistic neutrinos, Equation 2.15 becomes

$$E_k \simeq E + \frac{m_k^2}{2E}, \tag{2.23}$$

and thus

$$E_k - E_j \simeq \frac{\Delta m^2_{kj}}{2E}, \tag{2.24}$$

with $\Delta m^2_{kj} \equiv m^2_k - m^2_j$ and $E = |\vec{p}|$. The transition probability can then be expressed as

$$P_{\nu_\alpha \to \nu_\beta}(t) = \sum_{k,j=1,2,3} U^*_{\alpha k} U_{\beta k} U_{\alpha j} U^*_{\beta j} \exp\left(-i \frac{\Delta m^2_{kj} t}{2E} \right). \tag{2.25}$$

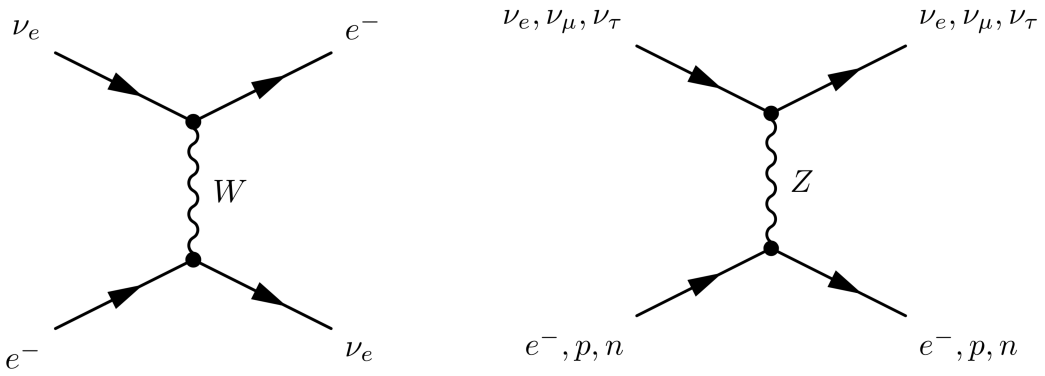
To make this formula more useful in practical experiments where the distance L travelled by the neutrino is measured, the relation $t = L$ (in natural units) can be used to write

$$P_{\nu_\alpha \to \nu_\beta}(L, E) = \sum_{k,j=1,2,3} U^*_{\alpha k} U_{\beta k} U_{\alpha j} U^*_{\beta j} \exp\left(-i \frac{\Delta m^2_{kj} L}{2E} \right). \tag{2.26}$$

It is often useful to separate the real and imaginary parts of the product $U^*_{\alpha k} U_{\beta k} U_{\alpha j} U^*_{\beta j}$ to get

$$\begin{aligned} P_{\nu_\alpha \to \nu_\beta}(L, E) = \delta_{\alpha\beta} &- 4 \sum_{k>j} \mathcal{R}\mathrm{e}[U^*_{\alpha k} U_{\beta k} U_{\alpha j} U^*_{\beta j}] \sin^2\left(\frac{\Delta m^2_{kj} L}{4E} \right) \\ &\pm 2 \sum_{k>j} \mathcal{I}\mathrm{m}[U^*_{\alpha k} U_{\beta k} U_{\alpha j} U^*_{\beta j}] \sin\left(\frac{\Delta m^2_{kj} L}{2E} \right), \end{aligned} \tag{2.27}$$

where the $(+)$ and $(-)$ sign are for the neutrino and anti-neutrino case respectively [24]. By virtue of the different sign, the last term is responsible for a different



(a) Charged current interaction for ν_e in matter.

(b) Neutral current interaction for each neutrino flavour in matter.

Figure 2.6: Feynman diagrams of neutrino interactions in matter. The diagram on the left-hand side is exclusively available to the electron neutrino. Diagrams from [24].

probability for the case of neutrinos and anti-neutrinos or, in other words, CP violation. From Equation 2.27 it is possible to see that the oscillation probability depends on the ratio L/E, which is a parameter typically fixed by the experimental conditions, and from constants of natures: the elements of the PMNS matrix U determine the amplitude of the oscillation, while the squared mass differences Δm^2_{kj} affect the oscillation phase. It also follows that an oscillation experiment is not sensitive to the absolute value of the neutrino masses, which can only be determined by other measurements such as the one designed for the KATRIN experiment [25]. Additionally, the mass hierarchy problem, i.e. the determination of the signs of the Δm^2_{kj}, can not in general be resolved by experiments that study oscillation in vacuum [26], and needs to be addressed by studying neutrino oscillations in matter.

2.4.2 Oscillations in Matter

When travelling through matter, neutrinos can interact with electrons, protons and neutrons. The Feynman diagrams of the interactions can be seen in Figure 2.6. While the neutral current interaction (Figure 2.6b) is possible for any neutrino flavour, the charged current interaction (Figure 2.6a) is only available to electron neutrinos. This asymmetry among the neutrino flavours can be described by introducing the effective

potential for electron neutrinos

$$V_{\mathrm{CC}} = \sqrt{2} G_F N_e, \tag{2.28}$$

where G_F is the Fermi constant and N_e is the electron density of the medium. The effective Hamiltonian which governs the ν_e propagation in matter contains extra elements and, as a consequence, the mass eigenstates are modified. A full treatment of neutrino oscillation in matter is beyond the scope of this thesis, but it can be found in many sources (for example [24]). The important effect of oscillations in matter is the resulting sensitivity to the sign of the mass differences [24, 27]. This is possible thanks to the additional terms in the oscillation probability that depend on the sign of the mass splitting Δm^2_{kj}. Since the neutrinos that are emitted by the sun have to travel through the sun itself, the study of their oscillation probability allowed to determine that $\Delta m^2_{21} > 0$ [28]. The sign of Δm^2_{23} or, equivalently, Δm^2_{31} is currently unknown. Both possibilities of normal ($m_1 < m_2 < m_3$) and inverted ($m_3 < m_1 < m_2$) mass ordering are shown in Figure 2.7.

2.4.3 Summary of Current Knowledge of Neutrino Oscillation Parameters

In the three-neutrino oscillation model, the mixing matrix of Equation 2.13 can be written in terms of three mixing angles $(\theta_{12}, \theta_{23}, \theta_{13})$ and one complex phase δ_{CP} by virtue of its unitarity and the fact that five of the six necessary phases can be absorbed in the neutrino wavefunction. U can therefore be expressed as [30]:

$$U = \begin{pmatrix} 1 & 0 & 0 \\ 0 & c_{23} & s_{23} \\ 0 & -s_{23} & c_{23} \end{pmatrix} \begin{pmatrix} c_{13} & 0 & s_{13} e^{-i\delta_{\mathrm{CP}}} \\ 0 & 1 & 0 \\ -s_{13} e^{i\delta_{\mathrm{CP}}} & 0 & c_{13} \end{pmatrix} \begin{pmatrix} c_{12} & s_{12} & 0 \\ -s_{12} & c_{12} & 0 \\ 0 & 0 & 1 \end{pmatrix}, \tag{2.29}$$

with $s_{ij} = \sin\theta_{ij}$ and $c_{ij} = \cos\theta_{ij}$. By breaking down the mixing matrix this way, it is possible to highlight the main components. The matrix that contains θ_{12} is referred to as the solar mixing matrix, the parameters of which are mainly determined by solar neutrino experiments. For the same reason, the matrix containing θ_{23} is often called the atmospheric mixing matrix. Finally, the reactor matrix contains θ_{13}

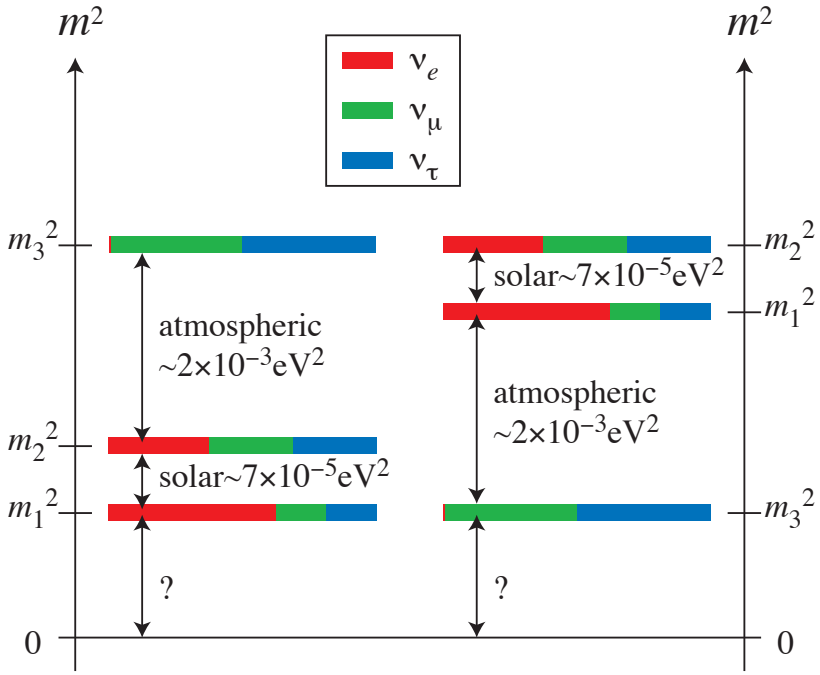


Figure 2.7: Cartoon showing the neutrino mass hierarchy for normal (left) and inverted (right) ordering. The various colours represent the flavour composition of each mass state. Taken from [29].

and the complex phase δ_{CP}. If $\delta_{\mathrm{CP}} \neq \{0, \pi\}$, the mixing matrix would allow for a different oscillation probability for neutrinos and anti-neutrinos: $P(\nu_\alpha \to \nu_\beta) \neq P(\bar{\nu}_\alpha \to \bar{\nu}_\beta)$. The mixing angles, δ_{CP} and the mass splitting have been investigated by many experiments, and global analyses (such as [31]) have been performed to combine the inputs of various measurements and give the best estimates. Different experiments contributes in different measure to the determination of each parameter. Solar neutrino experiments (such as Homestake [32], GALLEX/GNO [33], SAGE [34], SNO [35] and SuperKamiokande [36, 37, 38]) are combined with the KamLAND results [39, 40, 41] to precisely determine Δm^2_{21} and $\sin^2\theta_{12}$. Accelerator experiments like NOνA [42], T2K [43] and MINOS [44] give an important contribution to the measurement of $\sin^2\theta_{23}$ and $|\Delta m^2_{31}|$ together with atmospheric neutrino experiments (Super-Kamiokande [45], IceCube Deep-Core [46]). The main contribution for the measurement of $\sin^2\theta_{13}$ comes from reactor neutrino experiments (RENO [47], Daya Bay [48] and Double Chooz [49]). Reactor experiments also contribute to determine

$|\Delta m^2_{31}|$. The CP-violating phase δ_{CP} is currently constrained by the NOνA [42] and T2K experiments [43]. Figure 2.8 shows a comparison between the measurements from the two experiments and the global fit that includes data from the Super-Kamiokande experiment [31]. In the case of normal hierarchy (left panel of Figure 2.8) a clear

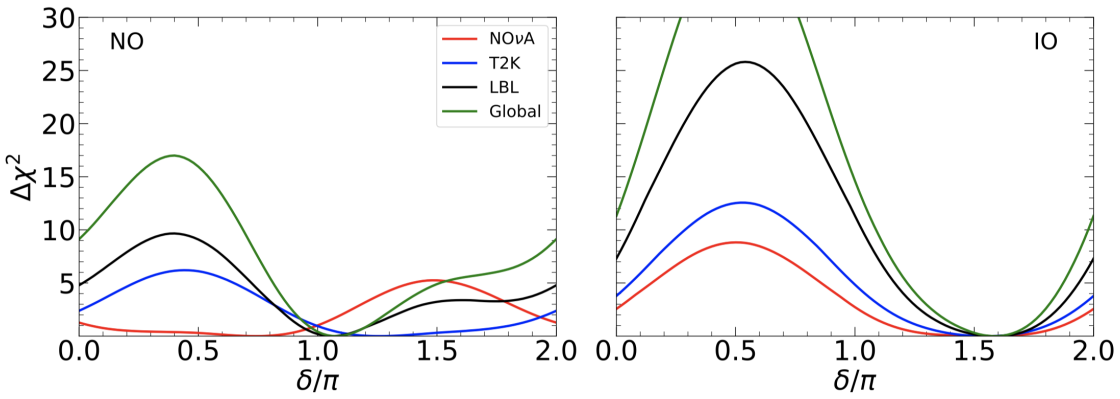


Figure 2.8: Comparison of the δ_{CP} measurements for both NOνA (red) and T2K (blue) together with the combined accelerator neutrino fit (black) and the global fit (green). The left (right) panel shows the comparison for normal (inverted) hierarchy. Figure taken from [31].

tension is visible between the NOνA and T2K data. However, excellent agreement is verified for inverted hierarchy (right panel). The value of $\delta_{\text{CP}} = 0$, which would imply CP-conservation, is disfavoured with $\Delta\chi^2 = 9.1$, while the other CP-conserving value $\delta_{\text{CP}} = \pi$ is allowed with $\Delta\chi^2 = 0.4$ for normal mass ordering and disfavoured with $\Delta\chi^2 = 14.6$ for inverted ordering [31]. Finally, data from T2K and NOνA to determine the mass ordering suggests that the inverted hierarchy is favoured with $\Delta\chi^2 = 2.4$. If reactor data is added to the fit, a preference for normal ordering is found with $\Delta\chi^2 = 1.4$. The precise determination of δ_{CP} and the mass hierarchy are currently open problems in neutrino physics. Future neutrino experiments, such as DUNE [50], are dedicated to addressing these open problems in neutrino physics. To conclude this section, a summary of the current best-fit values [31] for the oscillation parameters are reported in Table 2.1.

Table 2.1: Global fit values of neutrino oscillation parameters for both normal (NO) and inverted (IO) neutrino mass ordering. Values from [31].

Parameter	**Best Fit** $\pm 1\sigma$
Δm^2_{21}	$7.50^{+0.22}_{-0.20} \cdot 10^{-5}\text{eV}^2$
$\sin^2\theta_{12}$	0.318 ± 0.016
$\lvert\Delta m^2_{31}\rvert$ (NO)	$2.55^{+0.02}_{-0.03} \cdot 10^{-3}\text{eV}^2$
$\lvert\Delta m^2_{31}\rvert$ (IO)	$2.45^{+0.02}_{-0.03} \cdot 10^{-3}\text{eV}^2$
$\sin^2\theta_{23}$ (NO)	0.574 ± 0.014
$\sin^2\theta_{23}$ (IO)	$0.578^{+0.010}_{-0.017}$
$\sin^2\theta_{13}$ (NO)	$0.02200^{+0.00069}_{-0.00062}$
$\sin^2\theta_{13}$ (IO)	$0.02225^{+0.00064}_{-0.00070}$
δ_{CP}/π (NO)	$1.08^{+0.13}_{-0.12}$
δ_{CP}/π (IO)	$1.58^{+0.15}_{-0.16}$

2.4.4 Overview of Accelerator Neutrino Experiments

In accelerator experiments, neutrinos are artificially created employing a beam of protons. Accelerated protons hit a target of beryllium or graphite creating new particles including charged pions, which subsequently decay into (mainly) muon neutrinos and muons. Other charged particles resulting from the proton collision are stopped using an absorber of steel, copper and graphite. Magnets are used to select the charge of the pions, thereby choosing a neutrino or anti-neutrino mode according to the decays:

$$\pi^+ \to \mu^+ + \nu_\mu \quad \text{or} \quad \pi^- \to \mu^- + \bar{\nu}_\mu. \tag{2.30}$$

The pions decay in flight and the energy of the neutrino depends on the energy of the pion and the decay angle. Due to the stochastic nature of this method of production, neutrino beams generally have a wide distribution in energy and the initial (unoscillated) flux needs to be measured. A near detector, located close to the neutrino source, is usually employed for this purpose. The flux measured by the near detector is then used to extrapolate the flux to the location of the far detector, which is located downstream. The oscillated flux measured at the far detector is compared

to the extrapolated unoscillated flux to determine the oscillation probability. In reality, the number of events observed in both detectors is a convolution of the flux and the interaction cross section, whose precise knowledge is crucial for a significant measurement. To study the oscillation probability, the energy of the neutrino needs to be correctly reconstructed (see Section 2.4.1). Since the neutrino is not observed directly, its energy is reconstructed adding the energy of the detectable particles in the final state. The reconstruction exploits nuclear theories and modelling together with the measurement of the energy of the final-state particles. The work described in this thesis (Chapter 7) aims at improving the energy reconstruction for liquid argon neutrino detectors.

Chapter 3

The ProtoDUNE-SP Experiment

Contents

3.1 The Deep Underground Neutrino Experiment 27
3.2 Liquid Argon Time Projection Chambers 30
3.2.1 Charge Detection 31
3.2.2 Light Detection 32
3.3 ProtoDUNE-SP Overview and Goals 32
3.4 Detector 33
3.4.1 The LArTPC 34
3.4.2 The Photon Detection System 36
3.5 Beam Line 39
3.6 Cosmic-Ray Tagger 41
3.7 Data Acquisition, Timing and Trigger 42
3.8 Simulation 44
3.9 Track Object Reconstruction 45
3.9.1 Signal Processing 46
3.9.2 Hit Finding 46
3.9.3 Pattern Recognition 48
3.10 Charge and Energy Calibration 51
3.10.1 Space Charge Effect Calibration 52
3.10.2 Drifting Electron Lifetime 54
3.10.3 Detector Effect Mitigation 55
3.10.4 Calorimetry 57

This chapter will present a detailed technical description of the ProtoDUNE-SP experiment that has operated at the European Organization for Nuclear Research (CERN) Neutrino Platform since the summer of 2018. Section 3.1 will put ProtoDUNE-SP in the context of the broader DUNE program, briefly presented therein. Section 3.2 will be dedicated to describing the liquid argon time projection chamber (LArTPC) technology to illustrate the functioning and detection principle. An overview of the ProtoDUNE-SP goals are given in Section 3.3, while the main detector components are summarised in Section 3.4. ProtoDUNE-SP is situated downstream the H4 beam line at CERN. The beam line setup, with the description of the main components, will be discussed in Section 3.5. To tag and track cosmic-ray muons, ProtoDUNE-SP uses a cosmic ray tagger, briefly described in Section 3.6. Section 3.7 will present the data acquisition system and how the data are registered for reconstruction and Section 3.8 will illustrate the main steps for the simulation of beam and cosmic-ray data. Finally, Section 3.9 will give a review of the reconstruction algorithms and Section 3.10 will discuss the detector energy calibration.

3.1 The Deep Underground Neutrino Experiment

The Deep Underground Neutrino Experiment (DUNE) is a future accelerator neutrino experiment hosted by the Fermi National Accelerator Laboratory (Fermilab) in the United States. It will feature a new high-intensity neutrino beam and a near-far detector setup. The near detector will be positioned in proximity of the neutrino source at Fermilab, while the far detector will be situated 1.5 km underground at the Sanford Underground Research Facility (SURF) in South Dakota [51]. The distance between the near and far detector will approximately be of 1,300 km. Figure 3.1 shows a cartoon of the setup.

The DUNE main physics goals, as highlighted in [50], are:

- Measurements of neutrino oscillation parameters using a beam of ν_μ and $\bar{\nu}_\mu$. In particular, this will include the measurement of the δ_{CP} phase, the determination

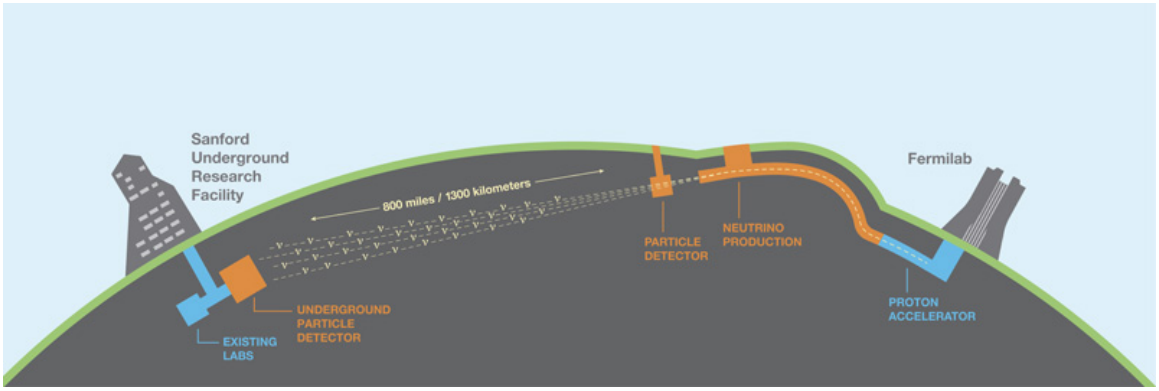


Figure 3.1: Cartoon showing the setup and the main components of the DUNE experiment. From [51].

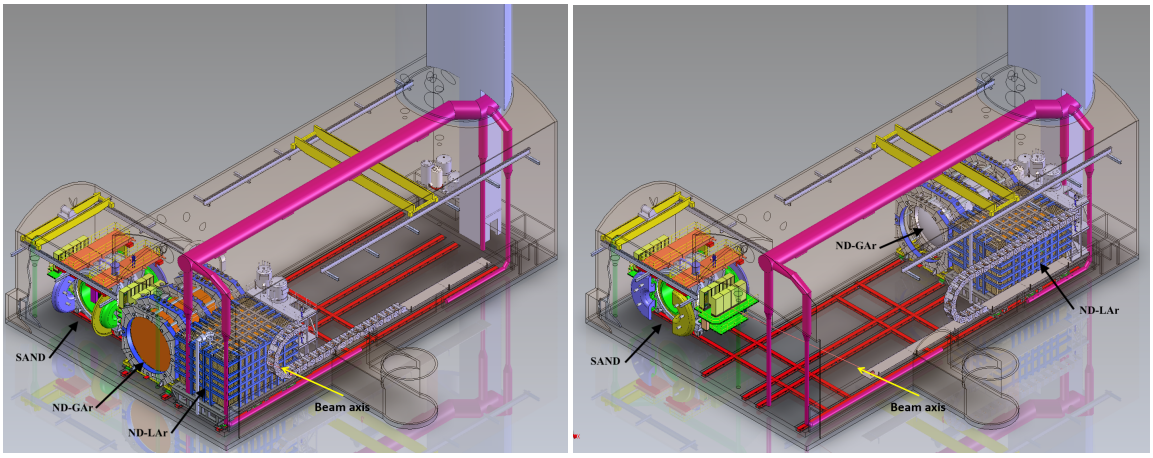
of the sign of Δm^2_{31} and the measurement of the mixing angle θ_{23}. The octant in which θ_{23} lies will also be determined. The mixing angle θ_{13} will also be measured through the ν_e and $\bar{\nu}_e$ appearance channels with a precision similar to that of reactor experiments.

- Search for proton decay.
- Study of early stages of supernova core-collapse through the measurement of the neutrino flux resulting from the collapse.

In addition to the main physics goals, other ancillary studies are possible: the search for sterile neutrinos, dark matter phenomena and Lorentz invariance violation and the measurement of atmospheric neutrino oscillations and neutrino cross sections. [50].

To accomplish these goals, a sophisticated design has been developed for both the near and far detector. The near detector will comprise of three main components [52]: (1) a liquid argon time projection chamber ("ND-LAr"), (2) a high-pressure gaseous argon time projection chamber ("ND-GAr") enclosed in a magnetised electromagnetic calorimeter (ECAL) and (3) a magnetised beam monitor (inner tracker + ECAL). A schematic of the three components is reported in Figure 3.2. ND-LAr has the same detection principles as the far detector described below, with differences in design aimed at adapting it to the higher beam intensity at the near detector. ND-Gar has a lower momentum threshold for the detection of charged particles and the better

identification of charged pions will be exploited to study the activity around the interaction vertex. Both ND-LAr and ND-Gar can be moved off-axis with respect to the neutrino beam direction, as shown in Figure 3.2. By moving off-axis they will be able to sample a narrower flux spectrum with different mean values, thereby taking data that can be used to deconvolve the neutrino flux and cross section, as well as mapping the detector energy response. This capability is referred to as DUNE-PRISM. The third near detector component, called "SAND", is designed to monitor the neutrino flux to detect changes in the beam composition. The different target in SAND will also be used to perform a systematic crosscheck with the flux measured by ND-LAr.



(a) (b)

Figure 3.2: Schematic of the DUNE near detector components. Left: all the components are positioned on-axis. Right: ND-LAr and ND-Gar are shown in the off-axis configuration. Figure from [52].

The far detector will be composed of four LArTPC detector modules, each with a fiducial mass of about 10 kt [51]. The use of the same target nucleus and similar technology in both near and far detector mitigates the uncertainty on nuclear effects and the detector systematics in performing the oscillation measurements. However, it is the first time that the LArTPC technology is being used on such a large scale. A large effort of prototyping the most important components to understand and characterise the response of the DUNE components is ongoing. It is in this context

that ProtoDUNE Single Phase (ProtoDUNE-SP), a LArTPC detector prototype, has been built and operated.

3.2 Liquid Argon Time Projection Chambers

There are in general two types of liquid argon time projection chambers (LArTPCs): single-phase (SP) and dual-phase (DP). Both technologies rely on the collection of ionisation charge and scintillation light resulting from a charged particle interaction with the argon atoms. In the single-phase technology, the ionisation electrons drift in liquid argon to reach an instrumented anode and a good signal-to-noise (S/N) ratio can be achieved thanks to low-noise electronics. The details of the dual-phase technology are not relevant for the content of this thesis, but can be found in a number of sources such as [51].

Single-phase LArTPCs, initially proposed in 1977 [53], are becoming popular types of neutrino detectors following the successful employment in experiments like ICARUS [54], ArgoNeuT [55], LArIAT [56] and MicroBooNE [57]. Their excellent calorimetry measurement capabilities and precise 3D reconstruction make them ideal for precision measurements. In general terms, they consist of a volume of liquid argon enclosed in a cryostat that keeps a temperature of around 87 K.

A scheme of the functioning principle is shown in Figure 3.3. When a charged particle travels in the detector it ionises or excites the argon atoms. Argon atoms in the exited states emit a photon during the dis-excitation process. An external electric field pulls the ionisation electrons and the parent ions apart. However, some of the ionisation electrons very quickly recombine with the parent ions also generating scintillation light. Both scintillation light and the surviving ionisation electrons are detected and the combined information is used for tracking and calorimetry reconstruction. The liquid argon needs to be purified to significantly reduce the presence of electronegative elements (O_2, H_2O) [59] that can attach to electrons and decrease the charge collected.

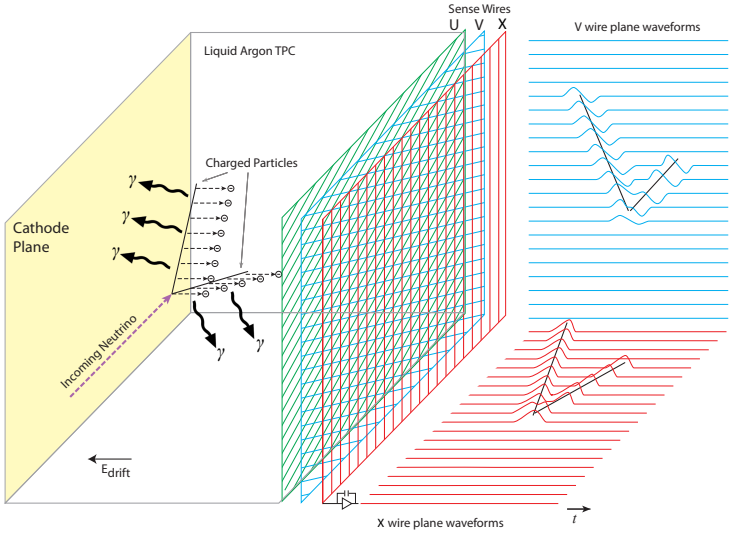


Figure 3.3: General operating principle of a single-phase LArTPC. Details are given in the text. Figure from [58].

3.2.1 Charge Detection

The ionisation electrons drift towards the TPC anode on a few millisecond time scale thanks to the constant and uniform external electric field [58]. The anode is a series of three instrumented parallel planes of conducting wires that are perpendicular to the electric field direction. Each plane is biased at a different potential to guarantee transparency to the drifting electrons to the first two planes. The electrons induce an electric signal on the wires of each plane while drifting and are collected on the last plane ("collection" plane). The two innermost planes are called "induction" planes. Because the charge travels through the first two planes, the signals induced on the induction wires present a bipolar shape, while the signals on the collection wires is unipolar. LArTPCs act as a multi-channel waveform recorder, recording the signal induced on wires in a predefined time window. Wires on different planes are at an angle between each other such that, by combining the coordinates of the wires on two different planes, a 2D reconstruction, in the plane perpendicular to the drift direction, is achieved. For a 3D reconstruction, the charge drift time needs to be calculated by

knowing the charged particle arrival time in the TPC (t_0) and the electrons arrival time at the anode. By combining that information with the drift velocity of electrons given by the electric field, the coordinate of the event in the direction perpendicular to the wire planes can be reconstructed.

The collected charge gives also information on the energy deposited by the particle: the number of electrons collected is related to the particle energy loss per distance travelled dE/dx. More detailed information on this will be given in the following sections and chapters.

3.2.2 Light Detection

The light produced by the de-excitation of argon atoms or by the recombination of ionisation electrons with argon positive ions constitutes a valuable source of information for the event reconstruction. Liquid argon is transparent to its own radiation so the prompt photons emitted are not reabsorbed and can be collected within a few nanoseconds [58]. Different arrangements, such as photo-multipliers (PMTs) [56] or light traps [58], can be implemented in LArTPCs to detect scintillation light. While light can be used to aid the reconstruction of deposited energy [60], its main use is to provide a measurement of t_0. Charge collection in LArTPCs is a relatively slow process, in that the electron drift velocity is of the order of $\sim$ mm/µs at typical electric field values and the charge needs to travel for meters. The lag in time between the charge creation and collection needs to be taken into account to correctly reconstruct the event position. On the other hand, light is detected within $\sim$ ns thereby providing a much more precise information on the time at which the ionisation takes place.

3.3 ProtoDUNE-SP Overview and Goals

ProtoDUNE-SP is a full-scale prototype and engineering test bed for the single-phase LArTPC DUNE far detector modules [61]. It is hosted by the Neutrino Platform at CERN where it has operated since 2018. ProtoDUNE-SP is the largest LArTPC ever built with a liquid argon mass of 0.77 kt. It replicates most of the DUNE far detector

module components at a 1:1 scale, with a total liquid argon mass ratio of 1:20 [61]. The detector was exposed to a particle beam in the momentum range 0.3 GeV/c - 7 GeV/c, allowing for studies of interaction of particles that are normally produced by a neutrino interaction (protons, kaons, muons, pions and electrons) with argon [62]. Additionally, being located on the surface, the detector is exposed to a large flux of cosmic rays. The main goals, as set out in [61], are:

- Prototype the construction and installation procedure for the DUNE far detector modules.
- Validate the basic detector performance using cosmic ray data.
- Collect beam data to understand and calibrate the detector response to different particle species.
- Demonstrate the long-term operational stability of the detector.

For the first run in 2018, analyses have shown that the protoDUNE performance met or exceeded the specifications for the DUNE detector demonstrating the effectiveness of the liquid argon technology at this scale [62].

3.4 Detector

The ProtoDUNE-SP detector is composed of two back-to-back LArTPCs that share a common planar cathode in the middle and have opposite electron drift directions. The TPCs are enclosed in a membrane cryostat [63] which stores the liquid argon at a temperature of around 87 K. The cryogenics setup is equipped with an argon purification system that continuously purifies the argon [62]. Purity monitors are installed at various heights in the detector to constantly monitor the concentration of impurities. To minimise the energy loss of beam particles crossing the detector material before entering the active volume, a beam plug is installed on the downstream detector face. The beam plug, one of the few elements of difference between the protoDUNE-SP and the DUNE far detector design, consists of a cylindrical pressure

vessel filled with gas nitrogen that extends inside the TPC allowing beam particles to enter the detector with minimum interaction with inactive material. Additionally, a Cosmic-Ray Tagger was installed to correctly reconstruct cosmic muon tracks, useful for calibration purposes.

3.4.1 The LArTPC

As mentioned above, the time projection chamber is divided in two volumes by the cathode. The planar cathode lies in the yz plane of the detector at the coordinate $x = 0$. The volume is around 6 m high (y coordinate), 7 m long (z coordinate, approximately in the beam direction) and 3.6 m wide in each volume (x coordinate, in the electron drift direction). The main TPC components, shown in Figure 3.4, are:

- the already mentioned cathode plane, composed of 18 cathode plane assembly (CPA) modules;
- two anode planes at each side of the cathode plane, each constituted of 3 anode plane assemblies (APAs);
- the cold electronics (CE), mounted on top of each APA;
- the field cage and the high voltage (HV) feedthrough.

Each of the 18 CPAs is 1.16 m wide and 2 m high. They are positioned in a grid of 6 columns and 3 rows [61]. A voltage of -180 kV is applied at the cathode to provide a 500 V/cm electric field across each TPC volume. At this electric field, the electron drift velocity is 1.59 mm/µs for a maximum drift time (cathode to anode) of 2.25 ms. A field cage surrounds the TPC to ensure electric field uniformity and the appropriate field boundary conditions. The CPAs are built in a resistive material called FR4, a fire-retardant fiberglass-epoxy composite material, which is laminated on both sides with a Kapton film [62]. A high voltage feedthrough is attached to the cathode enabling the connection to the HV power supply.

Each APA is composed by a stainless-steel frame 6.1 m high and 2.3 m wide. Three instrumented wire planes are attached to each side of the APA, as per the

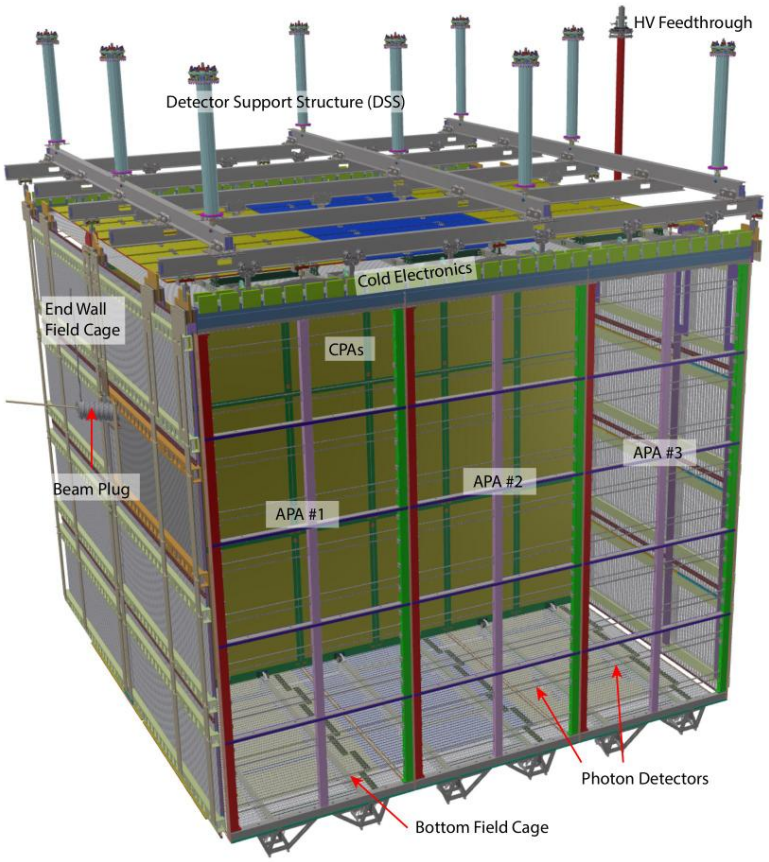


Figure 3.4: A schematic of the ProtoDUNE-SP TPC with the main components labelled. Figure from [61].

DUNE far detector requirements. An additional layer of non-instrumented wires is also present. From the inside out the wire planes and their wire orientation are: the G layer (vertical), the U layer (+35.7° from vertical), the V layer (-35.7° from vertical) and the X layer (vertical). The distance between each layer is 4.75 mm, the U and V plane have a wire pitch of 4.67 mm and the X and G layer have a pitch of 4.79 mm. Each plane is biased at a different potential to ensure that the drifting electrons can travel past the U and V layers to be collected on the X plane. For this reason, the U and V layers are referred to as "induction planes" and the X layer is the "collection plane". The G layer is added to the design to shape the pulse signal induced on the first induction plane: by shielding the U layer from the drifting charge it eliminates the long leading edge from the signals [61].

The read-out electronics are installed directly on top of the APAs inside the liquid argon and are referred to as cold electronics (CE). Front-End Motherboards (FEMBs) read the 2560 channels of each APA and amplify, shape and digitise the signal. Through a CE feedtrough, the FEMBs are connected to the Warm Interface Boards (WIBs), which further process and distribute the signal to the data acquisition (DAQ) system [61]. A more comprehensive description of the ProtoDUNE-SP electronics can be found in [64]. Figure 3.5 shows a photo of the ProtoDUNE-SP detector at the Neutrino Platform including the read-out electronics and the liquid argon purification system.

3.4.2 The Photon Detection System

Liquid argon is a prolific scintillator: at zero electric field 40,000 photons with a 128 nm wavelength are created for 1 MeV of energy deposited. The collection of light can add information on the event and it is particularly important to provide the event t_0 (with a resolution better than 1 µs) and to reduce the background in supernova events in DUNE [61].

The design of the photon detection system (PDS) in ProtoDUNE-SP has the objective of testing a number of different solutions to collect and detect the light. Each APA frame has 10 support structures for the PDS behind the wire planes, amounting

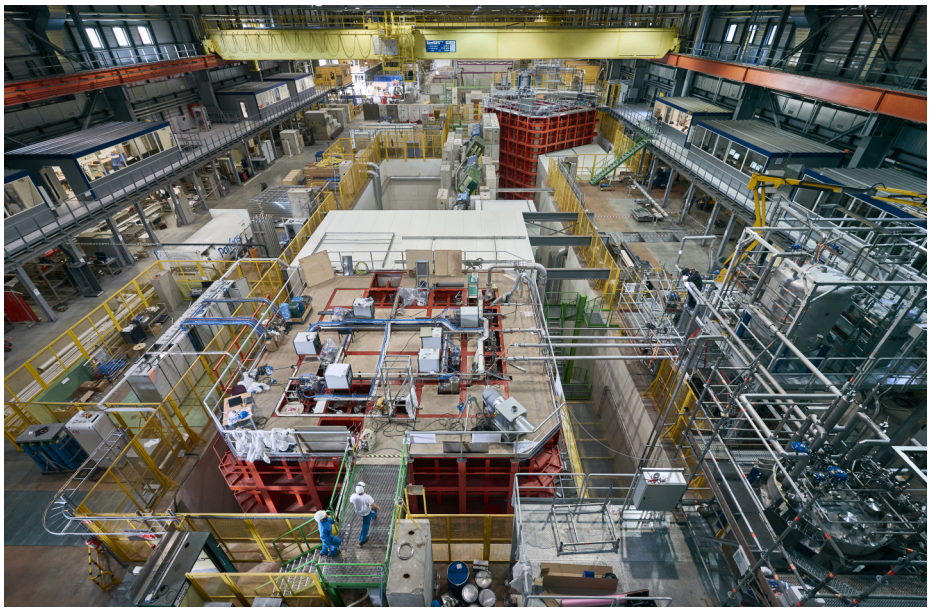


Figure 3.5: Photo of ProtoDUNE-SP at the Neutrino Platform showing the red cryostat with the read-out electronics on top. The liquid argon purification system is visible on the right-hand side. Photo from [65].

to a total of 60 slots. Of these, 58 slots are split equally between two similar types of light guides and 2 slots are reserved for a type of detector called ARAPUCA [66]. A common feature of each type of PDS is the need to convert the 128 nm light into longer-wavelength photons using wavelength shifter (WLS) compounds [62] before the light is sensed by silicon photomultipliers (SiPM) [67]. The two flavours of light guides differ in the number of times the photon wavelength is shifted. Double-shift light guides [68] have a radiator plate installed on top of wavelength-shifting polystyrene bars [61]. The plates are covered with tetraphenyl-butadiene (TPB) which converts the 128 nm wavelength to 430 nm. This blue light is then absorbed by the bar producing green light which is trapped by total internal reflection and transmitted to the end of the bar where the photosensor is mounted. The second design [69, 70] uses TPB-coated light guides, without the radiator plane installed. The detection principle is shown in Figure 3.6.

The ARAPUCA [66] modules are divided longitudinally in 12 cells. The first 8 cell are single detection units, while the last 4 cell are double-area cells. Regardless of the cell arrangements, the general detection principle of each cell is based on trapping

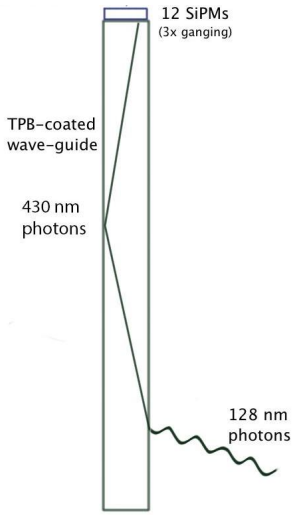


Figure 3.6: An illustration of a light guide detection principle. Figure from [61].

the light in a reflective box. An illustration is shown in Figure 3.7. A dichroic short-pass optical filter characterised by a tunable cut-off wavelength set at 400 nm is the central element of the ARAPUCA light detectors. Each side of the filter is coated with wavelength shifters with different emission wavelengths. The photons enter the cell crossing the WLS-coated external-facing layer, which shifts the wavelength to 340 nm. Crucially, the filter is transparent for photons below the cut-off wavelength, but is totally reflective for longer-wavelength photons. The WLS emission of the inside-facing layer of the filter is at 490 nm, which guarantees that the emitted photons are trapped inside the box. A fraction of the internal reflective surface is covered by SiPMs that can detect the trapped light [66].

In terms of the SiPM configuration, there is a distinction between light guides and ARAPUCAs. Each guide is read by 12 SiPMs, with one read-out channel for SiPM triplet. ARAPUCA cells also have 12 SiPMs but each SiPM has its own read-out channel. The signal from the photosensors is transmitted unamplified to a module called SiPM Signal Processor (SSP) for processing. The digitised signal is transmitted to the DAQ.

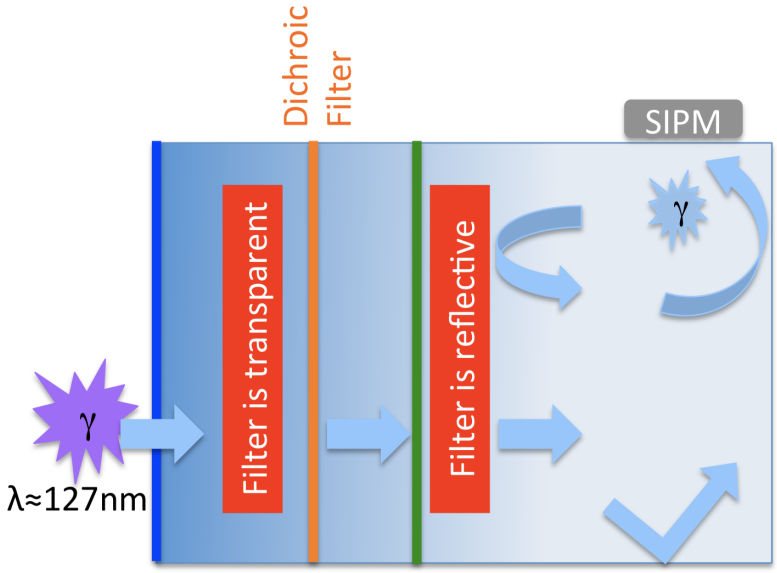


Figure 3.7: An illustration of the ARAPUCA detection principle. Figure from [66].

3.5 Beam Line

ProtoDUNE-SP is located just downstream of the H4 beam line, in the CERN North Area. The proton beam extracted from the Super Proton Synchrotron (SPS) is collided against a beryllium target giving origin to a mixed hadron beam of momentum 80 GeV/c. The secondary beam is then directed towards another target therefore producing a tertiary beam of momentum in the range 0.3 GeV/c - 7 GeV/c. The H4 beam line is designed to transport the tertiary beam to the ProtoDUNE-SP TPC [62].

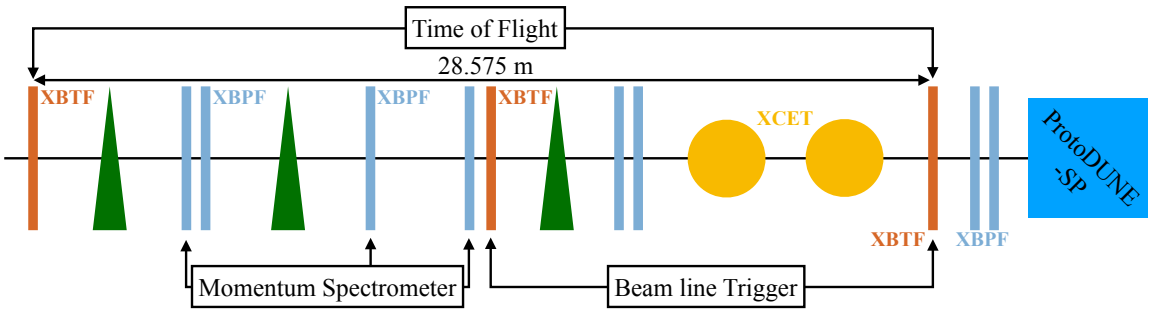


Figure 3.8: A diagram of the ProtoDUNE-SP beam line. The profile monitors (XBPF, blue), trigger counters (XBTF, orange), Cherenkov detectors (XCET, yellow) and bending magnets (green) are shown. Figure from [62].

Figure 3.8 shows a schematic diagram of the H4 beam line components in order. There are three types of detectors and three bending magnets [62]. Eight profile monitors (XBPF) [71] track the beam position on a single particle basis and can also be used to reconstruct the momentum of particles. The last two XBPFs (right-hand side of Figure 3.8) are especially important in that they measure the trajectory of the particles to be extrapolated inside the TPC. Trigger counters (XBTF) are positioned upstream, downstream and in the middle of the beam line. A coincident signal between the middle and downstream counters are used to trigger the TPC read-out during beam runs, while the upstream and downstream counters, separated by 28.575 m, are used to measure the time of flight (TOF) of particles. Prediction and measurement of the TOF as a function of the momentum of different particles are shown in Figure 3.9. In addition, two Cherenkov (XCET) counters aid the TOF measurement in identifying particle species. A more detailed description of the beam line design and instrumentation can be found in [72] and [73] respectively.

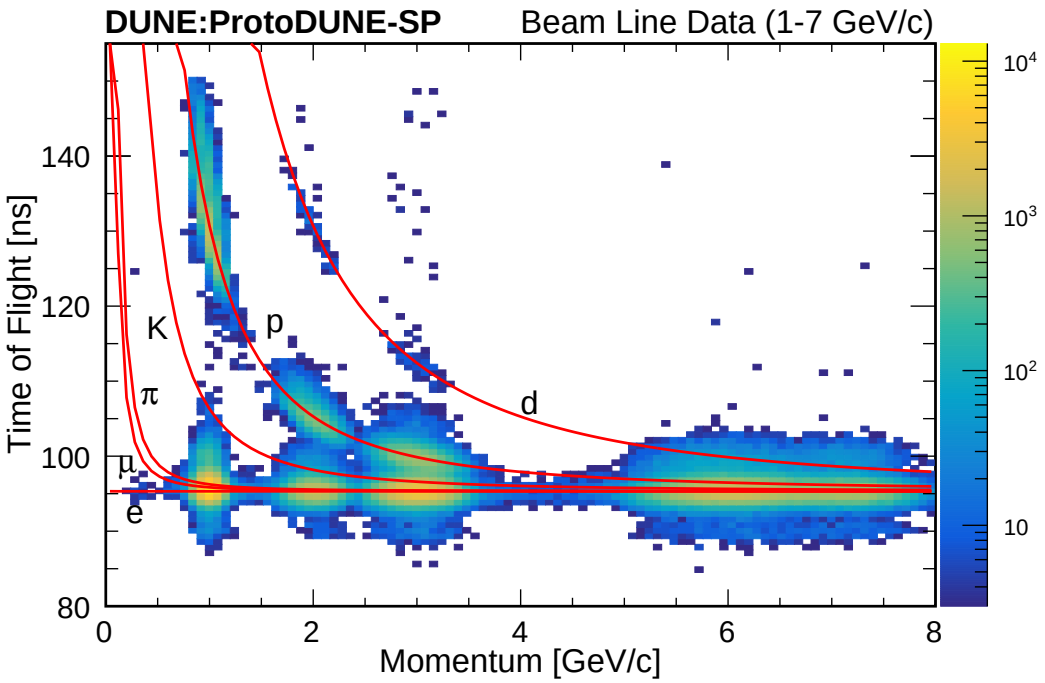
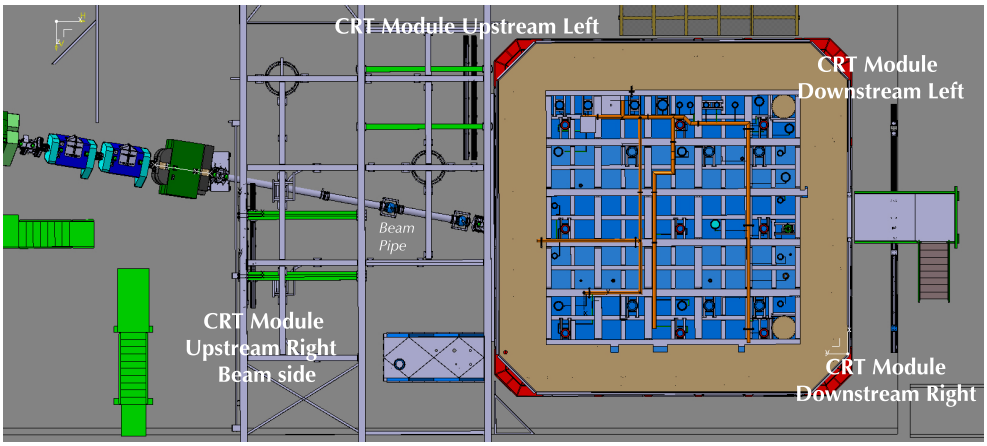


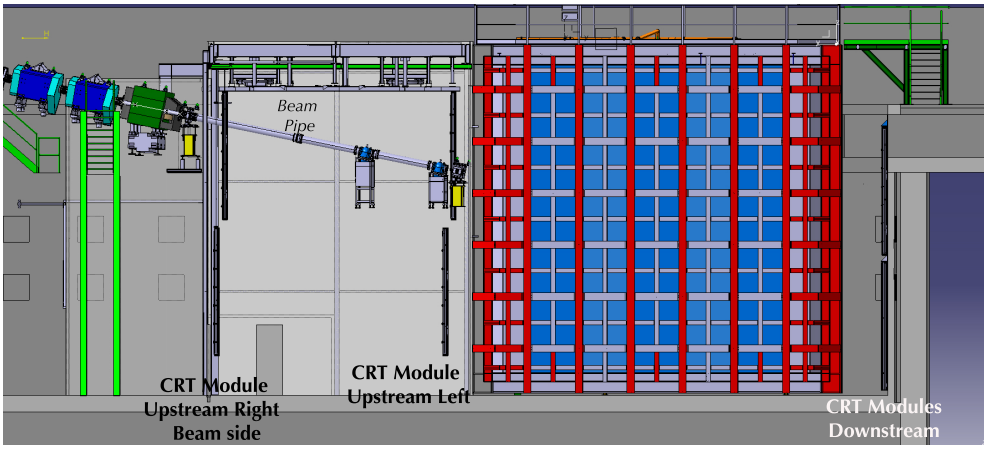
Figure 3.9: Prediction (red line) and measurement (2D histogram) of the TOF as a function of the momentum of e, μ, π, K, p and d using ProtoDUNE-SP data. Figure from [62].

3.6 Cosmic-Ray Tagger

The Cosmic-Ray Tagger (CRT) is a group of scintillator detectors positioned to cover the upstream and downstream faces of the TPC. The CRT is installed to provide the trigger for the TPC acquisition window based on cosmic-ray muon events travelling parallel to the anode planes. The surface TPC is exposed to a 20 kHz rate of cosmic-ray muons, amounting to around 60 muons in each 3 ms TPC acquisition window. This rich sample is particularly useful for calibration purposes. The arrangement of the CRT components can be seen in Figure 3.10. The CRT is made up of four



(a) Top view.



(b) Side view.

Figure 3.10: Top and side view of the Cosmic-Ray Tagger modules positioned upstream and downstream the ProtoDUNE-SP TPC. Figure from [62].

6.8 m high and 3.65 m wide assemblies. Two assemblies are positioned upstream with

respect to the TPC, while the other two are located downstream. The two upstream assemblies are offset to allow the passage of the beam pipe coming at an angle with respect to the detector main axes. Each assembly is constituted of sub-modules that contain scintillation strips in two perpendicular directions, allowing to record a two-dimensional hit when a particle travels through one of the assemblies. Track reconstruction with the CRT is achieved when hits in the front modules are matched with hits in the back modules within a coincidence time window calculated using the expected time of flight of the cosmic ray particle [62]. When a CRT-reconstructed track is matched to a TPC track, the track t_0 can be reconstructed.

3.7 Data Acquisition, Timing and Trigger

The data coming from the TPC, the PDS and the CRT is collected by the data acquisition system (DAQ). The DAQ is also responsible for reducing the volume of data using compression techniques and preparing the data for offline storing and processing. In the spirit of employing the ProtoDUNE-SP detector as a test-bed for DUNE, two distinct read-out solutions have been installed to read-out the TPC data. The signal from five APAs is read by processing units called Reconfigurable Cluster Elements (RCEs) [74]. The remaining APA is read by FELIX cards, designed for the ATLAS experiment [75]. Both types of units receive the signal directly from the WIBs. A diagram representing the data flow from the detector components to the DAQ and the offline storage is shown in Figure 3.11.

The timing system broadcasts a 50 MHz clock to each component and it also interfaces with the CERN SPS beam presence signal to select a beam or non-beam acquisition [62]. The trigger signal is provided by the Central Trigger Board (CTB). Low level trigger signals are generated by the subsystems such as PDS, SPS beam spill, CRT or beam instrumentation and are combined by the CTB into a high level trigger according to a configurable input logic of coincidences or anti-coincidences [61]. The timing system also validates or vetoes the trigger signal by checking if another trigger has already been issued. If a trigger is accepted, a read-out window (also

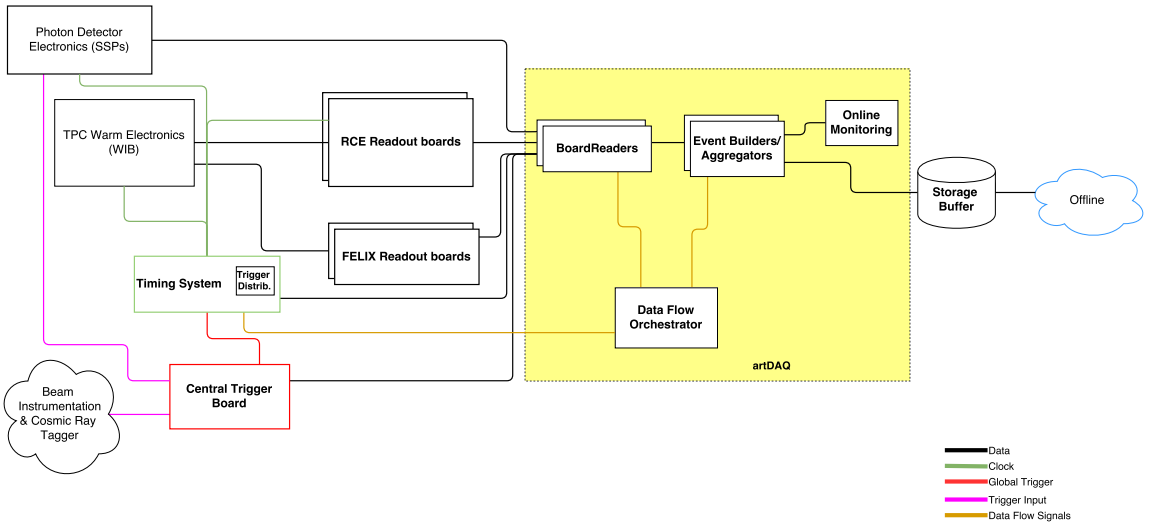


Figure 3.11: Diagram showing the data flow from the detector components through the DAQ elements to the offline storage. The timing and trigger signals are also shown. The software components of the artDAQ framework, discussed in the text below, are included in the yellow box. Figure from [61].

referred to as an "event") begins. Each TPC read-out window consists of 6,000 ADC samples digitised at a frequency of 2 MHz for a total duration of 3 ms. The period between each ADC sample lasts 500 ns and is called a "tick" [62]. With respect to the trigger absolute time, the read-out window is started 250 µs (500 ticks) earlier. This allows to collect the charge of particles which enter the TPC before the trigger time, but whose charge only reaches the anodes at around or later than the trigger time.

The DAQ software is based on artDAQ [76], developed by the Fermilab Scientific Computing Division. The software handles the data transfer and the event building and possesses some tools to perform event analysis [61]. There are a total of three consecutive procedures that are handled by artDAQ. The first process is the board reader process which provides hooks for configuring values for the hardware and reading out. The data from every board reader process is assembled by the event builder process into a raw data event. Finally, the aggregator process is in charge of writing the data to disk and also provides real time monitoring of the data acquisition.

3.8 Simulation

The event simulation in ProtoDUNE-SP is performed with LArSoft [77], a set of software tools for simulating, reconstructing and analysing events in liquid argon neutrino experiments. LArSoft is based on the Art event framework [78] developed at Fermilab. The LArSoft toolkit is used by many liquid argon experiments: they all share a common framework on top of which experiment-specific code is developed. The simulation in LArSoft can be divided in three consecutive steps: generation, particle propagation and detector simulation. In the generation step, the initial distribution of particle species, position and momenta is created. In the case of ProtoDUNE-SP, the full simulation includes beam particles, beam halo particles coming from the H4 and other upstream beam lines and cosmic rays. Beam particles are simulated using the G4Beamline event generator [79], FLUKA [80, 81] and MAD-X [82]. Cosmic-ray particles are generated using CORSIKA [83]. Additionally, a dedicated LArSoft generator simulates radionuclide decay products for radiological background studies [61]. The simulation geometry is described by GDML files [84]. GDML files contain the information on the location, shape, size and type of material of the TPC and the surrounding objects like the cryostat, the field cage and the experimental hall. The propagation of the generated particles through the materials described in the GDML files is performed by GEANT4 [84]. GEANT4 tracks the particles in 300 µm steps, a distance much smaller than the experiment resolution and that allows the simulation of processes like delta-ray emission and electromagnetic showers. The main output of the GEANT4 simulation is the energy deposited by each particle at each simulation step. The simulation of photons and electrons emission following the energy deposition is performed by LArSoft specific tools using parametric models that account for charge recombination. A minimum ionising particle has an approximate average energy loss of 2.12 MeV/cm. In liquid argon, it takes 23.6 eV to create an electron-ion pair and 19.5 eV to emit one photon, meaning that tens of thousands of electrons and photons would need to be tracked in the simulation for each cm of charged-particle track [61]. It would therefore be impractical to do so in GEANT4. The detector

simulation handles the propagation of electrons to the collection wires and photons to the PDS using approximation techniques that retain signal prediction accuracy and can be carried out in a reasonable time. Effects such as electron attachment to impurities, charge diffusion and space charge (created by positive ions left over from the ionisation) are also simulated in this step. The charge amount and arrival time at each wire is calculated, as well as the photons arrival time at the PDS. This information constitutes the input to the detector response simulation. The charge true arrival time is convoluted with the field response (i.e. the signal induced on the wires, simulated using GARFIELD [85, 86]) and the simulated electronics response to obtain waveforms. After applying the electronics gain and adding the simulated noise, the waveform is quantised to mimic the behaviour of an ADC [61]. The output of the detector simulation is then used for the event reconstruction.

Each of the three simulation steps can be run independently within LArSoft, taking as input the output ROOT [87] file that is produced by the previous step (except for the generation phase which does not require an input file). The modularity in the simulation makes it simple to change the simulation parameters to perform dedicated studies without having to re-run any previous step.

3.9 Track Object Reconstruction

The simulated and real data are subject to the same reconstruction procedures. This section will focus on the steps involved in reconstructing the charge signal, since the details of the PDS pulse reconstruction are not relevant for the work presented in this thesis.

LArTPC detectors generate large data volumes in the form of waveforms. The goal of the reconstruction algorithms is to identify and build track or shower objects comprising of calorimetry information starting from the raw data. This gets particularly complicated when trying to reconstruct tracks embedded by charge that has originated from other tracks or showers [88], situation the occurs frequently when looking at neutrino-argon interactions.

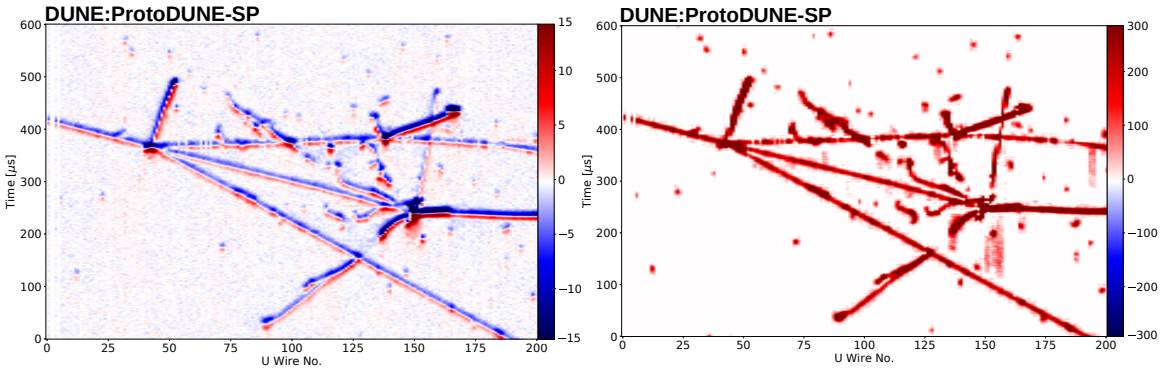
Different steps are involved and they are summarised in this section. To optimise the performance of the reconstruction steps, preliminary operations are performed on the waveforms. The data preparation includes running algorithms to evaluate the ADC pedestal, identify "sticky" code and remove correlated noise across channels. The detailed procedures are described in [62].

3.9.1 Signal Processing

The waveforms recorded on each readout channel are a convolution of the real charge-*vs*-time signal and detector artifacts, in particular the field and electronics response [88]. The goal of signal processing is to remove these artifacts and produce distributions of charge arrival time. The field response of the detector is obtained by simulating point charge drifts with GARFIELD and using the Shockley-Ramo [89] theorem to calculate the current induced by moving charges on the wires. An important finding of the field response simulation is that the current induced on a particular wire has significant contributions from moving charges that are far away from the wire itself. Because of this long-range effect, a 2D deconvolution involving both the time and the wire dimension is performed. A thorough description of this procedure can be found in two papers by MicroBooNE [90, 91]. Figure 3.12 shows the effect of the 2D deconvolution on raw waveforms after the noise filtering is applied. One important consequence of the signal deconvolution is that the bipolar signals on the induction plane are turned into unipolar signal, greatly simplifying the hit finding procedure. Lastly, to further reduce the noise and improve the resolution, techniques to identify signal regions of interest (ROI) within the waveform are implemented.

3.9.2 Hit Finding

In the LArTPC experiment jargon, a "hit" is a two-dimensional object representing a cluster of electric charge arriving at a given wire at a given time. It is obtained in practice by fitting peaks in each waveform. The hit finder algorithm searches for candidate hits in the region of interests and, when found, tries to fit a Gaussian shape. An example of three fitted hits in ProtoDUNE-SP is illustrated in Figure 3.13.



(a) After noise filtering. (b) After 2D deconvolution.

Figure 3.12: Interaction vertex of a beam event measured on the induction plane U. Left: raw waveform in ADC counts after noise filtering. Right: Ionisation expressed in number of electrons (scaled by 200) extracted with the 2D deconvolution. Figure from [62].

However, it can happen that the hit shape is not a simple Gaussian, for example in

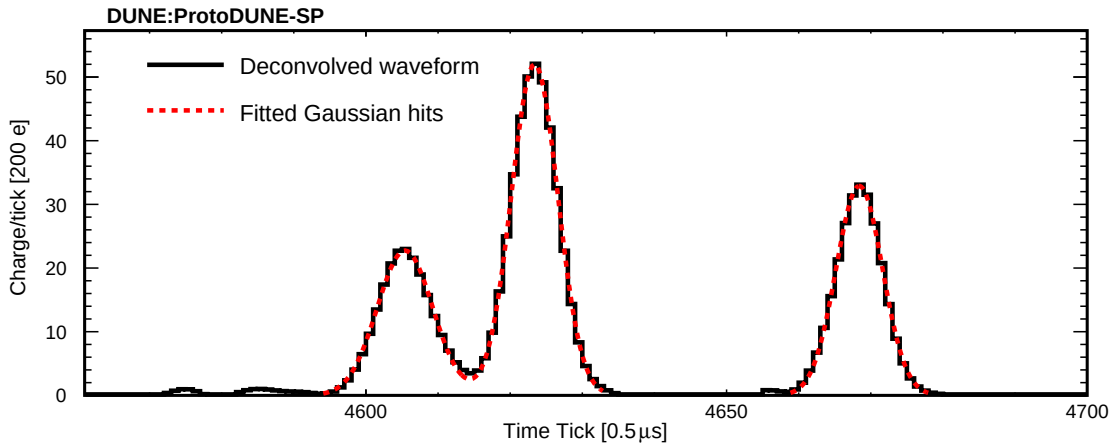


Figure 3.13: Example of a reconstructed waveform in ProtoDUNE-SP with hits fitted by the hit finder algorithm. Figure from [62].

the case of a track that lies in the plane defined by the wire and the electric field, for which multiple hits "pile-up" on the same wire in a short time. In this case, the pulse is divided in a number of hits that are spaced evenly [62].

The extracted properties of the hits are the parameters of the Gaussian fit: the area represents that total charge (times a calibration constant that converts Coulomb to ADCxtick) and the mean represents the hit peak time.

3.9.3 Pattern Recognition

The pattern recognition in ProtoDUNE-SP is performed by Pandora [92], a dedicated software toolkit extensively used in a number of LArTPC neutrino experiments such as MicroBooNE [93]. ProtoDUNE-SP specific algorithms were developed in Pandora to reconstruct charged beam particles, which are not present in neutrino experiments, and to deal with the two TPC volumes of ProtoDUNE-SP. Starting with the reconstructed hits, the pattern recognition proceeds in three main steps: (1) hit clustering, (2) reconstruction of track-like objects under the cosmic-ray hypothesis and (3) removal of cosmic-ray candidates and reconstruction of beam events. The final output of the reconstruction is called a particle "hierarchy", in which links are made between parent and daughter particles.

In the first step, a two-dimensional clustering of hits is performed for each readout plane independently. Then, the algorithms try to match the 2D clusters across the three planes, using the redundancy provided by the three independent views to also correct for possible mistakes in the preliminary 2D clustering. Once the match is performed, 3D hits are created (also called "space points") and the particle hierarchies are built.

Following the hit clustering, Pandora proceeds to reconstruct the clusters under the cosmic-ray hypothesis. An important step in this phase is the attempt at reconstructing the t_0 of the track. The t_0 is defined as the time at which the track enters the TPC and is measured with respect to the trigger (beam) event, which by definition occurs at $t = 0$. While the t_0 of a track can be reconstructed using the light information, the high number of cosmic tracks in each TPC readout window makes it challenging to assign a t_0 to each track. Alternative techniques to reconstruct the t_0 without using the light can be implemented for those tracks that cross one of the TPC boundaries that are perpendicular to the drift direction, in this case the CPA plane. Since the reconstruction assumes by default $t_0 = 0$, these tracks will be in general reconstructed as two separate segments characterised by the same distance from the cathode. The distance from the cathode is proportional to the real t_0 of the

track. This geometry topology is exploited by Pandora to search for two 3D clusters that are reconstructed in two different drift volumes and have consistent direction and similar distance from the cathode. If such match is found, a "stitch" is performed by shifting the two clusters to the x coordinate of the boundary and creating a single cluster object. The measurement principle for a cathode-crossing track is illustrated in Figure 3.14. In a similar manner, the t_0 of tracks that cross the anode can be reconstructed. In this case, the few hits in the "pseudo" TPC found between the anode planes and the cryostat can be used to provide a timing match with the hits inside the main TPC. The efficiency of this latter procedure is much smaller.

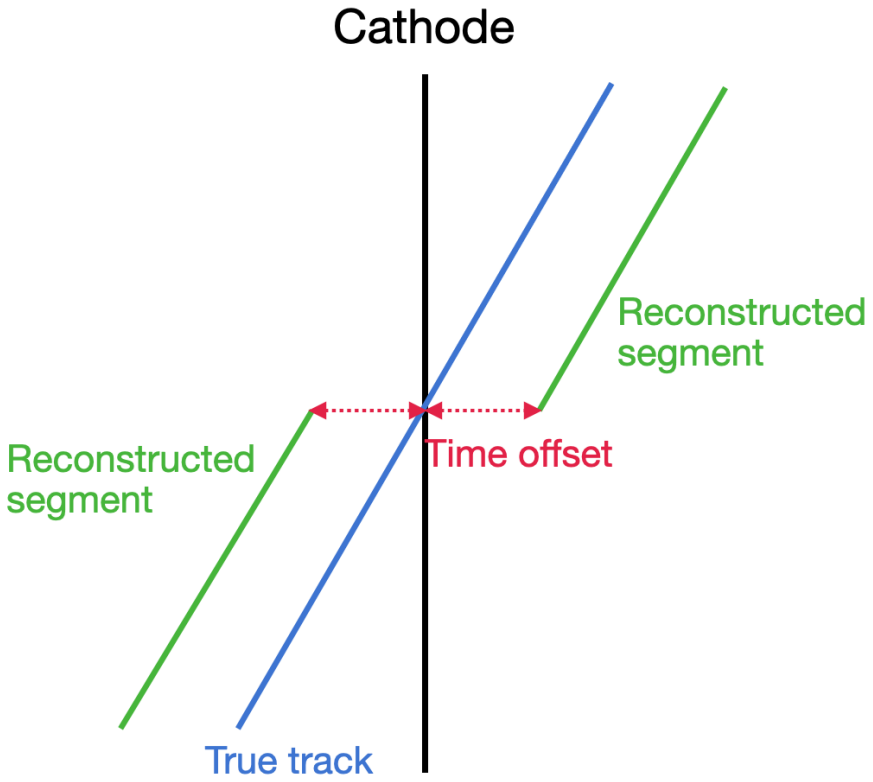


Figure 3.14: Illustration of two tracks segments stitched at the cathode. The blue line represents the true trajectory of a cosmic-ray particle. The two green segments show how such particle would appear in the reconstruction before the t_0 reconstruction. After the stitching, a single track is created with the correct t_0 extracted from the time offset.

A clear cosmic-ray candidate is identified if the track satisfies one or more of the following criteria [62]:

- the particle enters through the top and exits through the bottom of the detector ("through-going particle");
- the t_0 reconstructed through the stitching procedure is not consistent with the time of a beam particle;
- if, assuming $t_0 = 0$, any hit appears to be located outside the TPC volume, meaning that the object is not compatible with the beam time.

The identification of these tracks is important not only to more efficiently reconstruct beam particles, but they are also a critical sample for any calibration purpose. After the clear cosmic-ray particles are identified, their hits are removed from the event and the pattern recognition enters the third step.

In the third and last step, the remaining hits are grouped in 3D slices of the detector containing all the hits from a parent particle. Two distinctive sets of reconstruction algorithms are applied to each 3D slice. One is the cosmic-ray reconstruction mentioned above, to identify hits that were missed in the first pass. The other contains beam particle specific algorithms aimed at reconstructing the hierarchy of the particle decay chain [62]. A booster decision tree is then used to identify slices containing beam particles, based on topological information.

The output is in the form of "particle-flow" objects that contain the links among the beam particle interactions. Each particle flow object, called "PFParticle", represents a reconstructed track or shower and is the main starting point for most ProtoDUNE-SP analyses. Figure 3.15 shows an example of a simulated π^+ (magenta track) and the corresponding fully-reconstructed interaction hierarchy.

Supplementary information to that of Pandora is provided by a hit classification algorithm performed with a Convolutional Neural Network (CNN) [94]. The CNN score for each hit can be used to efficiently distinguish between hits originated by a track-like or shower-like energy deposition. Figure 3.16 shows the CNN track-like score for a reconstructed ProtoDUNE-SP event. Shower activities, delta rays and Michel electrons[1] present a low track score as expected. The CNN score can also

[1]Michel electrons are electrons resulting from muon decays at rest.

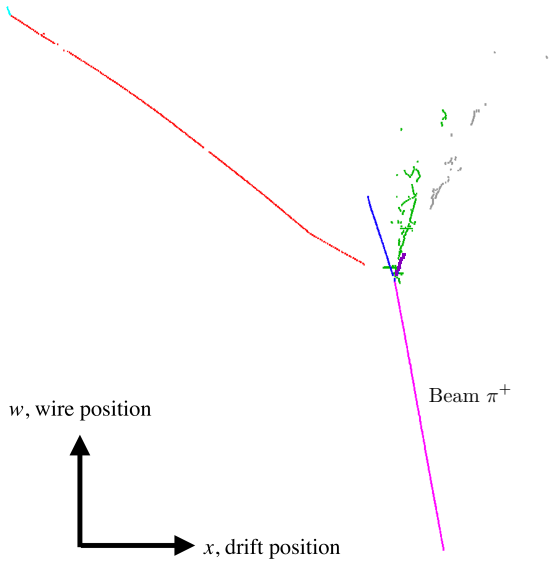


Figure 3.15: Example of reconstructed particle hierarchy using Pandora. The incoming particle is a simulated π^+ (magenta) and a number of secondary particles are visible in other colours. Figure from [62].

be used to specifically identify Michel electron hits that might mistakenly end up clustered together with the parent muon hits.

3.10 Charge and Energy Calibration

Precision calorimetry measurements are one of the reasons why LArTPCs were proposed for neutrino experiments. The accurate measurement of the final-state particle dE/dx is crucial to correctly reconstruct the energy of incoming neutrinos. In addition to demonstrating the feasibility of a precision calorimetry reconstruction in a large TPC volume, the correct dE/dx reconstruction is needed to correctly identify particles.

The energy calibration and reconstruction is a procedure that involves a number of steps and entails correcting the collected charge for space charge effects, argon impurities that mitigate the signal and other non-uniformities. A description of the main effects will be presented below. The starting point to reconstruct the charge per unit length dQ/dx is again the reconstructed hits. The charge dQ is the area of the Gaussian fit to the hit, which at this stage has units of ADC×ticks. The dx

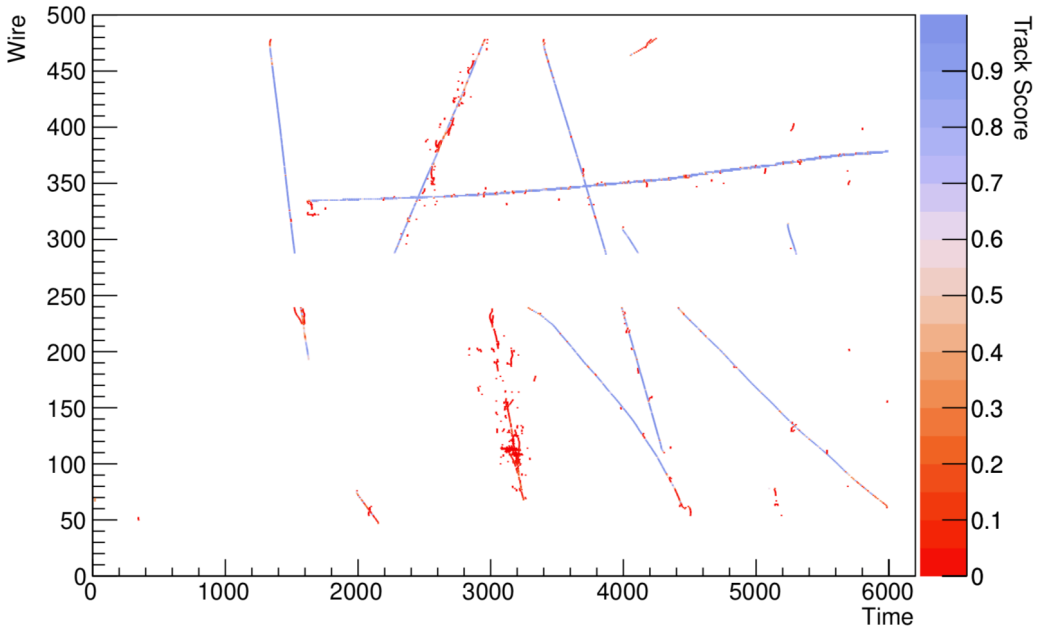


Figure 3.16: Track classifier score for a ProtoDUNE-SP event, represented by the colour scale. Time in ticks. Figure from [94].

is calculated as the wire pitch divided by the cosine of the angle between the track direction and the direction normal to the wire in the wire plane [62]. The dQ/dx obtained might substantially differ from the original dQ/dx at the location where the ionisation occurred and needs to be corrected before the charge deposition is converted into the energy loss dE/dx.

3.10.1 Space Charge Effect Calibration

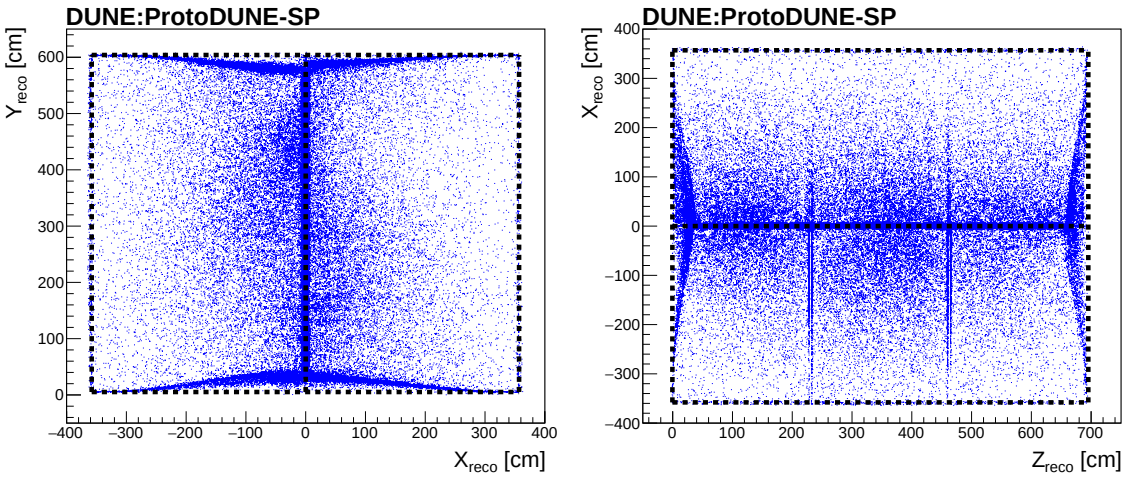
Space charge effects (SCEs) are one of the main sources of signal distortion in ProtoDUNE-SP. The surface TPCs are subject to a large flux of cosmic rays that constantly ionise the argon atoms. While the electrons travel to the anode with a velocity of $\sim$1.6 mm/µs, the more massive slow-moving ions are drifted to the cathode at $\sim$5 mm/s [88]. This results in a quick build-up of positive charge in the detector causing distortion in the external electric field. ProtoDUNE-SP, given its large drifting volume, is particularly susceptible to this effect compared to other LArTPCs. Unlike ProtoDUNE-SP, the DUNE far detector will be placed deep underground in order to have a natural shield from cosmic rays and thus the presence

of non-negligible SCEs is not expected. Therefore, to extrapolate ProtoDUNE-SP results to DUNE, it is important the SCEs are calibrated out.

The dQ/dx reconstruction is affected by SCE distortions in two ways. First, SCEs modify the electron drift paths, resulting in charge being reconstructed at a different location with respect to where the charge originated. As a consequence, the dx measurement is affected. This effect also needs to be corrected when reconstructing the track trajectory. Second, by virtue of the electron-ion prompt recombination dependence on the magnitude of the local electric field, the fraction of electrons that survive recombination becomes dependent on the location of the ionisation. This introduces a spatial dependence on the charge dQ observed.

The extent of SCE spatial distortions in ProtoDUNE-SP can be qualitatively understood by plotting the projections of the track end points of t_0-tagged cosmic-ray particles, for which it is assumed that the electrons have drifted in a straight line and with uniform velocity. These plots are shown in Figure 3.17.

The large effect (tens of centimeters) that can be observed in Figure 3.17 motivates the effort of studying and calibrating the electric field distortion. Data-driven three-dimensional distortion maps are produced for both spatial and electric field distortions by using cosmic-ray tracks. The detailed procedure, partially based on MicroBooNE work [95], can be found in [62]. The data-driven maps are used as an input to the ProtoDUNE-SP simulation to simulate the distortion. The maps can be inverted to correct for SCEs in both data and simulation. Two slices of the 3D map of the electric field distortion are shown in Figure 3.18. From the figure, it can be seen that distortions on the electric field can be up to 25% of the nominal value $E_0 = 500\,\mathrm{V/cm}$. Furthermore, the distortions about the cathode are not symmetrical, which is possibly due to the flow of liquid argon moving the ions and consequently altering their distribution in the TPCs [62]. The flow of liquid argon is the result of convective motions originating from temperature gradients in the detector and the effect of the purification system pumps. Any asymmetry in these effects could result into a space charge asymmetry, the extent of which should be confirmed with



(a) xy projection. (b) xz projection

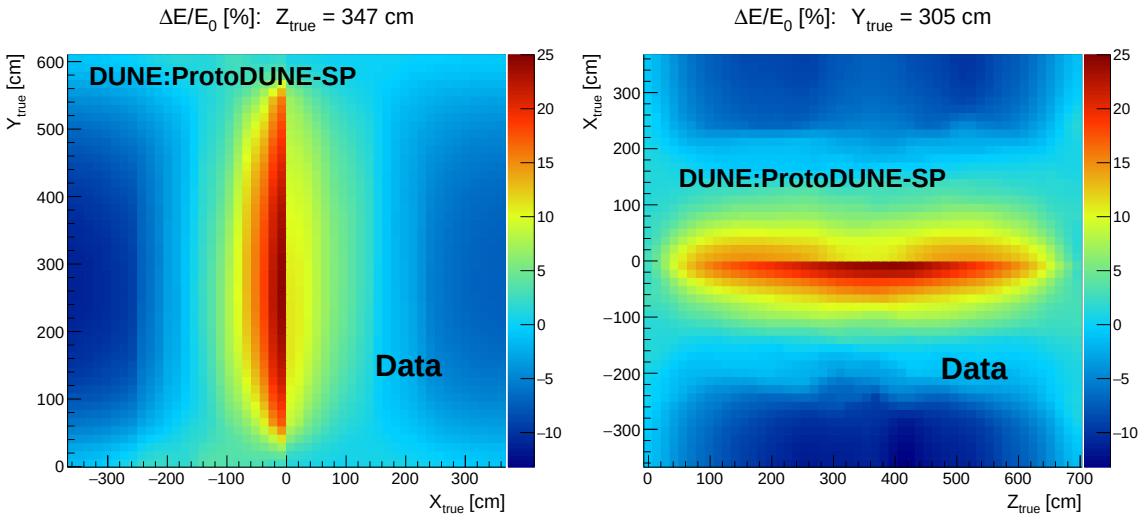
Figure 3.17: Projections of the end points of reconstructed t_0-tagged through-going cosmic muons in the xy and xz planes using ProtoDUNE-SP data. The points shown are reconstructed assuming the ionisation electrons travel in a straight line and with uniform velocity. The presence of large SCE, resulting in a distortion in the electron field and therefore in the electron actual trajectories and velocity, can be inferred by the large position offset between the projections and the TPC boundaries. Effects at the APA boundaries (vertical structures of points on the xz plane) can also be observed. They are due to the electric field distortions occurring in correspondence of the gaps. Figure from [62].

data-driven studies [62]. A detailed study of the space charge effect time variation is undergoing at the time of writing [62].

Distortion maps are used in the dQ/dx reconstruction to re-scale and correct the direction of the dx track segment. Corrections for the charge loss caused by recombination, described in Section 3.10.4 and in Chapter 4, are also based on electric field values retrieved from the distortion maps. Since SCEs introduce a spatial dependence on both the trajectory and charge reconstruction, it is crucial to precisely reconstruct the track t_0 to correctly apply the SCE correction.

3.10.2 Drifting Electron Lifetime

When ionisation electrons drift towards the anode, they can be captured by electronegative impurities (e.g. O_2, H_2O) contained in the liquid argon volume. Three purity monitors constantly measure the liquid argon purity and a sample of CRT-



(a) Map slice for the xy plane at $z = 347\,\text{cm}$. (b) Map slice for the xz plane at $y = 305\,\text{cm}$.

Figure 3.18: Two-dimensional slices of the data-driven distortion map for the electric field magnitude. Left: distortion on the xy plane at about halfway the z axis. Right: distortion on the xz plane at about half detector height. The electric field distortion is represented by the colour scale and is expressed as a percentage difference with respect to the nominal electric field. Figure from [62].

tagged cosmic muons can also be used to measure the concentration of contaminants [62]. The measurement is performed for each beam run. The electron attachments is modelled as an exponential decay, hence the name "electron lifetime". The electron lifetime is inversely proportional to the concentration of impurities [62]. The reconstructed $(dQ/dx)_{\text{meas}}$ can therefore be corrected using the formula:

$$\frac{dQ_0}{dx} = \left(\frac{dQ}{dx}\right)_{\text{meas}} \cdot \exp\left((t_{\text{hit}} - t_0)/\tau\right), \tag{3.1}$$

where dQ_0/dx represents the charge per unit length before the drift, t_{hit} is the hit time, t_0 is the track arrival time in the detector and τ is the measured electron lifetime.

3.10.3 Detector Effect Mitigation

The next step aims at calibrating out detector effects such as electron diffusion and non-uniform wire response due to dead channels. The procedure to equalise the detector response is described in [62] and follows the method developed by the MicroBooNE collaboration [96]. A summary of the main steps is given in this section.

Through-going cathode-crossing cosmic muons that are t_0-tagged using the stitching procedure of Figure 3.14 are used to perform the calibration in two steps:

- **YZ Correction Factors**: this step aims at correcting for electron transverse diffusion, non-uniform wire response and distortions caused by the wire support structures. The yz plane is divided in 5×5 cm^2 bins and for each bin the median of all the dQ/dx values of the hits in that bin is taken. The median value will be indicated as $(dQ/dx)^{\text{local}}_{\text{YZ}}$. The global median $(dQ/dx)^{\text{global}}_{\text{YZ}}$ across the whole plane is also taken. This process is done separately for each TPC volume. The YZ correction factor for a given bin is then:

$$C(y,z) = \frac{(dQ/dx)^{\text{global}}_{\text{YZ}}}{(dQ/dx)^{\text{local}}_{\text{YZ}}}. \tag{3.2}$$

- **X Correction Factors**: the corrections calculated in this step help mitigate effects such as longitudinal diffusion and residual electron lifetime effects. The drift volume is divided in 5 cm bins along the x coordinate. After correcting each dQ/dx value with the $C(y,z)$ calculated in the previous step, local median values $(dQ/dx)^{\text{local}}_{\text{X}}$ are calculated for each bin. As before, the global median $(dQ/dx)^{\text{global}}_{\text{X}}$ for all the hits is also calculated. The bin-dependent X correction factor is defined as:

$$C(x) = \frac{(dQ/dx)^{\text{global}}_{\text{X}}}{(dQ/dx)^{\text{local}}_{\text{X}}}. \tag{3.3}$$

The dQ/dx values are also normalised to the mean value at the two anodes:

$$N_Q = \frac{(dQ/dx)^{\text{anode}}}{(dQ/dx)^{\text{global}}}. \tag{3.4}$$

Finally, the fully corrected dQ/dx for each hit can be obtained with the following formula:

$$(dQ/dx)_{\text{corr}} = N_Q C(y,z) C(x) (dQ_0/dx). \tag{3.5}$$

3.10.4 Calorimetry

The last step in the calorimetry reconstruction is to calculate the dE/dx starting from the corrected $(dQ/dx)_{\text{corr}}$ measured in ADC×ticks. The dE/dx is calculated according to the equation:

$$\frac{dE}{dx} = \frac{1}{R}\left(\frac{dQ}{dx}\right)_{\text{corr}} \frac{W_{\text{ion}}}{C_{\text{cal}}}, \tag{3.6}$$

where R is the fraction of electrons that survive the recombination with ions, $W_{\text{ion}} = 23.6\,\text{eV}$ is the amount of energy required to ionise an argon atom and C_{cal} is a calibration constant that converts ADC×ticks in number of electrons and accounts for the electronics gain, ADC conversion and other residual effects.

C_{cal} is obtained by assuming a recombination model for R and fitting the most probable values of the dE/dx distribution calculated according to Equation 3.6 to the dE/dx theoretical prediction from the Landau-Vavilov theory [28] for a sample a stopping cosmic muons in the minimum ionising region [62]. In particular, ProtoDUNE-SP has so far used a parametrisation of R known as the "modified box model", developed by the ArgoNeuT collaboration [97] and discussed in detail in the next chapter.

Correctly modelling the recombination between electrons and argon positive ions is crucial to achieve a correct dE/dx reconstruction. In the next chapter, a number of recombination models will be illustrated, together with their main assumptions and application regimes.

Chapter 4

Fundamental Micro-Physics Processes in Liquid Argon

Contents

4.1 Ionisation and Excitation 59
4.2 Initial Microscopic Fast Processes 60
4.3 Processes Occurring During Drift Time 65
4.4 Electron-Ion Recombination in Liquid Argon 66
4.4.1 Recombination Models 67
4.4.2 Application of Recombination Models to LArTPC detectors 69

Ionisation electrons and scintillation photons, that constitute the source of signal for liquid argon neutrino experiments, are the result of a complex chain of processes that follow the initial energy deposition. An overview of the initial processes of ionisation and excitation, together with a model for the calculation of W_{ion}, will be presented in Section 4.1. Broadly speaking, it is possible to distinguish between processes that occur immediately following the ionisation (on the ps to µs scale) and processes that are spread over a longer time scale (ms scale) and therefore happen during the charge drift time. Section 4.2 and Section 4.3 will focus on each type separately. Section 4.4 will give a more specific summary of the main recombination models, how they have been developed and the current experimental knowledge.

4.1 Ionisation and Excitation

The interaction of charged particles in liquid argon results in the formation of either argon positive ions Ar^+ or argon atoms in an excited state Ar^* [98]. The ionised and excited argon atoms are produced in a ratio $N_{\mathrm{ex}}/N_{\mathrm{i}} = 0.21$ [99], where N_{i} and N_{ex} denote the average numbers of ions and excited atoms per unit of deposited energy respectively. In experiments that rely on the collection of charge to make accurate measurements of the energy deposited per unit length dE/dx, it is crucial to know the energy required to ionise the target material and create an electron-ion pair, denoted by W_{ion}. In the case of complete energy absorption, $W_{\mathrm{ion}} = T_0/N_i$ by definition [100] with T_0 the kinetic energy of the ionising particle. The energy balance for the energy deposited implies that

$$T_0 = N_{\mathrm{i}}E_{\mathrm{i}} + N_{\mathrm{ex}}E_{\mathrm{ex}} + N_{\mathrm{i}}\epsilon, \tag{4.1}$$

where E_i is the average energy loss per ionising collision, E_{ex} is the average energy expenditure to excite an argon atom and ϵ is the average kinetic energy of subionisation electrons [100]. After dividing both sides of Equation 4.1 by N_{i}, an expression for W_{ion} can be obtained:

$$W_{\mathrm{ion}} = E_{\mathrm{i}} + E_{\mathrm{ex}} \cdot (N_{\mathrm{ex}}/N_{\mathrm{i}}) + \epsilon. \tag{4.2}$$

Equation 4.2 can be expressed relatively to the ionisation potential I [100], which is usually assumed equal to the the band-gap energy of liquid argon E_g [98], leading to:

$$W_{\mathrm{ion}}/E_g = E_{\mathrm{i}}/E_g + E_{\mathrm{ex}}/E_g \cdot (N_{\mathrm{ex}}/N_{\mathrm{i}}) + \epsilon/E_g. \tag{4.3}$$

E_g is obtained by taking the band-gap energy of the electron band structure of solid argon. It is generally assumed that the same band structure exists in liquid argon; this can be justified by considering that the electron mobility in liquids and solids are of the same order of magnitude [98]. E_i can be taken to be equal to the mean value of the energy gap [98]. The ratio E_{ex}/E_g is estimated using the absorption spectrum of solid argon while the estimation of ϵ is based on a number of models described in [98]. By plugging the measured numbers (shown in Table 4.1), the value $W_{\mathrm{ion}} = 24.4\,\mathrm{eV}$ is

obtained, to be compared with the measured value of $W_{\text{ion}} = (23.6 \pm 0.3)$ eV using the electron-pulse method described in [98].

Table 4.1: Values used in the calculation of W_{ion} together with the predicted and measured value. Values from [99].

E_i [eV]	E_g [eV]	E_{ex} [eV]	$N_{\text{ex}}/N_{\text{i}}$	ϵ [eV]	W_{ion} [eV] pred.	W_{ion} [eV] meas.
15.4	14.3	12.7	0.21	6.3	24.4	23.6 ± 0.3

The argon ions and excited atoms will then go on to undergo two different processes, both resulting in scintillation light emission. The ionisation electron will first dissipate their kinetic energy to the surrounding medium over a mean distance of 2600 nm [101] and on a time scale of approximately 0.4 to 1.8 ns [101, 102] before recombining with the argon ions. If an external electric field is applied, a fraction of the free electrons can be collected. A treatment of the next steps is exposed in the following sections.

4.2 Initial Microscopic Fast Processes

The free ions and excited atoms created by the energy deposited by a charged particle immediately interact with other argon atoms ("self-trapping") within around 1 ps [103, 104] from the formation. This will start a series of reactions that will result in the emission of one scintillation photon for each ion or excited atom. According to [104], Ar^* undergoes the following reactions:

$$Ar^* + Ar + Ar \rightarrow Ar_2^* + Ar \quad \text{(self-trapped exciton formation via collision)} \tag{4.4}$$

$$Ar_2^* \rightarrow 2Ar + \gamma \quad \text{(scintillation)}. \tag{4.5}$$

The argon ions Ar^+ have a slightly longer chain of reactions [104]:

$$Ar^+ + Ar \rightarrow Ar_2^+ \quad \text{(ionic dimer formation)} \tag{4.6}$$

$$Ar_2^+ + e^- \rightarrow Ar^{**} + Ar \quad \text{(dissociative recombination)} \tag{4.7}$$

$$Ar^{**} \rightarrow Ar^* + \text{heat} \quad \text{(non-radiative transition)} \tag{4.8}$$

$$Ar^* + Ar + Ar \rightarrow Ar_2^* + Ar \quad \text{(self-trapped exciton formation via collision)} \tag{4.9}$$

$$Ar_2^* \rightarrow 2Ar + \gamma \quad \text{(scintillation).} \tag{4.10}$$

In this second case, the last two reactions (Equation 4.9 and 4.10) are identical to the reactions of argon excitons (Equation 4.4 and 4.5). The two processes can be seen summarised in the cartoon of Figure 4.1. The two chains of reaction can also be

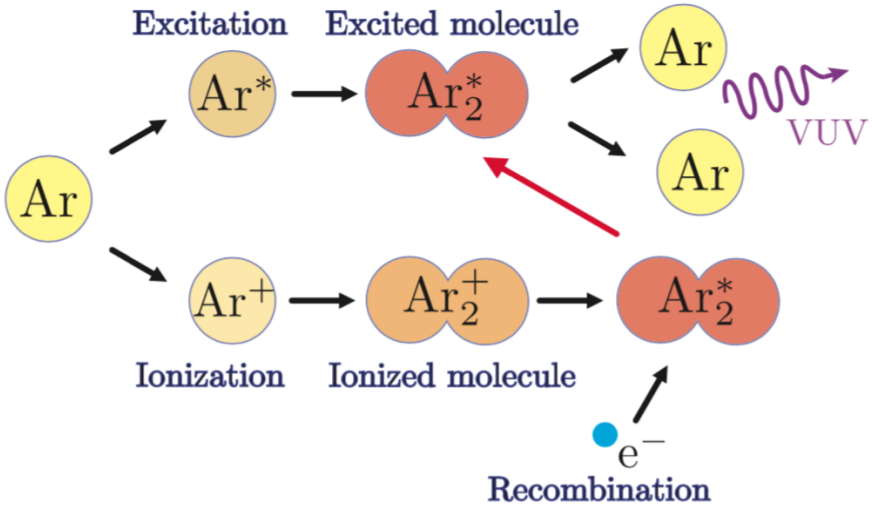


Figure 4.1: Cartoon summarising the processes that lead to a photon emission starting with Ar^+or Ar^*. It can be seen that in both cases the photon emission follows from the Ar_2^* dis-excitation. Figure from [105].

visualised in terms of the argon potential energy curves shown in Figure 4.2.

Equation 4.7 is what is generically referred to as the electron-ion recombination, where e^- indicates the thermalised ionisation electron. In LArTPCs, Ar_2^+ ions and electrons are pulled apart by the external electric field and the charge that survives the recombination is free and moves towards the anode or the cathode. The fraction of free electrons depends on the magnitude of the external electric field $\mathscr{E}$ and on the

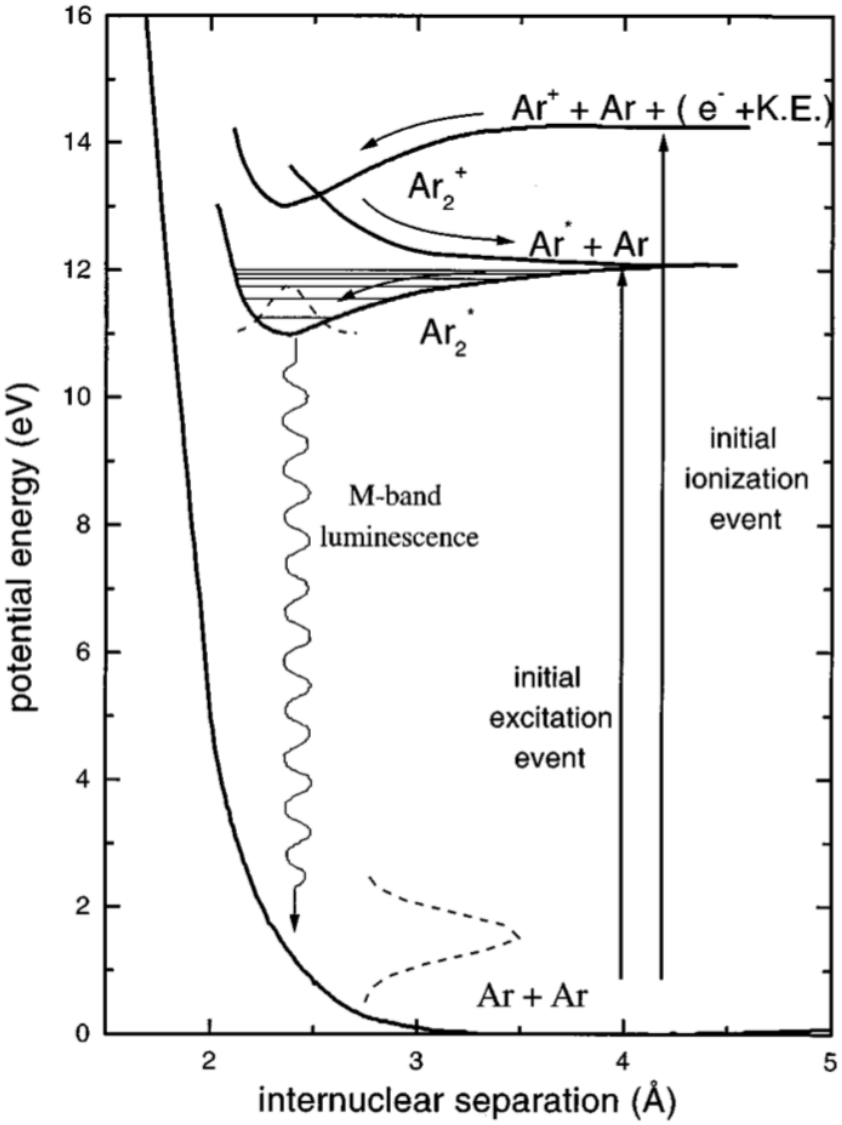
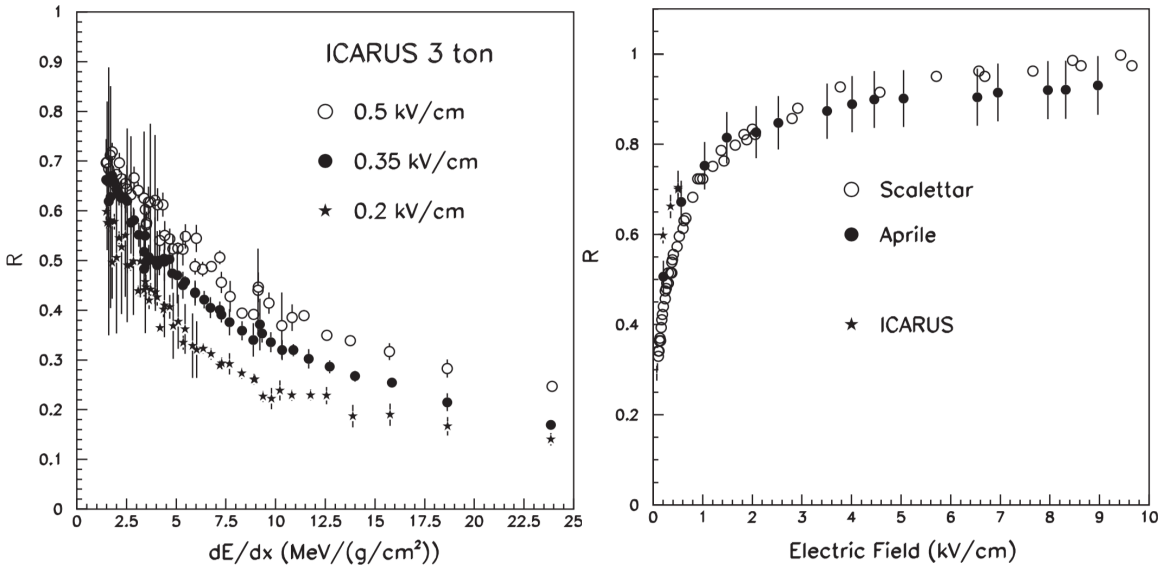


Figure 4.2: Event sequence for both Ar^+ and Ar^* following ionisation and excitation (represented by solid lines on the right hand side) visualised on the Ar potential energy curves in the solid state. It can be seen how the chain of reactions lower the potential energy until a photon of about 9.7 eV (128 nm) is emitted. Figure from [106].

density of the initial ionisation dE/dx. The stronger the electric field, the stronger is the force that pulls apart electrons and ions. In the ideal case of infinitely strong electric field, all the electrons created, Q_∞, are collected. Q_∞ is directly related to the energy deposited $E_{\text{dep}} = W_{\text{ion}} \cdot Q_\infty$. In the real case where some electrons recombine, the original charge can be obtained by correcting the surviving charge Q with the recombination factor R: $Q_\infty = Q/R$. R is obtained by modelling the recombination process and the model parameters are determined via a fit to the experimental data. Different models and the current knowledge of the recombination parameters for liquid argon will be discussed in Section 4.4. Generally speaking, R is a non-linear function of both the electric field and the ionisation density, as it can be seen in Figure 4.3.



(a) R as a function of dE/dx. (b) R as a function of the electric field.

Figure 4.3: Fraction of electrons that survive recombination (R) dependence on dE/dx and electric field. Left: R as a function of the stopping power for different values of the electric field. Right: R as a function of the electric field for 364 keV electrons (empty dots) [107], 976 keV electrons (filled dots) [108] and minimum ionising particles (stars) [109]. Figure from [109].

As illustrated above, a scintillation photon is the result of the decay of an exited dimer state Ar_2^*. The scintillation light emission is characterised by a wavelength of 128 nm and presents two separate time components, nano-seconds and micro-seconds, which are the lifetime of the singlet and triplet state of Ar_2^* respectively [99]. The

relative intensities of the two components are strongly affected by the ionisation density, information that can be used for particle identification. In particular, it is found that the relative proportion of the fast component increases at a higher ionisation density [110]. The amount of scintillation light can be reduced by the presence of N_2 contaminants [111]. The relevant process is the collision with nitrogen:

$$Ar_2^* + N_2 \rightarrow 2Ar + N_2, \tag{4.11}$$

where the reduction of the number of Ar_2^* can consequently reduce the number of photons emitted. This non-radiative kind of processes is known as "quenching" [111]. Doping the liquid argon with Xenon could improve the collection of light that is lost due to the nitrogen quenching [112].

Assuming the complete absence of impurities and zero electric field, each e^- recombines giving origin to a scintillation photon. The average energy required to produce one photon W_{ph} is given by considering that the number of photons N_{ph} produced following an energy deposition E_{dep} is [113]:

$$N_{\text{ph}} = N_{\text{i}} + N_{\text{ex}} = N_{\text{i}}(1 + N_{\text{ex}}/N_{\text{i}}) = \frac{E_{\text{dep}}}{W_{\text{ion}}}(1 + N_{\text{ex}}/N_{\text{i}}). \tag{4.12}$$

From Equation 4.12 it can be inferred that $W_{\text{ph}} = W_{\text{ion}}(1 + N_{\text{ex}}/N_{\text{i}}) = 19.5\,\text{eV}$, which implies a photon yield of 51,000 γ per deposited 1 MeV. At $\mathscr{E} = 0\,\text{kV/cm}$, no charge survives recombination. In general (for $\mathscr{E} \geq 0\,\text{kV/cm}$), the charge and the scintillation yield present a complementary behaviour, as illustrated in Figure 4.4. In reality, the ionisation density complicates the picture: a higher ionisation density implies larger recombination (see Figure 4.3a), therefore increasing the light yield. For a minimum ionising particle ($dE/dx \simeq 2.1\,\text{MeV/cm}$) at $\mathscr{E} = 0.5\,\text{kV/cm}$,[1] the measured values for the photon and electron yield are $\sim 24,000\ \gamma$/MeV and $\sim 29,000\ e^-$/MeV respectively [115].

[1] This is the nominal electric field value in ProtoDUNE-SP.

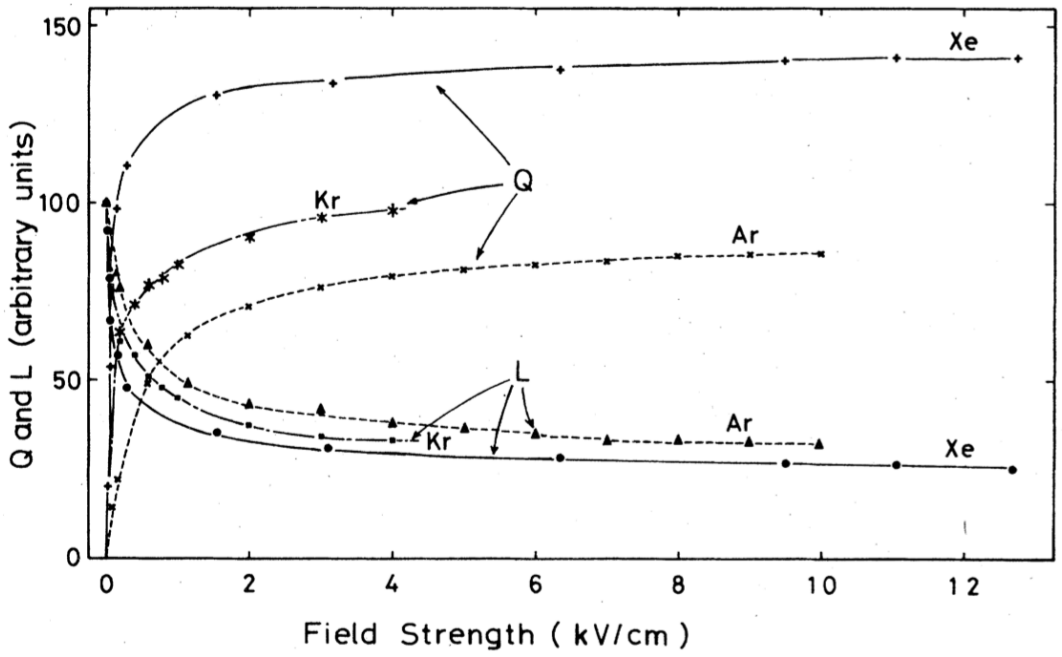


Figure 4.4: Charge (Q) and light (L) yield as a function of the external electric field magnitude for $\sim 1\,\mathrm{MeV}$ electrons. Data for liquid argon (Ar), krypton (Kr) and xenon (Xe) are shown. A clear complementary behaviour can be observed. Figure from [114].

4.3 Processes Occurring During Drift Time

Free electrons e^- and argon ions Ar_2^+ that survive the processes described in the previous section travel towards the anode and the cathode respectively under the influence of the external electric field. The drift velocity is a function of both the electric field and the liquid argon temperature [116, 117]. At the temperature of $T = 87\,\mathrm{K}$ and electric field $\mathscr{E} = 500\,\mathrm{V/cm}$ the electron drift velocity is measured as $v_e = 1.6\,\mathrm{mm/\mu s}$ [116], while that of positive ions is $v_+ = 8\,\mathrm{mm/s}$ [118].

While drifting, electrons can interact with electronegative impurities such as oxygen (O_2) or water ($\mathrm{H}_2\mathrm{O}$) according to the reaction:

$$e^- + X \to X^-, \tag{4.13}$$

where X^- indicates a generic contaminant. The rate per unit volume for the electron capture by a generic impurity X can be written as

$$\mathscr{R}_A = -k_A n_e n_X, \tag{4.14}$$

with k_A being the rate constant for the process and n_e and n_X the concentration of electrons and contaminant respectively. The rate constant is related to the electron lifetime τ of Equation 3.1 through the expression $\tau = 1/(k_A n_X)$ [119]. The constant k_A has been measured for oxygen to be $k_{\mathrm{O}_2} = 1.5 \times 10^{-16}\,\mathrm{m}^3/\mathrm{s}$ [120] while an analogue measurement for water is not found in the literature [119]. However, a significant impact of water on the electron lifetime has been observed [121].

In addition, electrons can recombine with argon ions drifting in the opposite direction, a process known as "volume recombination" [118]:

$$\mathrm{Ar}_2^+ + e^- \rightarrow \mathrm{Ar}_2^* \rightarrow 2\mathrm{Ar} + \gamma. \tag{4.15}$$

The rate constant for this process has been measured as a function of the electric field strength. For $\mathscr{E} = 500\,\mathrm{V/cm}$ it is measured to be $k_R = 1.1 \times 10^{-10}\,\mathrm{m}^3/\mathrm{s}$ [122]. Volume recombination represents an additional source of photons that is expected to be delayed with respect to the time of the original particle interaction in the TPC due to the slow-moving nature of argon ions.

Finally, drifting positive ions Ar_2^+ can interact with the negative-charged impurity molecules X^- created in the process of Equation 4.13 thereby undergoing a process called "mutual neutralisation" [118]:

$$\mathrm{Ar}_2^+ + X^- \rightarrow \mathrm{Ar}_2^* + X \rightarrow 2\mathrm{Ar} + X + \gamma. \tag{4.16}$$

Studies of this process in liquid argon at cryogenic temperatures are not present in the literature, although the rate constant for ion-ion mutual neutralisation has been measured in the temperature range 300-500 K [123].

4.4 Electron-Ion Recombination in Liquid Argon

Previous sections have given a concise summary of the main processes occurring in a LArTPC from the ionisation to the end of the drift time. This section will specifically focus on the prompt electron-ion recombination of Equation 4.7.

4.4.1 Recombination Models

Different theories have been developed to describe the recombination process. The Onsager geminate theory [124] describes the recombination process as the single electron re-attaching to the positive ion under the influence of the Coulomb field of the pair. Brownian motion is used to describe the scattering in the medium during the process. The escape probability depends on the initial separation between ion and electron after the electron thermalisation r_0 (a parameter obtained by a fit to the data) and on the strength of the external electric field. For low fields $\mathscr{E}$, the escape probability P_{escape} can be written as [125]:

$$P_{\text{escape}} = \exp\left(-\frac{r_c}{r_0}\right)\left(1 + \frac{e r_c}{2 k_B T}\mathscr{E}\right), \tag{4.17}$$

with $r_c = e^2/\epsilon_d k_B T$ the Onsager length, k_B the Boltzmann constant, T the temperature and ϵ_d the dielectric constant of the medium. The Onsager model does not predict a dependence of the escape probability on the ionisation density, but only considers the interaction between isolated electron-ion pairs.

The "columnar recombination" theory, developed by Jaffe [126], contains a different assumption: electrons and ions are distributed in a "column" around the trajectory of the ionising particle. The initial distribution for each charge sign in the plane perpendicular to the ionising particle trajectory is assumed to be Gaussian. Each distribution evolves under the influence of diffusion and the external electric field, with a recombination probability proportional to the product of the two charge densities. An additional underlying assumption is that electrons and ions have the same charge mobility. During the time evolution, both distributions remain Gaussian. Under these hypotheses, Jaffe concluded that the ratio of charge surviving recombination is:

$$\mathscr{R}_J = \frac{1}{1 + \frac{\alpha N_0}{8\pi D}\sqrt{\frac{\pi}{z'}}S(z')} \tag{4.18}$$

with

$$z' = \frac{b^2 \mu^2 \mathscr{E}^2 \sin^2\phi}{2D^2} \tag{4.19}$$

and

$$S(z') = \frac{1}{\sqrt{\pi}} \int_0^\infty \frac{e^{-s} ds}{\sqrt{s(1 + s/z')}}. \tag{4.20}$$

The parameters in Equation 4.18 and 4.19 are the following [97]: μ is the charge mobility, N_0 is the number of charge pairs per unit length, α is the recombination coefficient, D is the diffusion coefficient and b is a constant proportional to the average ion-electron distance. Equation 4.19 also exhibits a dependence on ϕ, which is the angle between the direction of the electric field and the ionising particle trajectory. In Equation 4.20 s characterises the overlap of the two distributions as a function of time. It can be shown [97] that $S(z') \sim 1$ for z' values in the range determined by the liquid argon properties, typical LArTPC electric field strengths and angles ϕ in the range $40° - 90°$. Therefore, Equation 4.18 can be rewritten as

$$\mathscr{R}_J = \frac{1}{1 + k_{\mathrm{Ar}} \frac{dE/dx}{\mathscr{E} \sin \phi}}, \tag{4.21}$$

with k_{Ar} a liquid argon specific constant and dE/dx the energy loss per unit length.

A simulation of electron thermalisation and recombination in [101] has shown that the probability of geminate recombination in liquid argon is very low ($\sim 10^{-3}$). Additionally, the electron-ion separation is larger than the separation between ions [97]. A columnar description of recombination is therefore favoured.

Another commonly used model to describe recombination is the "box model" developed by Thomas and Imel [127] to parametrise the effect of the electric field in the case of radioactive sources. As in the Jaffe's theory, the initial distribution of charge is the same for electrons and ions and evolves according to the equations:

$$\frac{\partial N_+}{\partial t} = -\mu_+ \vec{\mathscr{E}} \cdot \vec{\nabla} N_+ + d_+ \nabla^2 N_+ - \alpha N_+ N_- \tag{4.22a}$$

$$\frac{\partial N_-}{\partial t} = -\mu_- \vec{\mathscr{E}} \cdot \vec{\nabla} N_- + d_+ \nabla^2 N_- - \alpha N_+ N_-. \tag{4.22b}$$

N_+ and N_- are the ion and electron distributions, μ_+ and μ_- are the charge mobilities, α is the recombination coefficient and d_+ and d_- are the diffusion coefficients. While Jaffe solved the equations above by adding the recombination term as a perturbation, Thomas and Imel made different realistic assumptions to obtain analytical solutions.

In light of the small diffusion rate in liquid argon and the slow velocity of ions, the diffusion and ion mobility are neglected in Equation 4.22 obtaining:

$$\frac{\partial N_+}{\partial t} = -\alpha N_+ N_- \tag{4.23a}$$

$$\frac{\partial N_-}{\partial t} = -\mu_- \vec{\mathscr{E}} \cdot \vec{\nabla} N_- - \alpha N_+ N_-. \tag{4.23b}$$

These equations can be solved analytically by applying the box boundary conditions: the initial distributions $N_+(t=0) = N_-(t=0)$ are considered uniform within a box of side a or, in other words, N_0 units of each charge are present in the box at $t = 0$. After performing the integration over time, the following formula for the fraction of surviving electrons is obtained:

$$\mathscr{R}_{\text{Box}} = \frac{1}{\xi} \ln(1+\xi),\ \xi = \frac{N_0 \alpha}{4a^2 \mu_- \mathscr{E}}. \tag{4.24}$$

Both $\mathscr{R}_J$ and $\mathscr{R}_{\text{Box}}$ approach one in the high electric field limit and zero for small fields. It is important to notice that $\mathscr{R}_{\text{Box}}$ does not explicitly depend on the angle ϕ as a consequence of the box model boundary conditions that erase any dependence on the track direction.

4.4.2 Application of Recombination Models to LArTPC detectors

The ICARUS collaboration [109] made the first attempt at studying the recombination factor $\mathscr{R}$ as a function of the energy loss per unit length dE/dx at electric field values that are typical for LArTPC experiments. They approximated the Jaffe's recombination formula in Equation 4.21 with the so-called Birks law [128] that is also used to describe quenching phenomena in scintillators:

$$\mathscr{R}_{\text{Birks}} = \frac{1}{1 + k \cdot (dE/dx)/(\rho \mathscr{E})}, \tag{4.25}$$

where k is a fit parameter, ρ is the liquid argon density and the angular dependence is being explicitly ignored. The ICARUS analysis used data from two different LArTPCs: the 3-ton prototype and the T600 detector. In the former case, a mixed sample

of stopping cosmic muons and proton was used, while only stopping muons were selected in the latter case. The variation of dE/dx along the track trajectories allowed to study the recombination factor for different stopping powers. The Birks model of Equation 4.25 failed to describe the data at low electric field. Better agreement was obtained by adding a normalisation constant A to the fit:[2]

$$\mathscr{R}_{\text{ICARUS}} = \frac{A}{1 + k \cdot (dE/dx)/(\rho\mathscr{E})}, \tag{4.26}$$

Note that in this case $\mathscr{R}_{\text{ICARUS}} \to A$ for high electric fields whereas $\mathscr{R}_{\text{Box}} \to 1$. Figure 4.5 shows a plot for the inverse of the measured $\mathscr{R}$ as a function of the stopping power for different electric field values using the data from the 3-ton prototype. While the data show a linear relation as expected by the model in Equation 4.25, the intercept at $1/\mathscr{R} \neq 1$ justifies the introduction of the additional fit parameter A. A fit to the 3-ton data for all the electric field values gives $A_{3t} = 0.800 \pm 0.003$ and $k_{3t} = 0.0486 \pm 0.0006$ (kV/cm)(g/cm^2)MeV^{-1}. These values are in agreement with those obtained with the muon-only sample and the T600 detector: $A_{T600} = 0.81 \pm 0.05$ and $k_{T600} = 0.055 \pm 0.005$ (kV/cm)(g/cm^2)MeV^{-1}. The statistical significance of the T600 data is lower due to the smaller lever arm in the stopping power of the muon sample.

The ArgoNeuT experiment [97] studied the electron-ion recombination using a sample of stopping protons coming from several sources (e.g. neutrino and neutron interactions). The parameters of both the modified Birks model of Equation 4.26 and the box model of Equation 4.24 were measured. The study was performed at the fixed electric value of $\mathscr{E} = 0.481\,\text{kV/cm}$ and as a function of the charge density dE/dx which allowed them to write ξ in the form

$$\xi = \beta(dE/dx), \tag{4.27}$$

with β a parameter found by performing a fit to the data. The box model is also generalised by introducing an additional parameter α:

$$\mathscr{R}_{\text{MBM}} = \frac{1}{\beta(dE/dx)} \ln\left(\alpha + \beta(dE/dx)\right). \tag{4.28}$$

[2]This formula is also referred to as the Birks model in the literature. This convention will be followed throughout the rest of this thesis.

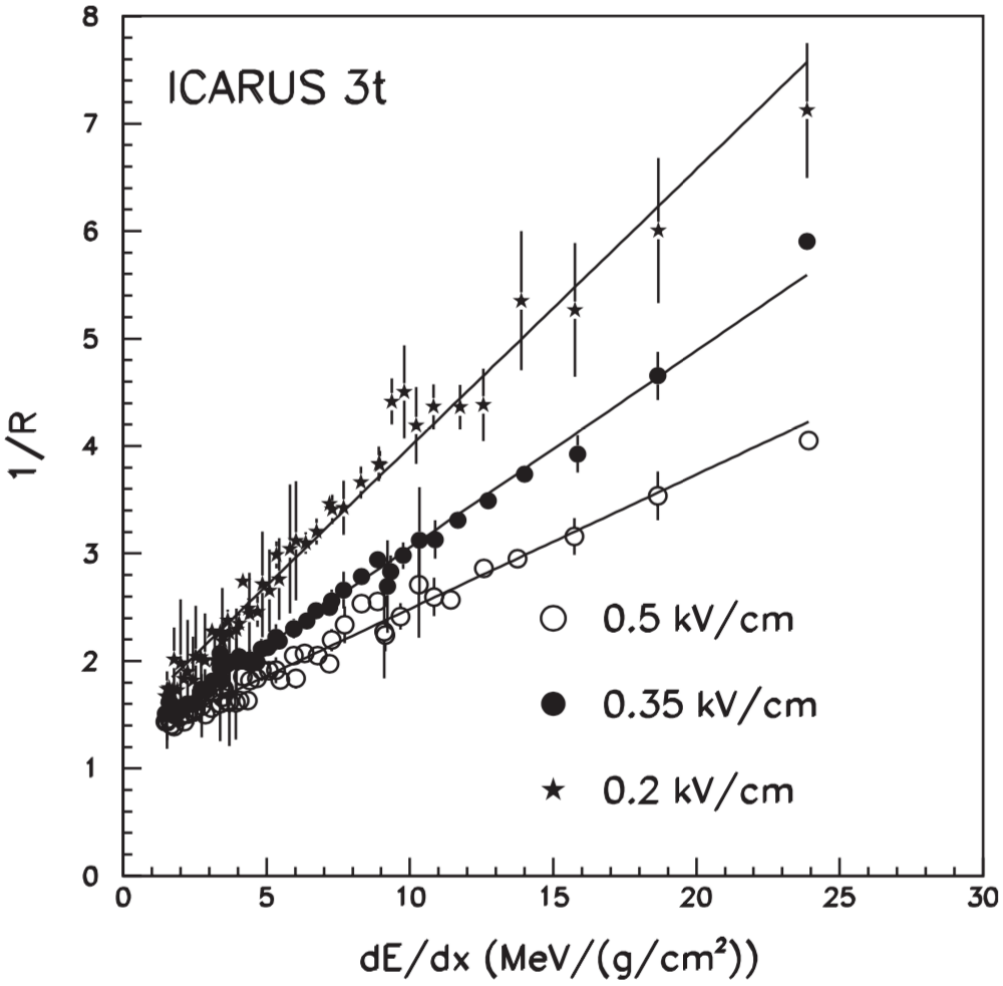


Figure 4.5: $1/\mathscr{R}$ as a function of dE/dx for a mixed sample of stopping proton and muons as measured by the ICARUS 3-ton prototype. Data for three different values of the electric field are shown. Figure from [109].

This formula is also known as the "modified box model". The original box model with $\alpha = 1$ fails to reproduce the behaviour of the modified Birks law at low dE/dx values, as illustrated qualitatively in Figure 4.6. The blue curve represents the Birks model with the ICARUS parametrisation at a 0.5 kV/cm electric field. The canonical box model (solid red line) can be matched to the blue curve in the middle dE/dx region by setting $\beta = 0.30\,\mathrm{cm/MeV}$. The agreement in the low dE/dx region can be recovered by setting $\alpha = 0.93$ while maintaining $\beta = 0.30\,\mathrm{cm/MeV}$. ArgoNeuT performed

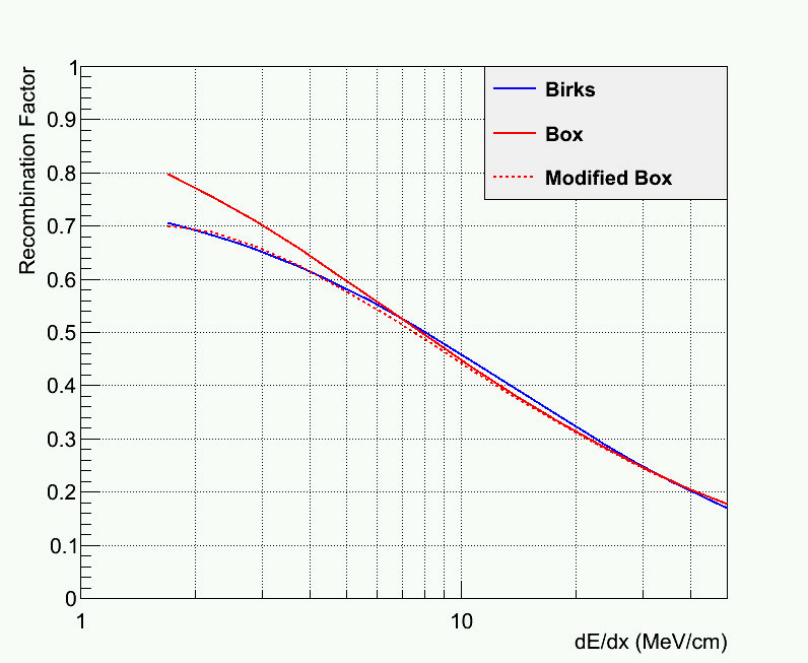


Figure 4.6: Qualitative comparison of the modified Birks formula with the ICARUS parametrisation (blue line) and the box model (solid red line). The dashed red line, representing the modified box model, better reproduces the behaviour of the Birks model. Figure from [97].

an analysis in the range $2\,\mathrm{MeV/cm} < dE/dx < 24\,\mathrm{MeV/cm}$ extracting the recombination parameters for both the modified Birks model and the modified box model. The proton track sample was divided into different angular bins (40°, 50°, 60°, 80°) with the aim of verifying the $\sin\phi$ angular dependence introduced by the columnar theory. Both models fit the ArgoNeuT data well, although the modified box model has a better agreement at high dE/dx. The $\sin\phi$ angular dependence was found to be over-estimating the angular modulation in data. The values for the parameters α

were found to be consisted across each angular bin, except for $\phi = 40°$, disproving the expectation of α being independent from ϕ. The weighted average of the measurements in each angle bin for both the modified box and Birks model can be found in Table 4.2. The Birks parameters are in good agreement with the ICARUS measurement, also shown in Table 4.2. To remove the dependence on the ArgoNeuT detector conditions, the parameter β can be rewritten as $\beta = \beta'/(\rho\mathscr{E})$ with ρ being the liquid argon density. Therefore $\beta'_{\text{Argo}} = 0.212 \pm 0.002$ (kV/cm)(g/cm^2)MeV^{-1}. The modified box model with the ArgoNeuT parametrisation, α_{Argo} and β'_{Argo} averaged across the angular bins, is the model chosen by ProtoDUNE-SP to both simulate and correct for the recombination of ionisation electrons [62], according to Equation 3.6. The reconstructed dE/dx can therefore be obtained starting from the corrected $(dQ/dx)_{\text{corr}}$ and C_{cal}:

$$\frac{dE}{dx} = \left(\exp\left(\frac{\left(\frac{dQ}{dx}\right)_{\text{corr}}}{C_{\text{cal}}} \frac{\beta'_{\text{Argo}} W_{\text{ion}}}{\rho\mathscr{E}} \right) - \alpha_{\text{Argo}} \right) \left(\frac{\rho\mathscr{E}}{\beta'_{\text{Argo}}} \right). \tag{4.29}$$

A similar measurement to that of ArgoNeuT was performed by the MicroBooNE collaboration [96] using a sample of stopping protons resulting from neutrino interactions with liquid argon at an electric field value of $\mathscr{E} = 0.273\,\text{kV/cm}$. In this case, the angular dependence was not considered. The Birks law with the ICARUS parametrisation describes the MicroBooNE data better than the modified box model with the ArgoNeuT parametrisation. This is not surprising since the Birks law was tuned by ICARUS for electric field values in the range $0.2\,\text{kV/cm} < \mathscr{E} < 0.5\,\text{kV/cm}$ and the ArgoNeuT modified box model parameters were measured at $\mathscr{E} = 0.481\,\text{kV/cm}$. The results obtained by MicroBooNE are also shown in Table 4.2. The parameters A and α are in agreement with ICARUS and ArgoNeuT, while k and β' are inconsistent with the other experiments as a consequence of their coupling with the electric field and the rather smaller electric field in MicroBooNE.

Overall, three independent measurements of the recombination parameters provide consistent sets of measured values, for which the only differences are related to the different operating conditions. The original Birks and box model do not provide

Table 4.2: Summary of fitted recombination parameters for the ICARUS, ArgoNeuT and MicroBooNE experiments. Values from [96, 97, 109]. Electric fields are specified in kV/cm, the Birks parameters k and the modified box model parameters β' are measured in $(\mathrm{kV/cm})(\mathrm{g/cm^2})\mathrm{MeV}^{-1}$. All the values for the ArgoNeuT experiment are the weighted average of the values of each angular bin.

	ICARUS 3-ton	ICARUS T600	ArgoNeuT	MicroBooNE
Particle	μ, p	μ	p	p
$\sin\phi$	No	No	Yes	No
$\mathscr{E}$ values	0.2, 0.35, 0.5	0.5	0.481	0.273
A	0.800 ± 0.003	0.81 ± 0.05	0.806 ± 0.010	0.816 ± 0.012
k	0.0486 ± 0.0006	0.055 ± 0.005	0.052 ± 0.001	0.045 ± 0.001
α	-	-	0.93 ± 0.02	0.92 ± 0.02
β'	-	-	0.212 ± 0.002	0.184 ± 0.002

a comprehensive description of data, but rather only work in some regimes of ionisation density dE/dx or electric field. This is not surprising when considering all the assumptions behind the development of the models. Both equations have been empirically modified by including an additional fit parameter to better accommodate the data and should therefore be considered as a phenomenological description of the recombination process. Measurements of the angular dependence predicted by the Jaffe's columnar theory have only been explored by ArgoNeuT, which found a much weaker dependence. Difference between the data and the models could be ascribed to experimental limitations or to the assumptions made to describe the recombination process. It has been observed [97, 109, 129] that the production of δ-rays can affect the recombination rate in a non-trivial fashion, which is strongly dependent on the δ-ray energy spectrum. A modification of the columnar model was recently proposed in [130], in which an alternative initial charge distribution is assumed, leading to a more complicated angular dependence than just $\sin\phi$.

Chapter 5

Cosmic Muons in ProtoDUNE-SP

Contents

5.1 Cosmic Ray Overview 75

5.2 Energy Loss of Muons in Liquid Argon 78

5.3 Michel Electrons 81

5.4 Monte Carlo dE/dx: Muon Particle Gun in ProtoDUNE-SP 84

This chapter will present an overview of cosmic ray muons in the ProtoDUNE-SP detector. Section 5.1 will give a brief summary of the main cosmic ray properties, including particle composition, energy spectrum and angular distribution. Section 5.2 will discuss the ionisation energy loss of muons in liquid argon. A brief discussion of Michel electrons and their energy loss will be given in Section 5.3. If not specified otherwise, Section 5.1, 5.2 and 5.3 contain information from [30]. Finally, Section 5.4 will present a Monte Carlo simulation to extract the stopping power of muons in liquid argon, whose results will be used throughout the rest of this thesis.

5.1 Cosmic Ray Overview

Primary Cosmic Rays (CRs) are particles and nuclei originated by astrophysical sources mainly located outside our solar system. This includes electrons, protons, helium and other nuclei like carbon, oxygen and iron. Their energies extend from a few MeV to tens of Joules. The flux of primary cosmic rays is affected by the solar activity and the geomagnetic field, especially in the low-energy region of the spectra.

As a result, the intensity in the GeV range depends on the time and the location. Their intensity in the range from several GeV to beyond 100 TeV can be modelled as a power law $\sim (E/1\,\mathrm{GeV})^{-\alpha}\ \mathrm{m}^{-2}\,\mathrm{s}^{-1}\,\mathrm{sr}^{-1}\,\mathrm{GeV}^{-1}$ with $\alpha \approx 2.7$.

Secondary CR particles are created when primary CRs interact with the air nuclei in the atmosphere. Figure 5.1 shows the vertical flux for the main components of cosmic ray particles in the atmosphere in the energy region where they are most numerous. Apart from the protons and electrons at a high altitude, all the particles are produced by the interaction of primary CRs. Muons, that originate from the decay of charged mesons [131],

$$\pi^{\pm} \rightarrow \mu^{\pm} \overset{(-)}{\nu}_{\mu} \quad \text{or} \tag{5.1}$$

$$K^{\pm} \rightarrow \mu^{\pm} \overset{(-)}{\nu}_{\mu}, \tag{5.2}$$

are the most abundant charged particles at sea level. This is due to their small energy loss in the atmosphere ($\sim 2\,\mathrm{GeV}$ [131]) and their relative long lifetime ($\sim 2.2\,\mu\mathrm{s}$).

The energy spectrum and the angular distribution of muons at surface is the result of the combined effect of the production energy spectrum, the interaction with the atmosphere and the decay rate of both the muons and the parent pions. The mean energy at the ground is about 4 GeV and the integrated vertical intensity is estimated as $I_{\mu}^{\mathrm{vertical}} = 70\,\mathrm{m}^{-2}\,\mathrm{s}^{-1}\,\mathrm{sr}^{-1}$ for muons with energy $E_{\mu} > 1\,\mathrm{GeV}$. The energy spectrum can be separated in three main regions. It is typically flat below $\sim 1\,\mathrm{GeV}$ (typical energy of muons that stop in ProtoDUNE-SP), since muons with this energy are typically absorbed or decay in the atmosphere and do not reach the Earth surface. The spectrum steepens[1] gradually in the range 10 GeV - 100 GeV following the energy spectrum of the parent pions and steepens further at higher energy becoming one power steeper than the primary spectrum for $E_{\mu} \gg 1\,\mathrm{TeV}$. The behaviour at high energies is due to the high-energetic pions interacting before decaying and producing tertiary pions which will then decay to muons of lower energies. The overall angular distribution for $\sim 3\,\mathrm{GeV}$ muons at the ground is $\propto \cos^2\theta_z$, where θ_z is the zenith angle.

[1] In other words, the spectrum presents a larger (negative) derivative in this region compared to the region previously mentioned.

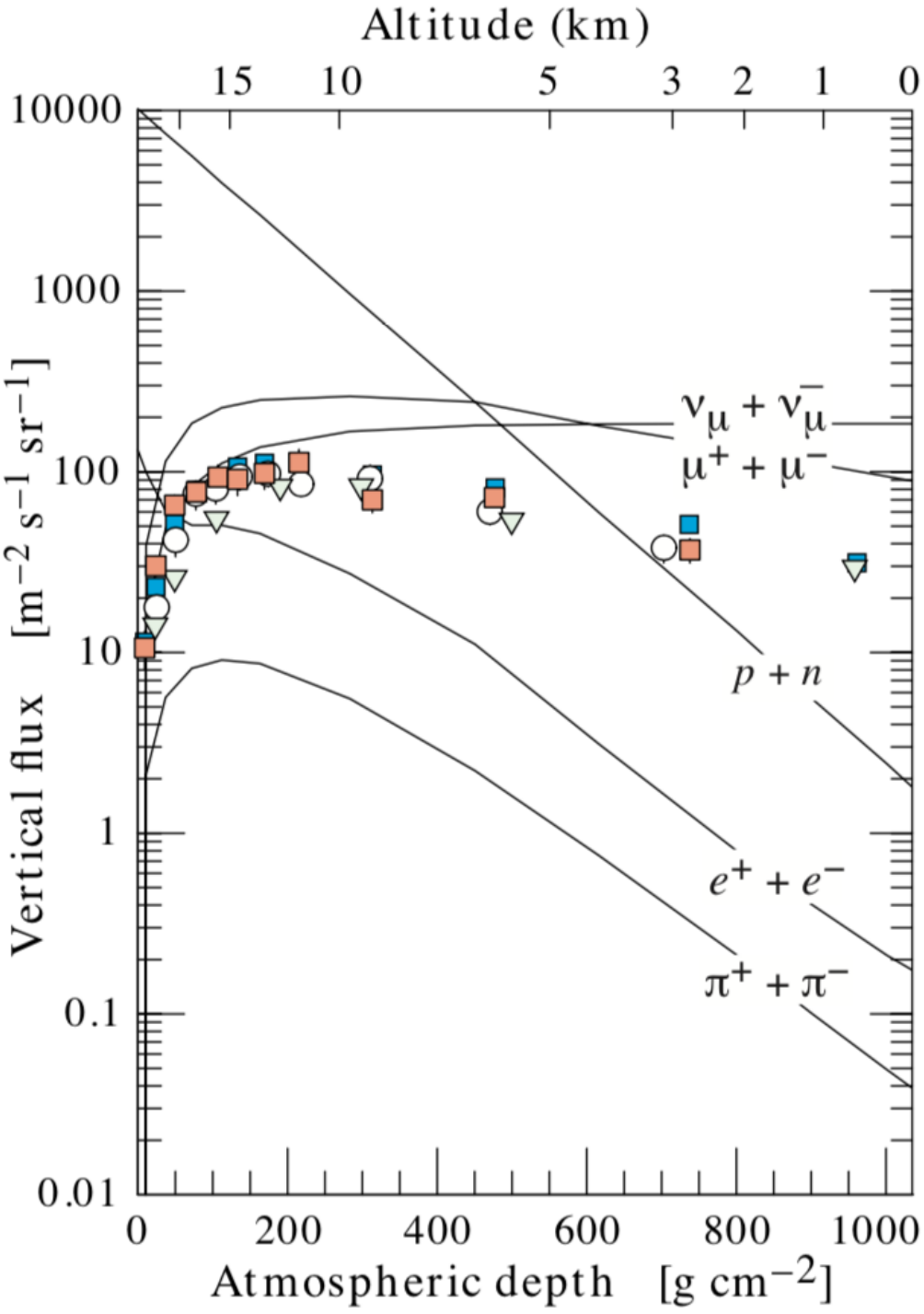


Figure 5.1: Vertical fluxes of cosmic ray particles in the atmosphere as a function of the altitude for energies $E > 1\,\mathrm{GeV}$ and estimated from the nucleon flux. The points represent measurements for negative charged muons with $E_\mu > 1\,\mathrm{GeV}$. Figure from [30].

The few-GeV muon intensity is reduced at high zenith angles due to the increased absorption effect of the thicker volume of air they have to cross. The dependence here is $\propto \cos^n \theta_z$ with $n \sim 2 \div 3$. In the intermediate energy range, up to $\sim 100\,\mathrm{GeV}$, the angular dependence is almost flat in $\cos\theta_z$. At high energies ($\sim 1\,\mathrm{TeV}$) the flux increases with $\cos\theta_z$. This behaviour is illustrated in Figure 5.2a. At large angles, high energy pions are more likely to decay before they interact, and therefore the average muon energy is larger. This effect is visible in Figure 5.2b, where the energy spectrum for muons at $\theta_z = 0°$ and $\theta_z = 75°$ is shown.

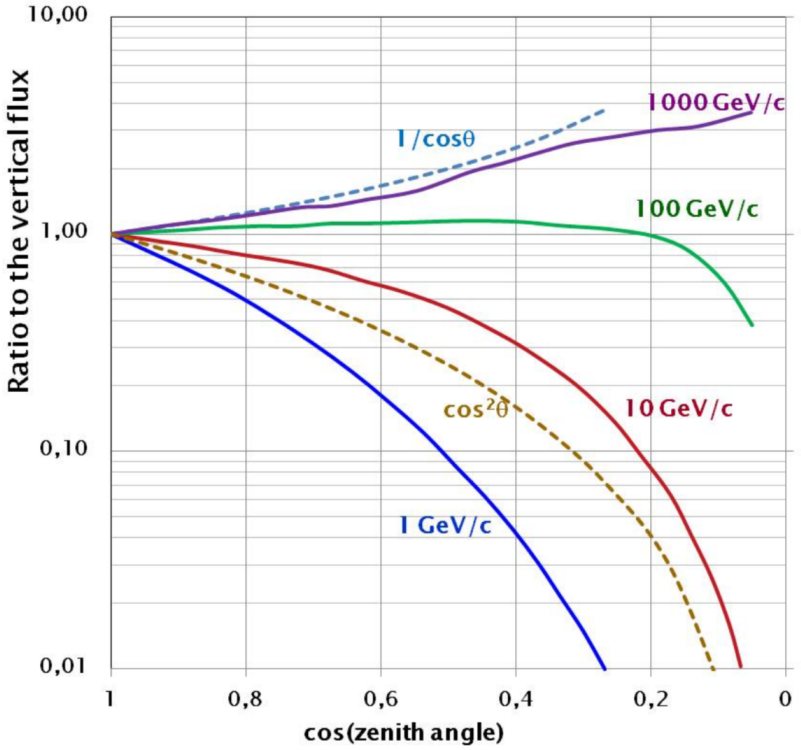
Cosmic rays at the surface level also have an electromagnetic component and nucleons, which are remnants of primary CRs, can be found as well. Low-energy electrons result from muon decays. The vertical intensity of electrons and positrons combined is approximately $I_{e^\pm}^{\mathrm{vertical}} = 30\,\mathrm{m^{-2}\,s^{-1}\,sr^{-1}}$ above $10\,\mathrm{MeV}$. The intensity of vertical protons with momentum greater than $1\,\mathrm{GeV}/c$ at sea level is $I_p^{\mathrm{vertical}} = 0.9\,\mathrm{m^{-2}\,s^{-1}\,sr^{-1}}$, approximately two order of magnitudes lower than that of muons.

5.2 Energy Loss of Muons in Liquid Argon

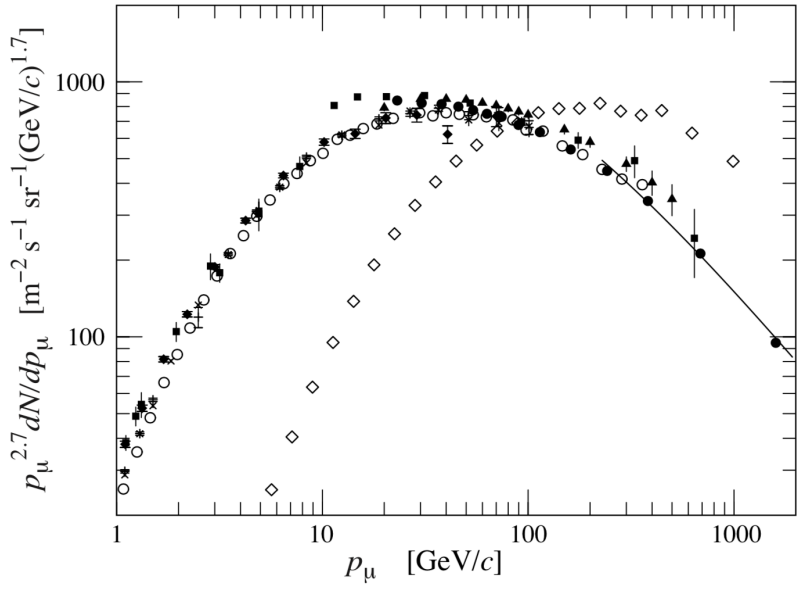
The energy loss for heavy charged particles in a material can be described as a sum of the energy lost due to the interaction with the electrons of the material and energy lost through radiative processes like *bremsstrahlung*. The relative importance of the two contributions depends on the mass and the energy of the particles. The critical energy of a given particle is defined as the energy for which the electronic losses are equal to the radiative losses [132]. The mean energy of cosmic muons at ground level ($\sim 4\,\mathrm{GeV}$) is considerably smaller than the muon critical energy of $\sim 484\,\mathrm{GeV}$ in liquid argon [133], and their energy loss can be described with sufficient accuracy only through the electronic component.

The mean energy loss $-\langle dE/dx \rangle$ [$\mathrm{MeV\,g^{-1}\,cm}$] of heavy particles (such as muons) as a function of the relativist factors β and γ can be described by the "Bethe-Bloch equation":

$$-\left\langle \frac{dE}{dx} \right\rangle = K z^2 \frac{Z}{A} \frac{1}{\beta^2} \left[\frac{1}{2} \ln \frac{2 m_e c^2 \beta^2 \gamma^2 W_{\max}}{I^2} - \beta^2 + \frac{\delta(\beta\gamma)}{2} \right], \tag{5.3}$$



(a) Angular distribution of muons at the ground for different muon energies.



(b) Energy spectrum for muons with $\theta_z = 0°$ and $\theta_z = 75°$.

Figure 5.2: Angular dependence of cosmic ray muons at the Earth surface. Top: muon flux for different energies as a function of $\cos\theta_z$ obtained with a Monte Carlo simulation and expressed as a ratio to the vertical flux. Bottom: Spectrum of muon momentum p_μ at $\theta_z = 75°$ (empty diamond shape) and $\theta_z = 0°$ (any other shape). Top plot from [131], bottom plot from [30].

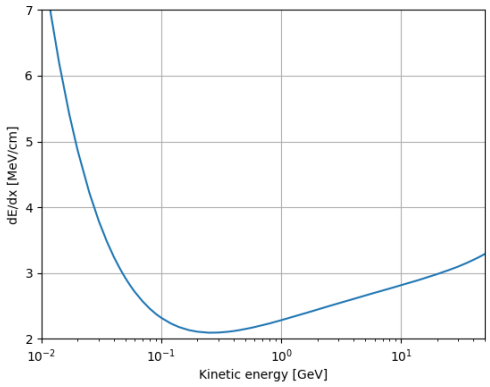
where $K = 4\pi N_A r_e^2 m_e c^2 = 0.307\,\mathrm{MeV\,mol^{-1}\,cm^{-2}}$ is a constant that depends on the electron mass m_e, classical electron radius r_e and Avogadro's number N_A, z is the charge number of the particle, while Z and A are the atomic number and the atomic mass of the material respectively. The factor $W_{\max}$ represents the maximum energy transfer in a single collision, I is the mean excitation energy and $\delta(\beta\gamma)$ is the density-effect correction, which accounts for the medium polarisation under the influence of the charged particle electric field. The Bethe-Bloch equation is valid in the region $0.1 \lesssim \beta\gamma \lesssim 1000$. The shape of Equation 5.3 is in general characterised by a broad minimum at around $\beta\gamma \approx 3$ ($T_\mu^{\mathrm{mip}} \approx 260\,\mathrm{MeV}$ kinetic energy for a muon in liquid argon [133]). This is what is referred to as the minimum ionising region and a particle with an energy close to the minimum of $\langle dE/dx \rangle$ is said to be a minimum ionising particle (MIP). Going from the minimum towards lower value of $\beta\gamma$ or T_μ, the $\langle dE/dx \rangle$ shape features a sharp rise known as "Bragg peak", signifying an increasing in energy deposition and therefore ionisation towards the end of a track. Similarly, but to a lesser extent, a rise in the $\langle dE/dx \rangle$ can be observed moving to high values of T_μ, due to the relativistic extension of the particle electric field. This behaviour is illustrated in Figure 5.3a for a muon in liquid argon. If a particle comes to a stop, the $\langle dE/dx \rangle$ as a function of the distance from the end of trajectory (also called "residual range") can be inferred, as shown in Figure 5.3b. Figure 5.3b features a relatively extended flat region corresponding to the muon being in the minimum-ionising regime in which the energy deposition per unit length stays constant with good approximation.

While the average energy loss is precisely expressed by Equation 5.3, the energy loss probability distribution is described by the highly-skewed Landau-Vavilov distribution [134, 135]. The corresponding most probable energy loss is:

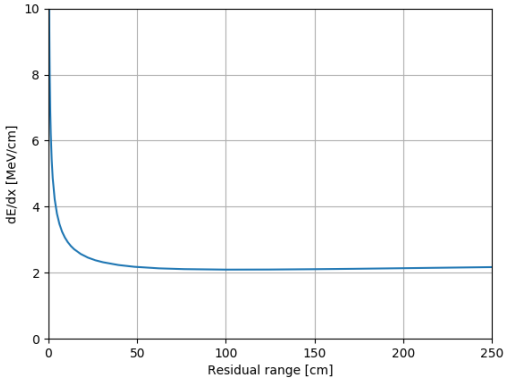
$$\left(\frac{dE}{dx}\right)^{\mathrm{LV}}_{\mathrm{MPV}} = \frac{\xi}{x[\mathrm{g/cm^2}]}\left[\ln\frac{2m_e c^2\beta^2\gamma^2}{I} + \ln\frac{\xi}{I} + j - \beta^2 - \delta(\beta\gamma)\right], \tag{5.4}$$

with $\xi = (K/2)(Z/A)z^2(x[\mathrm{g/cm^2}]/\beta^2)\,\mathrm{MeV}$ and $j = 0.2$. Unlike the average energy loss, the most probable value (MPV) depends on the target thickness x,[2] as shown

[2]For example the side of a liquid argon cell.



(a) Mean dE/dx vs. kinetic energy.



(b) Mean dE/dx vs. residual range.

Figure 5.3: Mean dE/dx vs. kinetic energy and residual range for a muon in liquid argon. The [0-250] cm residual range roughly corresponds to a [0-0.6] GeV interval in kinetic energy. Data from [133].

in Figure 5.4 where the most probable dE/dx is plotted as a function of the residual range for different target thickness values.

The picture of the charged particle energy loss is complicated by the presence of δ-rays, secondary electrons to which a significant amount of energy is transferred by the ionising particles such that they can produce further ionisation along or away from the primary track trajectory. To fully reconstruct the original particle energy, the electronic energy loss of δ-rays needs to be considered.

5.3 Michel Electrons

With an almost 100% branching ratio [30], a muon decays weakly into an electron and two neutrinos, as shown in the Feynman diagram of Figure 5.5. The resulting electron is called Michel electron.

The energy loss for electrons or positrons in matter differs from that of a heavy charged particle. At low energies, they mainly lose energy by ionisation, but other processes such as Møller [136] and Bhabha [137] scattering are possible. Together they constitute the collision stopping power. At higher energies, radiative processes dominate. Figure 5.6 shows the contributions from each individual component for electrons

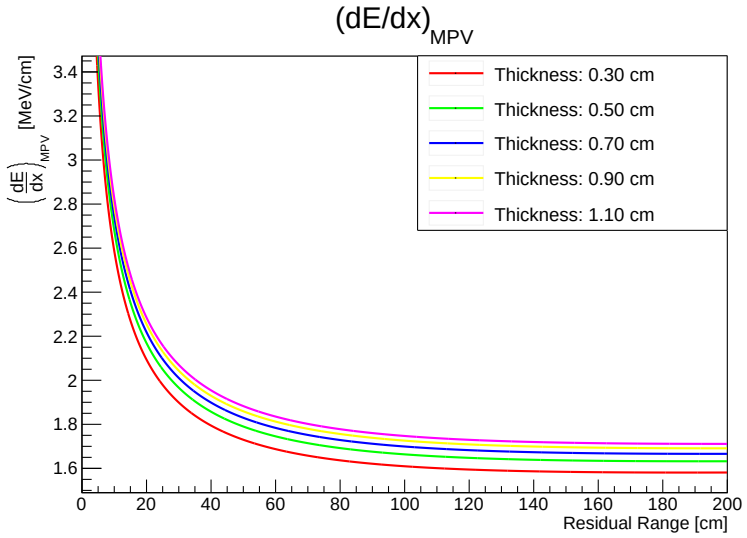


Figure 5.4: Plot of the most probable value of dE/dx according to Equation 5.4 as a function of the residual range for a muon in liquid argon. Different colours represent different thickness values.

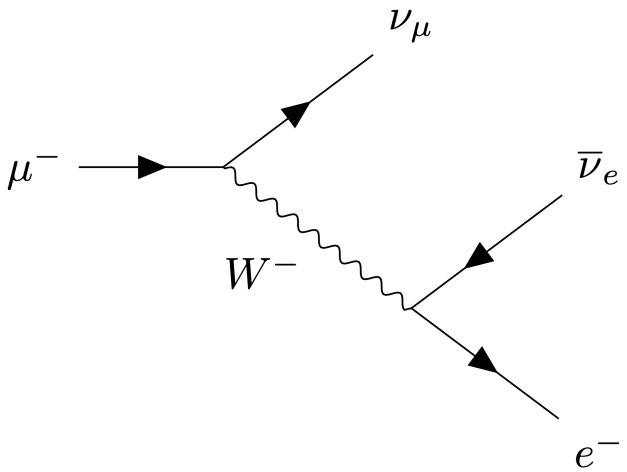


Figure 5.5: Feynman diagram for a negative muon decay in an electron, and electron anti-neutrino and a muon neutrino.

in liquid argon, together with the total stopping power. The plot for positrons is similar but presents small differences at low energies due to the different cross sections of the Møller and Bhabha scattering. It can be seen that the critical energy for electrons (and positrons) is much lower ($\sim 30\,\text{MeV}$) than in the case of muons.

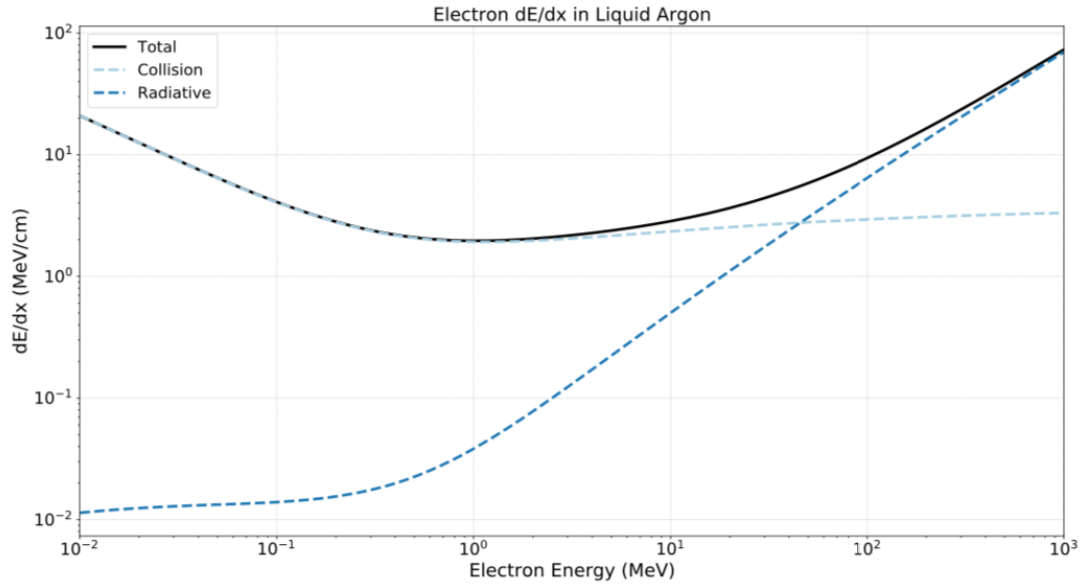


Figure 5.6: Stopping power for electrons in liquid argon as a function of the electron energy. The collision and radiative components are represented by the dashed lines, while the total stopping power is drawn as a solid line. Figure from [94].

The energy spectrum of Michel electrons is characterised by a slow rise starting from 0 MeV up to about 50 MeV (half of the muon mass), where it features a sharp cut-off. The capture of negatively charged muons by the nuclei before the decays results in a smearing of the spectrum cut-off [138]. In this energy range, both contributions from the collision and radiative energy loss are relevant. This translates to a signature for Michel electrons in liquid argon characterised by a short track of about 5-10 cm surrounded by energy deposition coming from radiated photons, which are only visible when the photons interact with argon and produce electrons that ionise the atoms. This event topology (illustrated in Figure 5.7) can make the reconstruction of Michel electron energy particularly challenging. The muon lifetime[3] is 2.2 µs [30], while the

[3]The nucleon capture implies a slightly different lifetime for negative muons in matter, but this small difference is not relevant for the argument proposed.

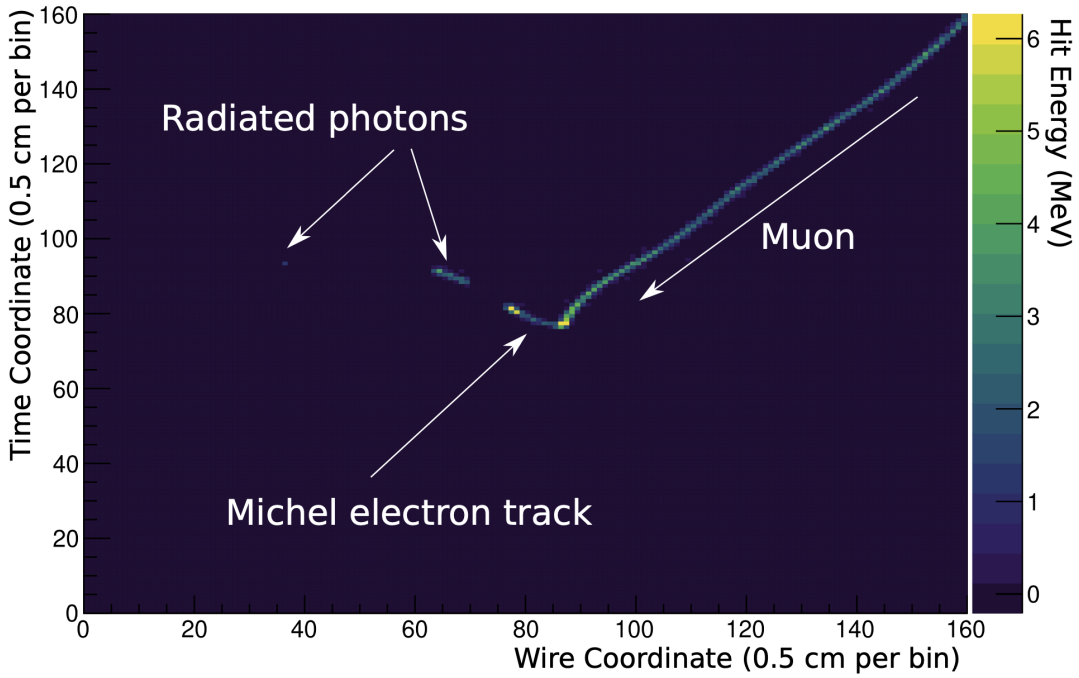


Figure 5.7: Event display of a stopping muon decaying into an electron in ProtoDUNE-SP data. The various sources of the energy depositions are highlighted. Figure from [94].

typical electron drift velocity in ProtoDUNE-SP is 1.59 mm/µs. Therefore, the short Michel track is effectively reconstructed attached to the muon track in ProtoDUNE-SP.

5.4 Monte Carlo dE/dx: Muon Particle Gun in ProtoDUNE-SP

The energy loss of a muon along its trajectory near the stopping point will be used extensively throughout this thesis. Their energy loss is very well known, and so is the energy dependence on the distance from the end of the track. Cosmic muons that stop inside the detector constitute a particularly useful sample, in that their energy can be reconstructed from the trajectory by walking backwards along the track starting from the end point.

To build a "map" between the muon dE/dx in liquid argon and the residual range, a dedicated particle gun Monte Carlo (MC) simulation was developed in the

ProtoDUNE-SP geometry. This method was preferred rather than using the Bethe-Bloch formula because it reflects the exact same procedure used to simulate the dE/dx from which the ionisation charge is calculated in the ProtoDUNE-SP Monte Carlo, as described in Section 3.8 of Chapter 3.

A sample of 10,000 down-going muons was generated with an identical momentum of $p_\mu = 800\,\text{MeV}/c$ ($T_\mu \simeq 701\,\text{MeV}$) and at the same starting position $(x, y, z) = (150, 500, 350)$ cm inside the ProtoDUNE-SP detector. The initial starting point is relatively close to the ceiling of the detector ($y \approx 600\,\text{cm}$) and around the middle of one of the two TPCs in the other two orthogonal axes. This guarantees that the great majority of the minimum ionising muons will be contained inside the liquid argon active volume. Each muon is then independently propagated through argon using GEANT4 and LArSoft. GEANT4 simulates the particle propagation in steps of average length 300 µm and for each step calculates the energy deposited by the muon. Delta rays and Michel electrons are also simulated, but the corresponding energy depositions are ignored. To calculate the dE/dx, the energy deposited at each step dE_i^{dep} is divided by the step length ds_i: $(dE/dx)_i \equiv dE_i^{\text{dep}}/ds_i$. The distance from the end of the track, or residual range, is not directly produced by GEANT4 but, since the position of each step is stored, it can be reconstructed by adding together the step lengths from the end point of the track to the desired location on the trajectory. By "crawling" backwards along the GEANT4 steps, the significant scattering the occurs towards the end of the muon track is precisely taken into account when constructing the residual range at each point. The result of the calculation of the dE/dx and the residual range is shown in Figure 5.8 with the theoretical calculation of the dE/dx most probable value from Equation 5.4 with thickness $x = 300\,\mu\text{m}$, the average step length in the simulation. Despite the qualitatively good agreement between the simulated most probable value and the theoretical values, a small discrepancy, likely due to the contribution of different step lengths, can be observed.

However, a more precise comparison can be performed by manually selecting a thickness in the simulation. As an example, the value $x = 0.75\,\text{cm}$, can be chosen.

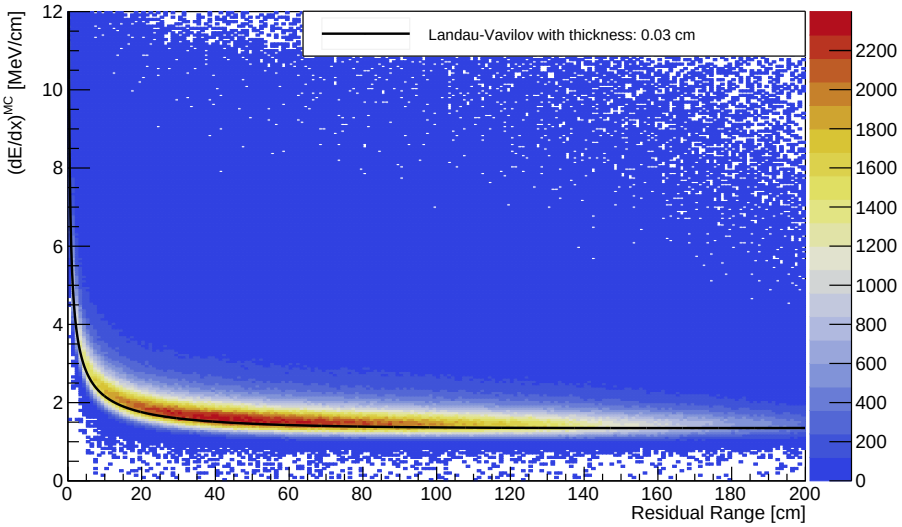


Figure 5.8: Simulated energy loss dE/dx as a function of residual range for a sample of stopping muons. The black line represents the theoretical prediction of the most probable value for the energy loss according to Equation 5.4 and using a thickness of 300 µm.

This is a realistic example since the anode wire pitch in ProtoDUNE-SP is about 0.5 cm and cosmic particles typically come at an almost vertical angle so that the track pitch "seen" by one collection wire is greater than the wire pitch. To construct dE/dx values for the chosen thickness, the muon trajectory is divided into 0.75 cm-long segments starting from the end point of each simulated muon and the step lengths ds_i within each segment are added together. The same is done for the corresponding energy depositions dE_i. The calculated $(dE/dx)^{\mathrm{MC}}_{0.75}$ for each segment of the track is then:

$$\left(\frac{dE}{dx}\right)^{\mathrm{MC}}_{0.75} = \frac{\sum_{i=0}^{n} dE_i}{\sum_{i=0}^{n} ds_i} \quad \text{with} \quad \sum_{i=0}^{n} ds_i \simeq 0.75\,\mathrm{cm}, \tag{5.5}$$

where the index i runs over the small GEANT4 steps within a segment and n is the number of necessary segments such that $\sum_{i=0}^{n} ds_i \simeq 0.75\,\mathrm{cm}$. The residual range is calculated with respect to the middle point of each 0.75 cm-long segment. The result can be seen in Figure 5.9, where a good agreement (within 2%) can be seen between the simulation and the dE/dx MPV calculated from Equation 5.4.

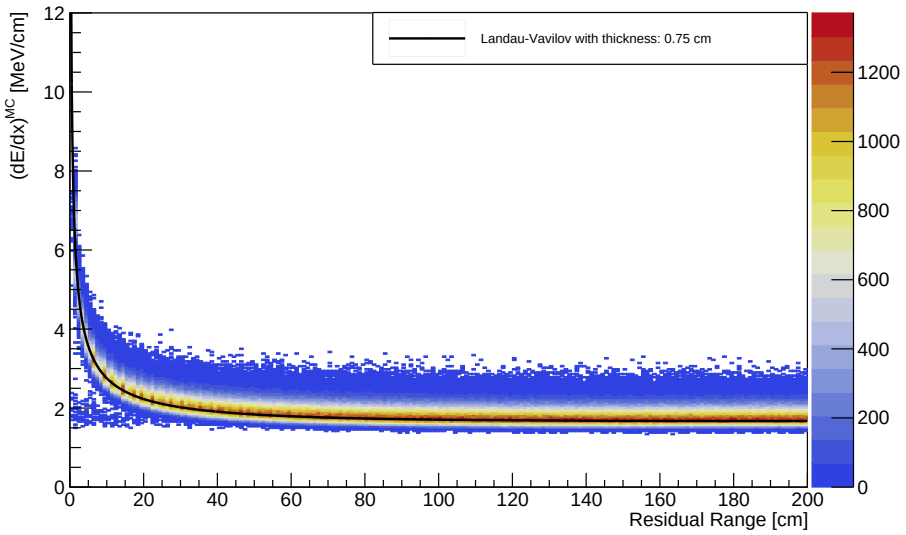


Figure 5.9: Simulated energy loss dE/dx with a simulation step of 0.75 cm as a function of residual range for a sample of stopping muons. The black line represents the theoretical prediction of the most probable value for the energy loss according to Equation 5.4 and using a thickness of 0.75 cm. The "MIP-like" dE/dx contribution at low residual range values comes from the few muons that decay in flight.

The mean dE/dx value can be extracted from the simulation of dE/dx in Figure 5.8. For each residual range bin, the corresponding dE/dx mean is obtained. The result is shown in Figure 5.10. While the mean dE/dx is more sensitive to single collisions with high-energy loss than the most probable value, its use is more practical since the mean does not depend on the thickness of the material traversed. This simplification becomes relevant when looking at cosmic-ray tracks in ProtoDUNE-SP, which have a broad angular distribution, for which the measured dx, and therefore the most probable value, depends on the relative direction of the track and the wire plane considered for the calorimetry measurements.

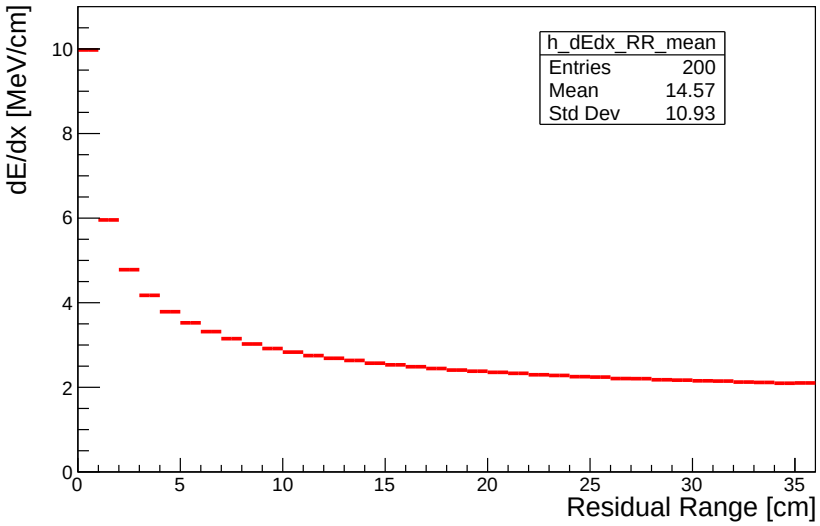


Figure 5.10: Mean simulated dE/dx as a function of residual range for stopping muons in liquid argon.

Chapter 6

A Selection of Stopping Cosmic Muons in ProtoDUNE-SP

Contents

6.1 Introduction and Motivations 90
6.2 Cathode-Crossing Muons 94
6.3 Anode-Crossing Muons 97
6.3.1 t_0 Calculation 104
6.4 Removing Broken Tracks 104
6.4.1 Multiple Segments 105
6.4.2 Single Segment 106
6.5 Cuts Validation 108
6.6 Summary of the Selected Sample 114
6.7 Michel Electron Contamination 116
6.8 dE/dx Shape Discriminator 118
6.9 Sample Preparation 122

Muons that stop in the active volume are a useful calibration tool to study the detector response to a given energy deposition since their energy can be inferred at any point along the trajectory by measuring the distance from the end of the track ("residual range"). This chapter will present a selection of cosmic muons that stop in the ProtoDUNE-SP detector. Section 6.1 will motivate the choice of selecting stopping cosmic muons and the selection method by highlighting the most important reconstruction features. Sections 6.2 and 6.3 will present a selection of muons that either cross the cathode or the anodes of the TPCs. Section 6.4 will illustrate cuts to

mitigate the contamination from broken tracks. The cuts described will be discussed and validated on data in Section 6.5. Section 6.6 will summarise the main results and give an overview of the selected samples. The contamination of Michel electrons in the muon tracks and a description of a method to validate the dQ/dx values along the residual range are described in Sections 6.7 and 6.8. Finally, Section 6.9 will explain how the sample is prepared to be used.

6.1 Introduction and Motivations

Energy calibration, in which known sources of energy deposition are used to measure the detector response, represents a crucial step for a particle detector. Given that ProtoDUNE-SP is a surface detector, the energy loss of cosmic muons can be employed. Cosmic muons are also present underground, with their rate depending on the depth, and can therefore also be used for the DUNE far detector. While muons that cross the TPC are approximately minimum ionising, only the energy of muons that stop in the detector can be reconstructed accurately by measuring the total distance travelled. For such particles, the dE/dx profile is precisely known and can be mapped at each point on the trajectory by walking backwards along the track starting from the end point. It is therefore possible to infer the energy deposited by ionisation by only using spatial information.

A sample of stopping muons can also be employed to study electron-ion recombination in liquid argon, following the ionisation resulting from the energy deposited by the muons. The fact that the energy loss per unit length dE/dx can be determined independently from the charge collected dQ/dx allows to study the dQ/dx as a function of the initial charge density. This is possible thanks to the increasing dE/dx towards the end of the track, which provides a known variable source of initial ionisation energy.

During a typical beam run, the detector acquisition window is triggered by a beam particle entering the TPC. The acquisition window lasts 3 ms or 6000 ticks and is started 250 µs before the beam event. The beam event occurs by definition at the

time $t = 0$. Cosmic-ray particles enter the detector each at their own time t_0 with respect to the beam event. Given that, in general, $t_0 \neq 0$, these particles are also referred to as "out-of-time" muons. Since the clock for the hit time is started when the time window is opened, the drift time for each beam particle hit can be reconstructed by correcting the hit peak time for the known time offset $t_{\text{offset}} = 250\,\mu\text{s}$: $t_{\text{hit}} - t_{\text{offset}}$, where t_{hit} is the hit peak time[1] representing the arrival time of the charge at the wire and is obtained by the Gaussian fit to the charge profile. The drift time can then be used to calculate the correct location of the track in the drift position, knowing the drift velocity. In the case of out-of-time particles, their t_0 is unknown *a priori*. The reconstruction algorithm that takes the raw hits to build track objects in Pandora is agnostic to the t_0 and by default it reconstructs every track as an on-time track or, equivalently, it assumes $t_0 = 0$, unless it is a cathode or anode-crossing particle identified by Pandora itself (as described in Section 3.9.3). In the general case when $t_0 \neq 0$, the reconstructed drift time is given by:

$$t_{\text{drift}} = t_{\text{hit}} - t_{\text{offset}} - t_0. \tag{6.1}$$

Since the reconstructed drift position x_{reco} for a given hit is proportional to t_{drift}, the error in reconstructing x_{reco} when assuming $t_0 = 0$ is proportional to the t_0 itself. This implies that if the t_0 can be calculated independently, the correct drift coordinate reconstruction can be achieved. This correction is not negligible given the slow velocity of the drifting electrons ($\sim$1.6 mm/µs).

Various techniques can be used to reconstruct the t_0. As already mentioned, the light detection system can provide an almost instant measurement of the t_0 thanks to the nearly instant emission and propagation of light, although it is challenging to correctly assign a t_0 to each single track in a busy readout window, like those of surface LArTPCs. Additionally, the cosmic-ray tagger can be used to correctly reconstruct the hit drift coordinates by matching the hits on the CRT modules with

[1]It must be noted that the hit times are usually measured in ticks, being them measured by the detector electronics clock, while the t_0 and t_{offset} are usually expressed in µs or ns. It is therefore necessary to convert one measuring system to the other by using the detector sampling frequency 1 tick = 500 ns.

the TPC hits. However, at the time of this study the hardware and the analysis techniques developed to reconstruct the t_0 using the PDS or the CRT were not mature enough to be used. Instead, it was decided to rely on geometrical and topological features to identify tracks that cross the cathode or one of the two anodes. For these tracks, the t_0 can be calculated. Such out-of-time tracks are reconstructed shifted with respect to the cathode or anode plane crossed but, if they are correctly identified, the real drift position can be obtained by "stitching" the track back to the crossed surface. Cathode-crossing particles are efficiently selected by the algorithm described in Section 3.9.3 of Chapter 3. Because they are being identified before the production of the track object, the shift is already corrected for when the track object is created by Pandora. A similar situation applies to anode-crossing tracks, for which Pandora tries to reconstruct the t_0 by matching the time of the track hits and the hits resulting from the ionisation charge created in the volume between the anode wires and the cryostat internal wall. These tracks will also have the correct drift position. Because it relies on a small number of hits on the cryostat side, this procedure is more challenging and most anode-crossing tracks are not identified. To summarise, three categories of cosmic tracks are returned by Pandora: (1) generic out-of-time tracks for which the t_0 is unknown and the drift coordinate is wrong (this includes anode-crossing tracks that are not identified), (2) corrected cathode-crossing tracks and (3) corrected anode-crossing tracks. In this chapter, a selection of stopping tracks is developed for both cathode and anode-crossing muons. In addition, an algorithm to identify tracks that enter through the anode planes and are missed by Pandora will also be presented. The spatial correction will be performed while determining their t_0.

Reconstructing the correct position of a track is important to correct for a number of detector effects that affect both the measured dQ/dx and the nominal energy loss dE/dx obtained from the residual range. Space charge effects and the electron lifetime impact the measured dQ/dx in many ways, described in Section 3.10. The reconstruction of the residual range along each track is affected by the distortion of the electric field which modifies the trajectory of the drifting electrons. Consequently,

the dE/dx obtained from the residual range will be incorrect. For these reasons, it is important to only work with tracks which have a correctly reconstructed t_0.

Every aspect of the acquisition window time structure and the reconstruction procedures described so far is identically reproduced in the ProtoDUNE-SP Monte Carlo. The Monte Carlo simulation was used to identify the interesting variables to cut on and the best cut values to optimise the signal/background separation. By using the Monte Carlo truth information, the selection purity can be estimated. The selection cuts were subsequently validated and optimised for the data. The simulation, reconstruction and analysis are performed with LArSoft [77].

The cuts implemented make extensive use of the ProtoDUNE-SP TPC geometry, here summarised for convenience and illustrated in Figure 6.1. The liquid argon active volume is around 600 cm high (y coordinate), 700 cm long (z coordinate) and each TPC is about 360 cm wide with the cathode located at $x_{\mathrm{C}} = 0$. Two angles

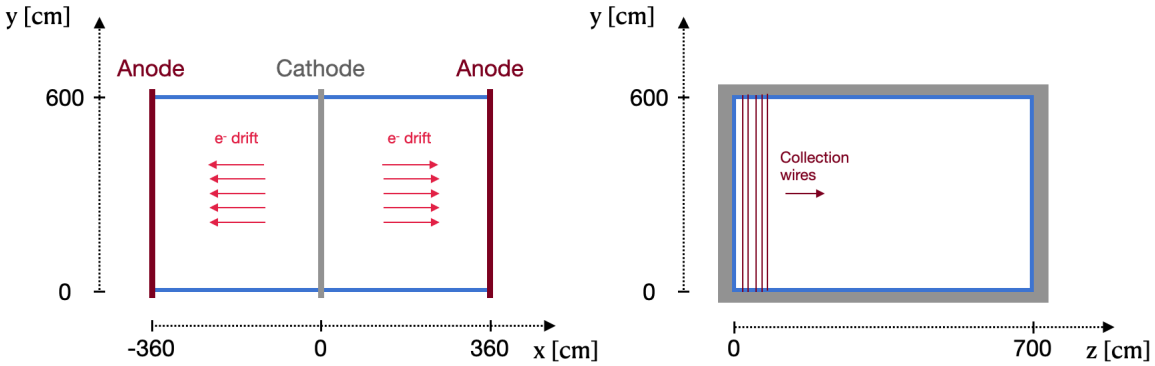


Figure 6.1: Active volume geometry and coordinate reference system for ProtoDUNE-SP (boundary values are approximate). The front view is shown on the left and the side view is shown on the right. The active volume border is represented by the blue contour. Cathode and anode are highlighted in grey and brown respectively. The electron drift direction is also indicated together with the direction of the collection plane wires.

are defined and are used to characterise the direction of tracks in the detector. The definition is shown in Figure 6.2. Both angles, θ_{xz} and θ_{yz}, are measured with respect to the z axis and span the xz and yz plane respectively.

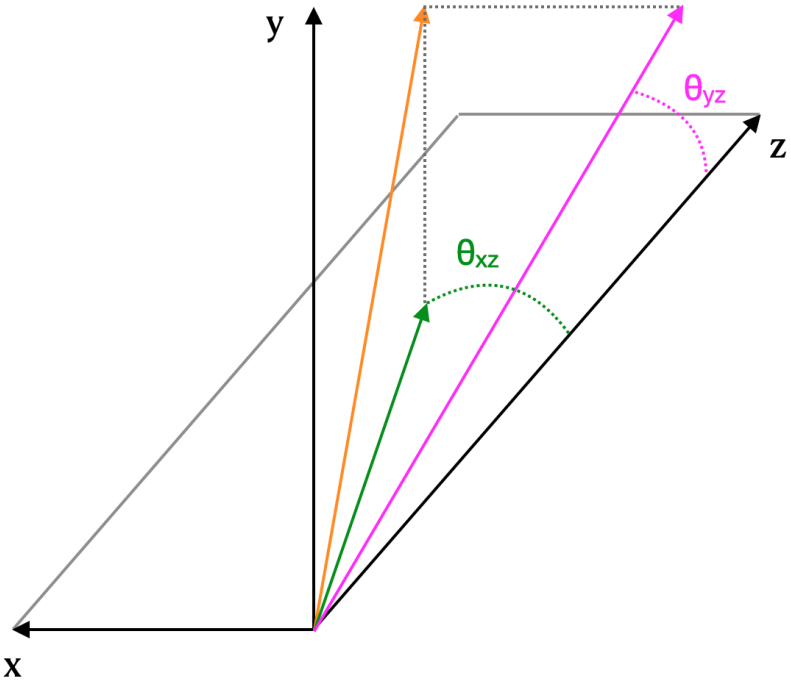


Figure 6.2: Definition of the angles θ_{xz} and θ_{yz} used throughout this chapter to characterise the track directions.

6.2 Cathode-Crossing Muons

Cathode-crossing muons can be easily identified by selecting those tracks in the read-out that have a reconstructed t_0 associated and for which the start and end points lie in two different TPCs. This is possible because tracks that are t_0-tagged by Pandora are flagged to the analyser. For cosmic tracks the start point is defined as the point with the highest y coordinate. To select well reconstructed tracks, two preliminary cuts on the track length and angle are performed. The cosmic track has to be at least 100 cm long to minimise the contamination of tracks that are only partially reconstructed. Among the three wire planes that constitute the anode, the collection wire is that with the highest signal to noise ratio [62]. It is therefore the preferred plane to be used to measure the dQ/dx. Tracks that lie on the plane defined by the collection wire direction and the electron drift direction will be poorly reconstructed, since most of the hits would be collected by the same wire in a potentially short time. With reference to Figure 6.2, the collection wires have direction $\theta_{yz} = 90°$, while the

(nominal) electric field vector is characterised by $\theta_{xz} = 90°$. Therefore tracks that have $60° < |\theta_{xz}| < 120°$ or $60° < |\theta_{yz}| < 120°$ are excluded from the selection. The distribution of θ_{yz} and θ_{xz} for muon tracks in the MIP region can be seen in Figure 6.3. The colour scale in the plot indicates the average dQ/dx in the bin. The angular cuts select combination of θ_{yz} and θ_{xz} with uniform and well reconstructed dQ/dx.

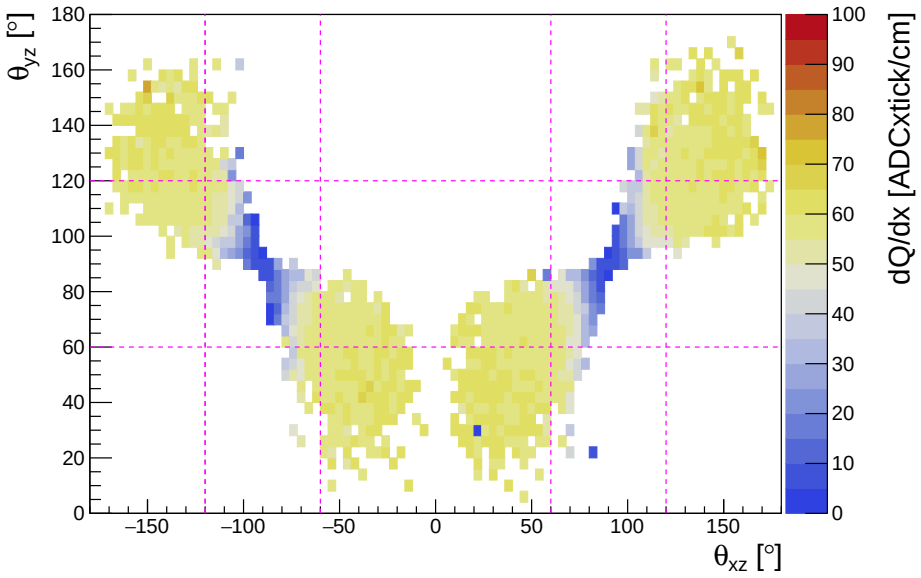


Figure 6.3: Distribution of θ_{yz} and θ_{xz}. The colour scale represents the average dQ/dx in each bin. It can be seen that for areas around $|\theta_{yz}| = 90°$ and $|\theta_{xz}| = 90°$ the dQ/dx is significantly reduced indicating a mis-reconstruction. The cuts indicated by the magenta lines select areas with uniform and well reconstructed dQ/dx.

To identify stopping cosmic muons, a set of variables to cut on is identified. This includes the coordinates of the reconstructed start and end point and the minimum and maximum hit peak time for each track. The cuts on the hit time are chosen to ensure that the tracks are fully contained in the readout window. The TPC readout is characterised by a 3 ms acquisition window. Given the slow electron drift, it can occur that a through-going cathode-crossing cosmic particle enters the TPC before the start of the acquisition window and that the window is triggered only when some of the charge, the closest to the anode, has finished drifting. In this case, the final portion of the track will not be reconstructed and the end point will appear to be

inside the active volume mimicking a stopping track. This situation is illustrated in Figure 6.4. A similar scenario occurs when particles enter the TPC nearly at the end of the readout window and not all the charge makes it to the anode before the end. The distribution of each reconstructed variable is plotted for true cathode-crossing

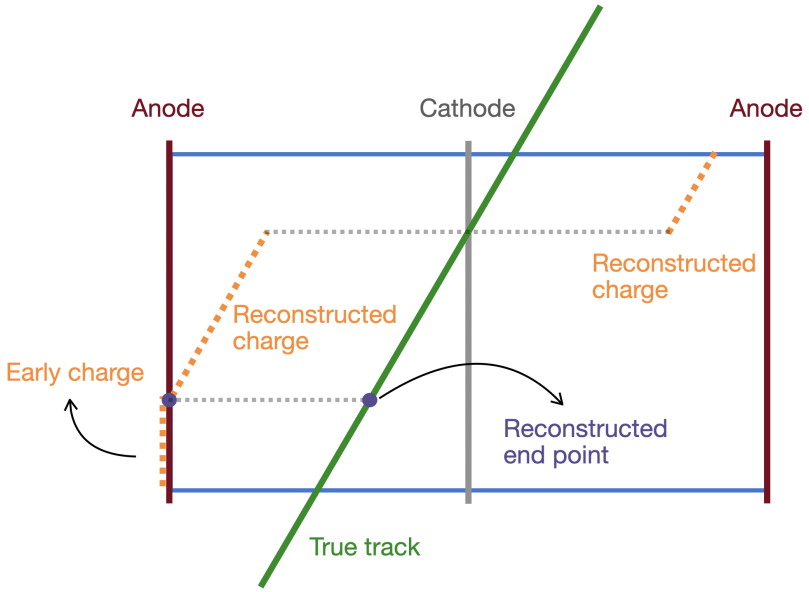


Figure 6.4: Diagram for a through-going cathode-crossing track in the xy plane entering the TPC before the readout window is opened. The situation depicted refers to the moment when the readout window is opened (tick = 0). While some of the charge is still drifting, the portion corresponding to the final (bottom) part of the track is not recorded. The end point is therefore reconstructed in the middle of the active volume, like in the case of a stopping track.

stopping muons (the "signal"), selected using the Monte Carlo truth information. The shape of the distributions for the signal are compared to those for all the cathode-crossing tracks. This is achieved by iterating over many readout windows. These plots are shown in Figure 6.5 for the position coordinates and in Figure 6.6 for the hit peak time. Only the tracks with a start point close to the ceiling and lateral walls are considered; this is done by requesting that the coordinates of the start points lie on the external regions determined by the vertical purple lines in Figures 6.5a, 6.5b and 6.5c. Conversely, only tracks with a well contained end point, within the region delimited by the two vertical lines of Figures 6.5d, 6.5e and 6.5f, are accepted. These cuts are placed so to exclude the excess of tracks which have a reconstructed point

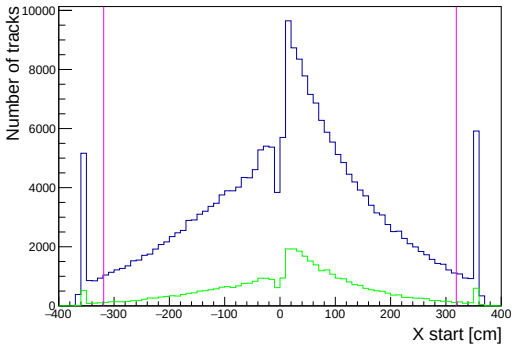
close to the active volume borders and are likely to be through-going muons. The horizontal asymmetry around $x = 0$ in Figures 6.5a and 6.5d is believed to be due to space charge effects that make the efficiency and resolution of the stitching algorithm different between the two TPCs. The features at $z \simeq 233\,\text{cm}$ and $z \simeq 466\,\text{cm}$ are due to the presence of partially reconstructed tracks and will be addressed in Section 6.4. The plots in Figure 6.6 are obtained by iterating over all the hits across the three wire planes that correspond to each track and selecting the minimum or maximum hit peak time. A track with a minimum hit time close to 0 ticks, the start of the time window, is likely to be a partially-reconstructed early track. Therefore only tracks with a minimum hit time greater than the value indicated by the purple line are accepted. Similarly, it is requested that tracks have a maximum hit time smaller than some number close to the end of the time window. The actual cut values are summarised in Table 6.1. These values are preliminary and will be optimised comparing the Monte Carlo distributions with data.

Table 6.1: Preliminary cut values for cathode-crossing stopping muons.

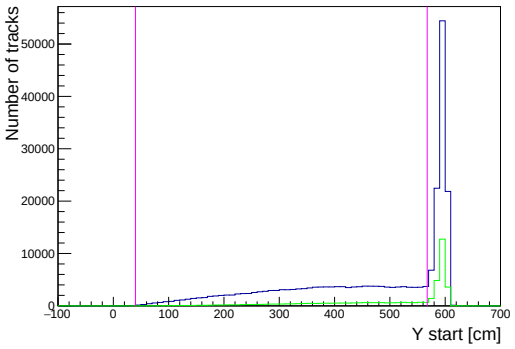
Variable	**Cut**
`Track Length`	$> 100\,\text{cm}$
`Angular Cuts`	$60^\circ < \lvert\theta_{xz}\rvert < 120^\circ$ or $60^\circ < \lvert\theta_{yz}\rvert < 120^\circ$ rejected
`Start Point`	Within 40 cm of the active volume borders
`End Point`	More than 60 cm away from the active volume borders
`Minimum Hit Peak Time`	Greater than 500 ticks
`Maximum Hit Peak Time`	Less than 4800 ticks

6.3 Anode-Crossing Muons

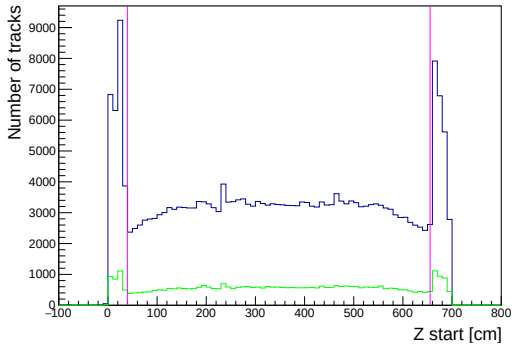
As anticipated in the introduction, some of the anode-crossing muons are identified by Pandora, but with a low efficiency. This section is dedicated to the development of an alternative selection of tracks that enter in the TPC piercing the anode planes. The cuts to select a general anode-piercing muon will not be able to rely on the reconstructed x (drift) coordinate, given that it will be in general reconstructed shifted



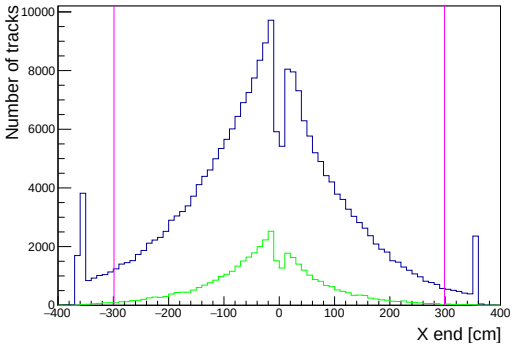
(a) Start point x distributions.



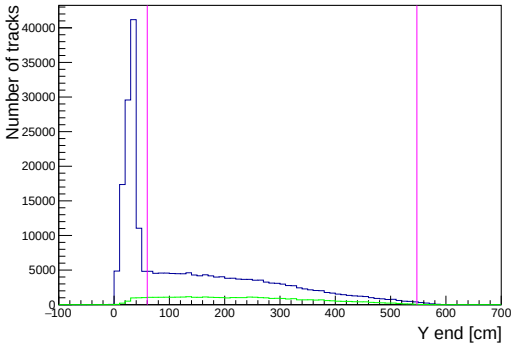
(b) Start point y distributions.



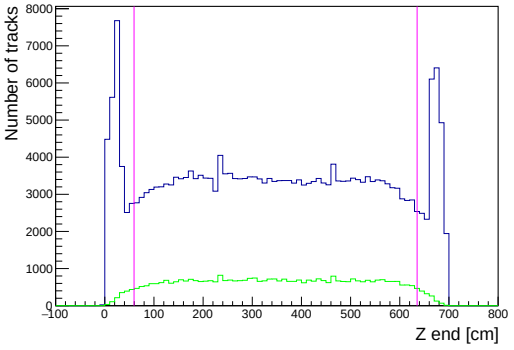
(c) Start point z distributions.



(d) End point x distributions.

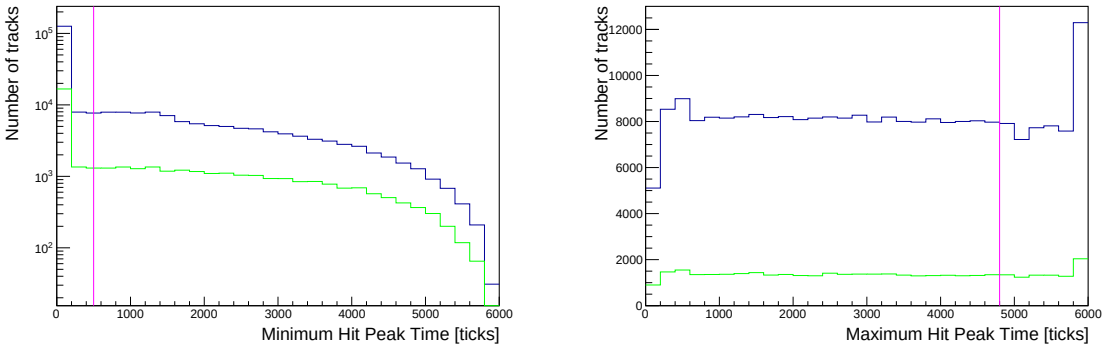


(e) End point y distributions.



(f) End point z distributions.

Figure 6.5: Distributions of reconstructed spatial variables for every cathode-crossing track in the events (blue) and true cathode crossing stopping muons (green). The vertical purple lines represent the chosen position for the cut. For the first three variables (start point, plot a, b, c) only the values that lie at the external of the cut position are accepted. For the last three variables (end point, plot d, e, f) the values within the two lines are accepted.



(a) Minimum hit peak time distributions. (b) Maximum hit peak time distributions.

Figure 6.6: Distributions of reconstructed time variables for every cathode-crossing track in the events (blue) and true cathode-crossing stopping muons (green). The vertical purple lines represent the chosen position for the cut. Tracks are accepted if their minimum (maximum) hit peak time is greater (less) than the value in correspondence of the cut position.

because of the wrong t_0 assumption. However, it can be observed that out-of-time particles with relatively long trajectory do not originate from inside the TPC.[2] Final state particles in a beam interaction originate inside the TPC, but they are on-time, i.e. with $t_0 = 0$. Therefore, if a track appears to have originated from within the active volume, the algorithm developed assumes that in reality the corresponding particle entered through the anode and the track is reconstructed shifted because of the wrong t_0. This situation is illustrated in Figure 6.7. To make sure that the start point is fully contained in the active volume, a cut on the y and z coordinates needs to be implemented to define a fiducial (2D) volume within the active volume in the yz plane (Figure 6.8). Like in the case of cathode-crossing tracks, the comparison between the distribution shapes of the true anode-crossing tracks and any track in the event can be used to establish a first hypothesis for the values at which the cuts should be placed. The distributions for the y and z coordinates of the start points are shown in Figure 6.9, where the purple lines indicate the cut location. Only the tracks with start points within the regions defined by the two lines are accepted. Cuts on

[2]Michel electrons reconstructed as tracks are originated inside the active volume but they are only 5-10 cm long.

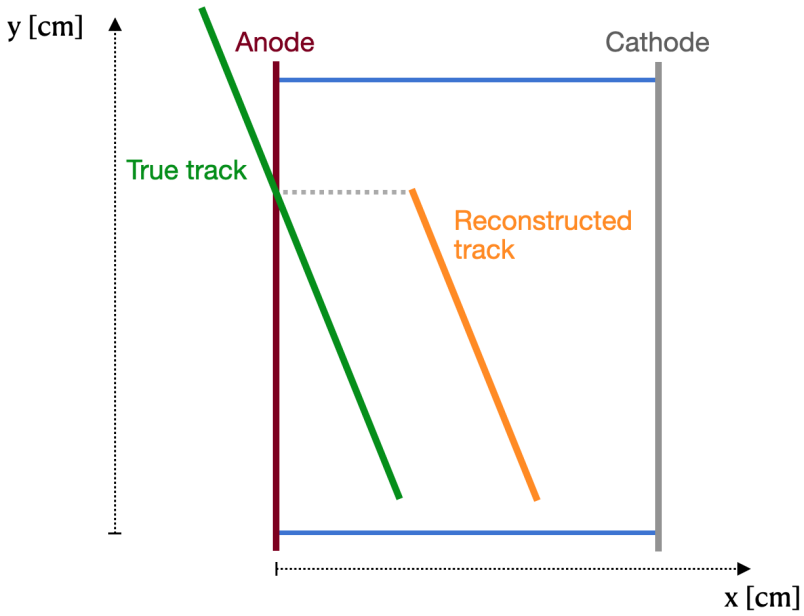


Figure 6.7: Diagram showing the selection principle for cosmic-ray muons that enter crossing the detector anode. The out-of-time track (green) will be reconstructed shifted (orange) by an amount proportional to its true t_0 and therefore will appear as if it originated from within the active volume. By requesting that the start point y and z coordinates are contained in the active volume, such tracks can be identified. The symmetric configuration applies to the other TPC.

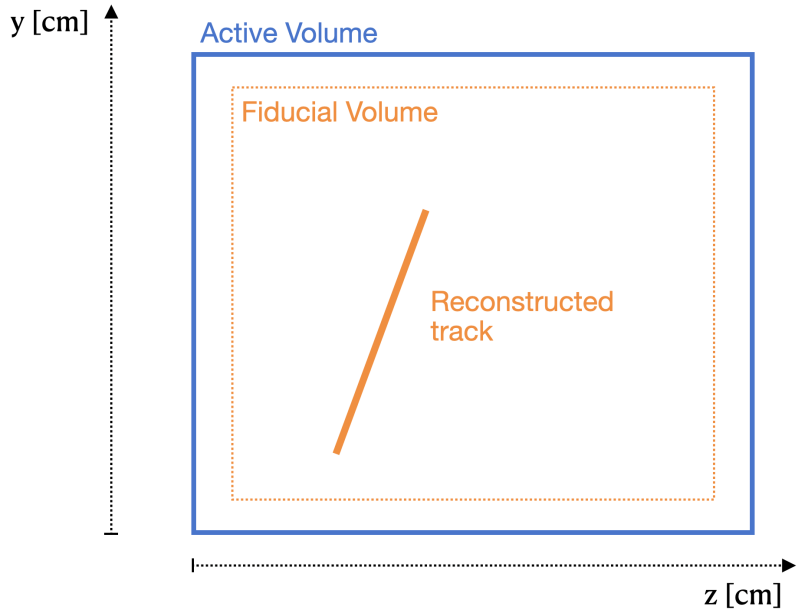
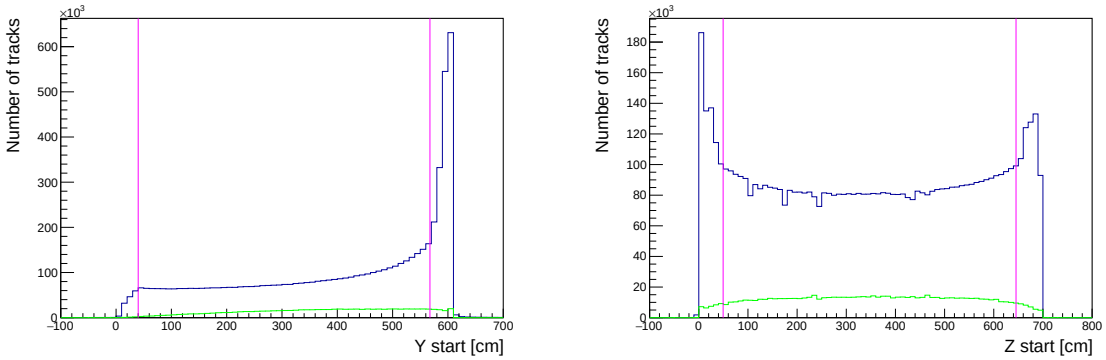


Figure 6.8: Diagram representing the requested condition on the start point to be considered as an anode-crossing track. The start point needs to be at a certain distance from the active volume borders to exclude tracks that enter from the top and the upstream and downstream faces of the TPC.



(a) Start point y distributions.

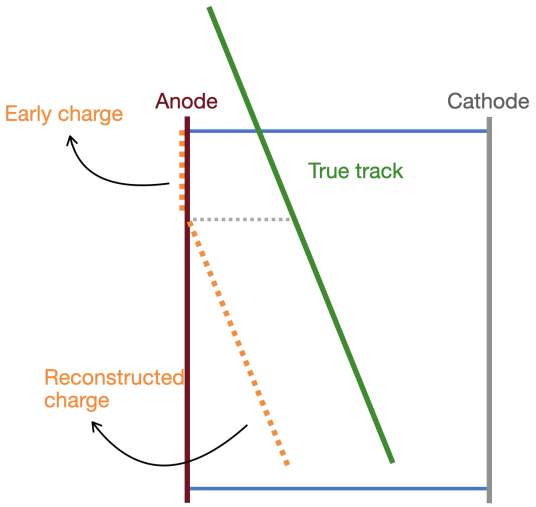
(b) Start point z distributions.

Figure 6.9: Preliminary distributions and selection cuts for the start points of anode-crossing stopping muons. Distributions are shown for every track in the events (blue) and for true anode-crossing stopping muons (green). The preliminary cut position is indicated by the vertical lines. The green distributions are scaled up by a factor 5 for visibility.

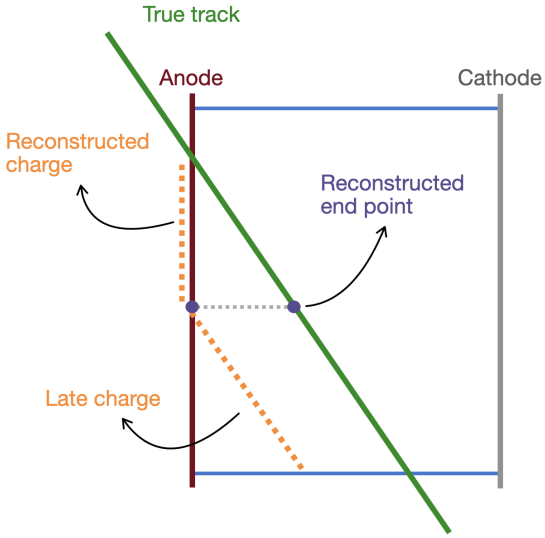
time variables are also relevant for this selection, as both early[3] and late[4] tracks can be misidentified. Situations in which these tracks can be mistaken for anode-crossing muons and stopping muons can be seen in Figure 6.10a and 6.10b respectively. To prevent from selecting tracks like in Figure 6.10a, a cut on the minimum hit peak time is introduced. Likewise, a cut on the maximum hit peak time is performed to avoid situations like in Figure 6.10b. They are both shown in Figure 6.11. To select contained tracks, a cut on the end point positions is implemented. The plots for the y and z coordinates of the end points are shown in Figure 6.12. Since the tracks are not corrected for the shift in the drift direction, a cut on the x coordinate can not be determined at this stage. As a preliminary choice, a 3D fiducial volume for the end points is defined for simplicity based on the cuts on the y and z projections. Finally, the same angular and length cuts as in the case of cathode-crossing muons are applied. The preliminary cuts are summarised in Table 6.2.

[3]Tracks that enter the TPC before the readout window is opened and the charge is still drifting after the trigger.

[4]Tracks that enter the TPC just before the readout window closes.

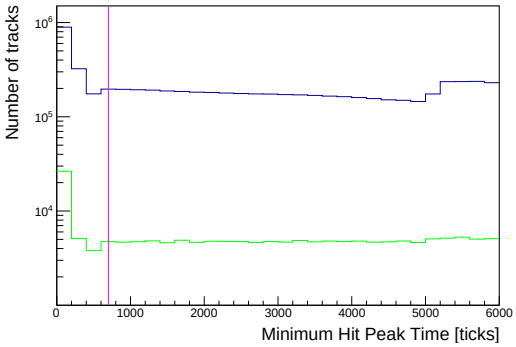


(a) Early track that is mistaken for an anode-crossing track.

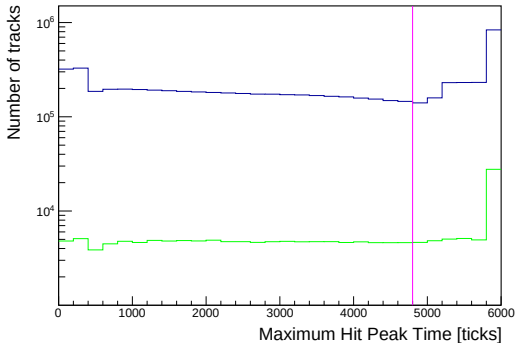


(b) Through-going anode-crossing late track that is mistaken for a stopping track.

Figure 6.10: Diagrams showing early and late tracks that can be mistaken for anode-crossing stopping muons. Left: the moment the readout window is opened (tick = 0) but some charge is still drifting; that track will be misidentified as crossing the anode due to the misreconstructed start point. Right: the moment the readout window is closed (tick = 6000) but the charge corresponding to the final portion of the track has not made it to the anode; the track will be identified as a false stopper.

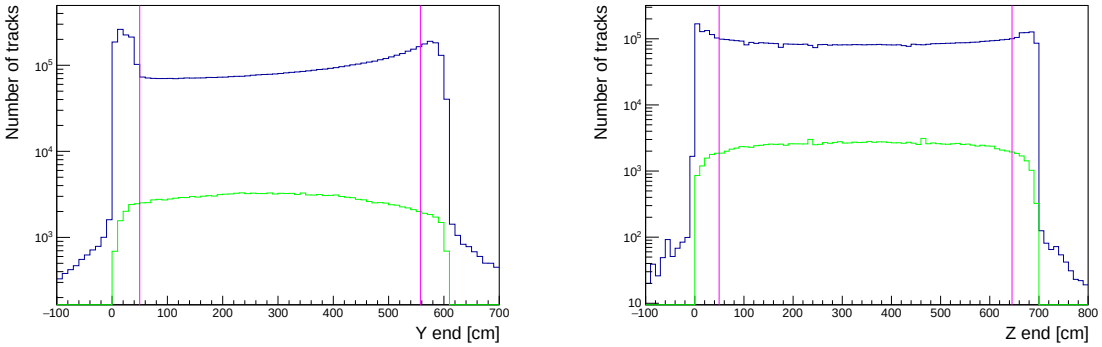


(a) Minimum hit peak time distributions.



(b) Maximum hit peak time distributions.

Figure 6.11: Distributions of reconstructed time variables for every track in the events (blue) and true anode-crossing stopping muons (green). The vertical purple lines represent the chosen position for the cut. Tracks are accepted if their minimum (maximum) hit peak time is greater (less) than the value in correspondence of the cut position.



(a) End point y distributions.

(b) End point z distributions.

Figure 6.12: Preliminary distributions and selection cuts for the end points of anode-crossing stopping muons. Distributions are shown for every track in the events (blue) and for true anode-crossing stopping muons (green). The preliminary cut position is indicated by the vertical lines.

Table 6.2: Preliminary cut values for anode-crossing stopping muons.

Variable	**Cut**
`Track Length`	$> 100\,\text{cm}$
`Angular Cuts`	$60^\circ < \lvert\theta_{xz}\rvert < 120^\circ$ or $60^\circ < \lvert\theta_{yz}\rvert < 120^\circ$ rejected
`Start Point Y`	More than 40 cm from the active volume borders
`Start Point Z`	More than 50 cm from the active volume borders
`End Point`	More than 50 cm away from the active volume borders
`Minimum Hit Peak Time`	Greater than 700 ticks
`Maximum Hit Peak Time`	Less than 4800 ticks

6.3.1 t_0 Calculation

When a track that enters from the anode is identified based on the cuts on the start point and the hit times, the t_0 needs to be calculated to correct the x coordinate and subsequently apply the correction for electron lifetime and space charge effects. The t_0 is calculated according to the formula:

$$t_0 = \frac{L_{\text{drift}} - |x_{\text{start}}^{\text{reco}}|}{v_{\text{drift}}}, \tag{6.2}$$

where v_{drift} is the electron drift velocity, L_{drift} is the total drift length of ProtoDUNE-SP and $x_{\text{start}}^{\text{reco}}$ is the reconstructed x coordinate of the start point. Knowing the t_0, the x coordinates for each hit, and in particular the start and end point, can be corrected according to:

$$x^{\text{corr}} = x^{\text{reco}} \pm (v_{\text{drift}} \cdot t_0), \tag{6.3}$$

where the sign depends on which of the two anodes are crossed.

6.4 Removing Broken Tracks

It was noticed that muon trajectories could be reconstructed as a series of one or more segments. Each segment is usually referred to as a "broken track". The reconstruction of long trajectories can present some challenges in busy events like those of surface detectors. These challenges include assigning the hits to the correct track. Additionally, the modularity of the TPC anodes can lower the reconstruction efficiency in correspondence to the gaps between assemblies. This results in a number of tracks that are broken at the z coordinates of the gaps, as shown by the features at $z \simeq 233\,\text{cm}$ and $z \simeq 466\,\text{cm}$ in Figures 6.5c and 6.5f. A small excess of events is also present in the corresponding plots of Figures 6.9b and 6.12b, although not visible due to the chosen binning. To avoid this problem, it is imposed that tracks must not have a start or end point with a z coordinate within 10 cm from the APA gaps.

While the cut on the z value has an important positive impact on the selection, broken tracks can still occur anywhere in the detector due to reconstruction inefficiencies. Some tracks are reconstructed as a series of segments, while others are simply

missing the initial or last part. Both types of events are problematic for a stopping muon selection since tracks that miss the last portion look exactly like tracks that stop inside the detector. At the same time, if a track misses the first section, it will be misidentified as an anode-crossing track. As a consequence, the residual range calculation will be incorrect affecting the predicted dE/dx. Both topologies are addressed separately with dedicated cuts.

6.4.1 Multiple Segments

When a cathode or anode-crossing muon candidate is identified, a check is conducted to look for the presence of other segments that would hint at the presence of a broken track. It is important to notice that, in the case of a cathode-crossing muon, a second segment will only be reconstructed downstream of the candidate track and will not be aligned. This is a consequence of the t_0 tagging of the candidate muon, necessary condition to be identified. The secondary segment is not t_0-tagged. For anode-crossing muons this misalignment between track segments happens only for the tracks identified directly by Pandora, but, in addition, the broken segment could be located both upstream or downstream the out-of-time candidate tracks. In implementing the algorithm to remove broken tracks, the segments are ordered from top to bottom based on the y coordinate of the start points, and the uppermost segment is referred to as the first segment regardless of which is the candidate muon track for the selection.

In general, the second segment can be located immediately nearby the first portion, but cases have been observed in which the two segments are even a few meters apart. Both situations are illustrated in Figure 6.13 where the segments corresponding to a single particle are highlighted by the orange arrow. To exclude these types of events from the selection, each time a candidate is identified the algorithm looks for other tracks in the same readout window that have the same direction.[5] Two angles, α and β, are defined as shown in Figure 6.14. The direction of the trajectories is approximated as a straight line joining the end points. The angle β is introduced

[5]Same direction is referred to the relative orientation of the straight lines in the 3D space. It does not necessarily imply that the two segments are on the same line, i.e. they can be parallel.

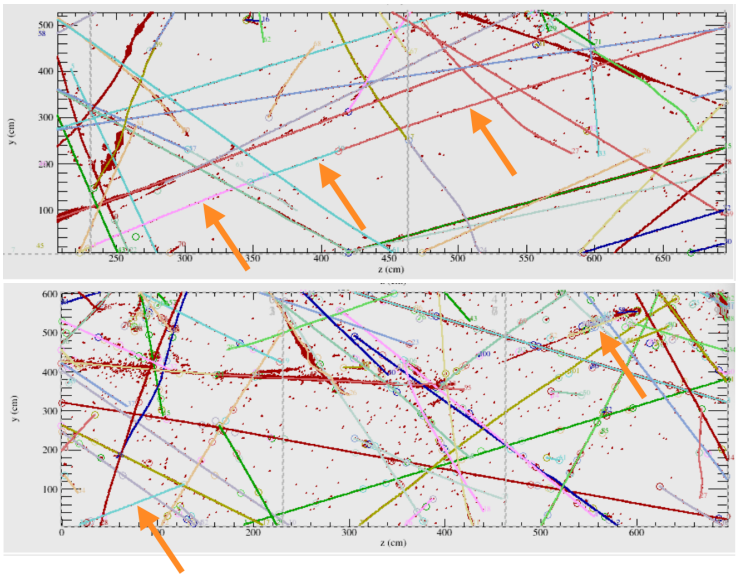


Figure 6.13: Two event displays of ProtoDUNE-SP Monte Carlo events showing examples of broken tracks in the yz plane. Reconstructed segments are highlighted by the orange arrow. Top: A particle is reconstructed as a series of three segments in sequence. Bottom: Only the initial and last part of the trajectory is reconstructed with a large gap in the middle.

to have an additional parameter to verify the alignment in the yz plane. Since the straight line approximation can be significantly imprecise at times, the angle β is defined as the angle between the first line and the line connecting the end point of the first segment to the middle point of the second. If the two tracks belong to the same particle, it is expected that $|\cos\alpha| \simeq \cos\beta \simeq 1$. Therefore, if another track in the event is found such that $|\cos\alpha| > 0.995$ and $\cos\beta > 0.995$, the candidate is discarded from the selection. In addition, a stricter condition on α ($|\cos\alpha| > 0.96$) is implemented if the start point of the second segment is within 50 cm from the first segment end point.

6.4.2 Single Segment

The scenario in which one muon is only partially reconstructed can be challenging to identify by only using geometrical conditions on the direction of the tracks. In some cases, it can happen that the space points are correctly reconstructed, but the track object does not fit them, like shown in Figure 6.15. Like in the previous case, such

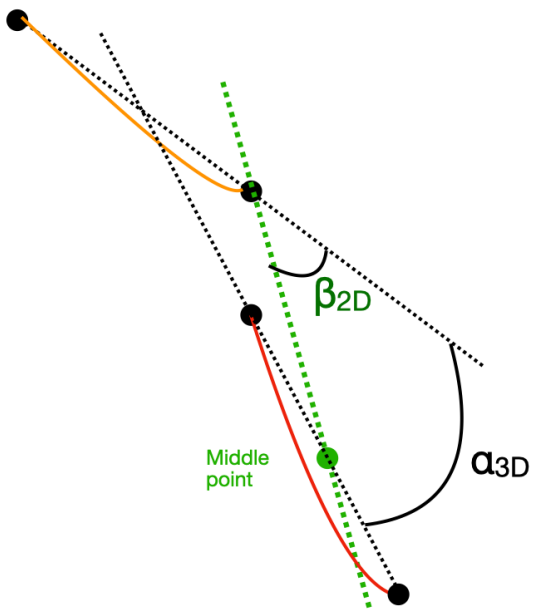


Figure 6.14: Diagram showing the definition of the angles for broken tracks removal. The direction of the tracks is approximated as a straight line connecting the track end points. α is the 3D angle between the first and the second segment. β is the angle between the first track projection in the yz plane and the line joining the end point of the first to the middle point of the second segment projection in the same plane.

tracks can be misidentified as stopping and/or anode crossing tracks. The latter case is due to ignored space points near the start point. To deal with such scenarios, a procedure was implemented whereby the presence of space points around the track extremities is investigated. In the case of cathode-crossing muons, a rectangular volume (50 cm $\times$ 10 cm) longitudinally aligned with the track direction is considered starting from the end point, as depicted in Figure 6.16. The rectangle lies in the yz plane because, while the track has been shifted to the cathode, the unfitted space points have not and therefore have the wrong x coordinate. If more than 10 space points are found in the rectangle, the track is rejected. The same cut applies to anode-crossing muon tagged by Pandora. For the anode-crossing muons that are not tagged by the reconstruction and therefore have the wrong drift coordinates, space points can also be searched in the xy, or equivalently xz plane, with the same criteria. Since the tagging algorithm for these additional track relies on the correct identification of

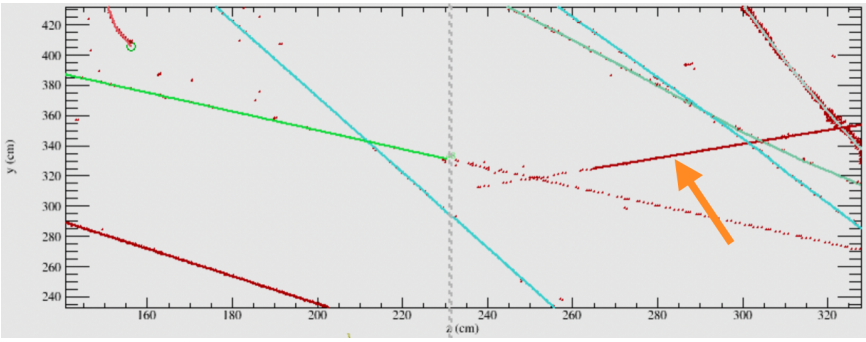


Figure 6.15: Event display of a ProtoDUNE-SP Monte Carlo event zoomed in on the region of interest in the yz plane. The red track pointed by the orange arrow is only partially reconstructed and unfitted space points (aligned red dots around the track end point) are visible. The event also contains a broken track whose reconstruction is interrupted at one of the APA gaps, indicated by the vertical grey dashed line.

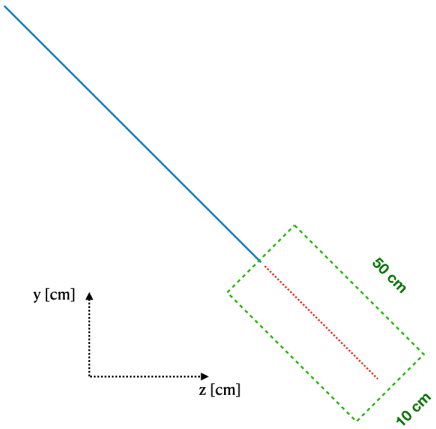


Figure 6.16: Diagram illustrating the geometry to apply the cuts on the number of nearby unfitted space points. The unfitted space points are represented by the red dotted line, the volume is shown as the green dashed rectangle.

the start point, the same strategy is applied to the track start point.

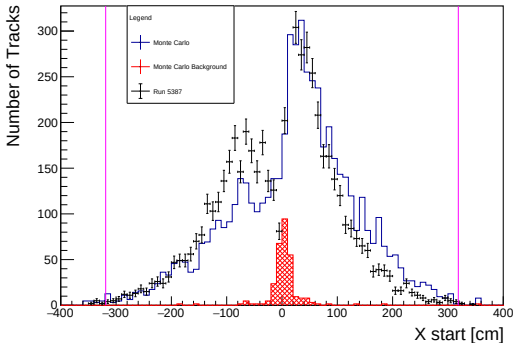
6.5 Cuts Validation

Preliminary sets of selection cuts have been identified and the track geometry has been used to remove broken tracks from the preliminary selection. So far, the cuts have been studied independently from one another, looking at the effect of one cut without applying the others. To study the overall efficacy of each cut and to optimise its position, the distributions for the variables of interest are plotted after applying

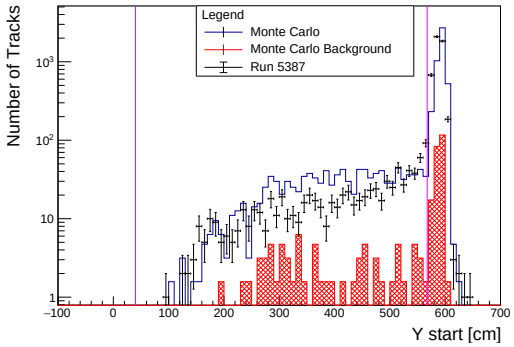
all the cuts but the one for the variable whose distribution is being plotted. These will be referred to as "N-1" plots. For each variable, the "signal" (true positives) and "background" (false positives) are identified using the Monte Carlo truth information. The definition of "signal" is a candidate track whose corresponding truth Monte Carlo particle crosses the cathode or one of the two anodes, stops in the active volume and is a cosmic muon (or anti-muon). Both distributions for any candidate track and the corresponding backgrounds are plotted at the same time. In addition, the same selection is applied to the data, in order to compare the shapes between data and Monte Carlo and validate the cuts. For this purpose, the selection is run on the events recorded during run 5387. The values for the cuts determined above are the starting point of an iterative procedure that, after updating one cut by looking at the corresponding N-1 plot, re-optimises the other cut positions one by one. The aim of the optimisation is to exclude areas with a predominant background presence. The procedure stops when all the cuts have converged to a stable value.

The N-1 plots for the spatial coordinates and hit times for cathode-crossing muons can be seen in Figures 6.17 and 6.18. Good agreement is observed between the shapes of data and Monte Carlo for the variables used, indicating that the efficiency in discriminating background in data is similar to that of Monte Carlo. The discrepancy observed in Figure 6.17a can be due to a difference between the real and simulated space charge effects or is related to the absence of fluid flow simulation which in turn can introduce differences in the t_0-tagging between MC and data, but it is not completely understood. It can also be seen that in Figure 6.17a there is a region where the background is significant around $x = 0$; tracks with a start point in that region will also be rejected. The dips in Figure 6.17f are due to the cuts on the z coordinates to remove broken track in correspondence to the APA gaps.

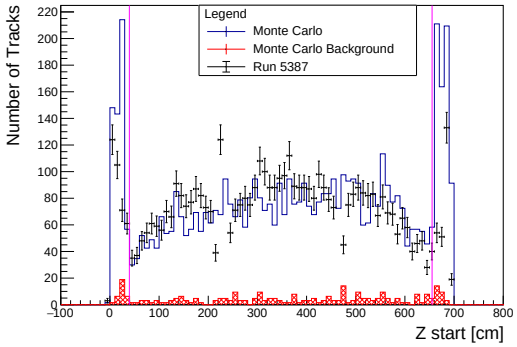
After correcting the position of the end points using the calculated t_0, the analogous plots are obtained for the anode-crossing muons, shown in Figure 6.19 and 6.20. For comparison, the plots for the end point x coordinate is shown for the selection discussed in this chapter and the tracks tagged by Pandora (Figures 6.19c and 6.19d).



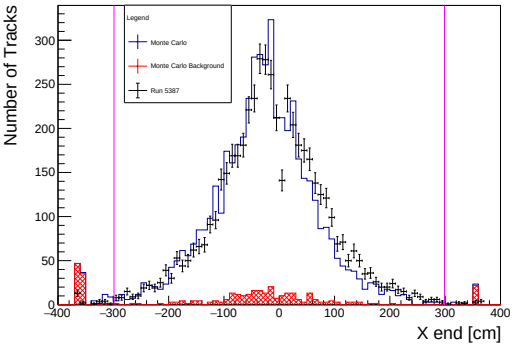
(a) Start point x distributions.



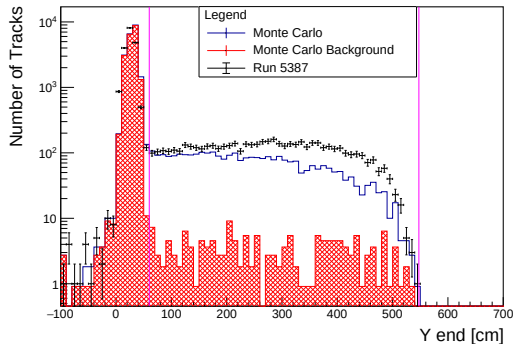
(b) Start point y distributions.



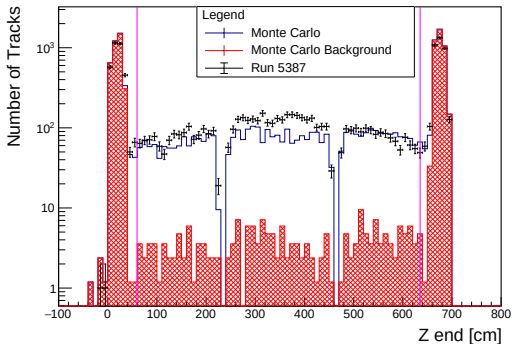
(c) Start point z distributions.



(d) End point x distributions.

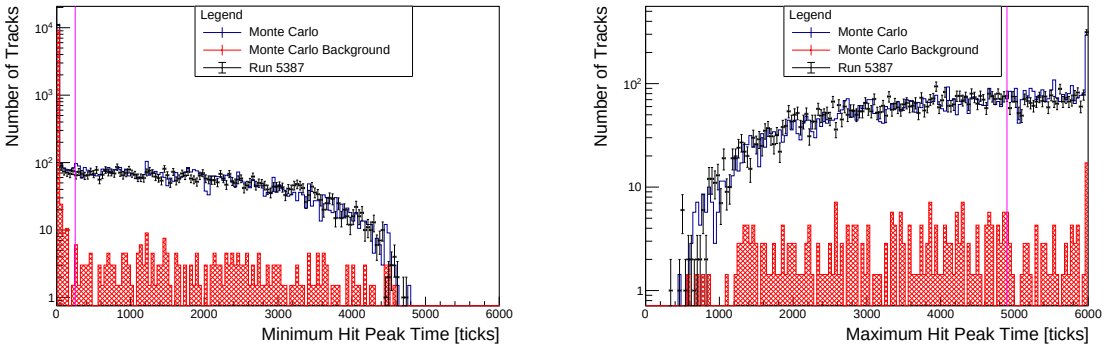


(e) End point y distributions.



(f) End point z distributions.

Figure 6.17: N-1 plots for the spatial selection of cathode-crossing stopping muons. The blue (black) histogram represents the selected track in the Monte Carlo (data). The red histogram is the Monte Carlo background. The vertical purple lines represent the chosen position for the cut. For the first three variables (start point, plot a, b, c) only the values that lie at the external of the cut position are accepted. For the last three variables (end point, plot d, e, f) the values within the two lines are accepted. The Monte Carlo histograms are scaled to the same number of tracks of the data histogram.



(a) Minimum hit peak time distributions. (b) Maximum hit peak time distributions.

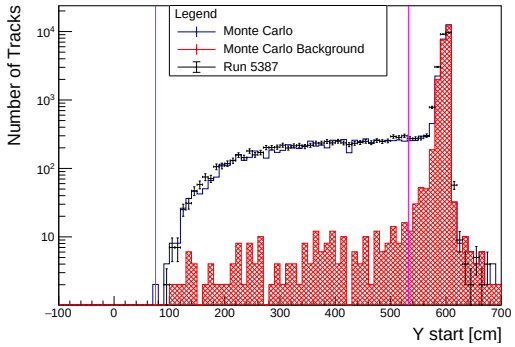
Figure 6.18: N-1 selection plots for the time selection cuts for cathode-crossing stopping muons. The blue (black) histogram represents the selected track in the Monte Carlo (data). The red histogram is the Monte Carlo background. The vertical purple lines represent the chosen position for the cut. Tracks are accepted if their minimum (maximum) hit peak time is greater (less) than the value in correspondence of the cut position. The Monte Carlo histograms are scaled to the same number of tracks of the data histogram.

It can be seen that the algorithm developed selects anode-crossing tracks more efficiently. The dips in Figures 6.19b and 6.19f are a consequence of the broken track cuts at the APA gaps.

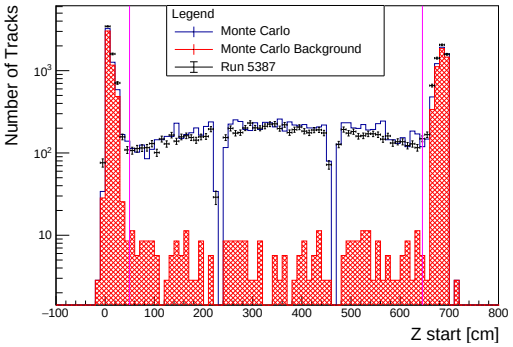
With this strategy, the procedure to determine the spatial and timing cuts to selected cathode or anode-crossing stopping muons is concluded. The agreement between the distribution shapes of data and Monte Carlo encourages to rely on these cuts for the selection of the same tracks in data. Table 6.3 and Table 6.4 summarise the numerical values for the cuts.

Table 6.3: Final cut values for cathode-crossing stopping muons.

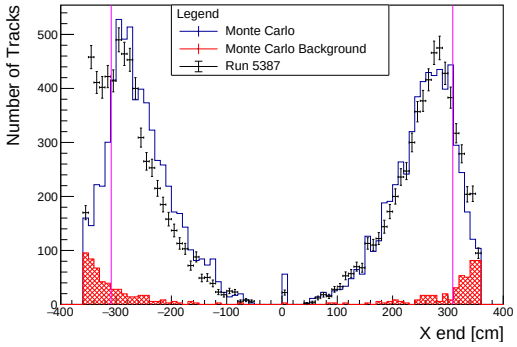
Variable	**Cut**
`Track Length`	$> 100\,\text{cm}$
`Angular Cuts`	$60^\circ < \lvert\theta_{xz}\rvert < 120^\circ$ or $60^\circ < \lvert\theta_{yz}\rvert < 120^\circ$ rejected
`Start Point`	Within 40 cm of the active volume borders
`Start` x	$\lvert\text{Start } x\rvert \geq 20$
`End Point`	More than 60 cm away from the active volume borders
`Minimum Hit Peak Time`	Greater than 250 ticks
`Maximum Hit Peak Time`	Less than 4900 ticks



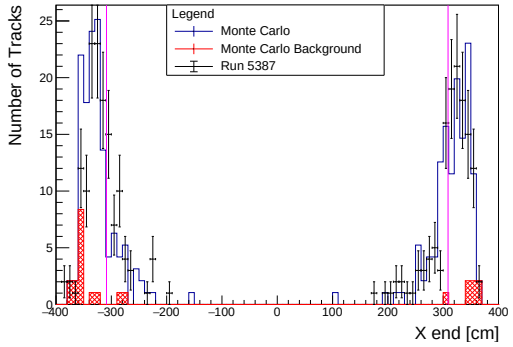
(a) Start point y distributions.



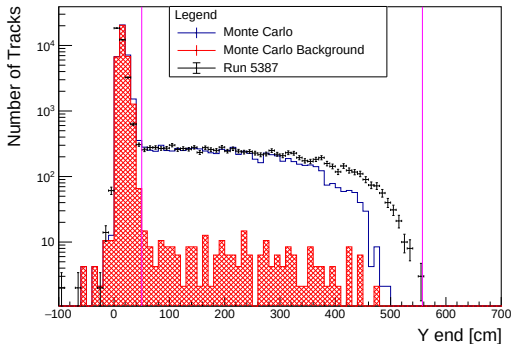
(b) Start point z distributions.



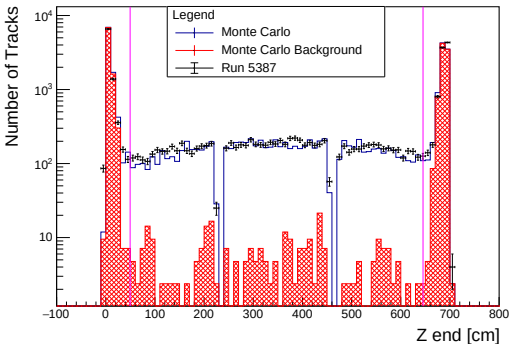
(c) End point x distributions (own selection).



(d) End point x distributions (Pandora selection).

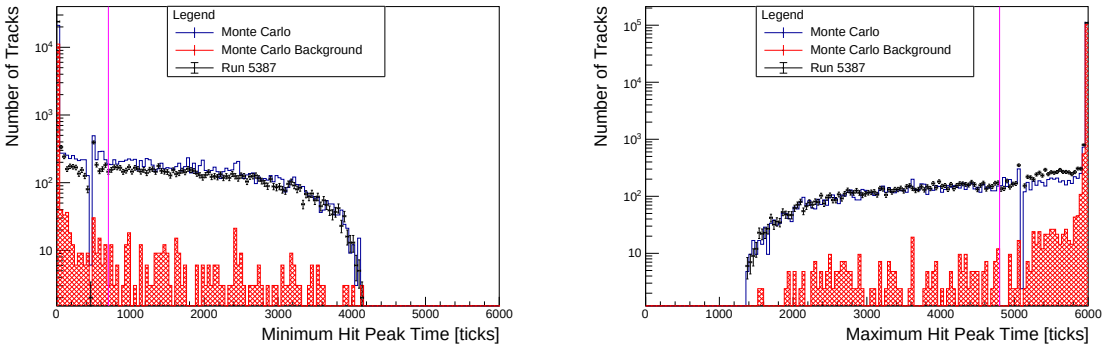


(e) End point y distributions.



(f) End point z distributions.

Figure 6.19: N-1 plots for the spatial selection of anode-crossing stopping muons. The blue (black) histogram represents the selected track in the Monte Carlo (data). The red histogram is the Monte Carlo background. The vertical purple lines represent the chosen position for the cuts. The accepted regions are contained between the two vertical lines.



(a) Minimum hit peak time distributions. (b) Maximum hit peak time distributions.

Figure 6.20: N-1 selection plots for the time selection cuts for anode-crossing stopping muons. The blue (black) histogram represents the selected track in the Monte Carlo (data). The red histogram is the Monte Carlo background. The vertical purple lines represent the chosen position for the cut. Tracks are accepted if their minimum (maximum) hit peak time is greater (less) than the value in correspondence of the cut position. The Monte Carlo histograms are scaled to the same number of tracks of the data histogram.

Table 6.4: Final cut values for anode-crossing stopping muons.

Variable	**Cut**
`Track Length`	> 100 cm
`Angular Cuts`	$60^\circ < \lvert\theta_{xz}\rvert < 120^\circ$ or $60^\circ < \lvert\theta_{yz}\rvert < 120^\circ$ rejected
`Start Point Y`	More than 75 cm from the active volume borders
`Start Point Z`	More than 50 cm from the active volume borders
`End Point`	More than 50 cm away from the active volume borders
`Minimum Hit Peak Time`	Greater than 700 ticks
`Maximum Hit Peak Time`	Less than 4800 ticks

6.6 Summary of the Selected Sample

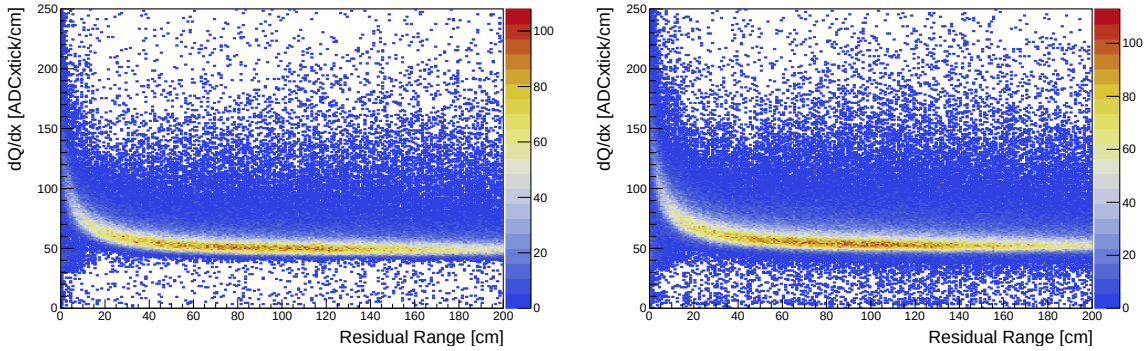
After applying the cuts, the quality of the selection is assessed by calculating the purity. The purity expresses what fraction of the selected tracks is correctly identified and is defined as

$$\text{Purity} = \frac{\text{Number of true cathode-crossing stopping muons selected}}{\text{Total number of tracks selected}} \tag{6.4}$$

for cathode-crossing muons and

$$\text{Purity} = \frac{\text{Number of true anode-crossing stopping muons selected}}{\text{Total number of tracks selected}}. \tag{6.5}$$

for anode-crossing muons. The purity is found to be 99% and 98% respectively. Some background is due to broken tracks that are not identified and from tracks that are not associated to a muon. The selection efficiency, defined as the fraction of stopping muons correctly selected with respect to the total number of muons crossing the cathode or the anode is of the order of 7% and 8% for cathode and anode crossing muons respectively. Figure 6.21 shows the reconstructed dQ/dx as a function of the reconstructed residual range for the selected anode-crossing tracks in both Monte Carlo and data. The characteristic Bragg peak near the stopping point and the qualitative agreement between Monte Carlo and data support the quality of the selection cuts.



(a) Monte Carlo. (b) Data (run 5387).

Figure 6.21: Reconstructed dQ/dx as a function of the residual range for the selected anode-crossing muons for both Monte Carlo and data. The corrections for detector uniformity response and electron lifetime are not applied.

The effort of developing a selection for anode-crossing tracks is not only justified by the increase in the number of t_0-tagged tracks that can be used for any calibration studies, but it also enables to study the response and calibration in a section of the detector that would otherwise be unexplored by the sole cathode-crossing tracks. Figure 6.22 shows the position of the hits of the combined samples in the xy plane. It can clearly be seen that cathode-crossing tracks only span the volume around $x = 0$, due to the cosmic rays arriving at a small zenith angle. The addition of anode-crossing tracks allows to explore the response at low drift distances.

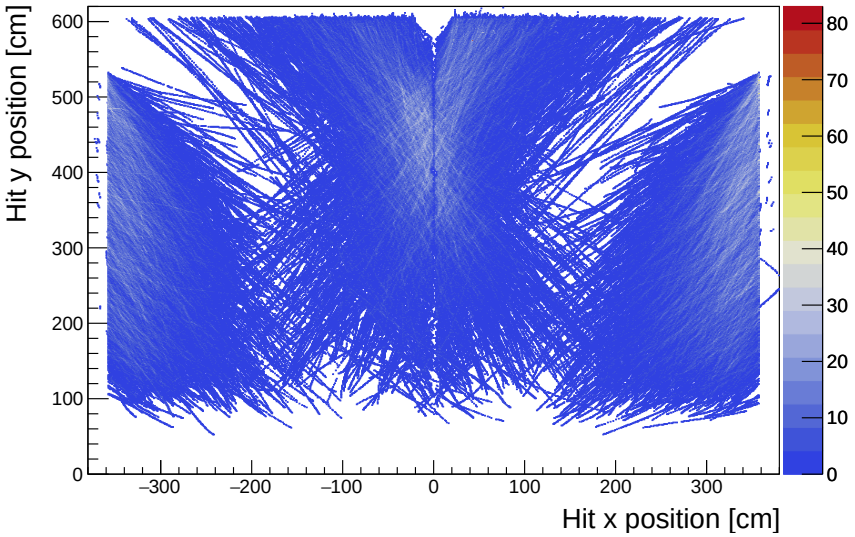


Figure 6.22: Hit positions in the xy plane for cathode and anode-crossing tracks in data.

Finally, a comparison between the calculation of the t_0 in data and Monte Carlo is shown for both samples in Figure 6.23. By virtue of the very different drift time that characterises the hits of the two types of topology, the t_0 distributions are well separated. In particular, most of the reconstructed cathode-crossing particles enter the TPC before the time window is opened but, because of the long drift distance, they are recorded in the readout.

A selection of cosmic stopping muons in ProtoDUNE-SP has been achieved with high purity. However, the high purity does not guarantee that the dQ/dx towards the end of the track is correctly reconstructed, as false stoppers are still present in

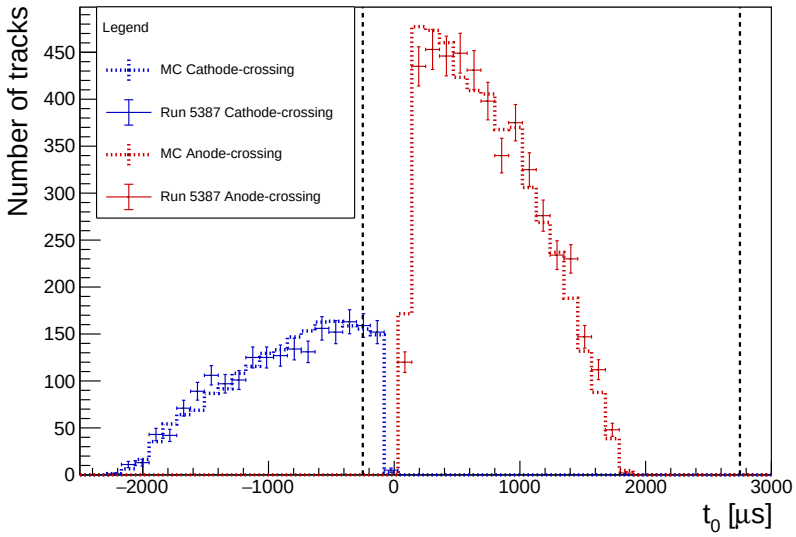


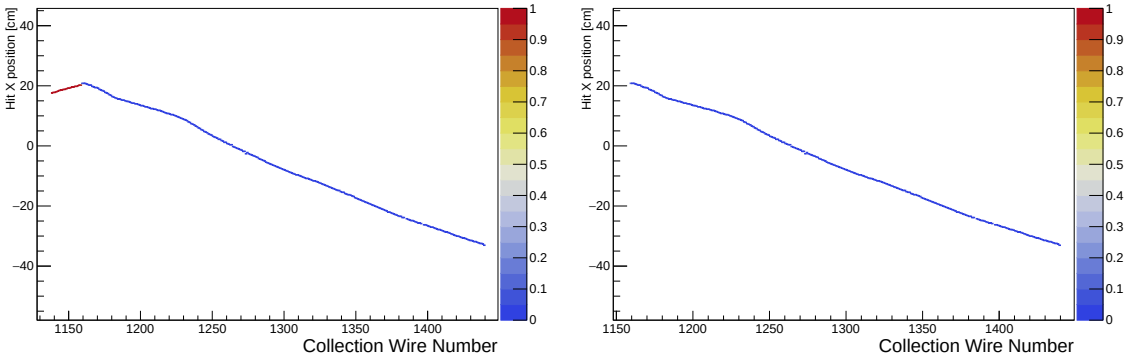
Figure 6.23: Calculated t_0 for cathode (blue) and anode-crossing (red) stopping muons in both Monte Carlo and data. The black vertical lines are the boundaries of the acquisition window.

the selection and Michel electron hits can be mistakenly incorporated in the track hits. Additionally, the end point might not be reconstructed with sufficient accuracy, leading to an incorrect reconstruction of the residual range. To use the sample of cosmic muons as a source of different value of dE/dx by varying the residual range, these effects need to be mitigated.

6.7 Michel Electron Contamination

Michel electrons are reconstructed as a short track near the muon stopping point. The contamination of Michel electron hits in the selected stopping muons needs to be mitigated since it would affect the reconstruction of the residual range. The point with residual range of 0 cm will be at some position on the Michel track, therefore shifting the residual range values at any other point as well as the predicted dE/dx. The presence of such reconstruction imperfections was investigated in the Monte Carlo by considering the hits on the collection plane for each track in the sample of selected muons. Different particles can in principle contribute to the same hit in terms of energy deposition. For example, this can happen when two tracks cross each other

or near the interaction or decay point. The simulation allows to extract the list of particles that contribute to a given hit, and verify how much energy deposited from each particle has resulted in the charge associated to that hit. Figure 6.24a shows the hits on the collection plane for a particular selected track. The colour scale indicates the fractional energy contribution to each single hit that came from an electron. It can be seen that a series of hits are due to the energy deposition of an electron. Those hits form a secondary small track at an angle with the primary muon trajectory. The reconstruction is mistakenly assigning those hits to the muon track.



(a) (b)

Figure 6.24: Hits on the collection wires for a selected stopping muon before (left) and after (right) the Michel hits are removed. The color scale represents the energy contribution coming from an electron to each hit. The collection wire number does not correspond to a TPC readout channel and follows a different numbering scheme implemented to better display the event. The hit x position was obtained after correcting for t_0 (notice that this is a cathode-crossing muon).

To identify Michel hits, the output of a Convolutional Neural Network (CNN), developed in [94], was used. The CNN is trained to assign to each hit a score from 0 to 1 expressing the likelihood that the hit is a Michel hit. The higher the score, the more confident the CNN is in its tagging. The score for the hits corresponding to a sample of stopping muons in both data and Monte Carlo can be seen in Figure 6.25.

From Figure 6.25 it can be seen that the CNN score presents an excess of events at around 1, indicating that the CNN is identifying some hits as coming from a Michel electron. In Figure 6.26, the sample of MC hits is divided in hits with an energy contribution of greater and less than 50% coming from an electron. Figure 6.26

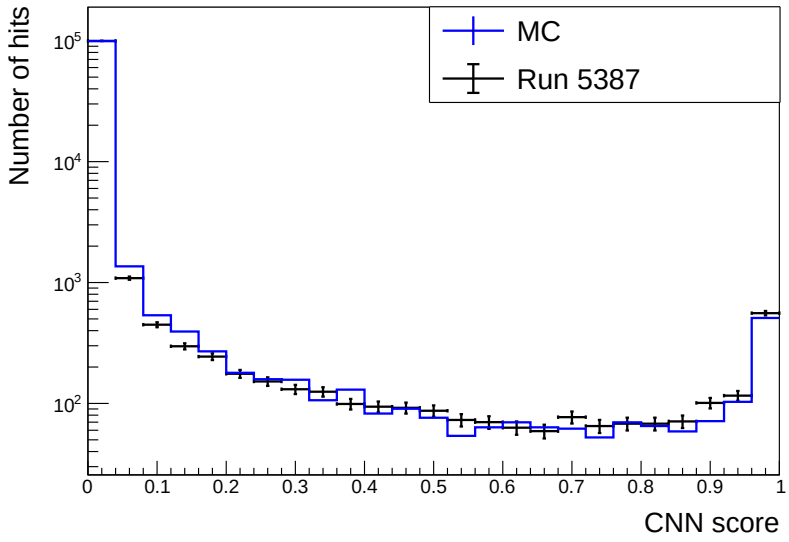


Figure 6.25: CNN score for stopping muon hits in data (run 5387) and Monte Carlo. The Monte Carlo histogram is scaled to the number of events in the data histogram.

shows that the hits with a high CNN score are indeed those with the majority of the energy contribution coming from electron energy depositions.

The hits on the collection plane are sorted based on their distance from the uppermost hit, corresponding to the start point. The method then scans through the list of ordered hits looking for the first hit with a score higher than or equal to 0.7. When such hit is found, the next 5 hits are considered and their scores are averaged. If the average score is less than 0.5, the method continues to scan the hits until it reaches the end or finds another hit with a score $\geq$ 0.7. Otherwise, the track is tagged as being contaminated from Michel hits. Figure 6.24b shows the same track of Figure 6.24a after the Michel hits are identified and removed. For simplicity, the contaminated tracks are removed from the selection.

6.8 dE/dx Shape Discriminator

After removing tracks that contain Michel electron hits, the sample can still be contaminated by tracks whose end point is not correctly reconstructed. These are broken tracks for which only the few tens of centimetres are missing and therefore are correctly identified as stopping but, since the last section is missing, the residual range

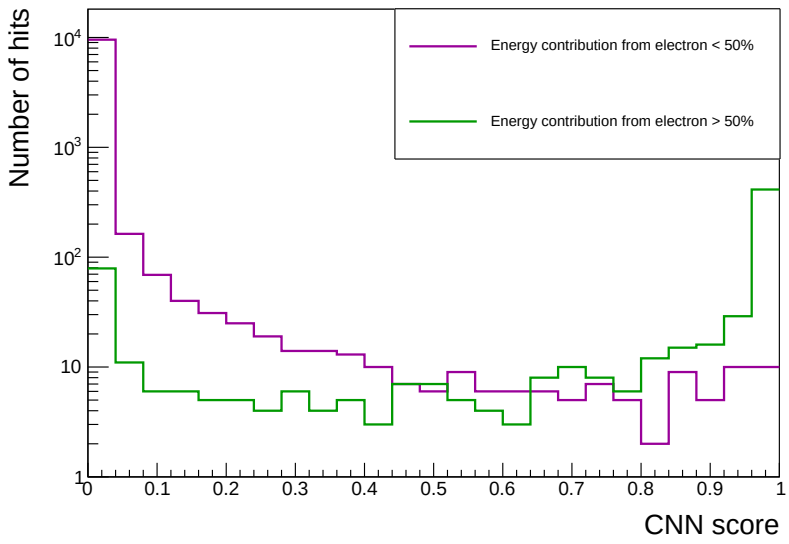


Figure 6.26: CNN score distributions for stopping muon hits in Monte Carlo and for different electron energy contribution.

is inexact. Tracks from other particles other than muons are also present in the sample. To exclude these tracks from the selection, a procedure aimed at comparing the dQ/dx of any given track with that of a true stopping muon was developed.

The stopping power as a function of the residual range was obtained from [133] and the data points can be seen in Figure 5.3b. The points are interpolated with a cubic spline S_{interp} in order to obtain an analytical function instead of discrete data points. On a track by track basis, the dQ/dx from each hit is corrected for detector effects, including space charge effects and drifting electron lifetime. The residual range is corrected for space charge distortions. More details on the corrections applied will be given in Section 6.9. To compare with the expected S_{interp} shape, the corrected $(dQ/dx)_{\text{corr}}$ needs to be converted to dE/dx. This is achieved by assuming the modified box model with the parameters measured by ArgoNeuT [97]:

$$\frac{dE}{dx} = \left(\exp\left(\frac{\left(\frac{dQ}{dx}\right)_{\text{corr}}}{C_{\text{cal}}} \frac{\beta'_{\text{Argo}} W_{\text{ion}}}{\rho \mathscr{E}} \right) - \alpha_{\text{Argo}} \right) \left(\frac{\rho \mathscr{E}}{\beta'_{\text{Argo}}} \right), \tag{6.6}$$

where C_{cal} is taken to be 0.001 ADCxtick/e, the nominal electronics gain. The electric field $\mathscr{E}$ is calculated at the location of each hit by using the space charge calibration maps described in Chapter 3.

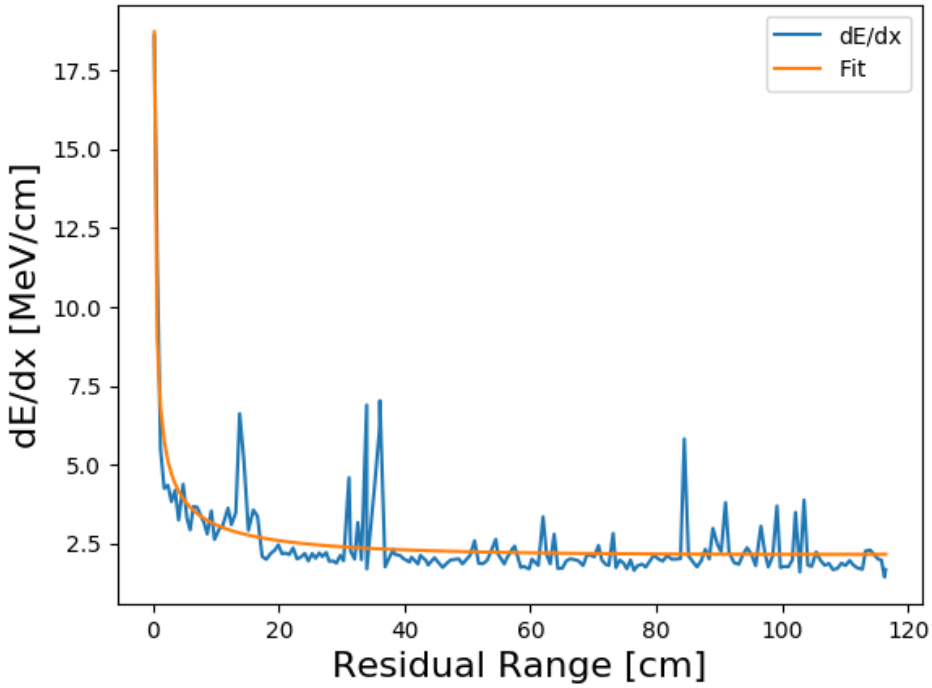


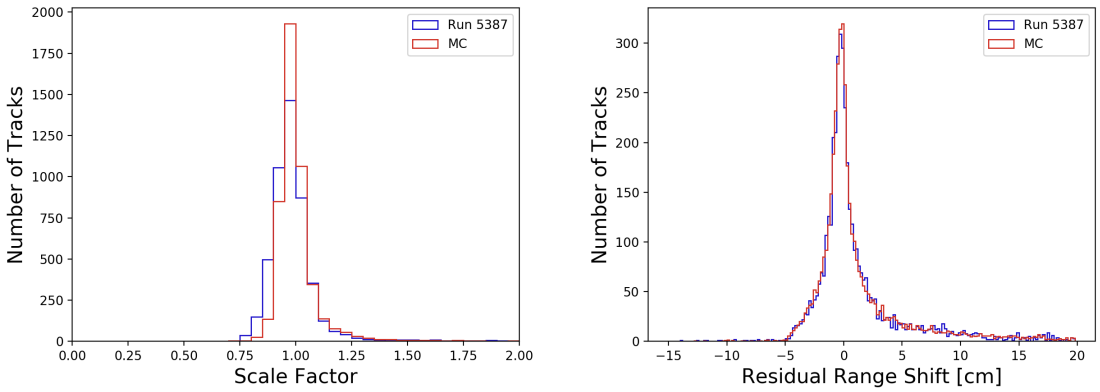
Figure 6.27: Fit to the theoretical dE/dx shape as a function of the residual range for a well reconstructed anode-crossing stopping muon in data. The hit dE/dx values are in blue, the fit function is in orange.

To study the agreement of the calculated dE/dx so defined with the theoretical calculations of [133], a fit function is defined as:

$$f_{\text{fit}} = p_0 \cdot S_{\text{interp}}(x + p_1), \tag{6.7}$$

where p_0 is a scale factor and p_1 is a parameter that measures the residual range offset of the track under scrutiny. If there is good agreement between the predicted and calculated shapes, it is expected that $p_0 \simeq 1$ and $p_1 \simeq 0$. Some quality cuts on the reconstructed hits are performed to eliminate hits with spurious dE/dx values. In addition, hits at the end of the track are cropped if their dE/dx is smaller than the dE/dx of other hits in the last 5 cm. Finally, for each selected stopping muon candidate a fit of the dE/dx vs residual range is performed with f_{fit} of Equation 6.7 to extract the parameters. An example of fit for a well reconstructed anode-crossing muon in data can be seen in Figure 6.27. It is interesting to look at the distributions

of the fit parameters for all the tracks in the selection. Figure 6.28 shows the two distributions for the sample of selected anode-crossing muons in data and Monte Carlo. It can be seen that both p_0 and p_1 are centered around the expected values for a stopping muon, but the distributions for the residual range shift present a tail on the right-hand side. High values of the residual range shift suggests that the track is misreconstructed as the dE/dx theoretical curve S_{interp} needs to be shifted beyond the end of the track to accommodate the data. In principle, it would be possible to use the fit results to correct the residual range calculation. However, by doing so the data would be biased towards the particular recombination model and parametrisation assumed to calculate the dE/dx for each hit. The next chapter will present a study of recombination models and parametrisation that exploits the stopping muons selected with this procedure. It was therefore decided to not apply the correction to the residual range, but to use the value of p_1 as determined by each fit only for identifying the tracks well reconstructed. Therefore, a track is rejected if the p_1 resulting from the fit is such that $|p_1| > 5\,\text{cm}$.

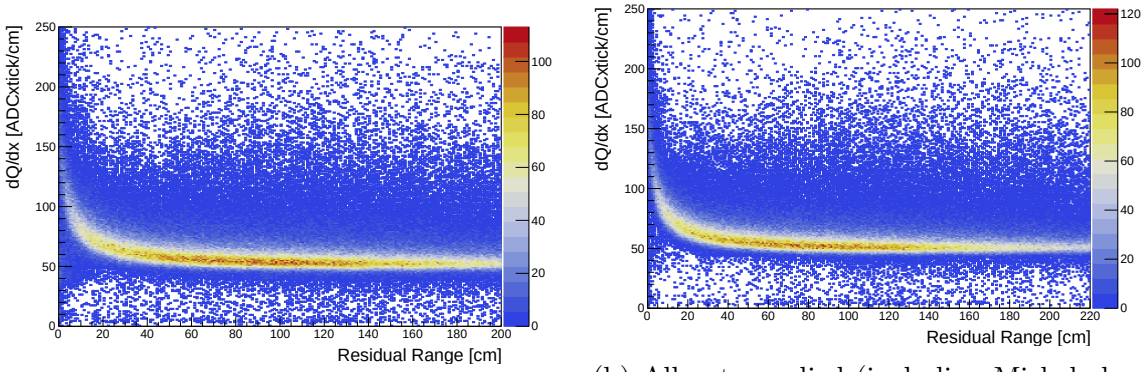


(a) Scale factor (p_0). (b) Residual range shift (p_1).

Figure 6.28: Distributions of the scale factor (p_0, left) and the shift in the residual range (p_1, right) for each track in the sample of anode-crossing stopping muons in MC (red) and data (blue). The MC histograms are scaled to the number of entries of the data histograms.

To conclude this section, a qualitative comparison of the dQ/dx before and after the cuts on the Michel electron hits and the shift in the residual range are applied is

shown in Figure 6.29. Importantly, the are fewer hits at low residual range and low dE/dx.



(a) With spatial and hit time cuts.

(b) All cuts applied (including Michel electrons hits and dE/dx shape).

Figure 6.29: Reconstructed dQ/dx as a function of the residual range for the selected anode-crossing muons for data. Left: with only spatial and hit time cuts. Right: all cuts applied.

6.9 Sample Preparation

The procedure described in this chapter achieves a selection of t_0-tagged cosmic-ray muons with high purity. The selected sample will be used to perform electron-ion recombination studies, and will make use of the measured dQ/dx and residual range for each hit. Both quantities need to be corrected for detector effects. The residual range is obtained by summing the distance between consecutive space points and it is therefore affected by the space charge spatial distortion. The space point position is corrected using the space charge map (discussed in Section 3.10) before calculating the residual range. The dx for each hit is again affected by the spatial distortion and corrected for in the same way. During the drift, some of the electrons are lost due to the attachment to impurities. This effect is corrected for in both Monte Carlo and data, using the simulated and measured electron lifetime respectively, according to Equation 3.1. The electron lifetime is 35 ms in the Monte Carlo, while for data it can vary due to a number of circumstances. Lastly, the overall dQ/dx is corrected for any

other detector effect using the calibration factors and Equation 3.5. Each factor in Equation 3.5 was calculated for both Monte Carlo and data independently [62].

Since the correction factors depend on the 3D position of the hits, they can only be applied correctly if the t_0 of the track is known. They are always applied automatically by the reconstruction algorithm, but for out-of-time tracks that are not t_0-tagged by the algorithm itself the correction factors are wrong, since they are based on the assumption that $t_0 = 0$. Therefore, for each anode-crossing muon selected the x position of the hits is re-calculated accordingly and the corrections are then applied with the revised hit 3D position as input.

Chapter 7

Electron-Ion Recombination Studies

Contents

7.1 Introduction 125
7.2 Monte Carlo Study 126
7.2.1 Simulating Angular Effects 126
7.2.2 Methodology 129
7.2.3 Fit Results 132
7.3 Validation of Method on the ProtoDUNE-SP Monte Carlo 135
7.4 Extracting Recombination Model Parameters 136
7.4.1 Angular Dependence 141
7.5 dE/dx Calculation 145
7.6 Discussion on Systematic Uncertainties 146
7.6.1 Selection Cuts, Reconstruction and Space Charge Effects . 147
7.6.2 Electron Lifetime Measurement 151
7.6.3 Determination of the Calibration Constant C_{cal} 153
7.6.4 Effect of δ-rays 155
7.7 Conclusion 156

This chapter will illustrate the procedure developed to extract the parameters of different electron-ion recombination models in liquid argon and its main results. Section 7.1 will give a brief introduction on the main analysis tools and preliminary ideas. Section 7.2 contains the description of a Monte Carlo simulation developed to study the recombination and to establish an algorithm to measure the simulated recombination parameters. The sensitivity of the procedure to the track direction is

also assessed. In Section 7.3, the method is then tested on the official ProtoDUNE-SP Monte Carlo with the sample of cosmic muons selected as described in Chapter 6. The core of the chapter is Section 7.4, in which the recombination parameters are measured using ProtoDUNE-SP data, exploring both cases with and without angular dependence in the recombination models. In Section 7.5 the dE/dx for stopping muons will be calculated using two different recombination models and the results will be compared with the theoretical expectations. A discussion on the systematic uncertainties is contained in Section 7.6. Finally, Section 7.7 will summarise the main findings.

7.1 Introduction

The sample of stopping muons obtained through the procedure described in the previous chapter can be used to study how the measured dQ/dx varies as a function of the muon energy loss dE/dx by using the residual range as a proxy to link the measured hit positions to the true dE/dx. In addition, cosmic muons enter the ProtoDUNE-SP detector from different directions, allowing to study this effect for tracks that come at different angles. This has the potential to provide insights on the recombination dependence on the angle ϕ between the track direction and the electric field, as advanced by Jaffe's theory (discussed in Section 4.4). When the measured dQ/dx is properly corrected for all the detector effects, it is expected that its dependence across the muon trajectory is solely due to the muon dE/dx varying along the trajectory, the local electric field at each hit position and, hypothetically, the angle ϕ. These parameters affect the rate of electron-ion recombination in a non-linear fashion.

Muons in ProtoDUNE-SP can travel several meters before stopping. The significant extent of the external electric field distortions, in both magnitude and direction, means that the electric field vector can be substantially different at different points along a track. Even a perfectly straight track will have different values for ϕ associated with each hit, given the distortions introduced by the space charge effects. Additionally, the muon trajectory tends to be more affected by multiple coulomb

scattering towards the end, which coincide with the most interesting region where the dE/dx variation is more accentuated. These considerations need to be taken into account when splitting the sample of stopping muons in angular bins and suggest that a "hit-by-hit" approach is to be preferred to a track-basis one when looking at the angular and electric field modulation.

For this study, only the hits on the collection plane, which exhibit the highest signal-to-noise ratio, will be used. The main ingredients are the hit 3D positions, the corrected dQ/dx (with the procedure in Equation 3.5) and the measured residual range values.

7.2 Monte Carlo Study

The method to extract the recombination parameters was developed on a custom-generated Monte Carlo sample of stopping muons. Each muon is simulated in its own acquisition window so to minimise reconstruction inefficiencies due to a busy environment. The generation point is distributed uniformly across the whole TPC volume, and the direction angles θ_{xz} and θ_{yz} are also uniformly distributed. This, combined with a constant initial momentum of $0.8\,\mathrm{GeV}/c$, implies that not all the muon trajectories are contained in the detector. The Monte Carlo truth information is used to select tracks that are contained and not broken.

7.2.1 Simulating Angular Effects

The main reason that motivates the generation of these additional simulated events is the fact that the original ProtoDUNE-SP Monte Carlo does not contain any angular dependence for the recombination. This was included in the custom Monte Carlo in the following way. At each GEANT4 step, the energy deposited E_{dep} is considered together with the coordinates of the start, middle and end position of the step. The electric field direction $\vec{\mathscr{E}}/|\vec{\mathscr{E}}|$ in correspondence of the step middle point is obtained using the space charge data-driven map. Similarly, the GEANT4 step direction $\vec{ds}/|\vec{ds}|$ is calculated using the coordinates of the end and the start points.

The angle ϕ between the electric field and the step direction is therefore obtained through

$$\phi = \arccos\left(\frac{\vec{\mathscr{E}} \cdot \vec{ds}}{|\vec{\mathscr{E}}||\vec{ds}|}\right). \tag{7.1}$$

The recombination factor is modelled like in the ProtoDUNE-SP original Monte Carlo, with the added angular dependence obtained by replacing $\mathscr{E}$ with $\mathscr{E}\sin\phi$:

$$\mathscr{R}_{\mathrm{MC}} = \frac{1}{\frac{\beta'}{\rho\mathscr{E}\sin\phi}\frac{dE}{dx}} \ln\left(\alpha + \frac{\beta'}{\rho\mathscr{E}\sin\phi}\frac{dE}{dx}\right), \tag{7.2}$$

where the parameters in the formula are those of the modified box model as measured by ArgoNeuT (Table 4.2). The added angular dependence can be used to verify the sensitivity of the parameter extraction procedure. Finally, the number of electrons N_e that are free to drift towards the anode are calculated as

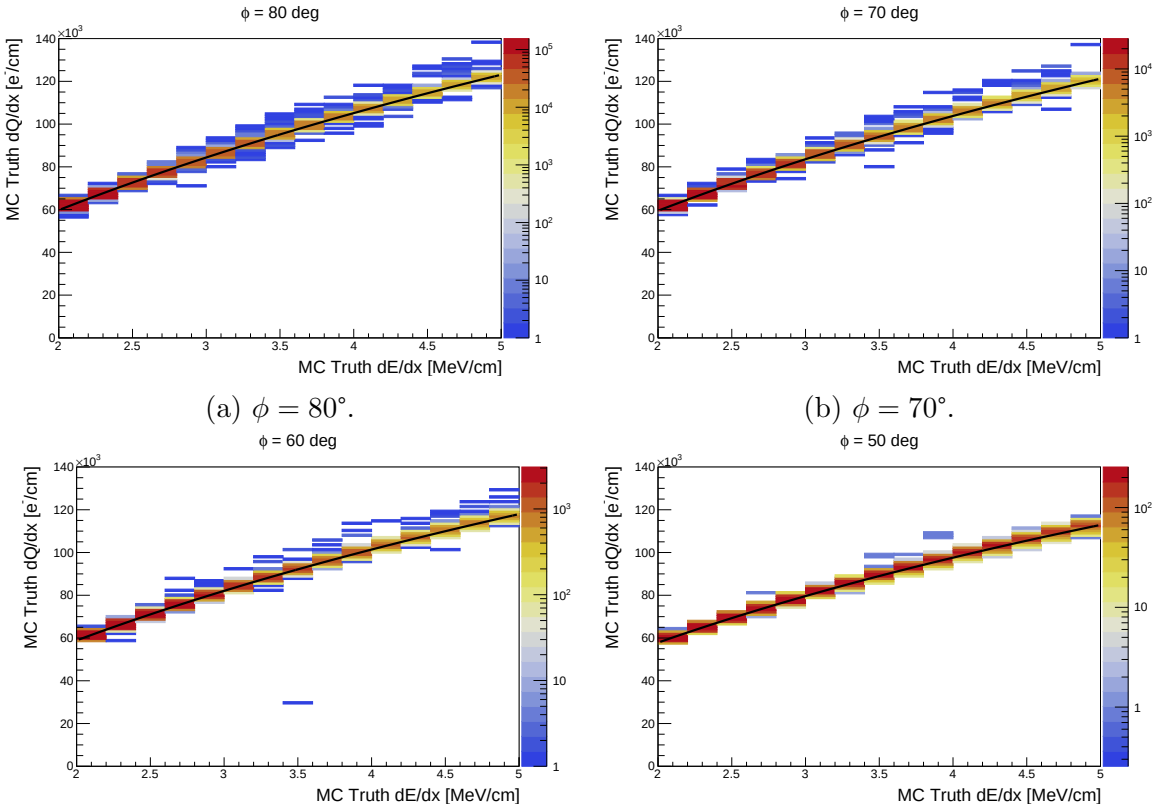
$$N_e = \mathscr{R}_{\mathrm{MC}} \cdot \frac{E_{\mathrm{dep}}}{W_{\mathrm{ion}}}. \tag{7.3}$$

The simulation of detector effects and the reconstruction algorithms are identical to those used in the official Monte Carlo.

A sanity check is performed to ensure that the behaviour of Equation 7.2 and 7.3 is correctly simulated and the angle ϕ calculation is accurate. For each step, the simulated dE/dx and dQ/dx are calculated by dividing the E_{dep} and N_e respectively by the step length. To compare with the analytical formula of Equation 7.2, four angular bins, 80°, 70°, 60°, 50°, are chosen. Only steps in a region in which $\mathscr{E} = (500 \pm 5)$ V/cm are selected. The resulting plots for the simulated charge dQ/dx as a function of the energy deposited per unit length dE/dx are shown in Figure 7.1 for each angular bin. The black lines on each plot represent the formula

$$\frac{dQ}{dx} = \frac{dE}{dx} \cdot \frac{1}{W_{\mathrm{ion}}} \cdot \mathscr{R}_{\mathrm{MC}}, \tag{7.4}$$

with the appropriate values of ϕ and $\mathscr{E}$. The good agreement between the simulated behaviour and the theoretical formula indicates that the theoretical model was simulated correctly.



(a) $\phi = 80°$.

(b) $\phi = 70°$.

(c) $\phi = 60°$.

(d) $\phi = 50°$.

Figure 7.1: Comparison of the simulated true dQ/dx as a function of dE/dx with Equation 7.4 (black line). The Monte Carlo steps located where the electric field value is $\mathscr{E} = (500 \pm 5)$ V/cm are sorted into angular bins of 80°, 70°, 60°, 50°.

7.2.2 Methodology

The next step is to establish a procedure to reconstruct the values of the modified box model parameters α and β' used in the simulation. The same angular cuts on θ_{xz} and θ_{yz} described in Tables 6.3 and 6.4 are applied. The location of the reconstructed 3D hits is used to calculate the local direction along the reconstructed tracks. At the location of the i-th hit $(x_i^{\mathrm{h}}, y_i^{\mathrm{h}}, z_i^{\mathrm{h}})$ the direction $\vec{n}_i$ of the track is given by

$$\vec{n}_i = (x_i^{\mathrm{h}}, y_i^{\mathrm{h}}, z_i^{\mathrm{h}}) - (x_{i-1}^{\mathrm{h}}, y_{i-1}^{\mathrm{h}}, z_{i-1}^{\mathrm{h}}) \quad \text{for } i \geq 1. \tag{7.5}$$

It is also imposed that $\vec{n}_0 \equiv \vec{n}_1$, with $i = 0$ the index of the first hit of the track, coinciding with the start point. Every muon track in the simulation is generated at $t_0 = 0$, therefore the shift correction is not needed. The electric field at each point is obtained using the space charge correction maps $\vec{\mathscr{E}}_i = \vec{\mathscr{E}}_{\mathrm{map}}(x_i^{\mathrm{h}}, y_i^{\mathrm{h}}, z_i^{\mathrm{h}})$. The angle ϕ_i for each hit is thus calculated in analogy with Equation 7.1:

$$\phi_i = \arccos\left(\frac{\vec{n}_i \cdot \vec{\mathscr{E}}_i}{|\vec{n}_i||\vec{\mathscr{E}}_i|}\right). \tag{7.6}$$

The hits are then sorted in four angular bins based on the value of ϕ_i: 80°, 70°, 60°, 50° with a 10° width. The distribution of ϕ_i can be seen in Figure 7.2, where the red vertical lines indicate the borders of the chosen angular intervals.

For each hit, the dQ/dx is considered. To compare the dQ/dx as a function of the dE/dx for each angular bin, the residual range is used as a proxy to extract the theoretical dE/dx. The simulation of stopping muons presented in Section 5.4 can be used to relate the residual range to either the most probable or the mean value of dE/dx and both options were explored. In the first case, given the dependence of the most probable value on the thickness of the material crossed or, in other words, the track pitch dx, the simulation was run for different values of the track pitch, in the same way described in Section 5.4. The dE/dx is then obtained for each hit based on the residual range and the track pitch. In the second case, the mean does not depend on the argon thickness, and therefore the map of Figure 5.10 can be used directly regardless of the track pitch. In both cases, the hits are further divided into

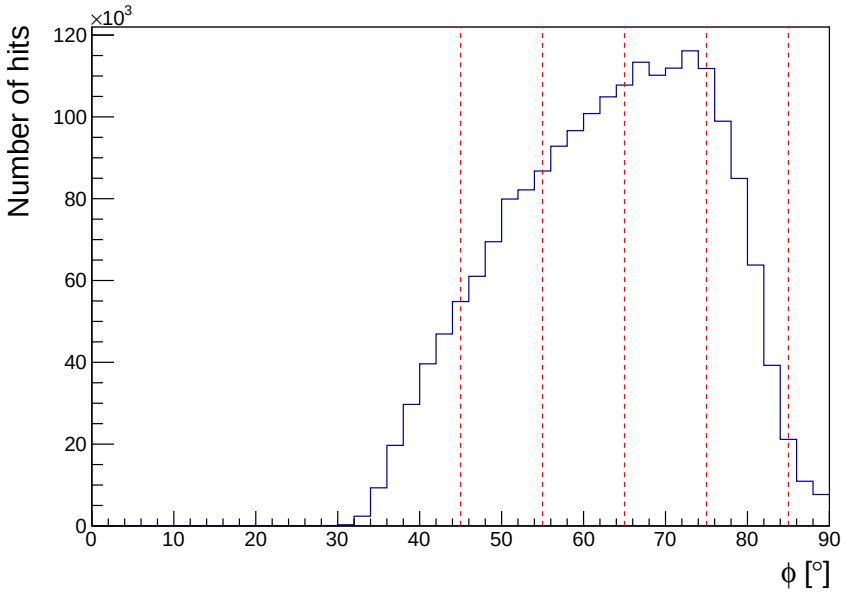


Figure 7.2: Distribution of the angle ϕ for each reconstructed hit in the generated Monte Carlo sample. The red vertical lines represent the border for the angular intervals chosen for the study.

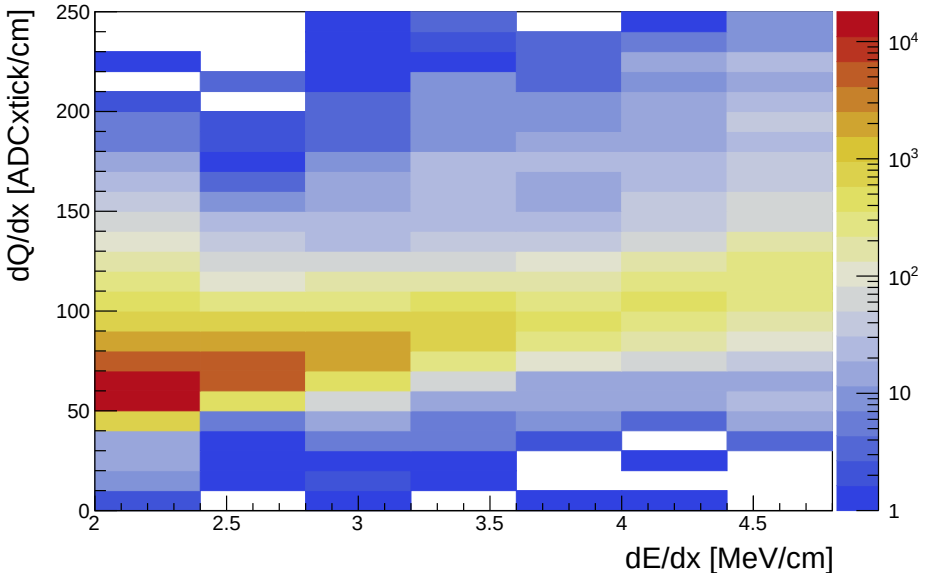
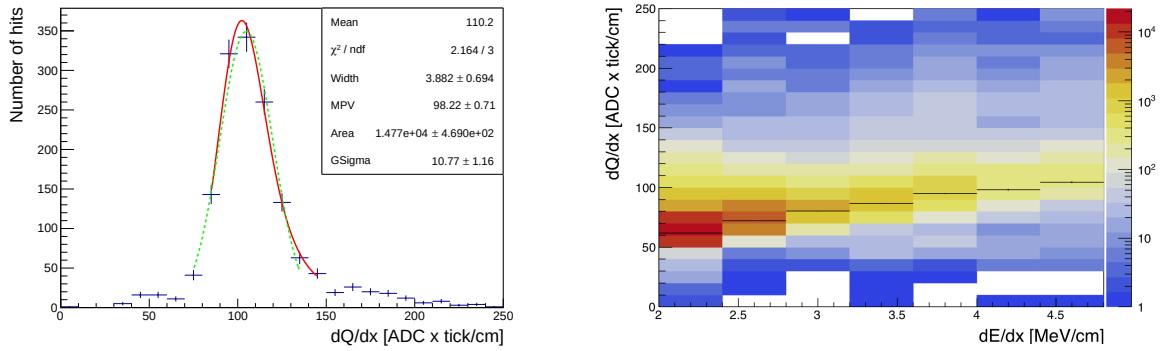


Figure 7.3: Charge per unit length (dQ/dx) for each hit vs. the expected theoretical mean dE/dx calculated using the residual range. The colour scale represents the number of entries. The plot is shown for the angle $\phi = 80°$.

dE/dx bins, as shown in Figure 7.3 for the case of the mean dE/dx and $\phi = 80°$. The representative dQ/dx value of each dE/dx bin is extracted accordingly by looking for the most probable or mean dQ/dx. To obtain the most probable value, a fit in each vertical slice is performed using a convoluted Landau and Gaussian function [139]. The Landau curve is used to retrieve the most probable value, while the Gaussian spread accounts for detector smearing effects. An example of a fit and the results for $\phi = 70°$ are shown in Figure 7.4. The mean dQ/dx is simply the mean of the

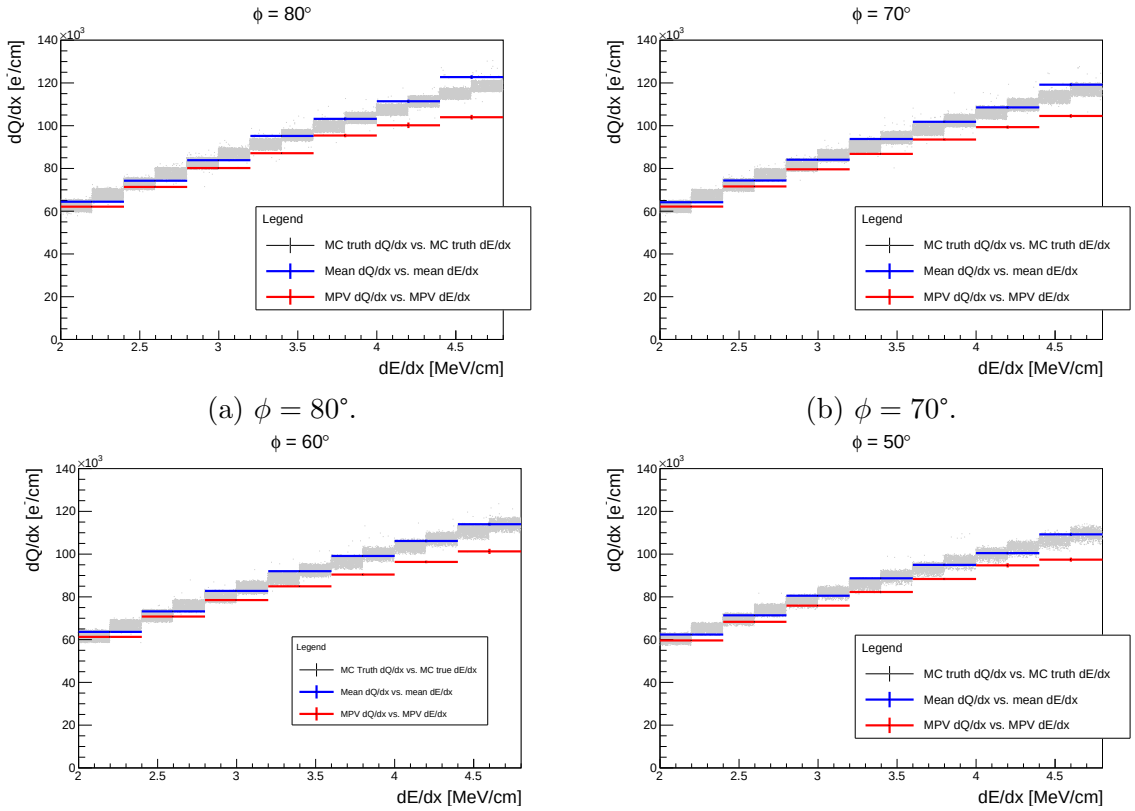


(a) (b)

Figure 7.4: Example of fit to the most probable value with a convoluted Landau and Gaussian function (left) and fit to the most probable value results in each dE/dx bin for $\phi = 70°$ (right) represented by the black histogram. On the left-hand side the green curve represents a preliminary Gaussian fit to the peak of the distribution. The mean of the green Gaussian is used to initialise the most probable value for the Landau distribution in the convoluted fit function shown in red.

entries for each dE/dx and ϕ bin. To understand which of the two calculations for the representative values of dQ/dx and dE/dx give the most accurate results, both techniques are compared with the Monte Carlo truth shape of Figure 7.1. This comparison is illustrated in Figure 7.5 for each angular bin. The grey dots represent the histograms of Figure 7.1, where the colour scale has been removed since it is irrelevant, and both the behaviours of the mean and the most probable values are shown in blue and red respectively. To obtain such plots, the dQ/dx was rescaled using C_{cal} as measured in the procedure mentioned in Section 3.10.4. The resulting dQ/dx has units of e^-/cm and can therefore be compared with the truth dQ/dx. The errors on the blue histogram entries represent the statistical error on the mean

while the uncertainties of the red histograms are the statistical error on the most probable value resulting from the fit. This comparison with the truth Monte Carlo behaviour is purely qualitative, and a more complete treatment of the errors will be carried out later on. Nonetheless, it can be observed that the distributions of the means reproduce the simulated behaviour more closely, suggesting that using the mean values has the potential to give more accurate results.



(a) $\phi = 80°$. (b) $\phi = 70°$.

(c) $\phi = 60°$. (d) $\phi = 50°$.

Figure 7.5: Comparison of the mean (blue) and most probable (red) values of dQ/dx with the Monte Carlo truth dependence of dQ/dx vs. dE/dx (grey clouds of dots) for each angular bin.

7.2.3 Fit Results

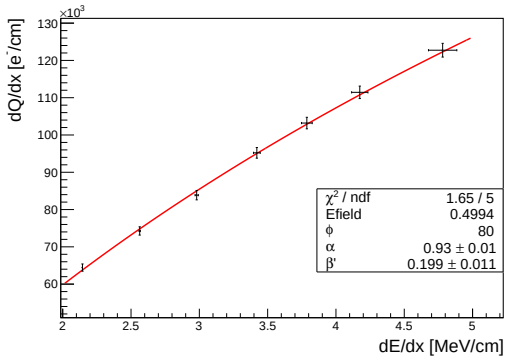
To perform the measurement of the modified box model parameters, a relative error of 1.5% is assigned to the mean dQ/dx in each bin. This is a preliminary estimation of the uncertainties related to the calibration chain [140]. The corresponding dE/dx value and its error are calculated in the following way. In each bin, and especially in

bins corresponding to larger dE/dx, the distribution of dE/dx entries is strictly non-uniform, as a consequence of the high slope of the theoretical curve for the stopping power. Therefore, the mean of the distribution inside every bin is considered, rather than just the bin central value. A first source of error on dE/dx is then the error on the mean. Additionally, a track stops half-way through the last wire cell on average, resulting in an intrinsic uncertainty on the reconstruction of the residual range of the order of $\sim 0.5\,\mathrm{cm}/\sqrt{12}$, where 0.5 cm is the wire pitch. The error on the residual range is propagated through the dE/dx vs. residual range formula obtained by converting the $\beta\gamma$ factor of Equation 5.3 to kinetic energy and then to residual range. This second source of error on dE/dx is summed in quadrature with the error on the mean to obtain the final dE/dx error and quickly becomes the dominant contribution. The dependence of dQ/dx on dE/dx is fitted with the equation:

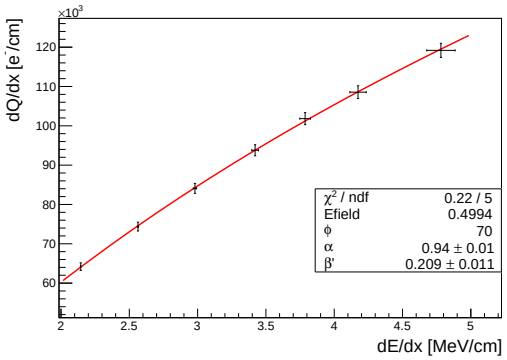
$$\frac{dQ}{dx}^{\mathrm{mbm}}\,[e^-/\mathrm{cm}] = \frac{1}{W_{\mathrm{ion}}}\cdot\frac{1}{\frac{\beta'}{\rho\mathscr{E}\sin\phi}}\ln\left(\alpha+\frac{\beta'}{\rho\mathscr{E}\sin\phi}\frac{dE}{dx}\right), \tag{7.7}$$

with α and β' free fit parameters and ϕ set at the appropriate value for each bin. The dQ/dx measured in [ADCxtick/cm] is converted to $[e^-/\mathrm{cm}]$ using the constant C_{cal} determined for the Monte Carlo sample as $1.011\times10^{-3}\,\mathrm{ADCxtick}/e$ using minimum ionising muons (see Section 3.10.4). While the electric field value is strongly dependent on the location, an "effective" electric field was defined as the average of the electric field values at the location of each hit, resulting in $\mathscr{E} = 0.4994\,\mathrm{kV/cm}$. The fits for each angular bin are visible in Figure 7.6. The fit range is restricted to the region of the stopping power curve starting from just before the Bragg peak. Overall, good agreement is found between the measured parameters and the input values of the Monte Carlo: $\alpha_{\mathrm{MC}} = 0.93$ and $\beta'_{\mathrm{MC}} = 0.212$ $(\mathrm{kV/cm})(\mathrm{g/cm^2})\mathrm{MeV}^{-1}$. This result indicates that the method designed has the potential to perform a reliable measurement of the recombination parameters in different angular bins.

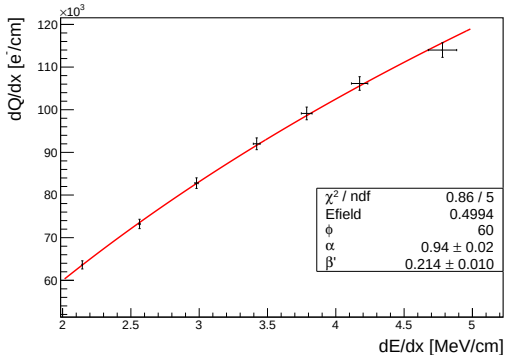
A single value can be extracted for each fit parameter by considering all the angular and energy bins at the same time. For this purpose, a χ^2 function has been defined



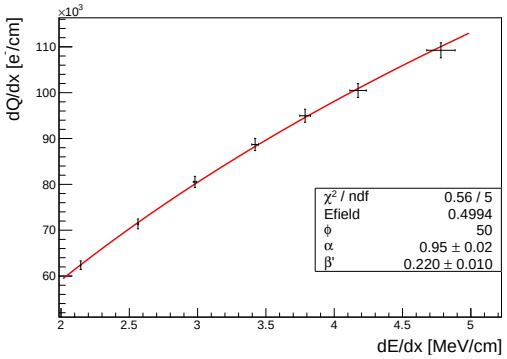
(a) $\phi = 80°$.



(b) $\phi = 70°$.



(c) $\phi = 60°$.



(d) $\phi = 50°$.

Figure 7.6: Fit to determine the recombination parameters α and β' used for muons in the particle gun simulation in each angular bin. A good agreement ($\lesssim 1\sigma$) is found between the measured parameters and the Monte Carlo input values.

as:

$$\chi^2(\alpha, \beta') = \sum_{i}^{\text{N bins}} \frac{\left[\left(\frac{dQ}{dx}\right)_i - \left(\frac{dQ}{dx}\right)_i^{\text{mbm}}\right]^2}{\sigma^2_{(dQ/dx)i} + \sigma^2_{(dE/dx)i} \cdot \left[D_{(dE/dx)i}\left(\frac{dQ}{dx}\right)_i^{\text{mbm}}\right]^2}, \tag{7.8}$$

where the index i runs over all the points in Figure 7.6, $\left(\frac{dQ}{dx}\right)_i^{\text{mbm}}$ represents the function in Equation 7.7 calculated at $\left(\frac{dE}{dx}\right)_i$ and with $\sin\phi_i$, $D_{(dE/dx)i}$ is the derivative operator with respect to $\left(\frac{dE}{dx}\right)_i$ and σ represents the uncertainties of the quantity in brackets. After minimising the χ^2 the values $\alpha = 0.936 \pm 0.007$ and $\beta' = (0.205 \pm 0.006)$ (kV/cm)(g/cm^2)MeV^{-1} are obtained, again in good agreement with the input parameters.

7.3 Validation of Method on the ProtoDUNE-SP Monte Carlo

While the ProtoDUNE-SP official Monte Carlo does not include any angular dependence, it is still interesting to see how the parameter extraction procedure performs on the sample selected as described in Chapter 6. The correct reconstruction of the last portion of the track is critical to perform an accurate measurement of the recombination parameters. With this test it is possible to verify the goodness of the reconstruction for the selected tracks. The official Monte Carlo simulates recombination with the modified box model without the $\sin\phi$ factor:

$$\mathscr{R}_{\text{PD-MC}} = \frac{1}{\frac{\beta'}{\rho\mathscr{E}}\frac{dE}{dx}} \ln\left(\alpha + \frac{\beta'}{\rho\mathscr{E}}\frac{dE}{dx}\right), \tag{7.9}$$

with α and β' from ArgoNeuT (Table 4.2) and the electric field being a function of the location in the detector. The errors on dQ/dx and dE/dx are treated likewise in the previous section. The hits are not divided into angle bins and coherently the fit function used does not contain the $\sin\phi$ term:

$$\frac{dQ}{dx}^{\text{mbm}}\,[e^-/\text{cm}] = \frac{1}{W_{\text{ion}}} \cdot \frac{1}{\frac{\beta'}{\rho\mathscr{E}}} \ln\left(\alpha + \frac{\beta'}{\rho\mathscr{E}}\frac{dE}{dx}\right). \tag{7.10}$$

However, the different geometrical distributions of the anode and cathode-crossing muon samples inside the detector must be taken into account. This implies that the average electric field for each sample is significantly different, as illustrated in Figure 7.7. As a consequence, the parameter $\mathscr{E}$ in Equation 7.10 will be set to the average electric field of the corresponding sample when fitting. The average electric fields are $\mathscr{E} = 0.5354\,\text{kV/cm}$ and $\mathscr{E} = 0.4534\,\text{kV/cm}$ for the hits of the cathode and anode-piercing tracks respectively. The fits for the two samples are shown in Figure 7.8. Like in the case for the particle gun Monte Carlo, the dQ/dx values are scaled by C_{cal} and the fit only includes points in a different energy range than that used to determine C_{cal} itself. Good agreement is again found between the extracted parameters and the Monte Carlo input. This positive result is to be ascribed to the additional cuts on the Michel hits and dE/dx shape (implemented in Chapter 6) that

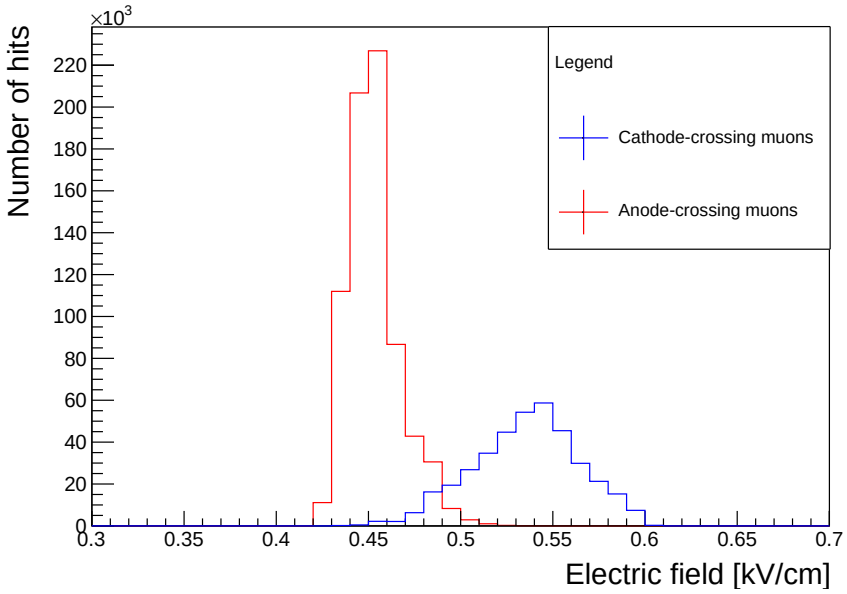
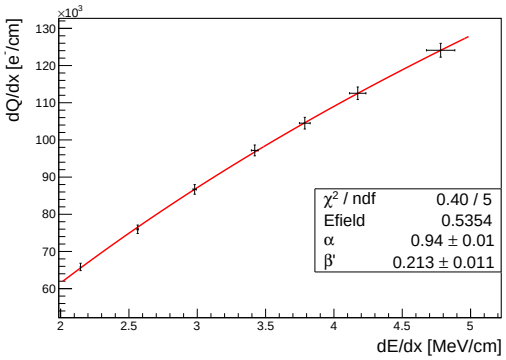


Figure 7.7: Comparison between the electric field at the location of each hit for the sample of cathode and anode-crossing muons. It can be noticed that the charge resulting from a cathode-crossing muon is subject to a significantly different electric field than that of an anode-crossing muon.

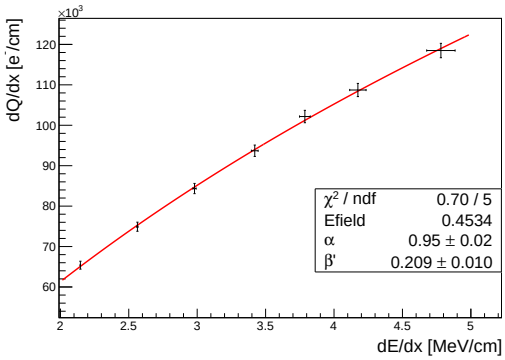
allow to select well reconstructed tracks. After validating the measurement on Monte Carlo, the next section will show the measurement on actual data.

7.4 Extracting Recombination Model Parameters

The muons in data are selected using the same cuts implemented in the Monte Carlo. For this study, the data from run 5387 taken in October 2018 is considered. For the events considered in the following studies, the average electron lifetime was around 17.5 ms, as measured by the purity monitors installed in the chambers. Around 700 cathode-crossing and 1800 anode-crossing well-reconstructed muons are selected after all the cuts are applied. In principle, it is expected to have roughly the same number of cathode-crossing and anode-piercing muons, since there are two anodes through which a muon can enter in the TPCs and only one cathode that can be crossed from both sides. The difference in the number of tracks is not intentional, but it is the result of the combined efficiencies of the different t_0-tagging procedures and the selection cuts which can differ substantially between the two samples. The parameters of the



(a) Cathode-crossing muons.

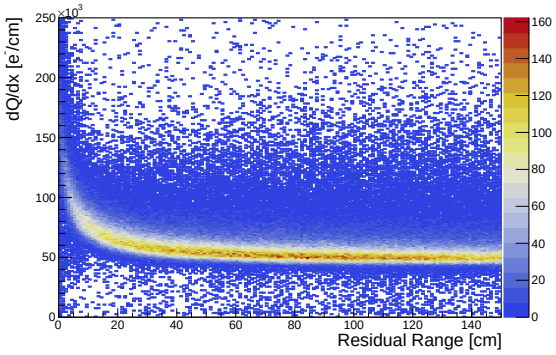


(b) Anode-crossing muons.

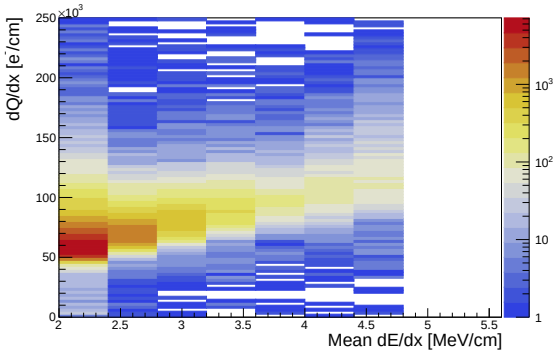
Figure 7.8: Recombination fit to determine the modified box model parameters used in the Monte Carlo simulation of ProtoDUNE-SP for both sample of cathode and anode-crossing muons separately.

recombination models can be studied for all the tracks in the selection and ignoring the angular dependence, like in the case of the ICARUS and MicroBooNE experiments, or each parameter can be determined as a function of the angle to see if that modulation effect is relevant at this ionisation scale. The results of both these two studies will be shown in this section.

The plots in Figure 7.9 show the reconstructed dQ/dx as a function of both the residual range and the mean dE/dx obtained from the residual range measurement for both anode and cathode-crossing muons and for any value of the angle ϕ. The dQ/dx



(a) dQ/dx vs. residual range.



(b) dQ/dx vs mean dE/dx.

Figure 7.9: Reconstructed dQ/dx as a function of the residual range (left) and the mean dE/dx (right) for anode and cathode-crossing muons in data run 5387.

in [e/cm] is obtained by dividing the dQ/dx in [ADCxtick/cm] by the calibration

constant measured for run 5387 $C_{\text{cal}} = 1.029 \times 10^{-3}$ ADCxtick/e. Because of the noisy region at very low residual range values in Figure 7.9a, the hits with residual range less than 2 cm are excluded from the analysis. Like in the Monte Carlo case, the tracks from the two samples are subject to a significantly different electric field, illustrated in Figure 7.10. Different approaches are possible, like dividing the sample in electric field

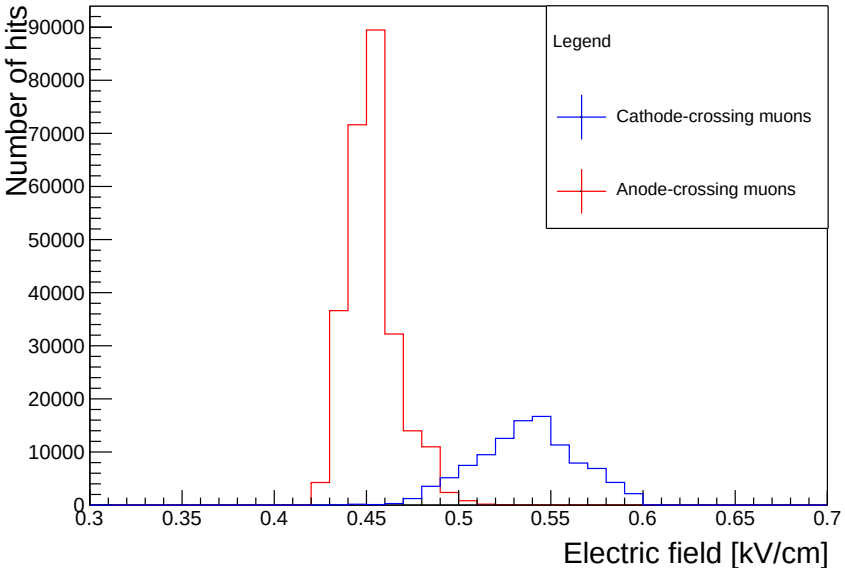


Figure 7.10: Electric field at the location of each hit considered in run 5387 according to the space charge calibration map.

bins and fit each bin with the corresponding field value in the recombination model. Alternatively, the electric field was kept fixed for each hit at the "effective" value of $\mathscr{E} = 0.4867\,\text{kV/cm}$, measured during beam runs [141]. The mean dQ/dx as a function of the mean dE/dx is fitted with both the modified box model of Equation 7.10 and the Birks model as modified by the ICARUS collaboration:

$$\left.\frac{dQ}{dx}\right|^{\text{Birks}} [e^-/\text{cm}] = \frac{1}{W_{\text{ion}}} \frac{dE}{dx} \cdot \frac{A}{1 + \frac{k}{\rho \mathscr{E}} \frac{dE}{dx}} \tag{7.11}$$

For simplicity, this will be referred to as just the Birks model in the rest of this thesis. The fits of the data to the modified box model and the Birks law are shown in Figure 7.11. The uncertainties on both the dQ/dx and the dE/dx are estimated in analogy with the Monte Carlo studies. It can be seen that both models fit the data

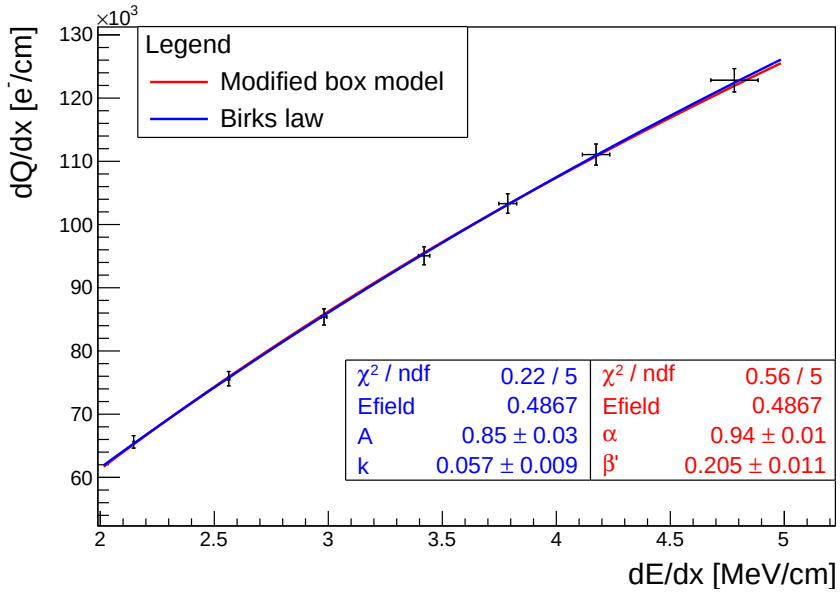
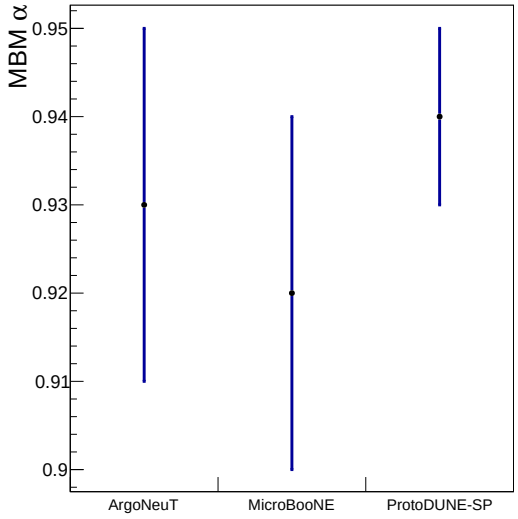
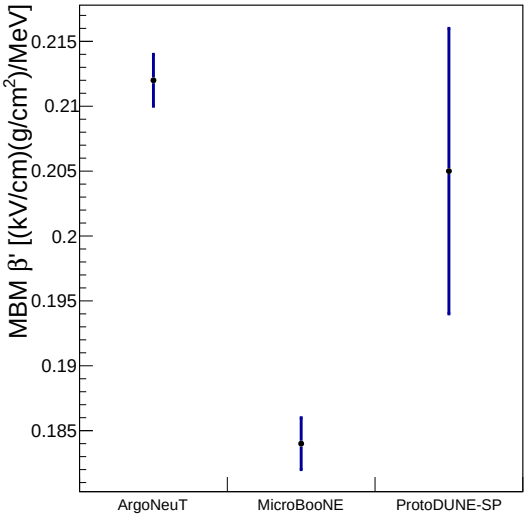


Figure 7.11: Fit to the modified box model (red curve) and Birks model (blue curve) for the combined sample of cathode and anode-crossing stopping muons and for any angle ϕ.

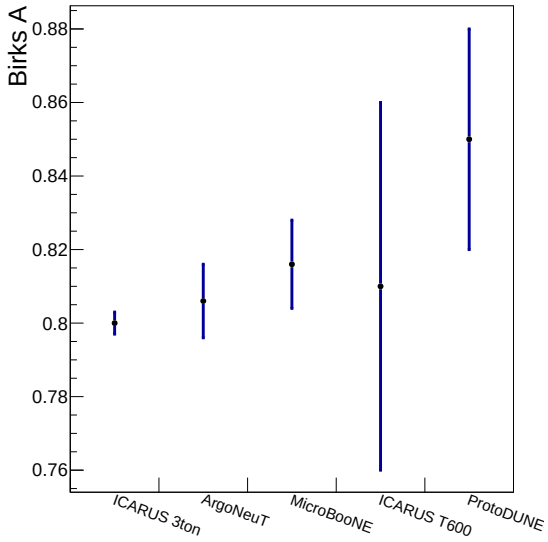
well. It is also worth pointing out that, just like in other liquid argon experiments, the normalisation factor A of the Birks model is significantly different than the expected unity, as discussed in Chapter 4. The parameters value show general good agreement with the values of Table 4.2, as illustrated in Figure 7.12. In particular, the measurement for α is consistent across all experiments that explored the box model parametrisation. The ProtoDUNE-SP value for β' is also compatible with that of ArgoNeuT, which has a very similar electric field, but the statistical significance of the ProtoDUNE-SP measurement is lower due to the smaller range in dE/dx for the muon Bragg peak compared to that of protons. The ProtoDUNE-SP data favours a larger value for the Birks model parameter A compared to other experiments. However, the value found is consistent with the measurement performed at the ICARUS T600 detector. Similar considerations apply to the parameter k. The MicroBooNE measurement found smaller values of the parameters β' and k due to the smaller electric field that is coupled with said parameters in both models.



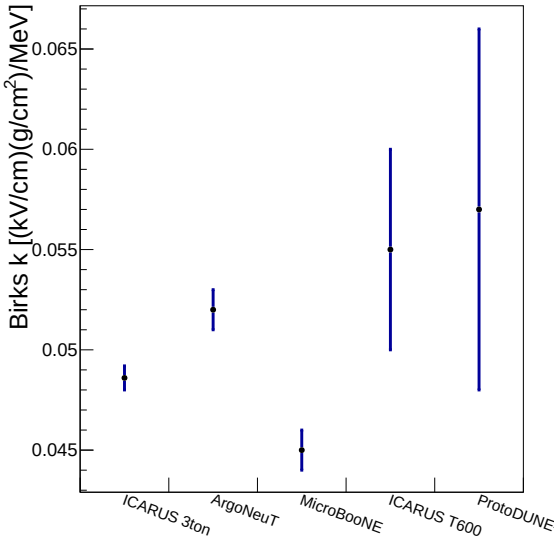
(a) Modified box model α.



(b) Modified box model β'.



(c) Birks model A.



(d) Birks model k.

Figure 7.12: Comparison of the recombination parameters of the modified box model (MBM) and Birks law between the values obtained from the fit of Figure 7.11 and the values from other liquid argon experiments from Table 4.2. The values for ArgoNeuT are the weighted average of the values found for each of their angular bins. ArgoNeuT and MicroBooNE performed the recombination studies using protons, while ICARUS T600 and ProtoDUNE-SP employ muons. ICARUS 3ton employs both.

7.4.1 Angular Dependence

Thanks to the relatively wide angular distribution of cosmic rays, it is possible to investigate the $\sin\phi$ dependence predicted by Jaffe's theory by using these samples of stopping muons. The angle ϕ for each hit is calculated using Equation 7.6. The resulting ϕ distribution for anode and cathode-crossing muons separately is illustrated in Figure 7.13, for data and Monte Carlo. While data and Monte Carlo have similar

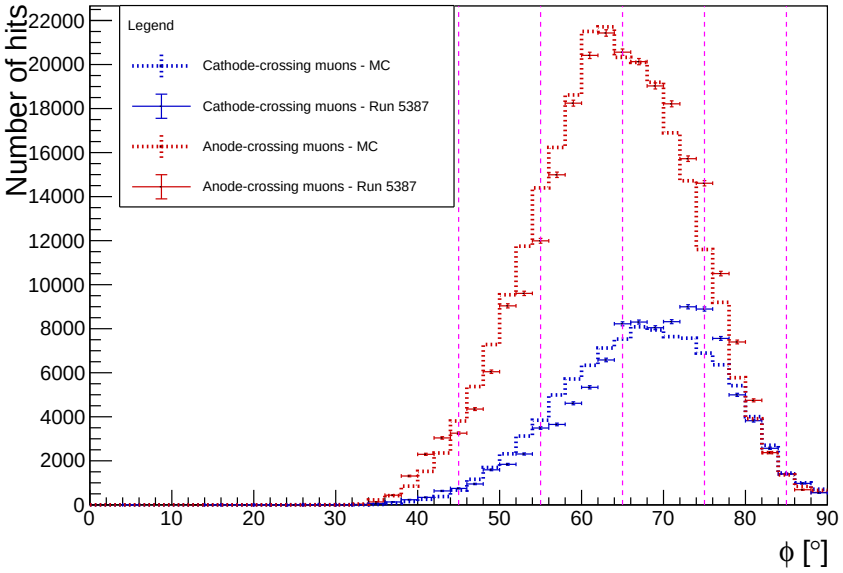


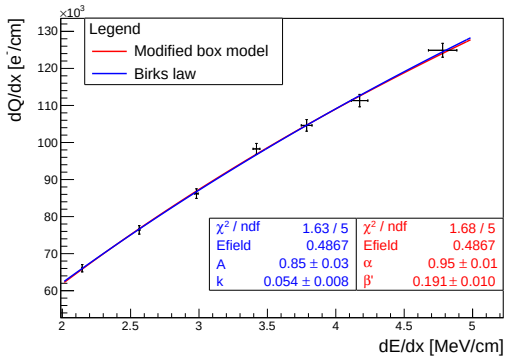
Figure 7.13: Comparison of the distributions of the angle between the local direction of the track at the position of each hit and the local electric field ϕ. Both distributions for anode (red) and cathode (blue) crossing muons are shown, for selected stoppers in data run 5387 and Monte Carlo. The vertical purple lines indicate the borders of the chosen angular bins at 50°, 60°, 70° and 80°.

shapes, small differences, currently not fully understood, can be noticed. Like in the Monte Carlo measurement of Section 7.2, the hits are divided into four bins centered at 50°, 60°, 70° and 80°, each with a total width of 10°. They are indicated by the purple lines of Figure 7.13. The function used to fit the data in angular bins are

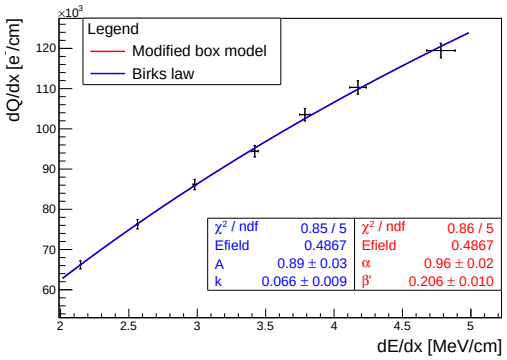
$$\frac{dQ}{dx}^{\text{mbm}}[e^-/\text{cm}] = \frac{1}{W_{\text{ion}}} \cdot \frac{1}{\frac{\beta'}{\rho\mathscr{E}\sin\phi}} \ln\left(\alpha + \frac{\beta'}{\rho\mathscr{E}\sin\phi}\frac{dE}{dx}\right) \tag{7.12}$$

for the modified box model and

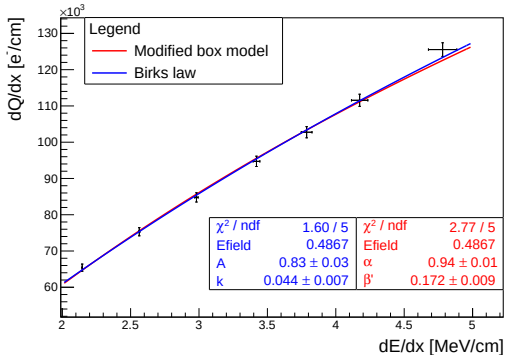
$$\frac{dQ}{dx}^{\text{Birks}}[e^-/\text{cm}] = \frac{1}{W_{\text{ion}}}\frac{dE}{dx} \cdot \frac{A}{1 + \frac{k}{\rho\mathscr{E}\sin\phi}\frac{dE}{dx}} \tag{7.13}$$



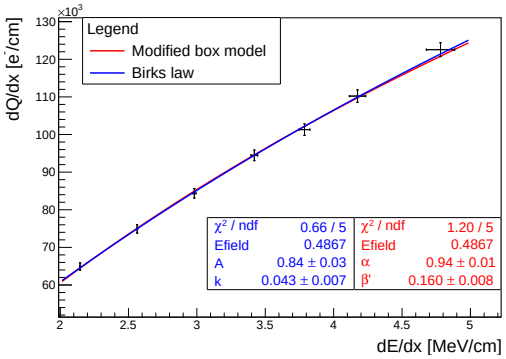
(a) $\phi = 80°$.



(b) $\phi = 70°$.



(c) $\phi = 60°$.



(d) $\phi = 50°$.

Figure 7.14: Recombination fits for the merged sample of anode and cathode-crossing muons from run 5387 for different values of the angle ϕ. Both the Birks (blue lines) and the modified box model (red lines) are used to fit the data.

for the Birks law with the added $\sin\phi$ dependence. From Equations 7.12 and 7.13 it can be seen that the fit is sensitive to the combination $\beta'/(\mathscr{E}\sin\phi)$ or $k/(\mathscr{E}\sin\phi)$. To extract β' and k the electric field is fixed at the effective value of $\mathscr{E} = 0.4867\,\mathrm{kV/cm}$ like in the previous case and ϕ is fixed at the central value of each angular bin. It is therefore expected to find that the values of β' and k are independent from the angle ϕ, if the $\sin\phi$ modulation is verified in the data. The resulting fits are shown in Figure 7.14. Both models can fit the data well across the whole range. To extract a single set of recombination parameters across all angles, a χ^2 designed in analogy with the example in Equation 7.8 is used:

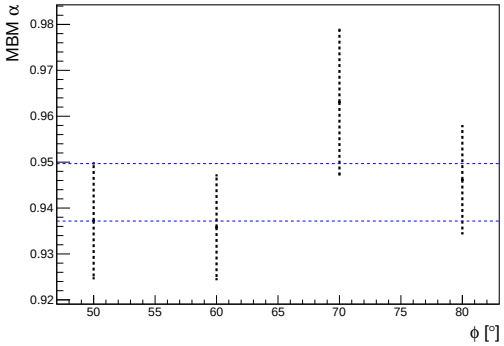
$$\chi^2_{\mathrm{data}}(\alpha,\beta') = \sum_{i}^{\text{N bins}} \frac{\left[\left(\frac{dQ}{dx}\right)_i - \left(\frac{dQ}{dx}\right)_i^{\mathrm{model}}\right]^2}{\sigma^2_{(dQ/dx)i} + \sigma^2_{(dE/dx)i} \cdot \left[D_{(dE/dx)i}\left(\frac{dQ}{dx}\right)_i^{\mathrm{model}}\right]^2}, \tag{7.14}$$

where $\left(\frac{dQ}{dx}\right)^{\text{model}}$ is given by Equation 7.12 or 7.13. The parameters obtained by minimising χ^2_{data} are summarised in Table 7.1. It can be seen that acceptable fits are obtained when using both models.

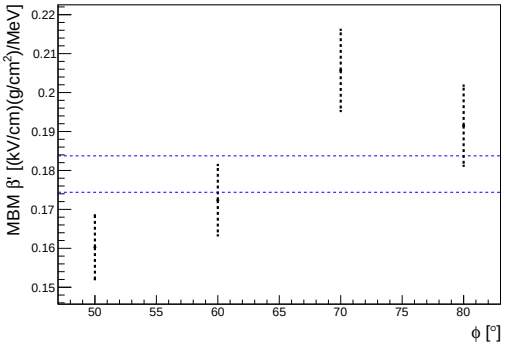
Table 7.1: Recombination parameters of the modified box and Birks model as obtained from a global fit with different angles ϕ. The units of β' and k are $(\text{kV/cm})(\text{g/cm}^2)\text{MeV}^{-1}$.

Modified Box Model	**Birks Model**
$\alpha = 0.937 \pm 0.005$	$A = 0.83 \pm 0.01$
$\beta' = 0.193 \pm 0.005$	$k = 0.049 \pm 0.004$
$\chi^2/\text{ndof} = 30.7/26$	$\chi^2/\text{ndof} = 26/26$

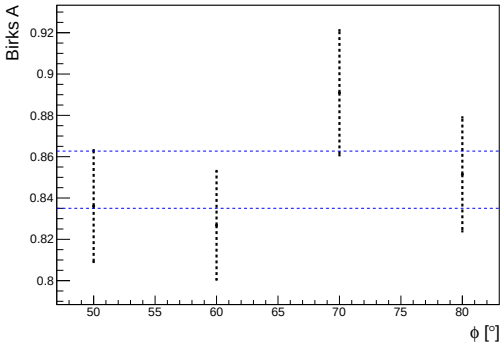
It is also interesting to examine the angular dependence of the parameters. To easily compare the resulting parameters among different angles, plots of their obtained values as a function of the angle ϕ are given in Figure 7.15. The interval within the two blue dashed lines represents the weighted average of the measurement with its uncertainty. It can be seen that the measurements of α and A agree among each other as expected, since they are not coupled with the value of the angle ϕ. The same can not be said about the parameter β', where the obtained values are not consistent, despite the expectation under the assumption of a pure $\sin\phi$ dependence. The case of k is similar, although only one measurement at 70° is in disagreement with the other values. These discrepancies suggest that the $\sin\phi$ dependence might not be effective at describing the data. The quantities $\beta \equiv \frac{\beta'}{\rho\mathscr{E}\sin\phi}$ and $K \equiv \frac{k}{\rho\mathscr{E}\sin\phi}$ are those actually measured by the fit. Their values against ϕ are given in Figure 7.16. The red lines in the corresponding plots represent a fit with the dependence $\sim 1/\sin\phi$ expected for the parameters β and K. The values recovered for β' and k are consistent with the weighted averages obtained from the values in Figures 7.15b and 7.15d. However, a better agreement to the data is seen in the case of the Birks parameter K. This should not be surprising, in that the Birks model is the closest to the original derivation of the columnar theory by Jaffe. The modified box model is obtained by assuming a uniform charge distribution in a box, and therefore it does not prescribe any functional



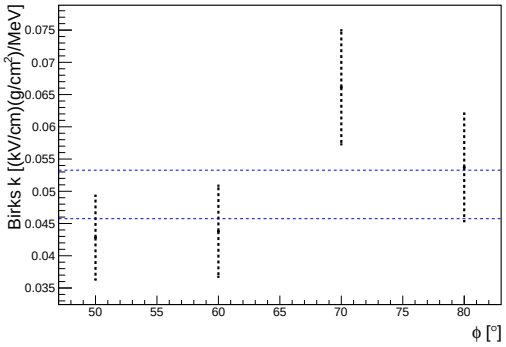
(a) α vs. ϕ.



(b) β' vs. ϕ.

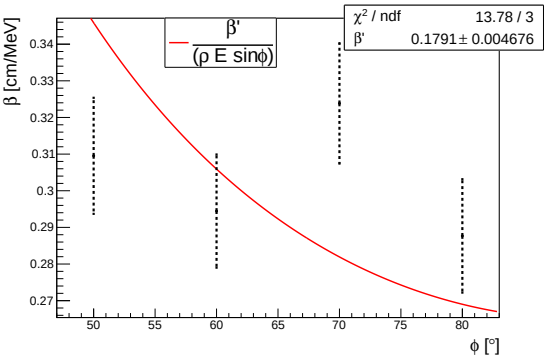


(c) A vs. ϕ.

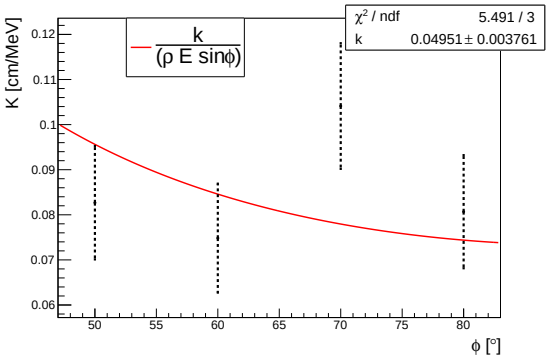


(d) k vs. ϕ.

Figure 7.15: Comparison of the recombination parameters of the modified box and Birks model for each angle ϕ in data run 5387 a obtained from the fits in Figure 7.14. The horizontal blue lines represent the interval determined by the uncertainties of the weighted average of the values in each plot.



(a) β vs. ϕ.



(b) K vs ϕ.

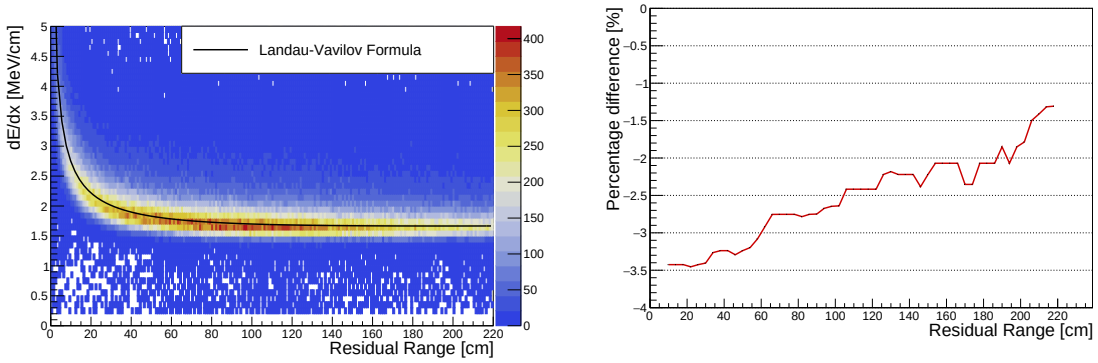
Figure 7.16: Parameters β and K as a function of ϕ. The red line represents a fit of the expected angular modulation $\sim 1/\sin\phi$ of the parameters.

dependence on ϕ. The angular dependence of the modified box model is introduced in retrospect through the substitution $\mathscr{E} \to \mathscr{E} \sin\phi$ in analogy with the Birks law. While the values of Table 7.1, obtained minimising the χ^2 of Equation 7.14, give an acceptable fit to the data, it can be noticed that the values for α and A are offset from the weighted averages of the values in Figure 7.15a and 7.15c, indicating that the minimising procedure needs to offset α and A to better accommodate the $\sin\phi$ dependence across all angular bins. The $\sin\phi$ modulation is not verified for the modified box model case, while it is acceptable in the Birks law case. In both circumstances, it would be useful to explore the regions at smaller angles, to better characterise the angular dependence. The angular distribution of muons crossing the cathode or the anodes shows a sharp decrease in statistics for $\phi < 45°$ (see Figure 7.13). The parameters β' and k are also coupled with the energy loss per unit length dE/dx. The study of heavier particles such as protons would give a greater handle to measure these parameters, improving the statistical significance of the angular dependence analysis.

7.5 dE/dx Calculation

Using the recombination parameters as obtained from the fit to ProtoDUNE-SP data (Figure 7.11), it is possible to update the value of C_{cal} calculated with ArgoNeuT parameters. The values obtained (using the procedure described in Section 3.10.4 and more extensively in [62]) are $C_{\text{cal}}^{\text{mbm}} = (1.007 \pm 0.001) \times 10^{-3}\text{ADCxtick}/e$, assuming the modified box model, and $C_{\text{cal}}^{\text{Birks}} = (0.977 \pm 0.001) \times 10^{-3}\text{ADCxtick}/e$, assuming the Birks parametrisation for recombination. The two values agree within 3%. With the updated values of C_{cal}, it is possible to calculate the dE/dx for each hit using the two recombination models with the parameters obtained for ProtoDUNE-SP. The results can be compared with the Landau-Vavilov formula of Equation 5.4, as a function of the residual range, selecting as a thickness the average dx across all selected hits ($\sim 0.7\,\text{cm}$). The plot in Figure 7.17a is obtained for the dE/dx calculated using the modified box model with $C_{\text{cal}}^{\text{mbm}}$ and the newly calculated parameters for ProtoDUNE-

SP. Figure 7.17b shows the percentage difference between the most probable value dE/dx obtained with a fit to a Landau-Gaussian convoluted function in each residual range bin of Figure 7.17a and the Landau-Vavilov formula evaluated at the bin center. A small systematic underestimation ($< 3.5\%$) of the theoretical most probable value can be observed. The plots in Figure 7.18 are instead for the dE/dx values calculated



(a) dE/dx with the modified box model.

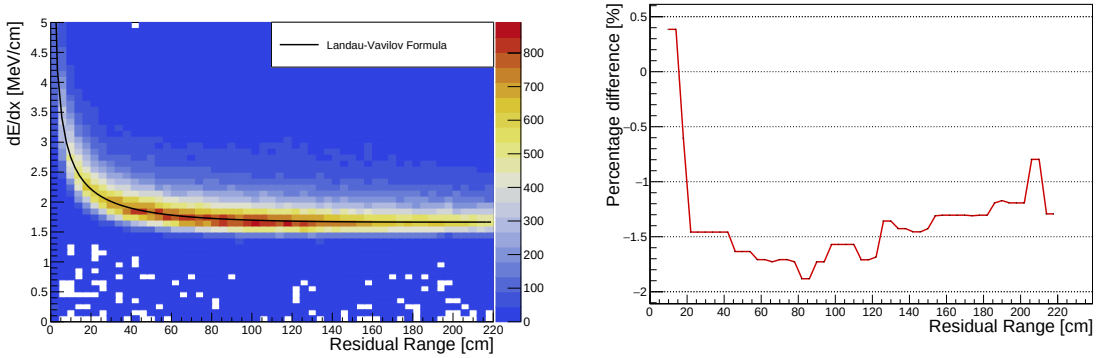
(b) Comparison with Landau-Vavilov formula.

Figure 7.17: Left: calibrated dE/dx as a function of the residual range for the selected muons in run 5387. The dE/dx is obtained from the fully calibrated dQ/dx using the parameters of the modified box model and the constant $C_{\text{cal}}^{\text{mbm}}$ resulting from the fit to ProtoDUNE-SP data. The black line indicates the expected behaviour from Equation 5.4. Right: comparison between the most probable value dE/dx in each residual range bin and Equation 5.4.

using the Birks model with the new values for A and k and the corresponding $C_{\text{cal}}^{\text{Birks}}$. It can be seen that the parametrisation using the Birks model reproduces the theoretical expectations more closely.

7.6 Discussion on Systematic Uncertainties

A number of sources of systematic uncertainties can affect the measurements performed in the previous sections. This section will focus on a discussion of what these sources are and the magnitude of some of the most important effects will be estimated.



(a) dE/dx with the Birks model.

(b) Comparison with Landau-Vavilov formula.

Figure 7.18: Left: calibrated dE/dx as a function of the residual range for the selected muons in run 5387. The dE/dx is obtained from the fully calibrated dQ/dx using the parameters of the Birks model and the new constant $C_{\text{cal}}^{\text{Birks}}$ resulting from the fit to ProtoDUNE-SP data. The black line indicates the expected behaviour from Equation 5.4. Right: comparison between the most probable value dE/dx in each residual range bin and Equation 5.4.

7.6.1 Selection Cuts, Reconstruction and Space Charge Effects

The selection cuts described in Chapter 6 can affect the energy reconstructed through the residual range, which in turn can affect the recombination fits. In addition, space charge effects influence the reconstruction of the residual range, and consequently the dE/dx, and the measurement of dQ/dx.

There are a number of ways in which the reconstruction of the t_0 can affect the results. In the first place, the reconstruction efficiencies can be different in data and in Monte Carlo. Additionally, the systematic uncertainties on the t_0 are closely connected to the space charge effects. The t_0 is calculated by assuming the nominal electron drift velocity which is in reality affected by SCEs. The extent of this effect is expected to be greater for charge deposited around the middle of the drift direction. The charge deposited near the cathode is less affected as the integral of the electric field along the drift direction is kept fixed by the external high voltage supply,[1] so the perturbations are averaged out. Charge near the anode is characterised by a shorter

[1]It is understood that the drift velocity is a monotonic function of the electric field.

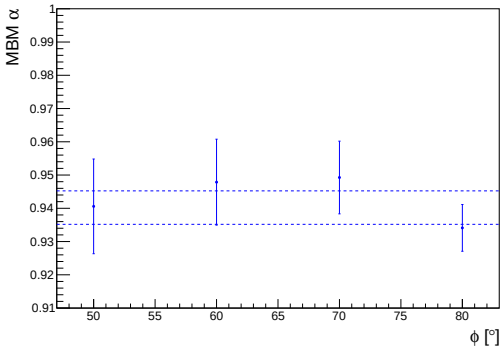
drift distance and therefore the impact on the drift time is limited. Furthermore, the electrons do not follow a simple straight path when drifting, as it is approximately assumed when reconstructing the t_0. Spatial distortions affect tracks that are close to the cathode more, since they experience space charge distortions for a longer time. The space charge maps are obtained using tracks who have an associated t_0, and therefore the systematic uncertainties are related. In the reconstruction, the amendments for space charge effects on the location are implemented after correcting the track position using the calculated t_0.

Lastly, the method used to tag muons in the case of anode and cathode-piercing tracks is entirely different, which can lead to different biases in the reconstructed t_0's. The two samples are also distributed in different volumes of the TPCs, and the space charge distortions are significantly different for the two samples (Figure 3.18). To see if there are factors that affect the measurement of the recombination parameters differently for anode or cathode-crossing tracks, they were measured separately for the two samples. Appendix A contains the recombination fits for the cases with and without the angular dependence on ϕ. To perform the fits, the electric field is set to the mean value for all the hits in each sample separately. When the angular dependence is ignored, the parameters given in Table 7.2 are obtained. Good agreement is found

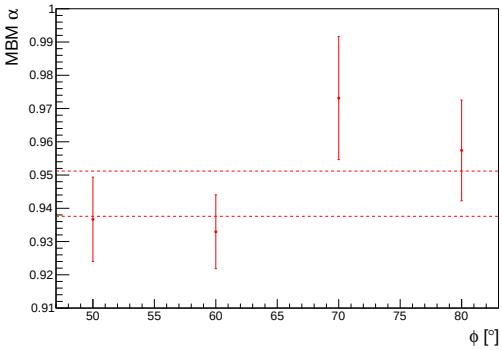
Table 7.2: Recombination parameters of the modified box and Birks model for the anode and cathode sample separately without angular dependence. The units of β' and k are $(\mathrm{kV/cm})(\mathrm{g/cm^2})\mathrm{MeV}^{-1}$.

	Cathode-crossing muons	**Anode-crossing muons**
Modified box model α	0.94 ± 0.01	0.95 ± 0.01
Modified box model β'	0.200 ± 0.011	0.199 ± 0.010
Birks model A	0.83 ± 0.03	0.85 ± 0.03
Birks model k	0.052 ± 0.009	0.057 ± 0.008

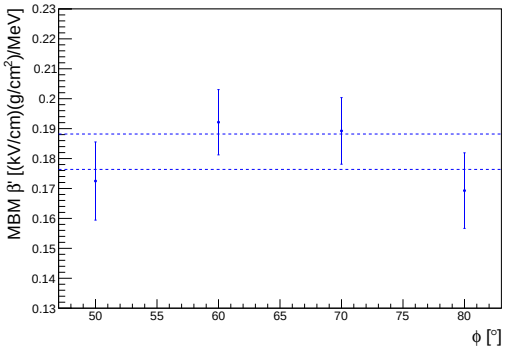
between the two samples and also when comparing to the fit results of the merged sample. The plots for the recombination parameters as a function of ϕ can be seen in Figures 7.19 and 7.20. The plots for each parameter can be compared row by row. It



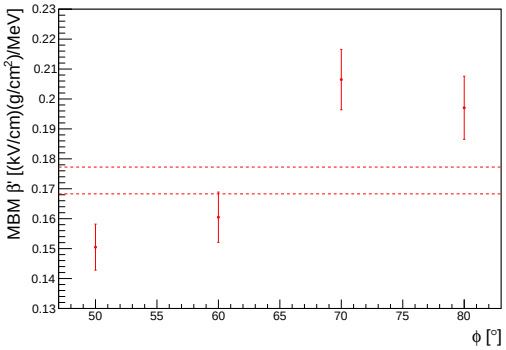
(a) α vs. ϕ (CC).



(b) α vs. ϕ (AC).

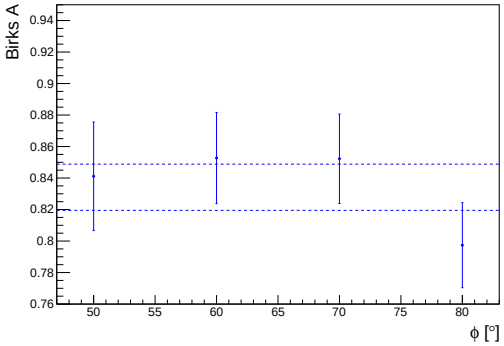


(c) β' vs. ϕ (CC).

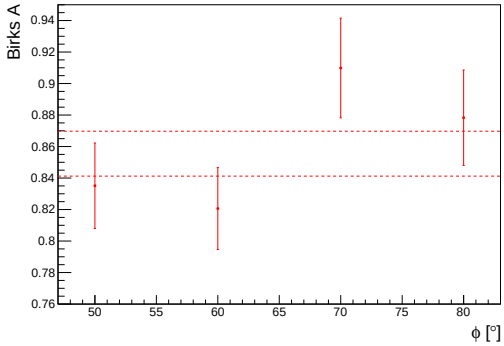


(d) β' vs. ϕ (AC).

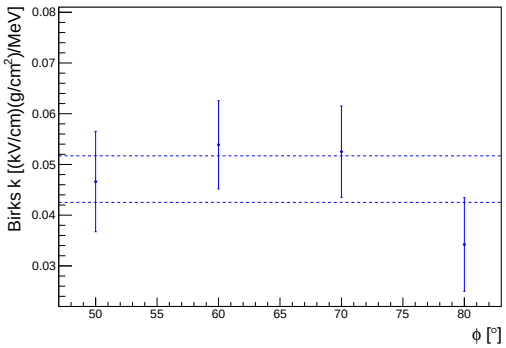
Figure 7.19: Modified box model recombination parameters as a function of the angle ϕ for the separate sample of cathode (CC, blue, left) and anode (AC, red, right) crossing muons. The plots for the same parameter have the same scale on the y axis such that the results can be compared for each parameter row by row. The dashed horizontal lines represent the interval defined by the weighted average of the measurements and its uncertainty.



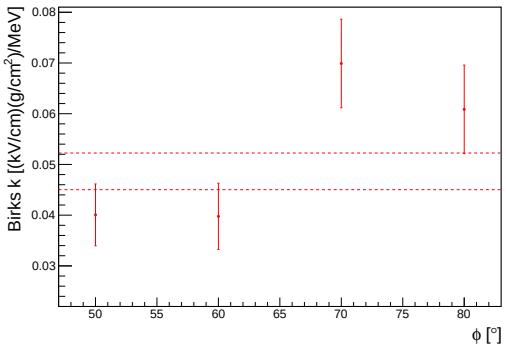
(a) A vs. ϕ (CC).



(b) A vs. ϕ (AC).



(c) k vs. ϕ (CC).



(d) k vs. ϕ (AC).

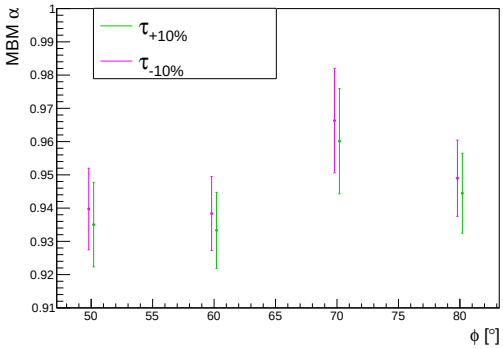
Figure 7.20: Birks recombination parameters as a function of the angle ϕ for the separate sample of cathode (CC, blue, left) and anode (AC, red, right) crossing muons. The plots for the same parameter have the same scale on the y axis such that the results can be compared for each parameter row by row. The dashed horizontal lines represent the interval defined by the weighted average of the measurements and its uncertainty.

can be seen that the weighted average on each plot on the left hand side is consistent with the weighted average of the corresponding plot for the other sample. This is an indication that there is no significant effect on the recombination parameters due to different magnitudes of space charge distortions, different t_0 calculations and selection algorithms.

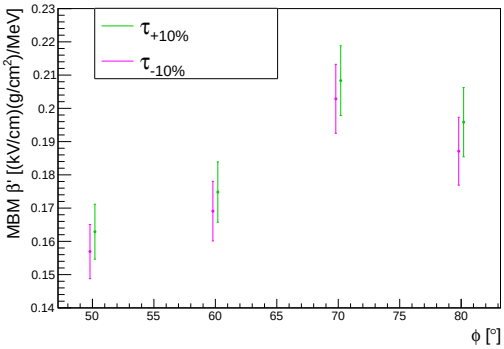
7.6.2 Electron Lifetime Measurement

The dQ/dx reconstructed is corrected for the impurities attachment using Equation 3.1 with the electron lifetime as measured by the purity monitors installed in the TPCs. Some limitations are related to this measurement. The purity monitors are positioned outside the field cage, and therefore do not provide a reading of the actual purity in the drift volume. In addition, the electric field in the purity monitors is different from the electric field in the active volume; this can affect the measured rate of impurity attachments [62]. As a consequence, the lifetime as provided by the purity monitors could be different than that in the TPCs. To estimate the impact of this difference, the lifetime measured for run 5387 (around $\tau = 17.5\,\text{ms}$) was changed by $\pm 10\%$, and the impact of this change on the recombination parameters was investigated using the merged sample of anode and cathode-crossing muons. The variation of $\pm 10\%$ was chosen based on the results of a preliminary study performed by the collaboration on the expected difference between the lifetime measured by the purity monitors and the lifetime measured using tracks in the TPC. The recombination fits are given in Appendix B. The lifetime obtained with a $+10\%$ (-10%) change will be denoted as $\tau_{+10\%}$ ($\tau_{-10\%}$). The parameters as a function of ϕ for both values of the electron lifetime are shown in Figure 7.21. Qualitatively, it can be noticed that the obtained values are shifted consistently for all angles, with the smallest effect observed for the parameter k. Table 7.3 summarises the percentage difference for each parameter when the lifetime is varied by $\pm 10\%$ defined as

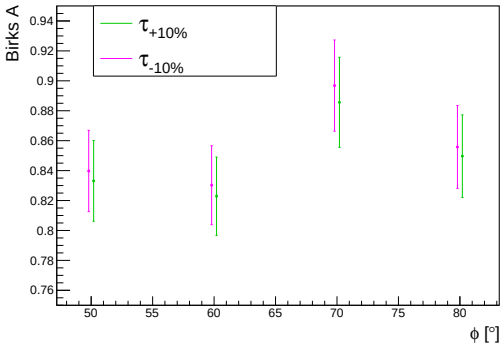
$$\frac{1}{2}\left[\left|\frac{P_{\tau_{+10\%}} - P_{\tau}}{P_{\tau}}\right| + \left|\frac{P_{\tau_{-10\%}} - P_{\tau}}{P_{\tau}}\right|\right] \tag{7.15}$$



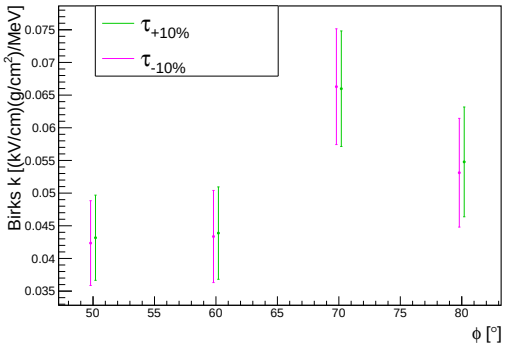
(a) α vs. ϕ.



(b) β' vs. ϕ.



(c) A vs. ϕ.



(d) k vs. ϕ.

Figure 7.21: Recombination parameters obtained with different values of the electron lifetime (±10% difference with respect to the measurement by the purity monitors). The points are slightly offset horizontally for better visibility.

for the generic parameter P calculated for the value of the lifetime expressed by the subscript. Overall, it can be concluded that the impact of the lifetime uncertainty

Table 7.3: Average percentage difference of the recombination parameters obtained with electron lifetime 10% larger and smaller than the lifetime measured by the purity monitors.

	No ϕ	$\phi = 80°$	$\phi = 70°$	$\phi = 60°$	$\phi = 50°$
α	0.5%	0.2%	0.3%	0.3%	0.3%
β'	1.7%	2.3%	1.3%	1.7%	1.8%
A	0%	0.4%	0.7%	0.5%	0.4%
k	0%	1.5%	0.2%	0.6%	1.0%

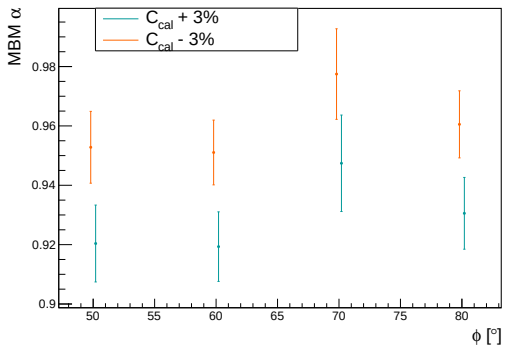
on the measurement is small, of the order of 2% in the worst case, with β' being the most affected parameter.

7.6.3 Determination of the Calibration Constant $C_{\mathbf{cal}}$

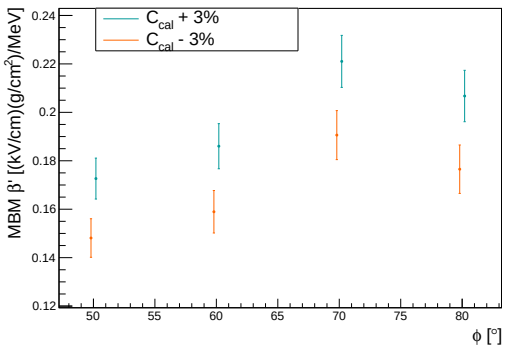
The calibration constant C_{cal}, that converts ADCxtick to the corresponding number of electrons, deserves a dedicated discussion. While the conversion to number of electrons is determined by the electronics and field response, an overall factor was calculated using a sample of stopping cosmic muons and by matching the expected dE/dx from the Landau-Vavilov theory with the dE/dx calculated using Equation 3.6 and assuming the modified box model with the ArgoNeuT parametrisation. As a consequence, C_{cal} not only represents a simple conversion of units, but it also includes the correction for effects left over by the calibration chain of Equation 3.5. The value of C_{cal} is also affected by the necessary assumption of a particular recombination model in its determination. In extracting the recombination parameters in the analysis presented in this chapter, care was taken in only considering regions in the residual range corresponding to the Bragg peak, so to avoid the MIP section used to determine C_{cal}. Trying to determine C_{cal} by including it in the recombination fits as a free parameter is problematic, since the overall constant dividing the dQ/dx would be completely degenerate with the Birks parameter A and highly correlated with β'. It

is thus necessary to assume a particular value of C_{cal} to perform the recombination fit.

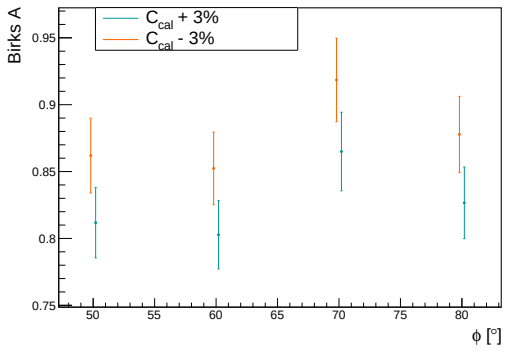
To estimate the impact of different values of C_{cal} on the recombination parameters, the value originally found can be increased and decreased by 3% and the parameters re-fitted to the data scaled with the new constants. These values of C_{cal} are identified by varying the modified box model parameters used to calculate the original value ($C^0_{\text{cal}} = 1.029 \times 10^{-3}\,\text{ADCxtick}/e$) within their uncertainty and picking the minimum and maximum difference obtained. This interval contains the value of the nominal electronics gain $1 \times 10^{-3}\,\text{ADCxtick}/e$. The recombination fits are given in Appendix C. The plots for the dependence of the recombination parameters on ϕ are shown in Figure 7.22. Table 7.4 summarises the percentage difference for each



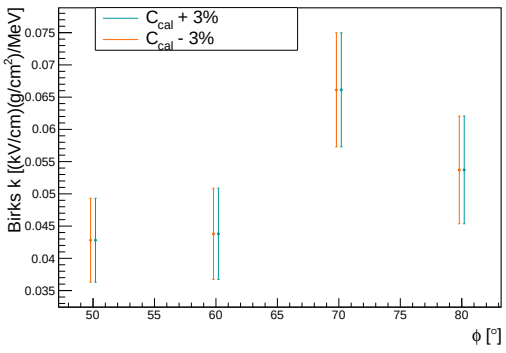
(a) α vs. ϕ.



(b) β' vs. ϕ.



(c) A vs. ϕ.



(d) k vs. ϕ.

Figure 7.22: Recombination parameters obtained with different values of C_{cal} ($\pm 3\%$ difference with respect to the value calculated with the method in [62]). The points are slightly offset horizontally for better visibility.

parameter when C_{cal} is varied by $\pm 3\%$, defined as

$$\frac{1}{2}\left[\left|\frac{P_{C^0_{\text{cal}}+3\%} - P_{C^0_{\text{cal}}}}{P_{C^0_{\text{cal}}}}\right| + \left|\frac{P_{C^0_{\text{cal}}-3\%} - P_{C^0_{\text{cal}}}}{P_{C^0_{\text{cal}}}}\right|\right] \tag{7.16}$$

for the generic parameter P calculated for the value of C_{cal} expressed by the subscript. From Figure 7.22 and Table 7.4 it can be observed that the value of C_{cal} significantly

Table 7.4: Average percentage difference of the recombination parameters obtained with different C_{cal} values.

	No ϕ	$\phi = 80°$	$\phi = 70°$	$\phi = 60°$	$\phi = 50°$
α	1.5%	1.6%	1.6%	1.7%	1.7%
β'	7.8%	7.9%	7.4%	7.8%	7.7%
A	3.5%	3%	3%	3%	3%
k	0%	0%	0%	0%	0%

impacts the modified box model parameters, with β' the most affected. The Birks parameters are overall less affected, as they are still compatible within one sigma in all cases, with k showing to be independent from C_{cal}. This can be understood looking at Equation 7.11: the change in the overall constant C_{cal} multiplying the dQ/dx is absorbed by the other global constant A, leaving k unchanged.

7.6.4 Effect of δ-rays

Delta rays produced by the muons ionise the argon with a variable ionisation density depending on their energy. At high energies, delta electrons are minimum ionising, but at lower energies they become highly ionising. Their ionisation density might be different than that of the primary particle, meaning that the charge produced is subject to different recombination rates depending on the local dE/dx, whether it is energy deposited from the muon or the δ-ray. Estimating this contribution is challenging, since it will vary depending on the particular δ-ray topology, like the emission energy spectra and direction and it remains as a possible future study.

7.7 Conclusion

A study of charge creation at low ionisation energy was presented in this chapter. Through a dedicated Monte Carlo simulation, a procedure to extract recombination model parameters in an environment with significant level of spatial and electric field distortions was implemented. The method was validated in the case of "perfectly" reconstructed muon tracks and on the tracks resulting from the selection developed in Chapter 6 in a realistic simulated reconstruction. Two models, the modified box model and the Birks law, were tested, and both were found to describe the data with good accuracy. The recombination parameters are in agreement with a previous measurement performed with muons at similar electric field values. The agreement is also good with measurements that employed stopping proton, but the limited dE/dx range that can be explored with muons is reflected into a larger uncertainty for the parameters that are coupled with the ionisation density. The obtained values are summarised in Table 7.5.

Table 7.5: Summary of the values obtained for the recombination parameters when ignoring the angular modulation in the fit functions.

Parameter	Value	Units
α	$0.94 \pm 0.01(\text{stat.}) \pm 0.01(\text{syst.})$	
β'	$0.205 \pm 0.011(\text{stat.}) \pm 0.016(\text{syst.})$	$(\text{kV/cm})(\text{g/cm}^2)\text{MeV}^{-1}$
A	$0.85 \pm 0.03(\text{stat.}) \pm 0.03(\text{syst.})$	
k	$0.0570 \pm 0.0090(\text{stat.}) \pm 0.0001(\text{syst.})$	$(\text{kV/cm})(\text{g/cm}^2)\text{MeV}^{-1}$

The angular effect predicted by the columnar theory was also explored. The parameters α and A, which are not coupled with the angular modulation term, were found to be independent from the angle, as expected. The modulation of the parameters β' and k does not exactly follow the predicted $\sin\phi$ dependence, even though the fit to data with this model is good. More studies are necessary to explore in details the angular dependence. In particular, a study with protons, which have a peak dE/dx of $\approx 25\,\text{MeV/cm}$, should in principle be performed to take advantage of the bigger lever arm to measure β' and k. The only significant source of protons in

the ProtoDUNE-SP detector is represented by the beam protons, which all travel in the same direction and are therefore not suitable to study the angular dependence. The values measured for the various recombination parameters are summarised in Table 7.6.

Table 7.6: Summary of the measurements of the recombination parameters for the different angular bins.

Angle	Parameter	Value	Units
$\phi = 80°$	α	$0.95 \pm 0.01(\text{stat.}) \pm 0.01(\text{syst.})$	
	β'	$0.191 \pm 0.010(\text{stat.}) \pm 0.016(\text{syst.})$	$(\text{kV/cm})(\text{g/cm}^2)\text{MeV}^{-1}$
	A	$0.85 \pm 0.03(\text{stat.}) \pm 0.03(\text{syst.})$	
	k	$0.053 \pm 0.008(\text{stat.}) \pm 0.001(\text{syst.})$	$(\text{kV/cm})(\text{g/cm}^2)\text{MeV}^{-1}$
$\phi = 70°$	α	$0.96 \pm 0.01(\text{stat.}) \pm 0.01(\text{syst.})$	
	β'	$0.206 \pm 0.010(\text{stat.}) \pm 0.015(\text{syst.})$	$(\text{kV/cm})(\text{g/cm}^2)\text{MeV}^{-1}$
	A	$0.89 \pm 0.03(\text{stat.}) \pm 0.03(\text{syst.})$	
	k	$0.0661 \pm 0.0090(\text{stat.}) \pm 0.0001(\text{syst.})$	$(\text{kV/cm})(\text{g/cm}^2)\text{MeV}^{-1}$
$\phi = 60°$	α	$0.94 \pm 0.01(\text{stat.}) \pm 0.02(\text{syst.})$	
	β'	$0.172 \pm 0.009(\text{stat.}) \pm 0.014(\text{syst.})$	$(\text{kV/cm})(\text{g/cm}^2)\text{MeV}^{-1}$
	A	$0.83 \pm 0.03(\text{stat.}) \pm 0.03(\text{syst.})$	
	k	$0.0438 \pm 0.007(\text{stat.}) \pm 0.0003(\text{syst.})$	$(\text{kV/cm})(\text{g/cm}^2)\text{MeV}^{-1}$
$\phi = 50°$	α	$0.94 \pm 0.01(\text{stat.}) \pm 0.02(\text{syst.})$	
	β'	$0.160 \pm 0.008(\text{stat.}) \pm 0.015(\text{syst.})$	$(\text{kV/cm})(\text{g/cm}^2)\text{MeV}^{-1}$
	A	$0.84 \pm 0.03(\text{stat.}) \pm 0.03(\text{syst.})$	
	k	$0.0428 \pm 0.0070(\text{stat.}) \pm 0.0004(\text{syst.})$	$(\text{kV/cm})(\text{g/cm}^2)\text{MeV}^{-1}$

It is important to note that the recombination models are developed with assumptions and approximations. They fail to describe the data unless some further adjustments are performed, like the introduction of the parameter A in the Birks law and $\alpha \neq 1$ in the box model, which are not justified by the columnar or box theory. Another approximation is that to assign the charge corresponding to a hit to a single initial energy contribution. This can be inaccurate when delta rays with a significantly different stopping power contribute to part of the charge collected. The common approach is therefore to consider the recombination models as effective

models, a prescription to convert the charge observed to the energy deposition with a data-driven parametrisation.

A set of recombination parameters was estimated for ProtoDUNE-SP. The use of these parameters has the potential to allow for a more precise simulation of recombination effects and improve the dE/dx reconstruction. It has been shown that such study can be performed with cosmic muons, which are also present in other DUNE detectors, though with a smaller rate in the deep underground chambers.

Chapter 8

Conclusion

This thesis has presented a selection of cosmic ray muons that stop in the ProtoDUNE-SP detector. They can both be used as a source of uniform (in the region far from their stopping point) and variable (in the Bragg peak region) energy deposition. The sample of cosmic muons includes particles which cross the TPC cathode and can therefore be fully reconstructed in the three dimensions. This topology was integrated with a sample of muons that cross the TPC anodes, identified thanks to the novel algorithm developed.

A study of the charge recombination that immediately follows the creation of electrons and positive argon ions by ionising muons was performed. Two models, the modified box model and the Birks law, were studied and their parametrisation measured using ProtoDUNE-SP data after developing and validating the measurement procedure using simulations. A set of parameters was measured assuming no angular dependence of recombination, in continuity with previous LArTPC experiments. The angular dependence predicted by the theory was also explored.

The main results of this thesis are:

- A novel selection of cosmic muons that enter through the TPC anodes, which complement the selection of cathode-crossing muons.
- A high-purity selection of fully-reconstructed muons that stop in the detector, span the majority of the active volume and can be used for calibration purposes.

- Both the Birks and the modified box models describe the ProtoDUNE-SP data well, but the use of Birks law results in a better agreement between data and theoretical expectations.

- The recombination models including the angular dependence fit the data well in all the angular bins. The $\sin\phi$ modulation, if included in the Birks law, gives a reasonably consistent set of recombination parameters across all angular bins in the explored dE/dx range. The same can not be said for the modified box model.

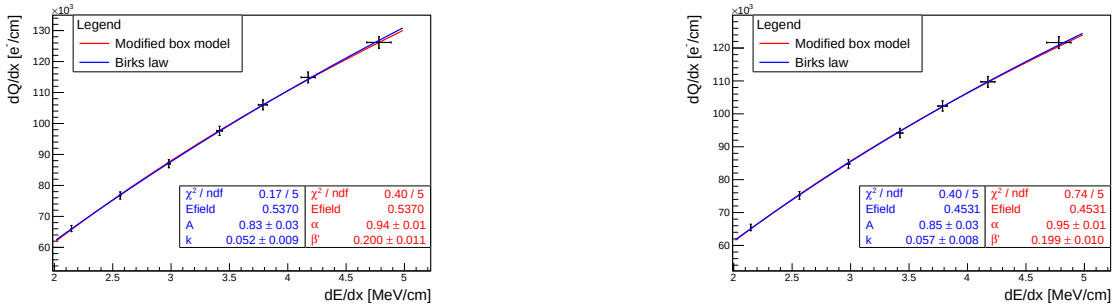
- The recombination model parameters were determined for the ProtoDUNE-SP experiment and show good agreement with previous measurements.

The methods developed and the measurements performed in this thesis represent useful results to understand and characterise the response of the ProtoDUNE-SP detector. They can be used to guide similar studies in the DUNE detectors, especially in the single phase modules, for which an energy threshold of $\mathcal{O}(10\,\mathrm{MeV})$ [50] is expected.

Appendix A

Additional Plots for Anode and Cathode-Crossing Muon Comparison

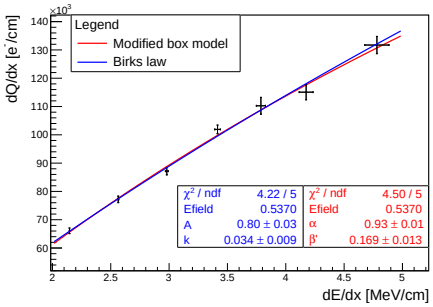
In Chapter 7 the sources of systematic uncertainties on the measurements of the recombination parameters are discussed. In this appendix, the fit to the anode and cathode-crossing muon samples are presented separately. Figure A.1 shows the fits for each sample when ignoring the angular dependence (Equations 7.10 and 7.11). The fits with the included $\sin\phi$ (Equations 7.12 and 7.13) are given in Figures A.2 and A.3.



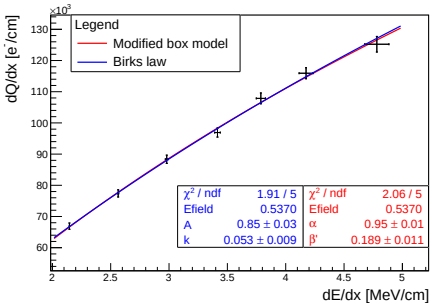
(a) Selected cathode-crossing track.

(b) Selected anode-crossing track.

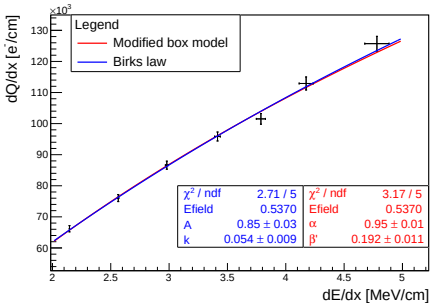
Figure A.1: Recombination fits for cathode (left) and anode (right) crossing stopping muons without the $\sin\phi$ dependence in data.



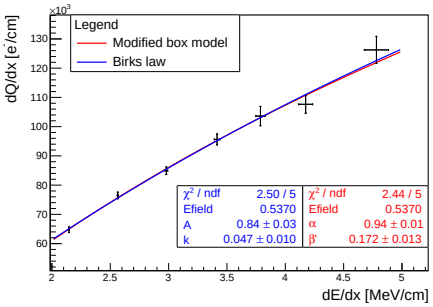
(a) $\phi = 80°$.



(b) $\phi = 70°$.

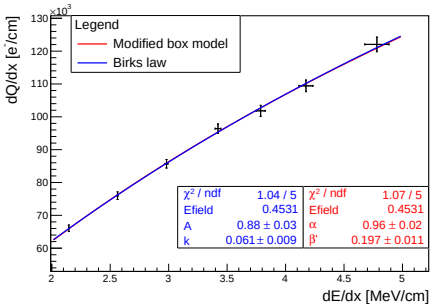


(c) $\phi = 60°$.

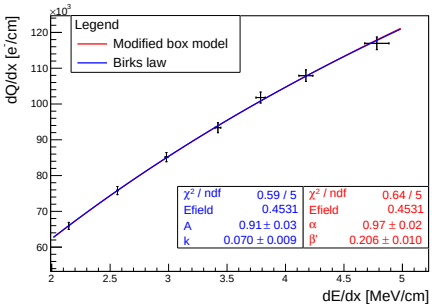


(d) $\phi = 50°$.

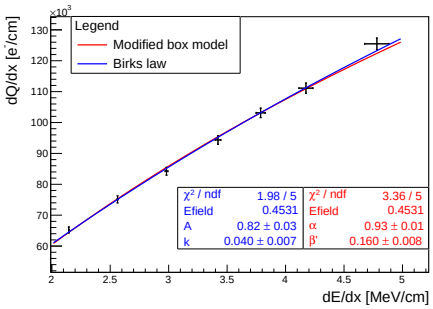
Figure A.2: Recombination fits for cathode-crossing stopping muons for different angular bins.



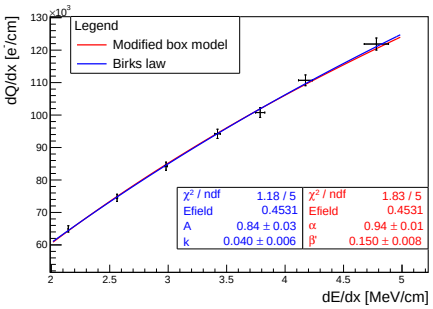
(a) $\phi = 80°$.



(b) $\phi = 70°$.



(c) $\phi = 60°$.



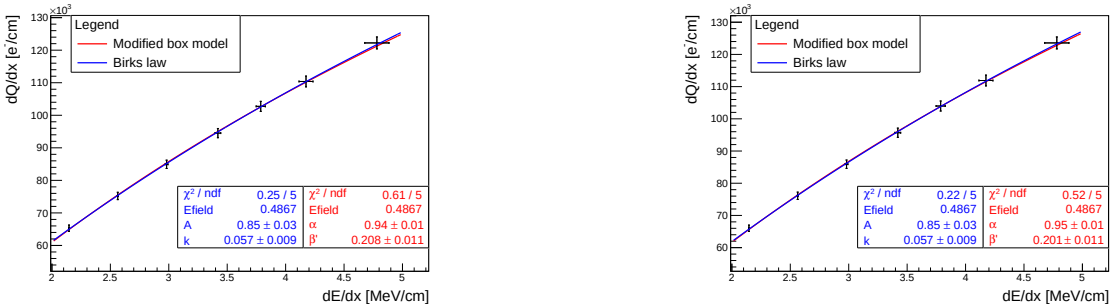
(d) $\phi = 50°$.

Figure A.3: Recombination fits for anode-crossing stopping muons for different angular bins.

Appendix B

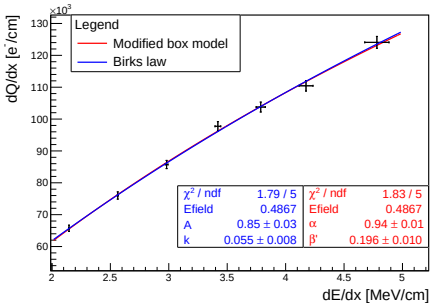
Additional Plots to Evaluate the Impact of the Electron Lifetime

Chapter 7 contains a brief study aimed at understanding the impact of the uncertainties on the electron lifetime correction on the measured recombination parameters. This appendix contains various recombination fits performed to extract the results discussed in the main text. Figure B.1 shows the fits for the merged sample for a lifetime variation of +10% ($\tau_{+10\%}$) and −10% ($\tau_{-10\%}$) with respect to the lifetime measured by the purity monitors when ignoring the angular dependence. Figures B.2 and B.3 show the fits for different values of the angle ϕ and with $\tau_{+10\%}$ and $\tau_{-10\%}$ respectively.

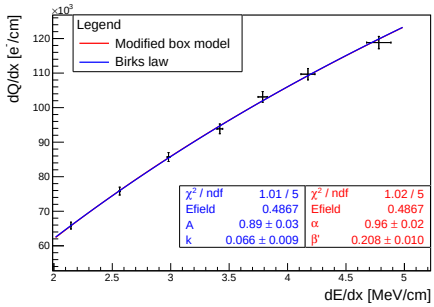


(a) $\tau_{+10\%}$. (b) $\tau_{-10\%}$.

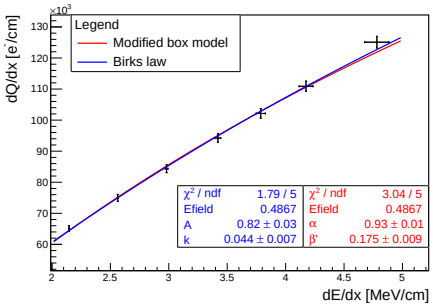
Figure B.1: Recombination fits for the selected stopping muons using all values of ϕ in the case of electron lifetime $\tau_{+10\%}$ (left) and $\tau_{-10\%}$ (right).



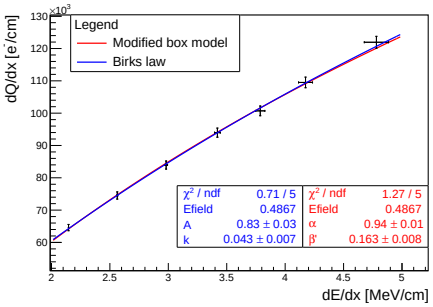
(a) $\phi = 80°$.



(b) $\phi = 70°$.

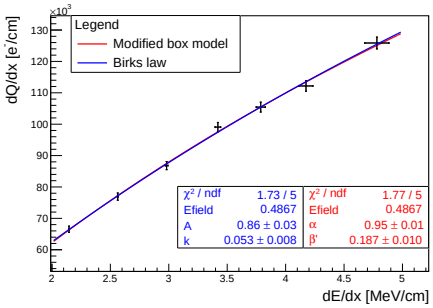


(c) $\phi = 60°$.

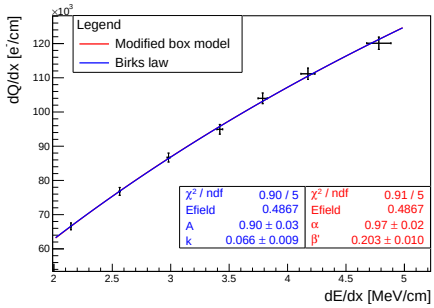


(d) $\phi = 50°$.

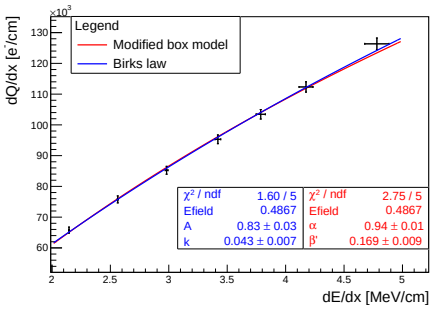
Figure B.2: Recombination fits for the selected stopping muons for each angular bin in the case of electron lifetime $\tau_{+10\%}$.



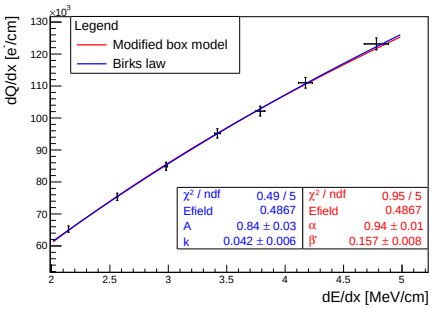
(a) $\phi = 80°$.



(b) $\phi = 70°$.



(c) $\phi = 60°$.



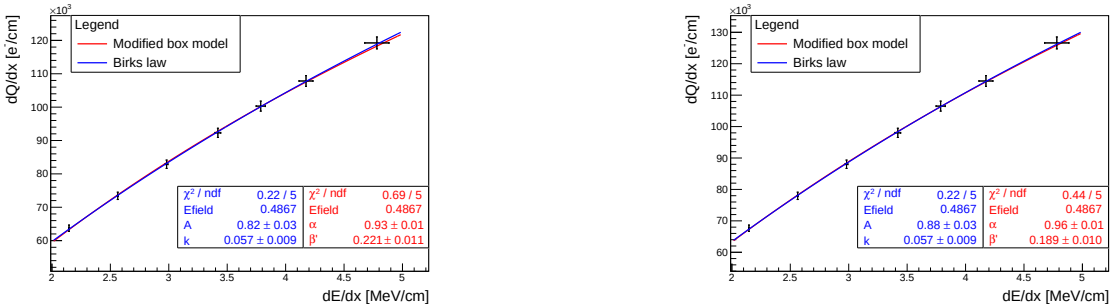
(d) $\phi = 50°$.

Figure B.3: Recombination fits for the selected stopping muons for each angular bin in the case of electron lifetime $\tau_{-10\%}$.

Appendix C

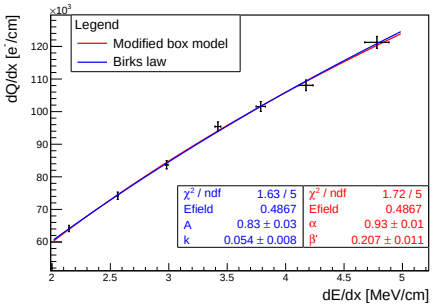
Additional Plots to Evaluate the Impact of different $C_{\mathbf{cal}}$ values

Chapter 7 contains a brief study aimed at understanding the impact of the calibration constant C_{cal} on the measured recombination parameters. This appendix contains various recombination fits performed to extract the results discussed in the main text. Figure C.1 shows the fits for the merged sample of anode and cathode-crossing muons for a C_{cal} variation of $+3\%$ and -3% with respect to the value used in [62] ($C^0_{\text{cal}} = 1.029 \times 10^{-3}$ ADCxtick/e) when ignoring the angular dependence. Figures C.2 and C.3 show the fits for different values of the angle ϕ and with the variation of $+3\%$ and -3% respectively.

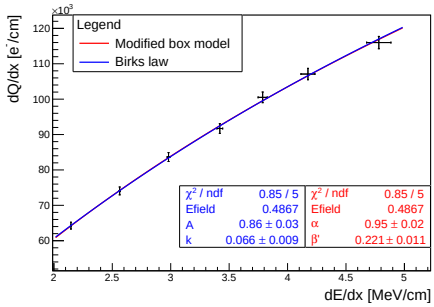


(a) $C^0_{\text{cal}} + 3\%$. (b) $C^0_{\text{cal}} - 3\%$.

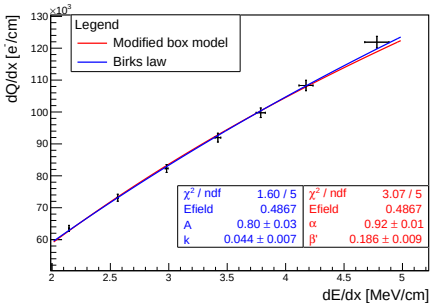
Figure C.1: Recombination fits for the selected stopping muons using all values of ϕ in the case of a C_{cal} variation of $+3\%$ (left) and -3% (right).



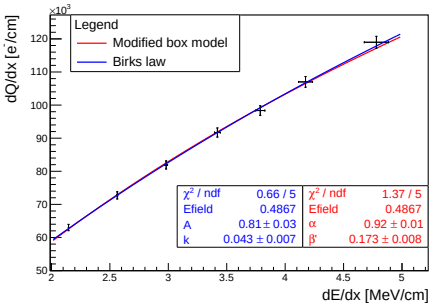
(a) $\phi = 80°$.



(b) $\phi = 70°$.

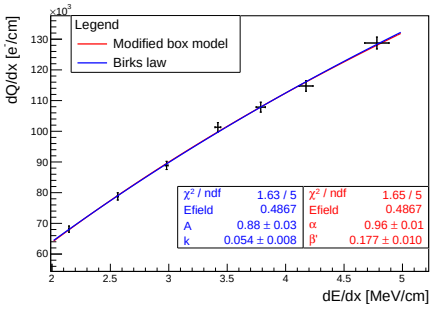


(c) $\phi = 60°$.

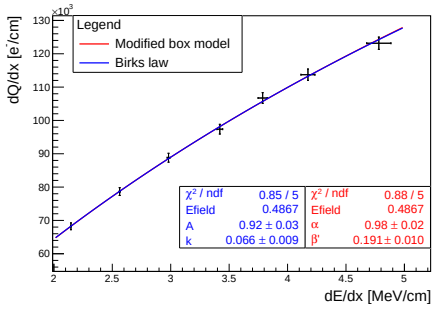


(d) $\phi = 50°$.

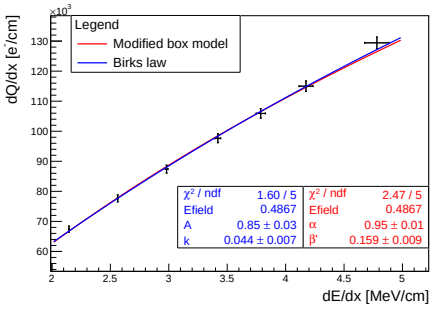
Figure C.2: Recombination fits for the selected stopping muons for each angular bin in the case of C_{cal} 3% larger than C^0_{cal}.



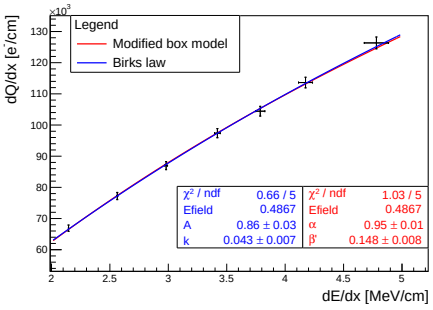
(a) $\phi = 80°$.



(b) $\phi = 70°$.



(c) $\phi = 60°$.



(d) $\phi = 50°$.

Figure C.3: Recombination fits for the selected stopping muons for each angular bin in the case of C_{cal} 3% smaller than C^0_{cal}.

References

[1] P. A. R. Ade et al. "Planck 2013 results. XVI. Cosmological parameters". In: *Astron. Astrophys.* 571 (2014), A16. DOI: 10.1051/0004-6361/201321591. arXiv: 1303.5076 [astro-ph.CO].

[2] J Chadwick. "Intensitätsverteilung im magnetischen Spectrum der β-Strahlen von radium B + C". In: *Verhandl. Dtsc. Phys. Ges.* 16 (1914), p. 383. URL: http://cds.cern.ch/record/262756.

[3] Wolfgang Pauli. "Pauli letter collection: letter to Lise Meitner". Typed copy. URL: https://cds.cern.ch/record/83282.

[4] Enrico Fermi. "Tentativo di una Teoria Dei Raggi β". In: *Nuovo Cim* 11 (1934). URL: https://doi.org/10.1007/BF02959820.

[5] H Bethe and R Peierls. "The "Neutrino"". In: *Nature* 133 (1934), p. 532. URL: https://doi.org/10.1038/133532a0.

[6] C. L. Cowan et al. "Detection of the free neutrino: A Confirmation". In: *Science* 124 (1956), pp. 103–104. DOI: 10.1126/science.124.3212.103.

[7] G. Danby et al. "Observation of High-Energy Neutrino Reactions and the Existence of Two Kinds of Neutrinos". In: *Phys. Rev. Lett.* 9 (1962), pp. 36–44. DOI: 10.1103/PhysRevLett.9.36.

[8] K. Kodama et al. "Observation of tau neutrino interactions". In: *Phys. Lett. B* 504 (2001), pp. 218–224. DOI: 10.1016/S0370-2693(01)00307-0. arXiv: hep-ex/0012035.

[9] G. Alexander et al. "Electroweak parameters of the Z^0 resonance and the Standard Model: the LEP Collaborations". In: *Phys. Lett. B* 276 (1992), pp. 247–253. DOI: 10.1016/0370-2693(92)90572-L.

[10] John N. Bahcall, Aldo M. Serenelli, and Sarbani Basu. "New solar opacities, abundances, helioseismology, and neutrino fluxes". In: *Astrophys. J. Lett.* 621 (2005), pp. L85–L88. DOI: 10.1086/428929. arXiv: astro-ph/0412440.

[11] Raymond Davis Jr., Don S. Harmer, and Kenneth C. Hoffman. "Search for neutrinos from the sun". In: *Phys. Rev. Lett.* 20 (1968), pp. 1205–1209. DOI: 10.1103/PhysRevLett.20.1205.

[12] D. Vignaud. "The GALLEX solar neutrino experiment". In: *Nucl. Phys. B Proc. Suppl.* 60 (1998). Ed. by J. N. Capdevielle, M. Froissart, and C. Meynadier, pp. 20–29. DOI: 10.1016/S0920-5632(97)00498-2.

[13] Q. R. Ahmad et al. "Direct evidence for neutrino flavor transformation from neutral current interactions in the Sudbury Neutrino Observatory". In: *Phys. Rev. Lett.* 89 (2002), p. 011301. DOI: 10.1103/PhysRevLett.89.011301. arXiv: nucl-ex/0204008.

[14] A. Yu. Smirnov. *Solar neutrinos: Oscillations or No-oscillations?* Sept. 2016. arXiv: 1609.02386 [hep-ph].

[15] K. S. Hirata et al. "Observation of a small atmospheric muon-neutrino / electron-neutrino ratio in Kamiokande". In: *Phys. Lett. B* 280 (1992), pp. 146–152. DOI: 10.1016/0370-2693(92)90788-6.

[16] Y. Fukuda et al. "Evidence for oscillation of atmospheric neutrinos". In: *Phys. Rev. Lett.* 81 (1998), pp. 1562–1567. DOI: 10.1103/PhysRevLett.81.1562. arXiv: hep-ex/9807003.

[17] K. Eguchi et al. "First results from KamLAND: Evidence for reactor anti-neutrino disappearance". In: *Phys. Rev. Lett.* 90 (2003), p. 021802. DOI: 10.1103/PhysRevLett.90.021802. arXiv: hep-ex/0212021.

[18] T. Araki et al. "Measurement of neutrino oscillation with KamLAND: Evidence of spectral distortion". In: *Phys. Rev. Lett.* 94 (2005), p. 081801. DOI: 10.1103/PhysRevLett.94.081801. arXiv: hep-ex/0406035.

[19] D. G. Michael et al. "Observation of muon neutrino disappearance with the MINOS detectors and the NuMI neutrino beam". In: *Phys. Rev. Lett.* 97 (2006), p. 191801. DOI: 10.1103/PhysRevLett.97.191801. arXiv: hep-ex/0607088.

[20] N. Agafonova et al. "Observation of a first ν_τ candidate in the OPERA experiment in the CNGS beam". In: *Phys. Lett. B* 691 (2010), pp. 138–145. DOI: 10.1016/j.physletb.2010.06.022. arXiv: 1006.1623 [hep-ex].

[21] N. Agafonova et al. "Final Results of the OPERA Experiment on ν_τ Appearance in the CNGS Neutrino Beam". In: *Phys. Rev. Lett.* 120.21 (2018). [Erratum: Phys.Rev.Lett. 121, 139901 (2018)], p. 211801. DOI: 10.1103/PhysRevLett.120.211801. arXiv: 1804.04912 [hep-ex].

[22] F. Vannucci. "Interactions of neutrinos with matter". In: *Progress in Particle and Nuclear Physics* 95 (2017), pp. 1–47. ISSN: 0146-6410. DOI: https://doi.org/10.1016/j.ppnp.2017.03.003.

[23] J. A. Formaggio and G. P. Zeller. "From eV to EeV: Neutrino Cross Sections Across Energy Scales". In: *Rev. Mod. Phys.* 84 (2012), pp. 1307–1341. DOI: 10.1103/RevModPhys.84.1307. arXiv: 1305.7513 [hep-ex].

[24] C. Giunti and C. W. Kim. *Fundamentals of Neutrino Physics and Astrophysics.* Oxford University Press, 2007.

[25] Max Aker et al. "First operation of the KATRIN experiment with tritium". In: *Eur. Phys. J. C* 80.3 (2020), p. 264. DOI: 10.1140/epjc/s10052-020-7718-z. arXiv: 1909.06069 [physics.ins-det].

[26] X. Qian and P. Vogel. "Neutrino Mass Hierarchy". In: *Prog. Part. Nucl. Phys.* 83 (2015), pp. 1–30. DOI: 10.1016/j.ppnp.2015.05.002. arXiv: 1505.01891 [hep-ex].

[27] Ara Ioannisian and Stefan Pokorski. "Three Neutrino Oscillations in Matter". In: *Phys. Lett. B* 782 (2018), pp. 641–645. DOI: 10.1016/j.physletb.2018.06.001. arXiv: 1801.10488 [hep-ph].

[28] M. Tanabashi et al. "Review of Particle Physics". In: *Phys. Rev. D* 98.3 (2018), p. 030001. DOI: 10.1103/PhysRevD.98.030001.

[29] Stephen F. King. "Neutrino Mass and Mixing in the Seesaw Playground". In: *Nucl. Phys. B* 908 (2016), pp. 456–466. DOI: 10.1016/j.nuclphysb.2015.12.015. arXiv: 1511.03831 [hep-ph].

[30] P. A. Zyla et al. "Review of Particle Physics". In: *PTEP* 2020.8 (2020), p. 083C01. DOI: 10.1093/ptep/ptaa104.

[31] P. F. de Salas et al. "2020 global reassessment of the neutrino oscillation picture". In: *JHEP* 02 (2021), p. 071. DOI: 10.1007/JHEP02(2021)071. arXiv: 2006.11237 [hep-ph].

[32] B. T. Cleveland et al. "Measurement of the solar electron neutrino flux with the Homestake chlorine detector". In: *Astrophys. J.* 496 (1998), pp. 505–526. DOI: 10.1086/305343.

[33] F. Kaether et al. "Reanalysis of the GALLEX solar neutrino flux and source experiments". In: *Phys. Lett. B* 685 (2010), pp. 47–54. DOI: 10.1016/j.physletb.2010.01.030. arXiv: 1001.2731 [hep-ex].

[34] J. N. Abdurashitov et al. "Measurement of the solar neutrino capture rate with gallium metal. III: Results for the 2002–2007 data-taking period". In: *Phys. Rev. C* 80 (2009), p. 015807. DOI: 10.1103/PhysRevC.80.015807. arXiv: 0901.2200 [nucl-ex].

[35] B. Aharmim et al. "Combined Analysis of all Three Phases of Solar Neutrino Data from the Sudbury Neutrino Observatory". In: *Phys. Rev. C* 88 (2013), p. 025501. DOI: 10.1103/PhysRevC.88.025501. arXiv: 1109.0763 [nucl-ex].

[36] J. Hosaka et al. "Solar neutrino measurements in super-Kamiokande-I". In: *Phys. Rev. D* 73 (2006), p. 112001. DOI: 10.1103/PhysRevD.73.112001. arXiv: hep-ex/0508053.

[37] J. P. Cravens et al. "Solar neutrino measurements in Super-Kamiokande-II". In: *Phys. Rev. D* 78 (2008), p. 032002. DOI: 10.1103/PhysRevD.78.032002. arXiv: 0803.4312 [hep-ex].

[38] K. Abe et al. "Solar neutrino results in Super-Kamiokande-III". In: *Phys. Rev. D* 83 (2011), p. 052010. DOI: 10.1103/PhysRevD.83.052010. arXiv: 1010.0118 [hep-ex].

[39] S. Abe et al. "Precision Measurement of Neutrino Oscillation Parameters with KamLAND". In: *Phys. Rev. Lett.* 100 (2008), p. 221803. DOI: 10.1103/PhysRevLett.100.221803. arXiv: 0801.4589 [hep-ex].

[40] A. Gando et al. "Constraints on θ_{13} from A Three-Flavor Oscillation Analysis of Reactor Antineutrinos at KamLAND". In: *Phys. Rev. D* 83 (2011), p. 052002. DOI: 10.1103/PhysRevD.83.052002. arXiv: 1009.4771 [hep-ex].

[41] A. Gando et al. "Reactor On-Off Antineutrino Measurement with KamLAND". In: *Phys. Rev. D* 88.3 (2013), p. 033001. DOI: 10.1103/PhysRevD.88.033001. arXiv: 1303.4667 [hep-ex].

[42] Alex Himmel. *New Oscillation Results from the NOvA Experiment*. July 2020. DOI: 10.5281/zenodo.3959581. URL: https://doi.org/10.5281/zenodo.3959581.

[43] Patrick Dunne. *Latest Neutrino Oscillation Results from T2K*. July 2020. DOI: 10.5281/zenodo.3959558. URL: https://doi.org/10.5281/zenodo.3959558.

[44] P. Adamson et al. "Combined analysis of ν_μ disappearance and $\nu_\mu \to \nu_e$ appearance in MINOS using accelerator and atmospheric neutrinos". In: *Phys. Rev. Lett.* 112 (2014), p. 191801. DOI: 10.1103/PhysRevLett.112.191801. arXiv: 1403.0867 [hep-ex].

[45] K. Abe et al. "Atmospheric neutrino oscillation analysis with external constraints in Super-Kamiokande I-IV". In: *Phys. Rev. D* 97.7 (2018), p. 072001. DOI: 10.1103/PhysRevD.97.072001. arXiv: 1710.09126 [hep-ex].

[46] M. G. Aartsen et al. "Measurement of Atmospheric Neutrino Oscillations at 6–56 GeV with IceCube DeepCore". In: *Phys. Rev. Lett.* 120.7 (2018), p. 071801. DOI: 10.1103/PhysRevLett.120.071801. arXiv: 1707.07081 [hep-ex].

[47] G. Bak et al. "Measurement of Reactor Antineutrino Oscillation Amplitude and Frequency at RENO". In: *Phys. Rev. Lett.* 121.20 (2018), p. 201801. DOI: 10.1103/PhysRevLett.121.201801. arXiv: 1806.00248 [hep-ex].

[48] D. Adey et al. "Measurement of the Electron Antineutrino Oscillation with 1958 Days of Operation at Daya Bay". In: *Phys. Rev. Lett.* 121.24 (2018), p. 241805. DOI: 10.1103/PhysRevLett.121.241805. arXiv: 1809.02261 [hep-ex].

[49] Y. Abe et al. "First Measurement of θ_{13} from Delayed Neutron Capture on Hydrogen in the Double Chooz Experiment". In: *Phys. Lett. B* 723 (2013), pp. 66–70. DOI: 10.1016/j.physletb.2013.04.050. arXiv: 1301.2948 [hep-ex].

[50] Babak Abi et al. "Deep Underground Neutrino Experiment (DUNE), Far Detector Technical Design Report, Volume II: DUNE Physics". In: (2020). arXiv: 2002.03005 [hep-ex].

[51] Babak Abi et al. "Deep Underground Neutrino Experiment (DUNE), Far Detector Technical Design Report, Volume I Introduction to DUNE". In: *JINST* 15.08 (2020), T08008. DOI: 10.1088/1748-0221/15/08/T08008. arXiv: 2002.02967 [physics.ins-det].

[52] Adam Abed Abud et al. “Deep Underground Neutrino Experiment (DUNE) Near Detector Conceptual Design Report”. In: (Mar. 2021). arXiv: 2103.13910 [physics.ins-det].

[53] C. Rubbia. “The Liquid Argon Time Projection Chamber: A New Concept for Neutrino Detectors”. In: (May 1977).

[54] M. Antonello et al. “Operation and performance of the ICARUS-T600 cryogenic plant at Gran Sasso underground Laboratory”. In: *JINST* 10.12 (2015), P12004. DOI: 10.1088/1748-0221/10/12/P12004. arXiv: 1504.01556 [physics.ins-det].

[55] R. Acciarri et al. “First Measurement of Neutrino and Antineutrino Coherent Charged Pion Production on Argon”. In: *Phys. Rev. Lett.* 113.26 (2014). [Erratum: Phys.Rev.Lett. 114, 039901 (2015)], p. 261801. DOI: 10.1103/PhysRevLett.113.261801. arXiv: 1408.0598 [hep-ex].

[56] Roberto Acciarri et al. “The Liquid Argon In A Testbeam (LArIAT) Experiment”. In: *JINST* 15.04 (2020), P04026. DOI: 10.1088/1748-0221/15/04/P04026. arXiv: 1911.10379 [physics.ins-det].

[57] R. Acciarri et al. “Design and Construction of the MicroBooNE Detector”. In: *JINST* 12.02 (2017), P02017. DOI: 10.1088/1748-0221/12/02/P02017. arXiv: 1612.05824 [physics.ins-det].

[58] Babak Abi et al. “Deep Underground Neutrino Experiment (DUNE), Far Detector Technical Design Report, Volume IV: Far Detector Single-phase Technology”. In: *JINST* 15.08 (2020), T08010. DOI: 10.1088/1748-0221/15/08/T08010. arXiv: 2002.03010 [physics.ins-det].

[59] R. Andrews et al. “A system to test the effects of materials on the electron drift lifetime in liquid argon and observations on the effect of water”. In: *Nucl. Instrum. Meth. A* 608 (2009), pp. 251–258. DOI: 10.1016/j.nima.2009.07.024.

[60] W. Foreman et al. “Calorimetry for low-energy electrons using charge and light in liquid argon”. In: *Phys. Rev. D* 101.1 (2020), p. 012010. DOI: 10.1103/PhysRevD.101.012010. arXiv: 1909.07920 [physics.ins-det].

[61] B. Abi et al. *The Single-Phase ProtoDUNE Technical Design Report*. 2017. arXiv: 1706.07081 [physics.ins-det].

[62] B. Abi et al. “First results on ProtoDUNE-SP liquid argon time projection chamber performance from a beam test at the CERN Neutrino Platform”. In: *JINST* 15.12 (2020), P12004. DOI: 10.1088/1748-0221/15/12/P12004. arXiv: 2007.06722 [physics.ins-det].

[63] D. Montanari et al. “Development of membrane cryostats for large liquid argon neutrino detectors”. In: *IOP Conf. Ser. Mater. Sci. Eng.* 101.1 (2015). Ed. by Peter Kittel and Michael Sumption, p. 012049. DOI: 10.1088/1757-899X/101/1/012049.

[64] D. Adams et al. "The ProtoDUNE-SP LArTPC Electronics Production, Commissioning, and Performance". In: *JINST* 15.06 (2020), P06017. DOI: 10.1088/1748-0221/15/06/P06017. arXiv: 2002.01782 [physics.ins-det].

[65] *DUNE publishes first physics results from prototype detector*. URL: https://news.fnal.gov/2020/12/dune-publishes-first-physics-results-from-prototype-detector/ (visited on 12/01/2022).

[66] A. A. Machado and E. Segreto. "ARAPUCA a new device for liquid argon scintillation light detection". In: *JINST* 11.02 (2016), p. C02004. DOI: 10.1088/1748-0221/11/02/C02004.

[67] Fabio Acerbi and Stefan Gundacker. "Understanding and simulating SiPMs". In: *Nucl. Instrum. Meth. A* 926 (2019), pp. 16–35. DOI: 10.1016/j.nima.2018.11.118.

[68] B. Howard et al. "A Novel Use of Light Guides and Wavelength Shifting Plates for the Detection of Scintillation Photons in Large Liquid Argon Detectors". In: *Nucl. Instrum. Meth. A* 907 (2018), pp. 9–21. DOI: 10.1016/j.nima.2018.06.050. arXiv: 1710.11233 [physics.ins-det].

[69] L. Bugel et al. "Demonstration of a Lightguide Detector for Liquid Argon TPCs". In: *Nucl. Instrum. Meth. A* 640 (2011), pp. 69–75. DOI: 10.1016/j.nima.2011.03.003. arXiv: 1101.3013 [physics.ins-det].

[70] Z. Moss et al. *A Factor of Four Increase in Attenuation Length of Dipped Lightguides for Liquid Argon TPCs Through Improved Coating*. 2016. arXiv: 1604.03103 [physics.ins-det].

[71] Inaki Ortega Ruiz. "Accurate Profile Measurement of the low Intensity Secondary Beams in the CERN Experimental Areas". Presented 23 Feb 2018. Feb. 2018. DOI: 10.5075/epfl-thesis-8278. URL: https://cds.cern.ch/record/2307347.

[72] N. Charitonidis and I. Efthymiopoulos. "Low energy tertiary beam line design for the CERN neutrino platform project". In: *Phys. Rev. Accel. Beams* 20.11 (2017), p. 111001. DOI: 10.1103/PhysRevAccelBeams.20.111001.

[73] A. C. Booth et al. "Particle production, transport, and identification in the regime of 1−7 GeV/c". In: *Phys. Rev. Accel. Beams* 22.6 (2019), p. 061003. DOI: 10.1103/PhysRevAccelBeams.22.061003.

[74] R. Herbst et al. "Design of the SLAC RCE Platform: A general purpose ATCA based data acquisition system". In: *2014 IEEE Nuclear Science Symposium and Medical Imaging Conference and 21st Symposium on Room-Temperature Semiconductor X-ray and Gamma-ray Detectors*. Mar. 2016. DOI: 10.1109/NSSMIC.2014.7431254.

[75] J. Anderson et al. "FELIX: a PCIe based high-throughput approach for interfacing front-end and trigger electronics in the ATLAS Upgrade framework". In: *JINST* 11.12 (2016), p. C12023. DOI: 10.1088/1748-0221/11/12/C12023.

[76] K. Biery et al. “artdaq: An Event-Building, Filtering, and Processing Framework”. In: *IEEE Trans. Nucl. Sci.* 60 (2013), pp. 3764–3771. DOI: 10.1109/TNS.2013.2251660.

[77] E. L. Snider and G. Petrillo. “LArSoft: Toolkit for Simulation, Reconstruction and Analysis of Liquid Argon TPC Neutrino Detectors”. In: *J. Phys. Conf. Ser.* 898.4 (2017). Ed. by Richard Mount and Craig Tull, p. 042057. DOI: 10.1088/1742-6596/898/4/042057.

[78] C. Green et al. “The Art Framework”. In: *J. Phys. Conf. Ser.* 396 (2012). Ed. by Michael Ernst et al., p. 022020. DOI: 10.1088/1742-6596/396/2/022020.

[79] T. J. Roberts et al. “G4Beamline Particle Tracking in Matter-dominated Beam Lines”. In: *Conf. Proc. C* 0806233 (2008). Ed. by Ivan Andrian and Christine Petit-Jean-Genaz, WEPP120.

[80] T. T. Böhlen et al. “The FLUKA Code: Developments and Challenges for High Energy and Medical Applications”. In: *Nucl. Data Sheets* 120 (2014), pp. 211–214. DOI: 10.1016/j.nds.2014.07.049.

[81] Alfredo Ferrari et al. *FLUKA: A multi-particle transport code (Program version 2005)*. 2005. DOI: 10.2172/877507.

[82] *Methodical Accelerator Design CERN*. URL: http://mad.web.cern.ch/mad/ (visited on 05/08/2021).

[83] D. Heck et al. *CORSIKA: A Monte Carlo code to simulate extensive air showers*. 1998.

[84] S. Agostinelli et al. “GEANT4–a simulation toolkit”. In: *Nucl. Instrum. Meth. A* 506 (2003), pp. 250–303. DOI: 10.1016/S0168-9002(03)01368-8.

[85] Rob Veenhof. *Methodical Accelerator Design CERN*. URL: https://garfield.web.cern.ch/garfield/ (visited on 06/08/2021).

[86] R. Veenhof. “GARFIELD, recent developments”. In: *Nucl. Instrum. Meth. A* 419 (1998). Ed. by M. Krammer et al., pp. 726–730. DOI: 10.1016/S0168-9002(98)00851-1.

[87] R. Brun and F. Rademakers. “ROOT: An object oriented data analysis framework”. In: *Nucl. Instrum. Meth. A* 389 (1997). Ed. by M. Werlen and D. Perret-Gallix, pp. 81–86. DOI: 10.1016/S0168-9002(97)00048-X.

[88] Bruce Baller. “Liquid argon TPC signal formation, signal processing and reconstruction techniques”. In: *JINST* 12.07 (2017), P07010. DOI: 10.1088/1748-0221/12/07/P07010. arXiv: 1703.04024 [physics.ins-det].

[89] Simon Ramo. “Currents induced by electron motion”. In: *Proc. Ire.* 27 (1939), pp. 584–585. DOI: 10.1109/JRPROC.1939.228757.

[90] C. Adams et al. “Ionization electron signal processing in single phase LArTPCs. Part I. Algorithm Description and quantitative evaluation with MicroBooNE simulation”. In: *JINST* 13.07 (2018), P07006. DOI: 10.1088/1748-0221/13/07/P07006. arXiv: 1802.08709 [physics.ins-det].

[91] C. Adams et al. "Ionization electron signal processing in single phase LArTPCs. Part II. Data/simulation comparison and performance in MicroBooNE". In: *JINST* 13.07 (2018), P07007. DOI: 10.1088/1748-0221/13/07/P07007. arXiv: 1804.02583 [physics.ins-det].

[92] J. S. Marshall and M. A. Thomson. "The Pandora Software Development Kit for Pattern Recognition". In: *Eur. Phys. J. C* 75.9 (2015), p. 439. DOI: 10.1140/epjc/s10052-015-3659-3. arXiv: 1506.05348 [physics.data-an].

[93] R. Acciarri et al. "The Pandora multi-algorithm approach to automated pattern recognition of cosmic-ray muon and neutrino events in the MicroBooNE detector". In: *Eur. Phys. J. C* 78.1 (2018), p. 82. DOI: 10.1140/epjc/s10052-017-5481-6. arXiv: 1708.03135 [hep-ex].

[94] Aidan Reynolds. "Evaluating the low-energy response of the ProtoDUNE-SP detector using Michel electrons". PhD thesis. University of Oxford, 2020.

[95] P. Abratenko et al. "Measurement of space charge effects in the MicroBooNE LArTPC using cosmic muons". In: *JINST* 15.12 (2020), P12037. DOI: 10.1088/1748-0221/15/12/P12037. arXiv: 2008.09765 [physics.ins-det].

[96] C. Adams et al. "Calibration of the charge and energy loss per unit length of the MicroBooNE liquid argon time projection chamber using muons and protons". In: *JINST* 15.03 (2020), P03022. DOI: 10.1088/1748-0221/15/03/P03022. arXiv: 1907.11736 [physics.ins-det].

[97] R. Acciarri et al. "A Study of Electron Recombination Using Highly Ionizing Particles in the ArgoNeuT Liquid Argon TPC". In: *JINST* 8 (2013), P08005. DOI: 10.1088/1748-0221/8/08/P08005. arXiv: 1306.1712 [physics.ins-det].

[98] M. Miyajima et al. "Average energy expended per ion pair in liquid argon". In: *Phys. Rev. A* 9 (1974), pp. 1438–1443. DOI: 10.1103/PhysRevA.9.1438.

[99] T. Doke. "Fundamental Properties of Liquid Argon, Krypton and Xenon as Radiation Detector Media". In: *Portugal. Phys.* 12 (1981), pp. 9–48.

[100] R.L. Platzman. "Total ionization in gases by high-energy particles: An appraisal of our understanding". In: *The International Journal of Applied Radiation and Isotopes* 10.2 (1961), pp. 116–127. ISSN: 0020-708X. DOI: https://doi.org/10.1016/0020-708X(61)90108-9.

[101] Mariusz Wojcik and M Tachiya. "Electron thermalization and electron–ion recombination in liquid argon". In: *Chemical Physics Letters* 379.1 (2003), pp. 20–27. ISSN: 0009-2614. DOI: https://doi.org/10.1016/j.cplett.2003.08.006.

[102] Ulrich Sowada, John M. Warman, and Matthijs P. de Haas. "Hot-electron thermalization in solid and liquid argon, krypton, and xenon". In: *Phys. Rev. B* 25 (5 Mar. 1982), pp. 3434–3437. DOI: 10.1103/PhysRevB.25.3434. URL: https://link.aps.org/doi/10.1103/PhysRevB.25.3434.

[103] Ettore Segreto. "Properties of Liquid Argon Scintillation Light Emission". In: *Phys. Rev. D* 103.4 (2021), p. 043001. DOI: 10.1103/PhysRevD.103.043001. arXiv: 2012.06527 [physics.ins-det].

[104] Tadayoshi Doke et al. "Absolute Scintillation Yields in Liquid Argon and Xenon for Various Particles". In: *Jap. J. Appl. Phys.* 41 (2002), pp. 1538–1545. DOI: 10.1143/JJAP.41.1538.

[105] V. Boccone. "Test in liquid argon of the light readout system for the ArDM experiment". In: *2009 IEEE Nuclear Science Symposium Conference Record (NSS/MIC)*. 2009, pp. 1597–1600. DOI: 10.1109/NSSMIC.2009.5402253.

[106] D. E. Grosjean et al. "Absolute luminescence efficiency of ion-bombarded solid argon". In: *Phys. Rev. B* 56 (11 Sept. 1997), pp. 6975–6981. DOI: 10.1103/PhysRevB.56.6975. URL: https://link.aps.org/doi/10.1103/PhysRevB.56.6975.

[107] R. T. Scalettar et al. "Critical test of geminate recombination in liquid argon". In: *Phys. Rev. A* 25 (4 Apr. 1982), pp. 2419–2422. DOI: 10.1103/PhysRevA.25.2419. URL: https://link.aps.org/doi/10.1103/PhysRevA.25.2419.

[108] Elena Aprile et al. "Energy Resolution Studies of Liquid Argon Ionization Detectors". In: *Nucl. Instrum. Meth. A* 261 (1987), pp. 519–526. DOI: 10.1016/0168-9002(87)90362-7.

[109] S. Amoruso et al. "Study of electron recombination in liquid argon with the ICARUS TPC". In: *Nuclear Instruments and Methods in Physics Research Section A: Accelerators, Spectrometers, Detectors and Associated Equipment* 523.3 (2004), pp. 275–286. ISSN: 0168-9002. DOI: https://doi.org/10.1016/j.nima.2003.11.423. URL: https://www.sciencedirect.com/science/article/pii/S0168900204000506.

[110] Shinzou Kubota, Masahiko Hishida, and Akira Nohara. "Variation of scintillation decay in liquid argon excited by electrons and alpha particles". In: *Nuclear Instruments and Methods* 150.3 (1978), pp. 561–564. ISSN: 0029-554X. DOI: https://doi.org/10.1016/0029-554X(78)90128-3. URL: https://www.sciencedirect.com/science/article/pii/0029554X78901283.

[111] R. Acciarri et al. "Effects of Nitrogen contamination in liquid Argon". In: *JINST* 5 (2010), P06003. DOI: 10.1088/1748-0221/5/06/P06003. arXiv: 0804.1217 [nucl-ex].

[112] D. Totani. *Xe doping.* URL: https://indico.fnal.gov/event/46995/contributions/204800/attachments/138579/173590/XEDopSArap.pdf.

[113] Tadayoshi Doke et al. "Let dependence of scintillation yields in liquid argon". In: *Nuclear Instruments and Methods in Physics Research Section A: Accelerators, Spectrometers, Detectors and Associated Equipment* 269.1 (1988), pp. 291–296. ISSN: 0168-9002. DOI: https://doi.org/10.1016/0168-9002(88)90892-3. URL: https://www.sciencedirect.com/science/article/pii/0168900288908923.

[114] Shinzou Kubota et al. “Dynamical behavior of free electrons in the recombination process in liquid argon, krypton, and xenon”. In: *Phys. Rev. B* 20 (8 Oct. 1979), pp. 3486–3496. DOI: 10.1103/PhysRevB.20.3486. URL: https://link.aps.org/doi/10.1103/PhysRevB.20.3486.

[115] R. Acciarri et al. “Oxygen contamination in liquid Argon: Combined effects on ionization electron charge and scintillation light”. In: *JINST* 5 (2010), P05003. DOI: 10.1088/1748-0221/5/05/P05003. arXiv: 0804.1222 [nucl-ex].

[116] W. Walkowiak. “Drift velocity of free electrons in liquid argon”. In: *Nucl. Instrum. Meth. A* 449 (2000), pp. 288–294. DOI: 10.1016/S0168-9002(99)01301-7.

[117] Norman Gee et al. “Ion and electron mobilities in cryogenic liquids: Argon, nitrogen, methane, and ethane”. In: *Journal of Applied Physics* 57.4 (1985), pp. 1097–1101. DOI: 10.1063/1.334552.

[118] X. Luo and F. Cavanna. “Ion transport model for large LArTPC”. In: *JINST* 15.03 (2020), p. C03034. DOI: 10.1088/1748-0221/15/03/C03034.

[119] Tingjun Yang. “Calibration of calorimetric measurement in a liquid argon time projection chamber”. In: *Instruments* 5.1 (2020), p. 2. DOI: 10.3390/instruments5010002. arXiv: 2012.01319 [physics.ins-det].

[120] George Bakale et al. “Effect of an electric field on electron attachment to sulfur hexafluoride, nitrous oxide, and molecular oxygen in liquid argon and xenon”. In: *The Journal of Physical Chemistry* 80.23 (Nov. 1976), pp. 2556–2559. DOI: 10.1021/j100564a006.

[121] R. Andrews et al. “A system to test the effect of materials on electron drift lifetime in liquid argon and the effect of water”. In: *Nuclear Instruments and Methods in Physics Research Section A: Accelerators, Spectrometers, Detectors and Associated Equipment* 608.2 (2009), pp. 251–258. ISSN: 0168-9002. DOI: https://doi.org/10.1016/j.nima.2009.07.024.

[122] Kyoji Shinsaka and Yoshihiko Hatano. “Electron-ion recombination in condensed nonpolar media”. In: *Nuclear Instruments and Methods in Physics Research Section A: Accelerators, Spectrometers, Detectors and Associated Equipment* 327.1 (1993), pp. 7–10. ISSN: 0168-9002. DOI: https://doi.org/10.1016/0168-9002(93)91397-6. URL: https://www.sciencedirect.com/science/article/pii/0168900293913976.

[123] Thomas M. Miller et al. “Behavior of rate coefficients for ion-ion mutual neutralization, 300–550 K”. In: *The Journal of Chemical Physics* 136.20 (2012), p. 204306. DOI: 10.1063/1.4720499.

[124] L. Onsager. “Initial Recombination of Ions”. In: *Phys. Rev.* 54 (8 Oct. 1938), pp. 554–557. DOI: 10.1103/PhysRev.54.554.

[125] M. Tachiya. “Breakdown of the Onsager theory of geminate ion recombination”. In: *The Journal of Chemical Physics* 89.11 (1988), pp. 6929–6935. DOI: 10.1063/1.455317.

[126] George Jaffé. "Zur Theorie der Ionisation in Kolonnen". In: *Annalen der Physik* 347.12 (1913), pp. 303–344. DOI: https://doi.org/10.1002/andp.19133471205.

[127] J. Thomas and D. A. Imel. "Recombination of electron-ion pairs in liquid argon and liquid xenon". In: *Phys. Rev. A* 36 (2 July 1987), pp. 614–616. DOI: 10.1103/PhysRevA.36.614.

[128] John B. Birks. *The Theory and practice of scintillation counting*. 1964.

[129] E. Aprile, W.H. Ku, and J. Park. "Delta electron production and the ultimate energy resolution of liquid argon ionization detectors". In: *IEEE Transactions on Nuclear Science* 35.1 (1988), pp. 37–41. DOI: 10.1109/23.12669.

[130] V. Cataudella et al. "Directional modulation of electron-ion pairs recombination in liquid argon". In: *JINST* 12.12 (2017), P12002. DOI: 10.1088/1748-0221/12/12/P12002.

[131] Stefano Cecchini and Maurizio Spurio. *Atmospheric muons: experimental aspects*. 2012. arXiv: 1208.1171 [astro-ph.EP].

[132] D E Groom, N V Mokhov, and S I Striganov. "Muon Stopping-Power and Range Tables: 10MeV - 100 TeV". In: *Atomic Data and Nuclear Data Tables* 78.2 (Dec. 1999). ISSN: 0092-640X. URL: https://www.osti.gov/biblio/788009.

[133] *Atomic and nuclear properties of liquid argon (Ar)*. URL: https://pdg.lbl.gov/2020/AtomicNuclearProperties/HTML/liquid_argon.html (visited on 06/08/2021).

[134] L. Landau. "On the energy loss of fast particles by ionization". In: *J. Phys. (USSR)* 8 (1944), pp. 201–205.

[135] P. V. Vavilov. "Ionization losses of high-energy heavy particles". In: *Sov. Phys. JETP* 5 (1957), pp. 749–751.

[136] C. Møller. "On the radiative collision between fast charged particles". In: *Proceedings of the Royal Society of London. Series A - Mathematical and Physical Sciences* 152.876 (1935), pp. 481–496. DOI: 10.1098/rspa.1935.0203. eprint: https://royalsocietypublishing.org/doi/pdf/10.1098/rspa.1935.0203.

[137] H. J. Bhabha. "The scattering of positrons by electrons with exchange on Dirac's theory of the positron". In: *Proceedings of the Royal Society of London. Series A - Mathematical and Physical Sciences* 154.881 (1936), pp. 195–206. DOI: 10.1098/rspa.1936.0046. eprint: https://royalsocietypublishing.org/doi/pdf/10.1098/rspa.1936.0046.

[138] R. Acciarri et al. "Michel Electron Reconstruction Using Cosmic-Ray Data from the MicroBooNE LArTPC". In: *JINST* 12.09 (2017), P09014. DOI: 10.1088/1748-0221/12/09/P09014. arXiv: 1704.02927 [physics.ins-det].

[139] *Convoluted Landau and Gaussian Fitting Example*. URL: https://root.cern.ch/root/html404/examples/langaus.C.html (visited on 10/09/2021).

[140] *dQ/dx Calibration*. URL: https://indico.cern.ch/event/1050785/contributions/4414849/attachments/2273194/3861042/Various_Thoughts_on_dQdx_Calibration.pdf (visited on 10/09/2021).

[141] *Electric Field Estimation*. URL: https://indico.fnal.gov/event/20939/contributions/59979/attachments/37548/45624/Efield_studies.pdf (visited on 10/09/2021).